Structural and electronic properties of fulleride superconductors

MCDONALD, MARTIN,THOMAS

Structural and electronic properties of fulleride superconductors

by

Martin T. McDonald

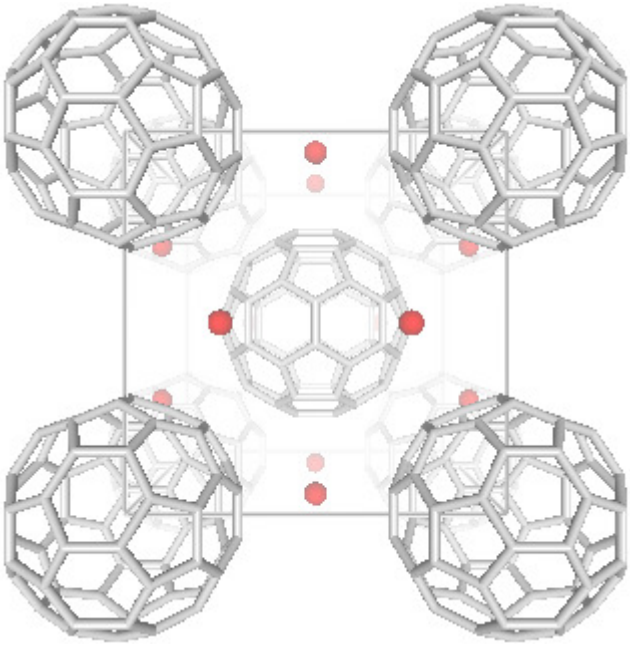

A dissertation submitted to the University of Durham in fulfilment of the requirements for the award of the degree of Doctor of Philosophy.

April 2010

Declaration

I hereby declare that this thesis has not been submitted, either in the same of different form, to this or any other university for a degree.

Signature:

Acknowledgements

First I'd like to acknowledge my supervisor Prof. Kosmas Prassides for offering me a position within his research group, as well as his supervision for the last 4 years. I'd like to thank him for giving me the opportunity to work at facilities such as ISIS in Oxford England, KEK synchrotron in Japan and ESRF in southern France.

Many thanks to my co-workers Dr. Yasuhiro Takabayashi, Dr. Takeshi Nagawanta and Dionisis Papanikalaou for their assistance in the technical and synthetic aspects of my work.

Special thanks to Prof. M. J. Rosseinsky and Dr. A. Ganin for their help and guidance in the interpretation of my results, as well as specialist training required for low temperature solvent C_{60}-based synthesis.

I am grateful to Prof. Y. Iwasa at the University of Tohoku in Japan and his research group for giving me the opportunity to visit Japan and work at the KEK synchrotron.

I would also like to thank Dr. S. Margadonna of the University of Edinburgh for the helpful discussion and advice/guidance.

I would like to express my gratitude to all those in the Chemistry of department of the University of Durham who have helped me to carry out a significant part of my work described herein and all those in stores and various workshops for their time and assistance.

Finally, I would like to thanks my mother Jane, my dad John and my sister Fiona for all their support in pursuit of my career.

University of Durham

Martin T. McDonald Degree: D.Phil

Structural and electronic properties of fulleride superconductors

Abstract

In the present thesis, I discuss some of the current advances in research in the field of the solid state science of fullerenes. The reaction of C_{60} with alkali metals using both conventional solid state and low temperature solution-based synthesis techniques has led to the production of fulleride salts with interesting structural and superconducting properties. In superconducting A_3C_{60} systems, it has been widely reported that T_c increases monotonically with interfulleride separation. Of particular interest is the family $Na_2Rb_{1-x}Cs_xC_{60}$ ($0 \leq x \leq 1$) as they display a much steeper rate of change of T_c with interfulleride spacing. Here we discuss the related family of quaternary fullerides, $Na_{2-x}K_xCsC_{60}$ in an attempt to explore the consequences of this trend and produce fulleride salts with elevated T_c's

In addition, the monotonic increase in T_c with increasing interfulleride separation has driven attempts towards the synthesis of new superconducting fullerides with very large lattice parameters. A key material among the A_3C_{60} systems is the end member, Cs_3C_{60}, which has remained elusive in attempts to synthesise it by traditional solid state techniques due to the thermodynamic instability of this phase caused by the accommodation of the large Cs^+ ion (r = 1.67 Å) in the small tetrahedral holes (r = 1.12 Å). Here we report the synthesis of “FCC rich” and "A15 rich" samples of the series, $Rb_xCs_{3-x}C_{60}$ ($0.0 \leq x \leq 0.5$) *via* low temperature synthetic techniques utilising the solvents ammonia and methylamine, respectively. This allowed us to study the effects of both chemical (by partial substitution of Cs^+ by the smaller Rb^+ cation) and physical pressure upon the electronic and superconducting properties of these materials.

For all samples, detailed structural studies have been performed using synchrotron X-ray powder diffraction and magnetic behaviour using SQUID magnetometry techniques.

Table of Contents

Chapter 1

Introduction - Fullerene C_{60} and fulleride salts

1.1 Introduction

Graphite and diamond are the two best-known allotropes of carbon with distinctly different chemical and physical properties. In both structures adjacent C's form strong covalent bonds; however, graphite is quite soft as there are only weak forces between layers. Intercalation of graphite by alkali metals has been extensively studied and superconductivity with a critical temperature (T_c) of 0.55 K was reported for the potassium composition, KC_8 as early as 1965.[1] The more recent discovery of the new allotropes of carbon (fullerenes), which are soluble in aromatic hydrocarbon solvents, has led to an interesting and challenging time in materials chemistry. A fullerene is any molecule composed entirely of carbon, in the form of a hollow sphere, ellipsoid, or tube. Spherical fullerenes are also called buckyballs and cylindrical ones are called carbon nanotubes. The spherical allotropes form a series of polyhedral cluster molecules, formula C_n (where *n* is even), and are comprised of pentagonal and hexagonal rings of carbon atoms.

The first fullerene, characterised by Kroto *et al*[2] in 1985, was C_{60}. This initiated the study of a new topic in carbon chemistry and physics. C_{60} was given the name buckminsterfullerene in honour of the architect R. Buckminster Fuller whose buildings comprised of geodesic domes, which use the same principal building blocks as the fullerenes. Kroto and his colleagues synthesised a product that contained a mixture of fullerenes (predominately C_{60}) by laser vaporising graphite in an atmosphere of He gas, temperatures achieved were in excess of $>10^4$ ^oC.

Three years later, a group led by Krätschmer *et al*[3] re-examined mass spectrometry data they obtained in 1983 from soot produced by striking an arc between graphite electrodes at about 3500^{o}C under a low pressure of helium gas. They found it to contain large concentrations of C_{60} and C_{70}. This has proven a very simple method for producing bulk mixtures of fullerenes. Later in 1990, pure samples of C_{60} were obtained by chromatographic separation of the above products[4] - this technique is widely used today to produce bulk quantities of C_{60}.

1.2 Molecular and crystal structures of C_{60}

The C_{60} molecule comprises sixty carbon atoms positioned at the vertices of a truncated icosahedron, which has 90 edges, 12 non-adjacent pentagons and 20 hexagons (~7 Å diameter). C_{60} has two distinct C-C bond lengths (1.40 and 1.45 Å), which indicates that the π electrons are not delocalised across the entire molecule. There are 30 short C-C (6:6) double bonds bridging adjacent hexagons and 60 long C-C (6:5) single bonds bridging hexagonal and pentagonal faces.

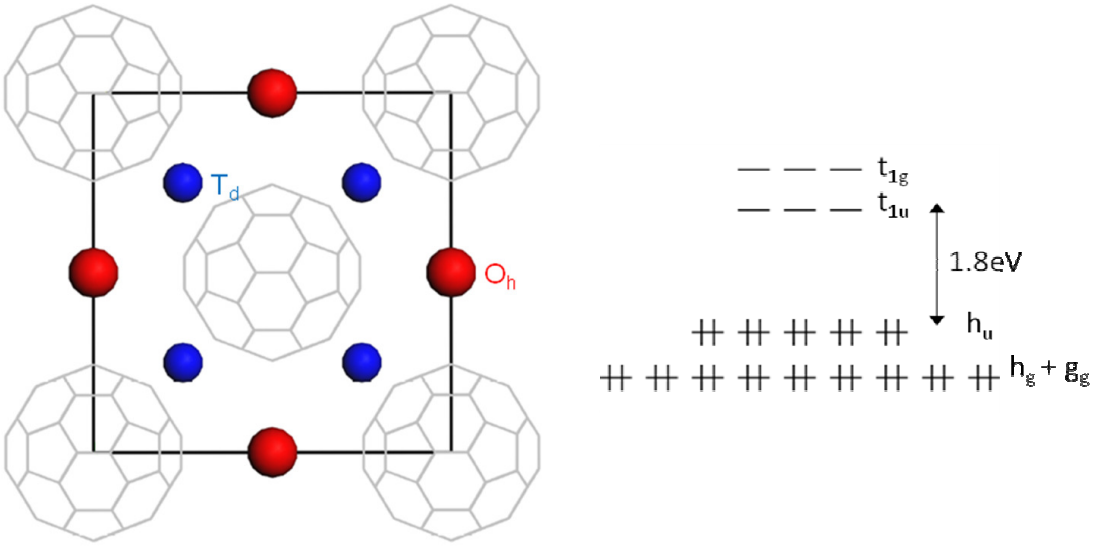

Fig 1.1: (**Left**) Schematic representation of the face-centred cubic structure (FCC) of solid C_{60}. Red spheres = octahedral cavities, blue spheres = tetrahedral cavities. (**Right**) The molecular orbital (labeled) scheme of the C_{60} molecule, the band gap between the HOMO and LUMO is shown.

At room temperature, C_{60} adopts an FCC cubic structure (space group $Fm\bar{3}m$) (Fig 1.1). The size of the unit cell at room temperature is 14.17(1) Å and the nearest neighbour C_{60}-C_{60} distances are 10.02(2) Å. Refinement of the synchrotron X-ray diffraction data shows that the C_{60} molecules are translationally ordered but rotationally disordered at room temperature.[5] As C_{60} is cooled below 260 K, additional Bragg peaks appear that violate the FCC lattice extinction rules. Instead the low-temperature crystal structure of C_{60} is characterized by primitive cubic symmetry

(space group $Pa\bar{3}$). The C_{60} molecules have rotationally ordered and can adopt one of two molecular orientations related by either a 98^{o} (major) or a 38^{o} (minor) anticlockwise rotation of each C_{60} unit about their local [111] axes. Further cooling below 90 K causes the molecules to freeze entirely (orientational glass)[6] and the C_{60} molecules no longer have enough energy to flip between the two orientations and their relative ratio remains constant on further cooling. 83.5% of the C_{60} molecules exist in the energetically more favourable orientation (orientation environment detailed further in the introduction of *chapter 5*).

Within the close-packed A_3C_{60} FCC structure, large cavities exist where smaller atoms, ions or molecules can be incorporated. There are two types of high-symmetry cavities: a larger cavity (r = 2.06 Å) defined by six C_{60} neighbours (octahedral symmetry, O_h) and a smaller cavity (r = 1.12 Å) defined by four C_{60} molecules (tetrahedral symmetry, T_d). These cavities are depicted in Fig 1.1. Due to the larger size of the O_h cavity, large alkali cations such as K^+ (r = 1.37 Å)[7] and Cs^+ (r = 1.67 Å) can be intercalated with little impact on the structural packing of the material. On the other hand, intercalation of larger cations into the T_d cavity causes a phase transition whereby the C_{60}^{3-} anions are no longer spherically disordered; instead they are merohedrally disordered with a 50:50 occupancy ratio of two molecular orientations. The structural cross over between spherically and merohedrally disordered systems is described in more detail in the introduction of *chapter 5*.

The electronic structure of C_{60} reveals the presence of a triply degenerate (t_{1u} symmetry) lowest unoccupied molecular orbital (LUMO). The energy gap between the highest occupied molecular orbital (HOMO) and the LUMO is relatively small (~1.8 eV) which renders the C_{60} molecule a good electron acceptor. The next unoccupied orbital (LUMO+1) is also triply degenerate (t_{1g} symmetry) and is also low lying and accessible. This allows C_{60} to accept up to 12 electrons.

1.3 Superconductivity in intercalated fullerides

Investigations of metal intercalation of C_{60} were initiated after Krätschmer's discovery of the method for producing C_{60} in the bulk (*section 1.1*), as researchers were able to employ traditional solid state synthesis techniques. The first major discovery was that by Haddon *et al*[8] who showed that intercalation of alkali-metal ions into C_{60} gave materials that exhibited metallic behaviour. Shortly after that it was discovered that some of these alkali-metal intercalated compounds were superconducting with transition temperatures still only surpassed by the high-T_c cuprates,[9] MgB_2,[10] and the iron pnictides.[11,12,13] Superconductivity in fullerides was first reported for K_3C_{60} at 18 K,[14] then Rb_3C_{60} at 29 K,[15] Rb_2CsC_{60} at 31 K and $RbCs_2C_{60}$ at 33 K,[16] these materials adopt the merohedrally disordered structure (Fig 1.2). Somewhat later, trace superconductivity at the <0.1% level was reported under pressure at 40 K for a fulleride salt with nominal stoichiometry Cs_3C_{60};[17] however, the identity and structure of this phase remained unknown for many years.

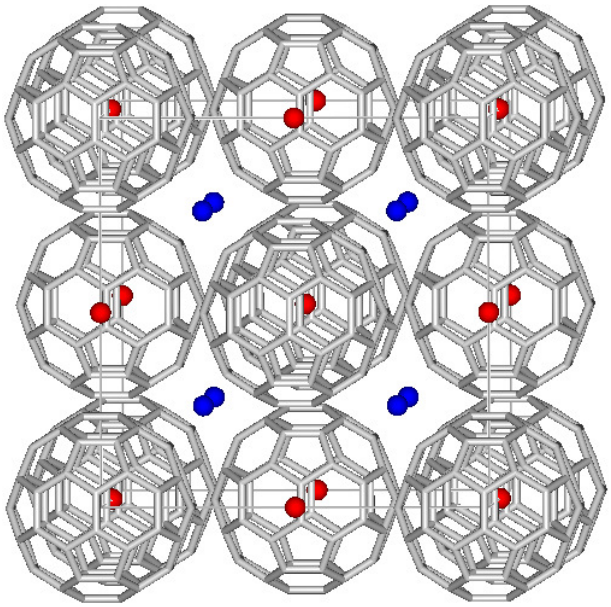

Fig 1.2: A_3C_{60} FCC unit cell (space group $Fm\bar{3}m$). Only one of the two C_{60}^{3-} anion orientations is present for clarity, orientations related by 90° rotation about [100] occur in a disordered manner. The A^+ ions are shown as red and blue spheres in order to signify symmetry-inequivalent positions in the unit cell.

Indeed the synthesis of a crystalline Cs_3C_{60} sample remained elusive until very recently; however, new solution-based low-temperature synthetic protocols involving solvents such as ammonia (NH_3) and methylamine ($MeNH_2$) were developed, allowing the synthesis and structural and electronic characterisation of the superconducting phase of Cs_3C_{60} which adopts a BCC-based (A15 structural type) crystal structure (Fig 1.3).[18,19,20] Studies utilising methylamine have shown that the material synthesised was not superconducting at ambient pressure; however, application of pressure induced an insulator-to-metal transition and a bulk superconducting phase with a transition temperature of 38 K and a shielding fraction of 68% was obtained at ~0.7 GPa. The FCC phase in these samples was isolated as a minority phase and was poorly crystalline. Before the start of this work there have been no reports of successfully synthesising FCC-rich crystalline Cs_3C_{60} materials.

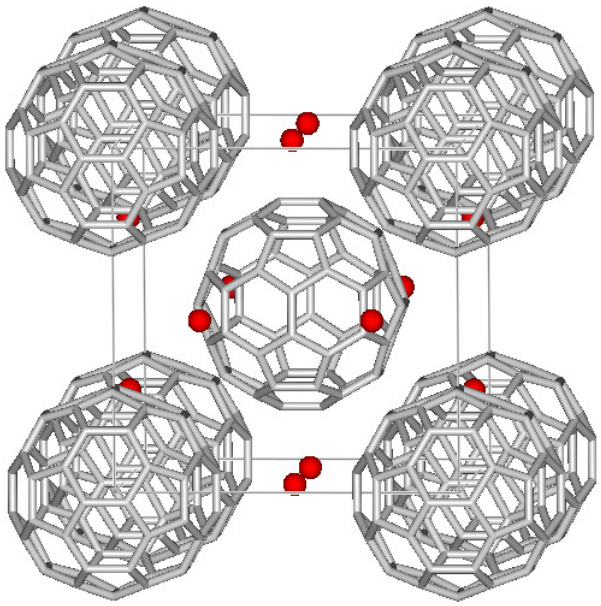

Fig 1.3: A_3C_{60} A15 unit cell (space group $Pm\bar{3}n$). Within this structure there is only one C_{60}^{3-} orientation. All Cs^+ ions (red spheres) are symmetry equivalent.

1.3.1 Superconductivity mechanism

Understanding the superconducting mechanism in the fullerides has been of particular importance. For a long time after superconductivity was discovered in the fullerides, the Bardeen-Cooper-Schrieffer[21] (BCS) theory developed for describing the superconductivity of metals and alloys appeared to account well for many of the observations in these systems.

In this model, superconductivity is a macroscopic effect that arises because pairs of electrons (Cooper pairs) can move freely through the crystal lattice of a material with no resistance (detailed further in *section 2.5.5*). The relatively large values of T_c in alkali-metal (A) doped C_{60} naturally arise because of the high density-of-states at the Femi level, $N(\varepsilon_F)$, and the strong coupling of electrons to high frequency phonons. The high frequency phonons implicated are those of the intramolecular modes of C_{60}, and are therefore relatively unaffected by the type of the alkali-metal dopant. In the weak-coupling BCS limit, T_c is determined by the phonon frequency (ω), the density-of- states at the Femi level and the extent of coupling between the electrons and lattice vibrations, V[22,23] by the following equation:

$$k_B T_c = \hbar\omega \exp\left(\frac{-1}{VN(\varepsilon_F)}\right) \qquad (1.1)$$

where $\hbar$ is Planck's constant and k_B is Boltzmann's constant.

The trend observed in FCC-structured A_3C_{60} materials is that T_c increases with increasing cation size in the tetrahedral cavity (and therefore increasing separation between C_{60} molecules); this simplified observation can be well interpreted using BCS theory. Increasing the lattice parameter leads to a narrowing of the t_{1u}–derived conduction band, whose width depends on the overlap of the wavefunctions of adjacent C_{60} molecules. Therefore, for a fixed band filling, the density-of-states at the Fermi level, $N(\varepsilon_F)$ increases, leading to an increase in T_c.[24]

1.3.2 The t_{1g} superconducting fullerides

The literature contains many examples of superconducting A_3C_{60} materials where the LUMO t_{1u} orbital is half full; however, there are also additional reports of superconductivity in higher valence systems (when the nominal valence of the C_{60} anion necessitates population of the LUMO+1 t_{1g} orbital). There have been less systematic investigations undertaken in this fulleride family, although interesting structural and electronic properties are encountered on a wide range of different compositions. The reason why the solid state chemistry is limited here is due to the difficulties associated with the synthesis of pure phase materials, which involves the reductive intercalation of C_{60} with metals with relatively low vapour pressures under very high annealing temperatures.

In the early 90s, Kortan *et al.* discovered a range of alkali metal intercalated C_{60} compounds with interesting structural and electronic properties. The first relevant study was on the Ca_xC_{60} family of materials[25] where a T_c of 8.4 K was observed for the composition Ca_5C_{60}. It was postulated that when $x < 5$ the Ca^{2+} ions are intercalated directly into the FCC framework with Ca^{2+} occupying the T_d and O_h sites of C_{60}. For stoichiometries of $x \geq 5$, a phase transition occurs and a simple cubic structure is found ($a = 14.01$ Å). In the case of Ca_5C_{60} the electrons donated by the Ca atoms occupy the t_{1u} band and also partially occupy the t_{1g} band.

Kortan *et al*. also reported superconductivity in materials containing Sr^{2+} and Ba^{2+} with higher reductive states of C_{60} (I.e. A_xC_{60}; $A > 3$).[26] Initially the superconducting phases were identified as body-centered-cubic-structured (BCC) Ba_6C_{60} and Sr_6C_{60} (Fig 1.4(b), space group $Im\bar{3}$), until Baenitz *et al*. suggested that along with Ba_6C_{60} there was another superconducting phase (Ba_4C_{60}) which had a much larger superconducting fraction (Ba_4C_{60} ~22% compared to Ba_6C_{60} ~3%).[27] However, this conclusion remained controversial due to the small volume fraction of the body-centred-orthorhombic (BCO) Ba_4C_{60} phase (Fig 1.4(a)). It was subsequently established that Ba_6C_{60} and Sr_6C_{60} were not superconducting but metallic,[28] and bulk superconducting samples were produced for the BCO phases, Ba_4C_{60} ($T_c = 6.7$ K) and Sr_4C_{60} ($T_c = 4.4$ K).[29]

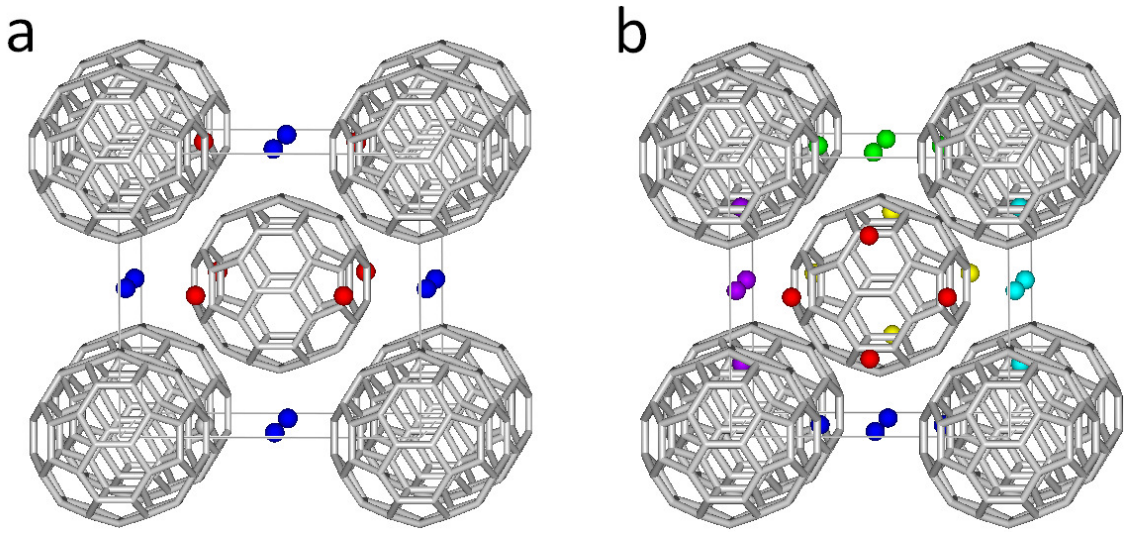

Fig 1.4: **a**, BCO unit cell (space group *Immm*), for Ba_4C_{60} and Sr_4C_{60}. **b**, BCC unit cell (space group $Im\bar{3}$), for Ba_6C_{60} and Sr_6C_{60}. In both **a** and **b**, one unique orientation of the C_{60}^{3-} anions is present. In **a**, the Ba^{2+} and Sr^{2+} ions are shown as red and blue spheres in order to signify symmetry-inequivalent positions in the unit cell. In **b**, there is only one cation environment; however, each face of the unit cell has its cations coloured differently for clarity.

It is also worth nothing that when synthesising AE_6C_{60} (AE = Ba, Sr) and AE_4C_{60} materials, AE_3C_{60} often forms as a minor impurity phase. Ba_3C_{60} and Sr_3C_{60} are stable insulating materials, which have a completely filled t_{1u} band, and adopt the A15 structure type (space group $Pm\bar{3}n$).[30] This is also the structure adopted by Cs_3C_{60}, which has a T_c of 38 K under high pressure.[18]

Bulk superconductivity is also observed in mixed alkali-alkaline earth fullerides, $A_3AE_3C_{60}$ (A = alkali, AE = alkaline earth). X-ray diffraction studies have shown that these materials adopt a BCC structure (space group $Im\bar{3}$). For systems where AE = Ba^{2+} and A = K^+, Rb^+ Cs^+, T_c decreases with increasing cell volume which is opposite to the trend observed in A_3C_{60} materials. $K_3Ba_3C_{60}$ and $Rb_3Ba_3C_{60}$ have transition temperatures of 5.6 K and 2.0 K, respectively, while $Cs_3Ba_3C_{60}$ is not a superconductor down to 0.5 K.[31,32]

In the late 90s, rare-earth metals were also successfully intercalated into C_{60}, and superconductivity was reported for the phases with composition $RE_{2.75}C_{60}$ (RE = Yb, Sm). The critical temperatures were reported for $Sm_{2.75}C_{60}$ and $Yb_{2.75}C_{60}$ as 8 K[33] and 6

K^{34}, respectively. However, subsequent magnetisation studies on numerous samples showed that the reports of bulk superconductivity have been erroneous.[35,36] Interestingly, the temperature evolution of the structural properties of $Sm_{2.75}C_{60}$ obtained by synchrotron X-ray diffraction at various temperatures between 4 and 295 K revealed that $Sm_{2.75}C_{60}$ exhibits isotropic negative thermal expansion (NTE) in the temperature range 4 to 32 K.[37] The origin of the NTE behaviour has been attributed to temperature induced mixed valence transitions between Sm^{2+} and Sm^{3+} states and are determined by the coupling of the strongly correlated rare-earth metal 4*f* and 5*d* bands with the narrow C_{60} t_{1u} band.

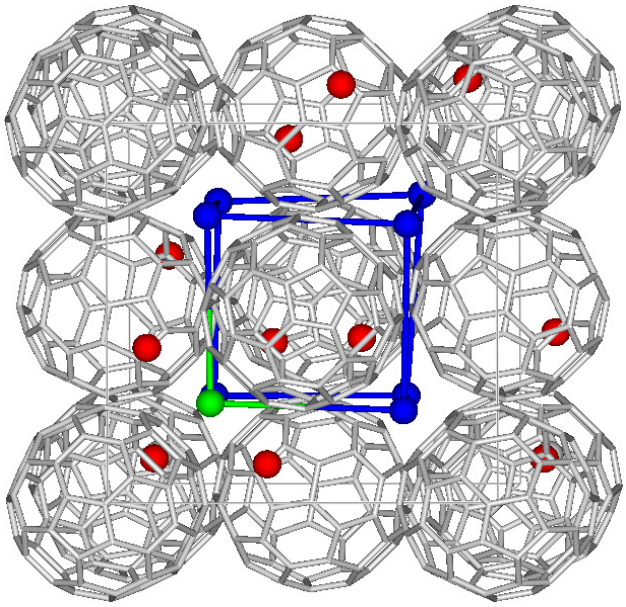

Fig 1.5: Building block of the orthorhombic superstructure of $RE_{2.75}C_{60}$ that can be obtained by doubling the sub-cell along all three lattice directions. Rare-earth cations residing in distorted octahedral and tetrahedral holes are represented by red and blue spheres, respectively. The tetrahedral rare-earth defect is shown as green sphere.

X-ray diffraction studies of $Yb_{2.75}C_{60}$ determined that Yb cations are located in both T_d and O_h cavities of a standard FCC array, and X-ray absorption near-edge structure (XANES) measurements showed that Yb cations exist in the +2 oxidation state. The resolved crystal structure of $Yb_{2.75}C_{60}$ is orthorhombic with space group *Pcab* (Fig 1.5), which is a direct subgroup of $Pa\bar{3}$. The aspects which differentiate the crystal

structure from a standard FCC A_3C_{60} array are the following: the Yb^{2+} cations occupy all O_h and T_d sites; however, one out of every eight T_d sites is vacant. This in turn leads to large displacements of the cations from the centres of the O_h sites (~ 2.3 Å), but smaller displacements from the centres of the T_d sites (~ 0.4 Å). These displacements are directed towards the nearest T_d defects and the mid-point of two neighbouring C_{60} molecules. As a result the T_d defects have long range order and are responsible for the unit cell having dimensions twice as large as those commonly encountered in FCC structures. It has also been shown that the Sm analogue has an identical structure to its Yb counterpart.[38]

The RE_6C_{60} (RE = Eu[39], Sm[40], Yb) family has also be studied; they adopt a BCC structure isostructural to Ba_6C_{60} (Fig 1.4(b)). They are not superconducting; however, Eu_6C_{60} is found to be ferromagnetic below 14 K.[41]

1.3.3 Lithium and sodium fullerides

In superconducting A_3C_{60} systems, it has been widely reported that T_c increases monotonically with interfulleride separation.[8,42,43,44,45] However, distinct anomalies have been encountered for Na- and Li-containing fullerides. The Li_3C_{60} phase has not been synthesised, as the Li^+ cation is too small to stabilise the A_3C_{60} FCC structure.[46] Correlation of literature T_c values with unit cell volume suggests that for Na_3C_{60} the T_c should be 16 K for the observed lattice parameter. Significantly no superconductivity is observed down to 2 K,[47] as below 250 K the Na_3C_{60} phase disproportionates into Na_2C_{60} and Na_6C_{60}. Superconducting compounds containing smaller alkali metals can be found in $A_2A'C_{60}$, where A = Na or Li and A' = K, Rb or Cs, with the exception of Li_2CsC_{60} and Li_2RbC_{60}, which do not show superconductivity down to 50 mK. The absence of superconductivity in the Li fulleride family has been associated with the presence of strong bonding Li^+-C interactions,[48] which lead to a reduced formal charge of the C_{60}^{n-} ions in Li_2AC_{60}, established experimentally to be ~2.5 by Raman measurements.[49] Half filling the t_{1u} band was achieved for Li_3CsC_{60} which is a bulk superconductor with T_c of 10.5 K, isostructural with the $Na_2A'C_{60}$ phases.[50]

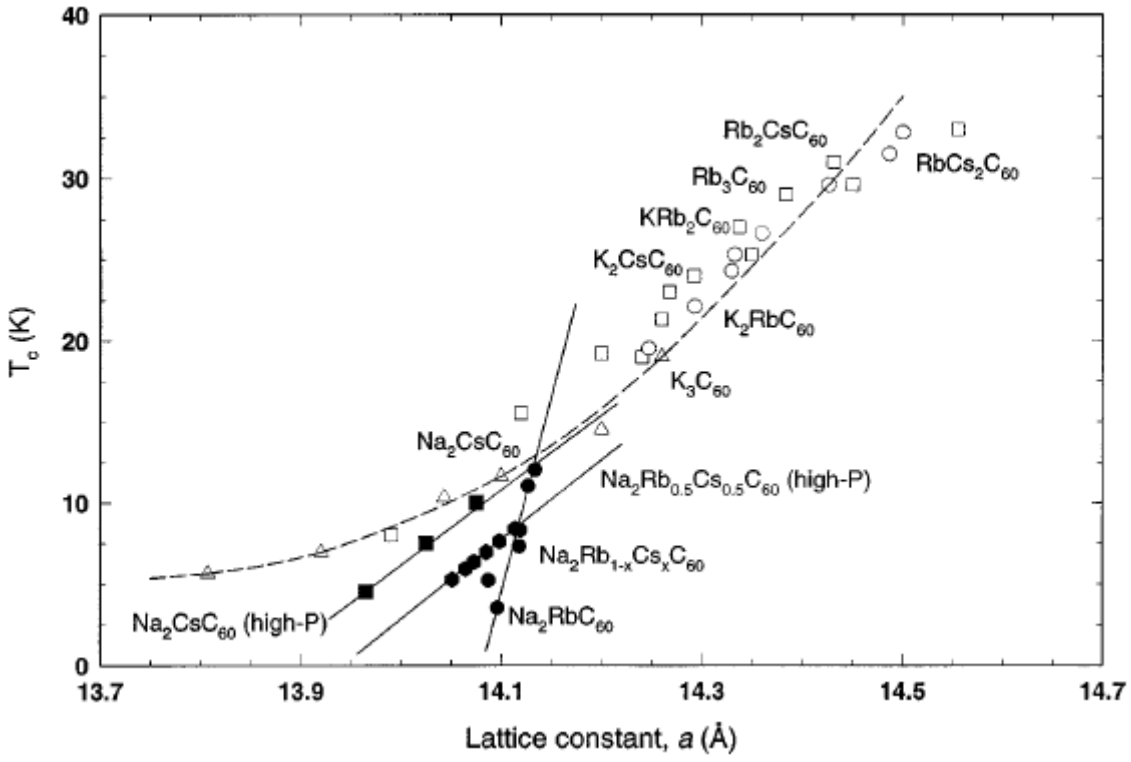

Fig 1.6: Relationship between the superconducting transition temperature T_c and the cubic lattice constants (a) of fulleride salts over a wide range of values for a. Data indicated by open symbols are experimental measurements on fulleride salts with the $Fm\bar{3}m$ structure at both ambient and elevated pressures. Data indicated by solid symbols are experimental measurements on fulleride salts with the $Pa\bar{3}$ structure at ambient (circles) and elevated (squares for Na_2CsC_{60} and hexagons for $Na_2Rb_{0.5}Cs_{0.5}C_{60}$) pressures. The dotted line is the T_c-a relationship expected from BCS theory using $N(\varepsilon_F)$ values obtained by local density approximation (LDA) calculations, while the straight lines are guides to the eye.[50]

The $Na_2Rb_{1-x}Cs_xC_{60}$ ($1 \leq x \leq 0$)[51] family of materials are of particular interest as they display a much steeper rate of change of T_c with interfullerene spacing. This phenomenon could be related to the change in orientational state of the C_{60}^{3-} anions in the $Pa\bar{3}$ structure. NMR measurements[52] of Na_2KC_{60}[53] and Na_2RbC_{60} confirm that the $N(\varepsilon_F)$ values are strongly suppressed in agreement with their observed anomalously low T_c values. In these materials the change of the unit cell volume is achieved by changing the size of the cation residing in the octahedral interstices (chemical pressure). On the other hand, magnetic susceptibility measurements at high pressure on Na_2CsC_{60}[54] have led to the conclusion that the effect of physical and chemical pressure on the superconducting properties of the $Pa\bar{3}$ phases are not identical with

chemical pressure suppressing T_c much faster; indeed, physical pressure leads to the same rate of change of T_c as that found in the merohedrally disordered $Fm\bar{3}m$ systems. The structure and electronic properties of sodium fullerides are also sensitive to cooling protocols. For instance, slow cooling of Na_2RbC_{60} causes a dramatic loss in symmetry. Low temperature data collected on this sample showed the formation of a non-superconducting quasi-one-dimensional polymer phase with a monoclinic structure and short inter-ball distances of 9.38 Å, consistent with the formation of singly-bonded C_{60}-C_{60} chains.[55]

1.3.4 $Rb_xCs_{3-x}C_{60}$ ($0.0 \leq x \leq 0.5$)

For samples where x is outside the above described range (i.e. $3.0 \geq x > 0.5$), traditional high temperature direct synthesis techniques have proven very successful, producing crystalline FCC phases with transition temperatures as high as 33 K.[13,14] These techniques begin to fail as we approach the parent material of the series, Cs_3C_{60}.[56] The lack of success can be rationalised in terms of the thermodynamic instability of these phases caused by the attempt to accommodate the large Cs^+ ion (r = 1.70 Å) in the small tetrahedral holes (r = 1.12 Å). As a result, Cs_3C_{60} disproportionates to give the thermodynamically stable Cs_1C_{60} and Cs_4C_{60} phases. In 1995, Palstra *et al* attempted to synthesise Cs_3C_{60} by using ammonia in a solution-based low-temperature synthesis technique;[16] however, the resultant materials were multi-phase and poorly crystalline. This solvent-based synthesis technique inspired later work by Dahlke *et al*, where they again utilised ammonia to isolate the series of compounds, $A_xCs_{3-x}C_{60}$ [where A is either Rb ($0.3 \leq x \leq 1$) or K ($0.3 \leq x \leq 1$)].[57] In their investigations the largest lattice parameter obtained was a = 14.6925(4) Å for a sample with nominal composition $Rb_{0.32}Cs_{2.65}C_{60}$. On reducing the Rb content further in order to achieve larger interfulleride separations there was no increase in the T_c, in fact the volume fractions were substantially suppressed.

More recently low temperature solution techniques involving the solvent methylamine have been employed by Ganin *et al* in the synthesis of C_3C_{60}.[58,59] Their

comprehensive study led to the isolation of a three-phase material.[18] Low-field magnetisation measurements showed that the material was not superconducting at ambient pressure; however, application of a modest pressure induced superconductivity with a maximum T_c of 38 K at an applied pressure of 0.7 GPa. The majority A15 phase responsible for the high T_c was BCC-structured. Two additional polymorphs are observed, notably the elusive FCC phase is present in reasonable fraction; however, due to the low annealing temperatures it is poorly crystalline. The third phase was identified as a non-superconducting body-centred orthorhombic (BCO) phase. Using density functional theory (DFT), the electronic properties of the A15 and FCC polymorphs were compared.[19] For the partially occupied t_{1u} band it was found that both the density of states (DOS) at the Fermi level and the bandwidth were larger for the A15 phase. This is surprising as V/C_{60} is larger for the A15 (818 Å) than the FCC (807 Å) phase, as if the model were controlled only by packing density, then W for the A15 phase should be smaller. This peculiarity can be traced back to the differences that exist in the inter-anion overlap between the C_{60}'s. In the A15 phase, adjacent C_{60}'s meet with hexagonal faces interacting, while in the FCC phase, near-neighbour contact is via single C-C bonds. Therefore it can be said that the A15 phase displays more effective overlap interactions between neighbouring anions, thus showing that the A15 and FCC phases are electronically different classes of fulleride superconductors.

1.4 Outline of Thesis

The aim of my thesis is to research into the synthesis of selected key members of the alkali fulleride families and to investigate their structural, superconducting and electronic properties, using principally experimental techniques such as synchrotron X-ray powder diffraction and SQUID magnetometry. The experimental techniques as well as their theoretical aspects are discussed in detail in *chapter 2* of the thesis.

Chapter 3 describes the synthesis of "FCC rich" samples of the series, $Rb_xCs_{3-x}C_{60}$ ($0.0 \leq x \leq 0.5$) *via* low temperature synthetic techniques utilising NH_3 as the solvent. Previous studies were not able to successfully synthesise crystalline samples of this FCC polymorph. In order to drive the formation of the FCC phase, a high annealing temperature of 450^{o}C of the reaction precursors for extended periods of time was found to be necessary. Following the successful synthesis, the evolution of the electronic properties with unit cell volume is documented; this was achieved by tuning the interfullerene separation both by physical and chemical pressure.

Chapter 4 mimics the style of chapter 3 but focuses on samples of the "A15 rich" series of $Rb_xCs_{3-x}C_{60}$ ($0.0 \leq x \leq 0.5$) materials. The samples studied in this chapter were prepared in the department of Chemistry at the University of Durham by Manolis Tzirakis, aided by Mr MT McDonald and Professor Kosmas Prassides. Preparative details of these samples were comparable to those employed for the FCC-rich analogues; however, the solvent used in this case was $MeNH_2$ and the annealing temperatures and times were much lower and shorter than those used in the NH_3 based method (180^{o}C for 48 hrs). Earlier studies in this laboratory have been restricted to the evolution of the properties of the A15 phase of Cs_3C_{60}. Here the work is extended to include chemical pressure effects, i.e. Rb^+ cation substitution.

In *chapter 5* the synthesis of the series of quaternary fullerides, $Na_{2-x}K_xCsC_{60}$ ($0.0 \leq x \leq 2.0$) is presented along with the investigation of their structural and superconducting properties. The superconducting behaviour has been also studied as a function of K^+ content for selected compositions for two cooling protocols: samples were either slowly cooled or quenched into liquid nitrogen in an attempt to

differentiate between formation of possible thermodynamically and kinetically stable products.

Finally, Chapter 6 summarises the results of the present work, its contribution to our understanding of the properties of fullerene-based materials, and the future directions.

1.5 References

[1] Hannay B. W., Geballe T. H., Matthias B. T., Andres K., Schmidt P., MacNair D. *Phys. Rev. Lett.* **1965**, 14, 225-226

[2] Kroto H. W., Heath J. R., O'Brien S. C., Curl R. F., Smalley R. E. *Nature* **1985**, 318, 162–163

[3] Krätschmer W., Lamb. L. D., Fostiropoulos K., Huffman D. R. *Nature* **1990**, 347, 354-358

[4] Taylor R., Hare J. P., Abul-sada A. K., Krot–o H. W. *J. Chem. Soc., Chem. Commun.* **1990**, 1423-1425

[5] Heiney P. A., Fischer J. E., McGhie A. R., Romanow W. J., Denenstein A. M., McCauley J. P., Smith A.B., Cox D. E. *Phys. Rev. Lett.* **1991**, 66, 2911-2914

[6] David W. I. F., Ibberson R. M., Dennis T. J. S., Hare J. P., Prassides K. *Europhys. Lett.* **1992**, 18, 219-225

[7] Shannon R. D., *Acta Cryst. A* **1976**, 32, 751-767

[8] Haddon R. C,. Herbard A. F., Rosseinsky M. J., Murphy D. W., Duclos S. J., Lyons K. B., Miller B., Rosamilla J. M., Fleming R. M., Kortan A. R., Glarum S. H., Makhija A. V., Muller A. J., Eick R. H., Zahurak S. M., Tycko R., Dabbagh G., Thiel F. A. *Nature* **1991**, 350, 320-322

[9] Fleming R. M., Ramirez A. P., Rosseinsky M. J., Murphy D. W., Haddon R. C., Zahurak S. M., Makhija A. V. *Nature* **1991**, 352, 787-788

[10] Nagamatsu J., Nakagawa N., Muranaka T., Zenitani Y., Akimitsu J. *Nature* **2001**, 410, 63-64

[11] Kamihara Y., Watanabe T., Hirano M., Hosono H. *J. Am. Chem. Soc.* **2008**, 130, 3296-3297

[12] Wu G., Xie Y. L., Chen H., Zhong M., Liu R. H., Shi R. H., Li Q. J., Wang X. F., Wu T., Yan Y. J., Ying J. J., Chen X. H. J. *Phys. Condens. Matter.* **2009**, 21, 142203

[13] Takabayashi Y., McDonald M. T., Papanikolaou D., Margadonna S., Wu G., Liu R. H., Chen X. H., Prassides K. *J. Am. Chem. Soc.* **2008**, 130, 9242-9243

[14] Hebard A. F., Rosseinsky M. J., Haddon R. C., Murphy D. W., Glarum S. H., Palstra T. T., Ramirez A. P., Kortan A. R. *Nature* **1991**, 350, 600-601

[15] Rosseinsky M. J., Ramirez A. P., Glarum S. H., Murphy D. W., Haddon R. C., Hebard A. F., Palstra T. T., Kortan A. R., Zahurak S. M., Makhija A. V. *Phys. Rev. Lett.* **1991**, 66, 2830-2832

[16] Tanigaki K., Ebbesen T. W., Saito S., Mizuki J., Tsai J. S., Kubo Y., Kuroshima S. *Nature* **1991**, 352, 222-223

[17] Palstra T. T. M., Zhou 0., Iwasa Y., Sulewski P. E., Fleming R. M., Zegarski B. R. *Solid State Commun.* **1995**, 93, 327–330

[18] Ganin A. Y., Takabayashi T., Khimyak Y. Z., Margadonna S., Tamai A., Rosseinsky M. J., Prassides K. *Nature Materials* **2008**, 7, 367-371

[19] Darling G. R., Ganin A. Y., Rosseinsky M. J., Takabayashi Y., Prassides K. *Phys. Rev. Lett.* **2008**, 101, 136404-136408

[20] Takabayashi Y., Ganin A. Y., Jeglic P., Arcon D., Takano T., Iwasa Y., Ohishi Y., Takata M., Takeshita N., Prassides K., Rosseinsky M. J. *Science* **2009**, 232, 1585-1590

[21] Bardeen L., Cooper L. N., Schrieffer J. R. *Phys. Rev.* **1957**, 108, 1175-1204

[22] Prassides K. Curr. Opin. *Solid State Mater. Sci.* **1997**, 2, 433-439

[23] Rosseinsky M. *J. Chem. Mater.* **1998**, 10, 2665-2685

[24] Margadonna S., Prassides K. J. *Solid State Chem.* **2002**, 168, 639–652

[25] Kortan A. R., Kopylov N., Glarum S., Gyorgy E. M., Ramirez A. P., Fleming R. M., Thiel F. A., Haddon R. C. *Nature* **1992**, 355, 529-532

[26] Kortan A. R., Kopylov N., Glarum S., Gyorgy E. M., Ramirez A. P., Fleming R. M., Zhou O., Thiel F. A., Haddon R. C. *Nature* **1992**, 360, 566-568

[27] Baenitz M., Heinze M., Lüders K., Werner H., Schlögl R., Weiden M., Spam G., Steglich F. *Solid State Commun.* **1995**, 96, 539-544

[28] Gogia B., Kordatos K., Suematsu H., Tanigaki K., Prassides K. *Phys. Rev. B* **1998**, 58, 1077-1079

[29] Brown C. M., Taga S., Gogia B., Kordatos K., Margadonna S., Prassides K., Iwasa Y., Tanigaki. K., Fitch A. N., Pattison P. *Phys. Rev.* **1999**, Lett. 83, 2258-2261

[30] Kortan A. R., Kopylov N., Fleming R. M., Zhou O., Thiel F. A., Haddon R. C. *Phys. Rev. B* **1993**, 47, 13070-13073

[31] Iwasa Y., Hayashi H., Furudate T., Mitani T. *Phys. Rev. B* **1996**, 54, 14960-14962

[32] Iwasa Y., Kawaguchi M., Iwasaki H., Mitani T. *Phys. Rev. B* **1998**, 57, 13395-13398

[33] Chen X. H., Roth G. *Phys. Rev. B* **1995**, 52, 15534-15536

[34] Özdas E., Kortan A. R., Kopylov N., Ramirez A. P., Siegrist T., Rabe K. M., Bair H. E., Schuppler S., Citrin P. H. *Nature* **1996**, 375, 126-129

[35] Akada M., Hirai T., Takeuchi J., Yamamoto R., Kumashiro R., Tanigaki K., *Phys. Rev. B* **2006**, 73, 094509

[36] Arvanitidis J., Papagelis K., Margadonna S., Prassides K., Fitch A. N. *Nature* **2003**, 425, 599-602

[37] Margadonna S., Arvanitidis J., Papagelis K., Prassides K. *Chem. Mater.* **2005**, 17, 4474-4478

[38] Sun Z., Chen X. H., Takenob, T., Iwasa Y. *J. Phys. Condens. Matter.* **2000**, 12, 8919-8926

[39] Ksari-Habiles Y., Claves D., Chouteau G., Touzain P., Jeandey C., Oddoou J. L., Stepanov A. *J. Phys. Chem. Solids* **1997**, 58, 1771-1778

[40] Chen X. H., Liu Z. S., Li S. Y., Chi D. H., Iwasa Y. *Phys. Rev. B* **1999**, 60, 6183-6186

[41] Ishii K., Fujiwara A., Suematsu H., Kubozon, Y. *Phys. Rev. B* **2002**, 65, 134431

[42] Sparn G., Thompson J. D., Huang S. M., Kaner R. B., Diederich F., Whetten R. L., Gruner G., Holczer K. *Science* **1991**, 252, 1829-1831

[43] Zhou O., Vaughan G. B. M., Zhu Q., Fischer J. E., Heiney P. A., Coustel N., McCauley J. P., Smith A. B. *Science* **1992**, 255, 833-835

[44] Chen C. C., Kelty S. P., Lieber C. M. *Science* **1991**, 253, 886-888

[45] Movshovich R., Thompson J. D., Chen C. C., Lieber C. M. *Phys. Rev. B* **1994**, 49, 3619-3621

[46] Gu C., Stepniak F., Poirier D. M., Jost M. B., Benning P. J., Chen Y., Ohno T. R., Martins J. L., Weaver J. H., Fure J., Smalley R. E. *Phys. Rev. B* **1992**, 45, 6348-6351

[47] Rosseinsky M. J., Murphy D. W., Fleming R. M., Tycko R., Ramirez A. P., Siegrist T., Dabbagh G., Barrett S. E. *Nature* **1992**, 356, 416-418

[48] Hirosawa I., Prassides K., Mizuki J., Tanigaki K., Gevaert M., Lappas A., Cockcroft J. K. *Science* **1994**, 264, 1294-1297

[49] Kosaka M., Tanigaki K., Prassides K., Margadonna S., Lappas A., Brown C. M., Fitch A. N., *Phys. Rev. B* **1999**, 59, R6628-R6630

[50] Margadonna S., Prassides K., Fitch A. N., Kosaka M., Tanigaki K. *J. Am. Chem. Soc.* **1999**, 121, 6318–6319

[51] Brown C. M., Takenobu T., Kordatos K., Prassides K., Iwasa Y., Tanigaki K. *Phys. Rev. B* **1999**, 59, 4439-4444

[52] Maniwa Y., Saito T., Kume K., Kikuchi K., Ikemoto I., Suzuki S., Achiba Y. *Phys. Rev. B* **1995**, 52, R7054-R7057

[53] Yildirim T., Fischer J. E., Dinnebier R., Stephens P. W., Lin C. L. *Solid State Commun.* **1995**, 93, 269-274

[54] Mizuki J., Takai M., Takahashi H., Mori N., Tanigaki K., Hirosawa I., Prassides K. *Phys. Rev. B* **1994**, 50, 3466-3469

[55] Prassides K., Vavekis K., Kordatos K., Tanigaki K., Bendele G. M., Stephens P. W. *J. Am. Chem. Soc.* **1997**, 119, 834-835

[56] Zhou O., Cox D. E. *J. Phys. Chem. Solids* **1992**, 53, 1373–1390

[57] Dahlke P., Denning M. S., Henry P. F., Rosseinsky M. J. *J. Am. Chem. Soc.* **2000**, 122, 12352-12361

[58] Ganin A. Y., Takabayashi Y., Bridges C. A., Khimyak Y. Z., Margadonna S., Prassides K., Rosseinsky M. J. *J. Am. Chem. Soc.* **2006**, 128, 14784–14785

[59] Takabayashi T., Ganin A. Y., Rosseinsky M. J., Prassides K. *Chem. Commun.* **2007**, 870–872

Chapter 2

Experimental techniques

2.1 Introduction

The purpose of this chapter is to outline and detail the analytical procedures utilised. Extensive use of powder X-ray diffraction has been made in order to study the structures of a variety of fulleride compounds as a function of temperature. In particular, the use of high-resolution diffractometers based at synchrotron radiation facilities was essential for studying the structural properties of the synthesised alkali-metal doped fullerides. Magnetic properties were also explored using a SQUID Magnetometer (Magnetic Property Measurement System - MPMS5). High pressure magnetic measurements were made possible using the easyLab Mcell-10. This chapter will focus on the techniques used along with some of the theoretical background associated with each. The synthetic part of the work is included in the subsequent relevant chapters.

2.2 Powder X-ray Diffraction

Powder X-ray diffraction (XRD) is a powerful structural characterisation technique used in solid state chemistry predominantly in situations where single crystals are not available. Its main strengths lie in its ability to determine quantitatively the volume fraction of different phases in multiphase materials (thus the identification of separate crystalline phases) and to structurally characterise powdered materials via refinement of an initial structural model.

The ideal bulk sample should contain crystallites of 1-10 μm in size that are randomly oriented so that all crystallite orientations necessary for scattering are present. In contrast with single crystals, perfect bulk powdered samples will always contain some crystallites to satisfy the orientation necessary for Bragg scattering. However, coarse crystallites can cause several problems including extinction, incorrect particle statistics and micro-absorption. Additionally, crystallite shapes can occasionally cause uneven

distribution of orientations; a simple example would be if the individual crystallites are flat and “plate”-shaped. When spread evenly onto a sample holder, such crystallite shapes will lead to a preferred orientation in the scattering, manifesting itself as incorrect measured relative peak intensities. Corrections accounting for preferred orientation can be made in the analysis software; however, rapid rotation of the sample during data acquisition can also improve the situation considerably.

2.2.1 Unit cell and unit cell symmetry

Crystallites are a conglomerate of repeating structural motifs which contain atoms or molecules. The unit cell is the smallest parallel-sided unit by which the complete crystal structure can be constructed using translational symmetry operations only. The sides of a unit cell are denoted as a, b and c and the angles between them are indicated as α, β and γ.[1] A cell in which $a \neq b \neq c$ and $\alpha \neq \beta \neq \gamma$ is named triclinic. If $a \neq b \neq c$, $\alpha = \gamma = 90^{o}$ and $\beta \neq 90^{o}$, the cell is known as monoclinic, while in the case where $a = b$, $\alpha = \beta = 90^{o}$ and $\gamma = 120^{o}$, the cell is hexagonal. The situation where $a = b =$ c and $\alpha = \beta = \gamma \neq 90^{o}$ is referred to as rhombohedral. Often the rhombohedral system is combined with the hexagonal system and grouped together into a larger hexagonal family. For cells in which all three angles are 90^{o}, if $a = b = c$, it is cubic; if $a = b \neq c$, the cell is tetragonal; and if $a \neq b \neq c$, the cell is orthorhombic. Triclinic, monoclinic, hexagonal, rhombohedral, cubic, tetragonal and orthorhombic are collectively recognised as the 7 crystal systems.

In crystallography, there are 14 unique Bravais lattices. Each one is generated by combining one of the 7 crystal systems with one of the lattice centerings (*P*, *A*, *B*, *C*, *I*, or *F*). Primitive centering (*P*) designates lattice points only at each corner of the unit cell. Body centred (*I*) adds an additional lattice point at the centre of the primitive unit cell. Face centred (*F*) places an extra lattice point at the centre of each face of the primitive unit cell, in contrast to systems centred using a single face (A, B or C centering), which

places a supplementary lattice point at the centre of only one of the cell faces. There are in total 42 possible Bravais lattice combinations; however, not all are unique and this reduces the number of combinations to the conventional 14.

A crystallographic point group is a mixture of discrete symmetry operations (such as rotations, reflections and inversions) about a fixed point where the atomic arrangement of the product is identical to the original. The constituting symmetry elements needed to describe symmetry operations are: translation, axial rotation and mirror plane reflection. Combinations of these elements construct more complex symmetry operations, such as centres of symmetry, screw axes and glide planes. If one considers each operation individually, translation simply illustrates movement by an exact distance in a specific direction. A rotation axis is defined by the number in the space group symbol, e.g. 4 would represent a fourfold rotational axis. A screw axis entails rotation followed by translation, and the notation n_m symbolises an *n*-fold screw axis with a translation along the unit cell of *m*/*n*. A glide plane is a reflection, followed by a translation parallel to the mirror plane. This is denoted by *a*, *b* or *c*, depending on which axis the glide is along. There is also the *n*-glide, which is a glide along the half of a diagonal of the unit cell face, and a *d*-glide which is either quarter of a diagonal of a face or body diagonal of the unit cell.

The space group is a description of the symmetry elements, and is identified by its short Hemann-Mauguin symbol, such as $P2_12_12_1$. The capital letter in this notation designates the centering of the Bravais lattice (*P*, *C*, *I*, or *F*) and the other symbols represent the most prominent symmetry operations that can be carried out on the unit cell without changing its physical appearance. Another example is *Pnma* which designates a primitive lattice with an *n*-glide plane perpendicular to the x-axis, a mirror plane perpendicular to the y-axis, and an *a*-glide plane perpendicular to the z-axis. There are 230 unique space groups constituting combinations of the 32 crystallographic point groups (11 of which are centrosymmetric, i.e. contain an inversion centre) with the 14 Bravais lattices.

A practical way to describe unit cell symmetry is by enumerating the equivalent positions, which are positions in the cell that are superimposed on top of one another by the symmetry operations. The International tables for X-ray crystallography[2] contain lists of the equivalent positions for the 230 space groups. Certain symmetry elements cause specific reflections to be missing referred to as systematic absences, and are crucial for the identification of the symmetry for a given material.

2.2.2 X-ray diffraction from crystals

In a crystal structure the atoms are arranged in a regular periodic array, classified by a Bravais lattice. Points within the array are known collectively as lattice points and are generated by translation of the unit cell. Lattice planes can be drawn between the lattice points; these are parallel and equally spaced with every lattice point lying on one of the planes. Lattice points can be portrayed by the position vector **R**:

$$\mathbf{R} = n_1\mathbf{a} + n_2\mathbf{b} + n_3\mathbf{c} \qquad (2.1)$$

where n_i are any integers and **a**, **b**, **c** are known as the primitive vectors. An important concept in the context of crystallography is that of the reciprocal lattice.[3] The reciprocal lattice consists of points on a regular grid which represent diffraction possibilities; each point is marked with a Miller index which corresponds to planes from which we imgaine diffraction occuring. This concept is demonstrated in Fig 2.1, which shows only one layer (*l* = 0) corresponding to possible *h*,*k*,0 reciprocal lattice points. The next layers, above and below this zero layer, would be *h*,*k*,1 and *h*,*k*,-1. The reciprocal lattice points are generated from the real space lattice by the following primitive vectors:

$$\mathbf{a}^* = 2\pi\frac{\mathbf{b}\times\mathbf{c}}{\mathbf{a}\cdot(\mathbf{b}\times\mathbf{c})} \qquad \mathbf{b}^* = 2\pi\frac{\mathbf{c}\times\mathbf{a}}{\mathbf{a}\cdot(\mathbf{b}\times\mathbf{c})} \qquad \mathbf{c}^* = 2\pi\frac{\mathbf{a}\times\mathbf{b}}{\mathbf{a}\cdot(\mathbf{b}\times\mathbf{c})} \qquad (2.2)$$

In single crystal diffraction the reciprocal lattice can be combined with another abstract concept known as the Ewald Sphere. The origin of the reciprocal lattice is located on the circumference of the Sphere. Rotating the crystal is equivalent to rotating the reciprocal lattice about the origin. Diffraction occurs whenever a reciprocal lattice vector comes in contact with the Ewald Sphere surface, this is illustrated in 2 dimensions in Fig 1.2 for the case where *h*,*k*,*l* = -2,3,0.

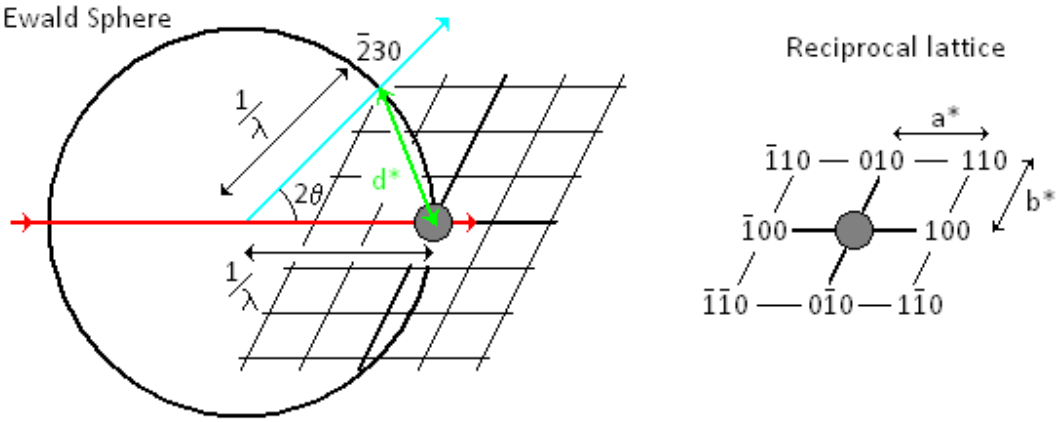

Fig 2.1: Diffraction in reciprocal lattice space (**left**), and reciprocal lattice (**right**). X-ray emerges from the crystal when reciprocal lattice point ($\bar{2}30$) intersects the circle

From the above relations it can be determined that reciprocal lattice vectors can be only linear combinations of **a***, **b***, and **c*** with integer coefficients *h*, *k*, *l*, i.e.

$$\mathbf{d^*} = h\,\mathbf{a^*} + k\,\mathbf{b^*} + l\,\mathbf{c^*} \qquad (2.3)$$

The reciprocal lattice vectors, **d***, are perpendicular to the lattice planes, and are therefore related to the distance between the lattice planes by the following relationship: $\mathbf{d^*} = 1/d_{hkl}$. Therefore the diffraction pattern of a crystalline sample can be used to

determine the reciprocal lattice vectors, and using this process the cell dimensions can be determined.

The concept of the reciprocal lattice becomes more complicated when a powdered sample is considered. If each crystallite within the powder has its own reciprocal lattice then overall we have an infinite number of randomly orientated reciprocal lattices that statistically form spheres, each having a radius **d*** from the origin. Therefore the Ewald Sphere will be intersected by many reciprocal lattice spheres; as a result the diffracted rays will describe a cone. In a diffraction experiment the distance d_{hkl} is related directly to the wavelength, λ and the angle, ϑ of the diffracted X-ray beam. In order to observe a sharp peak in the scattered intensity the Bragg equation for constructive interference between successive lattice planes should be satisfied.

2.2.3 Bragg's Law

Diffraction is a wave-property of radiation that causes it to curve as it passes by an edge or through an aperture. Diffraction effects intensify as the size of the aperture decreases and approaches the wavelength of the radiation. The resulting constructive and destructive interference effects are useful for structure determination of crystalline materials. X-rays and neutrons are commonly used radiation sources in diffraction measurements as their wavelength can be tuned to values similar to that of atomic distances (approximately 1 Å). In addition, the sources of radiation interact differently with solid matter; for example, X-rays interact only with electrons, while neutrons are influenced by atomic nuclei and unpaired electrons.

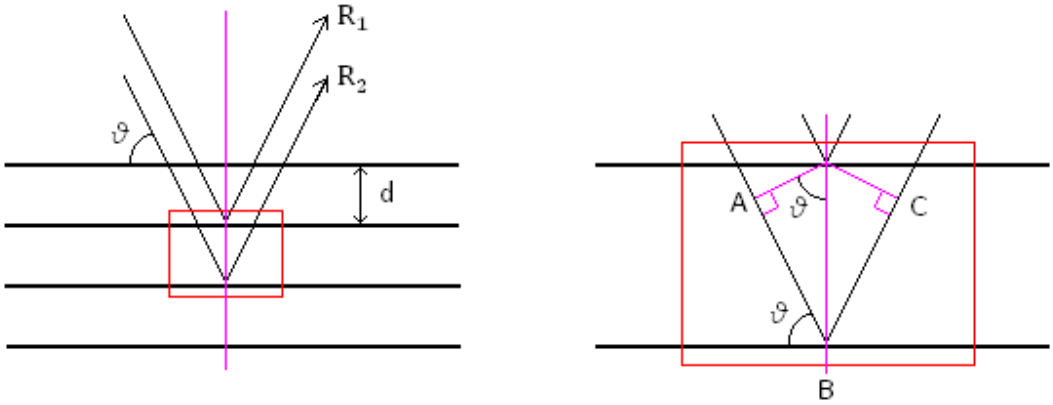

Fig 2.2: Representation of Bragg's Law for reflection of incident X-rays from planes with indices *h*, *k and l*. *d* is the distance between the *hkl* planes.

Rather than using the reciprocal lattice construct above, lattice planes can be thought of as mirrors, which reflect incident X-ray beams. The path difference of the two rays shown in Fig 2.2 is $AB + BC = 2d_{hkl}\sin\vartheta$, where ϑ is the glancing angle of the incident beam. In order for constructive interference to occur from successive planes, the path difference must be an integral multiple (n) of the wavelength (λ), resulting in the following relationship:

$$AB + BC = 2d_{hkl}\sin\vartheta = n\lambda \qquad (2.4)$$

This is known as the Bragg equation and represents the condition for diffraction to take place. Angles of interference that do not satisfy Bragg's law lead to cancellation of the diffracted beam intensity.[4] The sum of the contributions to scattering of all scatterers in the unit cell can be expressed as:

$$F_{hkl} = |F_{hkl}|e^{i\varphi} \qquad (2.5)$$

where $|F_{hkl}|$ is the amplitude of the diffracted ray and φ is the phase. F_{hkl} is known as the structure factor which is a mathematical term that describes how a material scatters

incident radiation. $|F_{hkl}|$ is proportional to the square root of the scattered intensity, $I(hkl)$, thus leading to the following relationship:

$$|F_{hkl}|^2 = sI(hkl) \tag{2.6}$$

where s is a collection of constant factors that are dependent on the sample and experimental setup, and can be expressed as:

$$s = \left(\frac{I_0 \lambda^3 I_s}{8\pi r} \right) K_R K_G \frac{J_h}{V_c^2} L_p \tag{2.7}$$

I_0 is the intensity of the incident beam, λ is the wavelength of the radiation source, I_s is the height of the detector slit, r is the sample-to-detector distance, J_h is the multiplicity for reflection (h, k, l), V_c is the unit cell volume and for X-rays, L_p is the combination of the Lorentz and polarisation factors for the diffractometer geometry. K_R and K_G are constants for a given sample and set of experimental conditions. $K_R = (e^2/m_e c^2)^2$, where e and m_e are the charge and mass of an electron and c the speed of light. K_G is $(1/8)\mu$ for Bragg-Brentano geometry (where the sample mount is tilted by an angle ϑ while the detector rotates by 2ϑ), and $V/4$ for X-ray Debye-Scherrer geometry (referred to by my peers as "capillary mode" - whereby the sample spins on an axis to reduce preferred orientation while the detector moves by 2ϑ) (μ is the linear absorption coefficient of the sample and V the volume of the sample irradiated by the beam).

The structure factor can be expressed as a Fourier series, in which each term represents the contribution of each atom to the hkl reflection. The atomic structure factor, f_{hkl}, representing the contribution of atom i to reflection hkl is given as:

$$f_{hkl} = f_i \exp(2\pi i(hx_i + ky_i + lz_j)) \tag{2.8}$$

The exponential term signifies a three-dimensional periodic function in which the x_i, y_i and z_i terms represent the fractional coordinates of atom *i* in the unit cell and *h*, *k* and *l* are again the Miller indices. f_i is the atomic scattering factor for atom *i* defined as:

$$f_i^2 = (f_0 + \Delta f')^2 + (\Delta f'')^2 \qquad (2.9)$$

where $\Delta f'$ and $\Delta f''$ are the real and anomalous dispersion terms; the first term f_0 depends on the scattering angle 2ϑ. The atomic scattering factor also increases with the atomic/electron numbers, implying larger atoms have a larger scattering factor. The phase of the wave (φ, equation 2.5) is part of the exponential component of the structure factor and from equation 2.10, and depends only upon the atomic coordinates (x_i, y_i, z_i) of the atom. More specifically the phase for one atom is $\varphi = 2\pi(hx_i + ky_i + lz_i)$. Tying in these concepts with Bragg's law, all atoms on a set of equivalent parallel planes will diffract in phase with one another.

The structure factor equation can be expanded to accommodate multiple atoms. For a unit cell containing *n* atoms, the structure factor expression (F_{hkl}) is a sum of all the structure factor values for individual atoms:

$$F_{hkl} = \sum_{i=1}^{n} f_i \exp\left[-B_i \frac{\sin^2\vartheta}{\lambda^2}\right] \exp\left[2\pi i\left(hx_i + ky_i + lz_i\right)\right] \qquad (2.10)$$

where B_i is the Debye-Waller displacement factor for atom *i* (in Å^2). The exponential term, $\exp[-B_i\sin^2\vartheta/\lambda^2]$ takes into account the effect of thermal vibration of the electron density, making it more diffuse and reducing the scattering efficiency at high angles.

2.2.4 Radiation Sources

The powder diffraction datasets analysed within this thesis were all collected at synchrotron X-ray radiation facilities. In order to understand the advantages of X-ray radiation, it is also worth drawing some comparison to neutron radiation.

In a laboratory source X-rays are generated by bombarding a metal plate with high energy electrons. Atoms within the metal absorb the high energy electrons and emit a radiation with a continuous range of wavelengths knows as Bremsstrahlung radiation. Within the continuum are characteristic high-intensity peaks which arise from collisions of the incoming electrons with core electrons of the metal atoms. As the core electrons are displaced, electrons from higher energy orbitals fall into the vacancy emitting their excess energy as X-rays (photons). If the electron falls into the *K* shell (n=1), they are classified as *K*-radiation and are labelled K_α, K_β etc. Copper is often used as the metal target source in laboratory diffractometers which utilise X-ray radiation. In the case of copper, there are two prominent transitions that occur, 2p ⇨ 1s and 3p ⇨ 1s, labelled as K_α (1.5418 Å)and K_β (1.3922 Å), respectively. K_α is actually a doublet, $K_{\alpha1}$ = 1.5406 Å and $K_{\alpha2}$ = 1.5443 Å, as there are two possible spin states of the 2*p* electron which have slightly different energies. In laboratory X-ray diffractometers, $K_{\alpha1}$ is used as its transition is more intense than $K_{\alpha2}$ and K_β. Monochromators can be used to filter out the desired X-ray wavelength.

Neutrons are elementary particles found in atomic nuclei. Neutrons can be produced as a result of nuclear fission. High energy neutrons generated in a reactor are slowed using a moderator, such as graphite, to a speed of about 4 km s^{-1} and a wavelength of about 1 Å (similar to X-ray wavelengths). Like X-rays, a monochromatic beam can be obtained. Neutrons interact with the atomic nuclei, as a result the intensity with which neutrons are scattered is independent of the number of electrons in the element. In contrast, X-ray scattering factors increase with the number of electrons present. Therefore neutron diffraction is suitable for measuring the positions of lighter elements

such as hydrogen, and it is also possible to distinguish neighbouring elements in the periodic table as well as isotopes. Another feature of neutrons that is different to X-rays is their possession of a magnetic moment (due to their spin). This can give rise to magnetic scattering which is important for investigating magnetically ordered systems.

2.3 Radiation Facilities (Instrumentation)

2.3.1 European Synchrotron Radiation Facility (ESRF)

Synchrotron radiation is high energy electromagnetic radiation that covers a range of wavelengths from visible light to X-rays (10^{3} - 10^{-1} Å). The ESRF is a third generation synchrotron source. Electrons are produced using an electron gun and transferred to a Linear Accelerator (LINAC). The LINAC uses pulsed electric fields to accelerate the electrons until their energy reaches ~200 MeV. The electrons are then transferred to a booster ring and are accelerated using radio frequency waves. When the electrons have enough energy (6 GeV) to produce light, an injection system transfers them from the booster ring to the storage ring which is equipped with bending magnets and insertion devices.

Large dipole magnets bend the electrons in a non-linear trajectory around the circumference of the storage ring; as a result the radiation emitted is fan-shaped. The insertion devices (called undulators and wigglers) consist of periodic arrays of magnets of alternating polarity which adjust the trajectory of the electrons slightly and as a result aid in collimating the beam in the straight sections of the ring.

The circumference of the storage ring is 844 m and supplies a maximum current of 200 mA for a beam lifetime of ~50 h; therefore a regular top-up injection is required every 24 hours. When the synchrotron light is tapped by a beamline there are devices utilising

various monochromators (double crystal monochromators, multi-layer monochromators, and bent mirrors for saggital focussing) to select the desired wavelength for the experiment; sample focusing is also handled by variable slits and additional undulators, which are present on the beamlines themselves.[5]

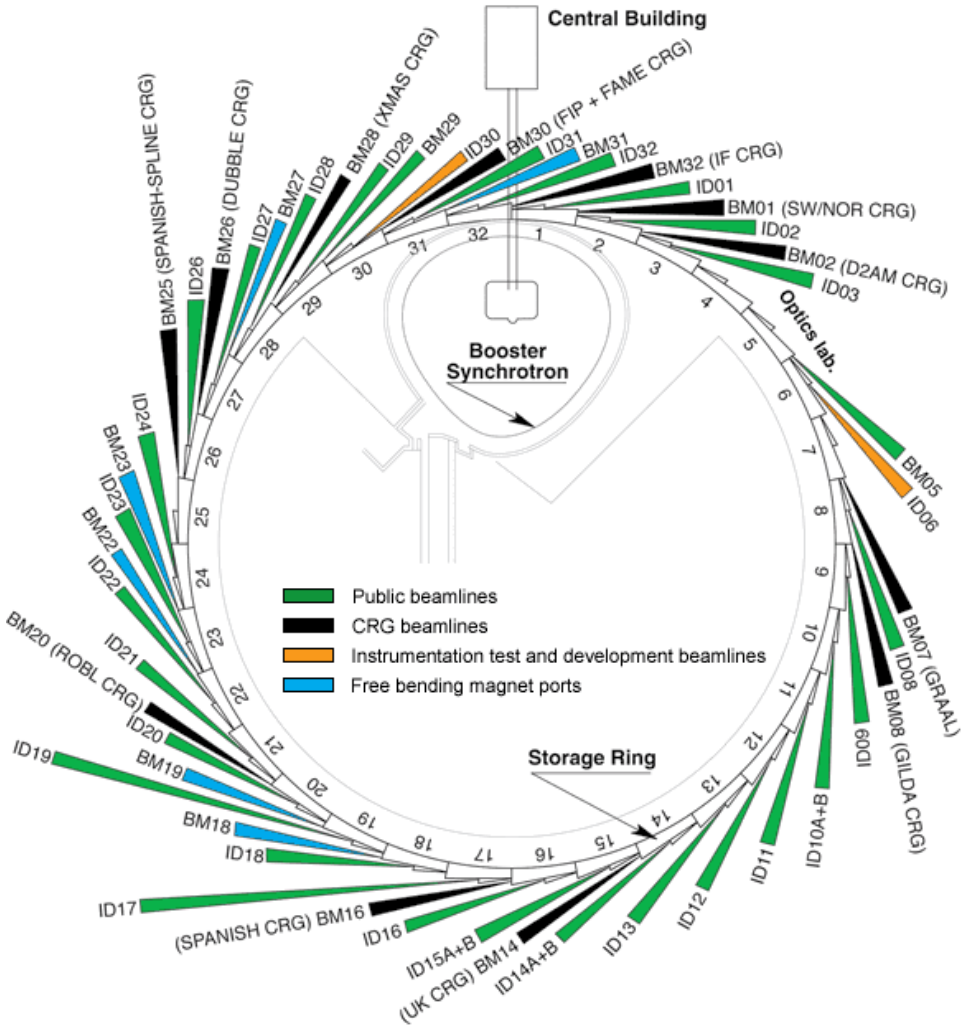

Fig 2.3: Schematic diagram of the ESRF facility at Grenoble.[6]

2.3.2 ID31 – High-resolution X-ray powder diffraction

ID31 is a beamline designed for high-resolution powder diffraction studies with fast data acquisition times. The beamline optics are fairly simple and are described henceforth; three 11 mm ex-vacuum undulators are able to tune the imminent X-rays over a broad range of wavelengths varying from 2.48 to 0.21 Å.[7] The incident beam is monochomated by a cryogenically cooled Si(111) double-crystal monochromator. The first crystal of the monochromator is cooled by copper blocks, which are themselves cooled by liquid nitrogen. The cooling on the second crystal is maintained by a piezoelectric feedback system, which monitors fluctuating temperature gradients and adjusts the cooling heaters to maintain a temperature at 60 ± 0.5 ^{o}C. The size of the beam incident to the monochromator and sample is defined by mechanically operated, water-cooled slits.

As my samples are all air sensitive, the samples were mounted as capillaries; ID31 is also capable of measuring samples mounted on flat plates. Capillary samples can be spun at 3000 rpm to minimise preferred orientation effects; however, this is by no means perfect as needle-like samples may still align along the direction of the capillary. ID31 uses a bank of 9 detectors, ~2^{o} apart; each detector is preceded by a Si(111) crystal analyser. The net result of a system using monochromators before and after sample interaction is an increase in data accuracy as many instrumental effects are improved; however, there is an overall loss in intensity, therefore leading to longer data acquisition times. Fortunately the 9 detectors at ID31 move simultaneously producing 9 high resolution diffraction patterns in parallel, [8] which can be summed into a single data set; this is a very elegant solution which drastically improves the main drawback of low data acquisition time. Physically knowing the exact offset between the 9 detectors is not critical as the offset is calibrated accurately through the software; this process needs repeating after a new wavelength is selected. The calibration step is performed using a highly crystalline Si standard.

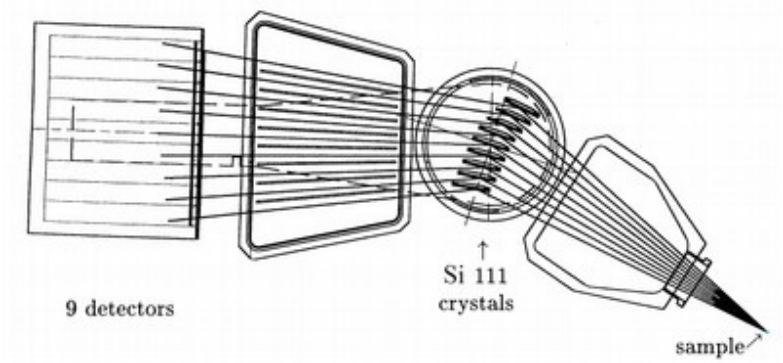

Fig 2.4: Detector system utilised at the ID31 diffractometer.

The beamline allows experiments to be carried out under a wide range of environmental conditions; for example, a liquid-helium-cooled cryostat can cool the sample inside the capillary down to ~5 K (or lower with pumping). At such low temperatures, it is imperative that the capillary be sealed under He gas only, as gases in the air or an inert gas such as Ar will freeze, thus inhibiting an accurate thermal gradient within the capillary. Additionally, a cryostream cold-nitrogen-gas blower is also available, allowing temperature control in the range 80-500 K.

2.3.3 BM01 – The Swiss-Norwegian Beamline

The incoming horizontal fan of radiation to BM01 is divided into 2 parts by a splitter vessel; each separate beam arrives at its own independently operated hutch (BM1A and BM1B). At BM1B the dispersed beam first passes through a set of mechanically operated slits before reaching a cooled Be-window, which is used to filter low energy X-rays. The beam then passes through a vacuum chamber containing a water-cooled channel-cut Si(111) monochromator. The white beam is prevented from further entering the hutch by a removable beam-stop. A narrowing of the incoming radiation is achieved

by a further set of horizontal and vertical slits, before the beam then passes through a second Be-window and eventually reaching the sample.

In the case of BM1A station, the dispersed beam first passes through the primary focusing slits before deflecting off a Rh-coated Si mirror which aids in collimating the beam horizontally. After deflection from this mirror, the incident radiation passes through a double-crystal monochromator. There is a variable gap between the two crystal monochromators to allow a constant beam height to be maintained. The first crystal monochromator is water cooled, while the second is sagittally bent for horizontal beam focusing. Similar to the setup of BM1B a set of Be-windows are placed before and after the monochromator. A secondary mirror, identical to the first, provides vertical focusing onto the sample in the hutch at BM1A. Finally another set of mechanically operated slits helps collimate the beam onto the sample. An image-plate area detector (MAR) was used for powder diffraction work in this thesis.

2.3.4 Diamond Light Source

The Diamond Light Source is a synchrotron X-ray research facility located in Oxfordshire, United Kingdom. Like the ESRF, the electrons circulating the storage ring at Diamond are initially created by an electron gun, which in conjunction with the LINAC accelerates electrons to an energy of ~100 MeV. The electrons are then injected into a booster ring. Here the electrons follow a non-circular trajectory consisting of two straight sections joined together with two semicircular curves (reminiscent of an athletics track). 36 dipole bending magnets, capable of fields of 0.8 Tesla, surround the curved sections of the booster ring and are used to bend the electrons into the correct trajectory. A radio frequency voltage source accelerates the electrons in the straight sections of the ring until an energy of 3 GeV is achieved. Another injection system then transfers the electrons from the booster ring to the storage ring.

Like the booster ring at Diamond, the storage ring is also not circular. It consists of 24 straight sections angled together to form a closed loop with a circumference of 561.6 m. Each angled section of the ring consists of two bending magnets, and has an identical arc of 15^{o} ($360^{o}/24$). Insertion devices (undulators primarily) are placed around the straight sections of the ring and are necessary to ensure a narrow intense beam of electrons. Diamond operates using a top-up injection system, injecting current every 10 minutes; this helps to maintain a constant beam current (ESRF injection system is typically only once every 24 hours).

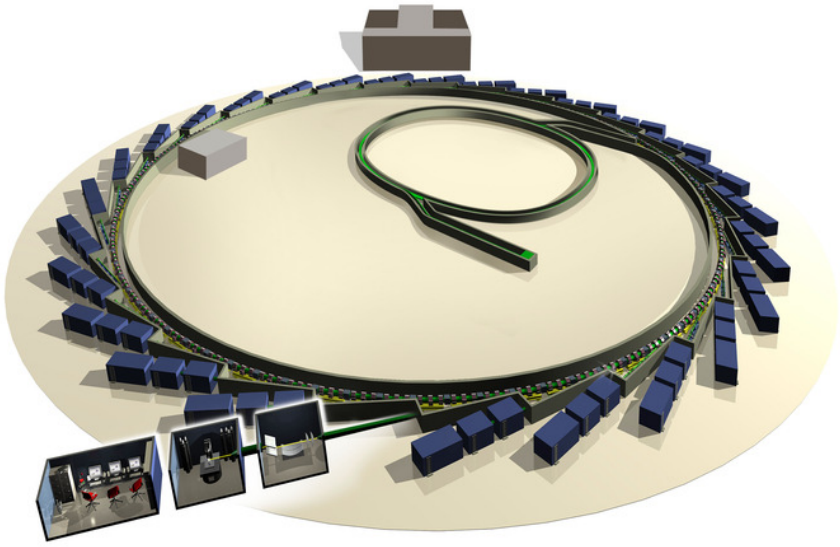

Fig 2.5: 3D schematic representation of the Diamond synchrotron facility.[9]

2.3.5 I11 - High resolution powder diffraction

At the I11 beamline, undulators tune the imminent X-rays over a broad range of wavelengths, varying from 2.5 to 0.4 Å. The optics system in I11 is relatively straightforward; the incident beam first passes though a set of mechanically operated slits before being monochomated by a cryogenically cooled Si(111) double-crystal monochromator, and then passes through a second set of slits before deflecting off an harmonic rejection mirror and finally passing through two more sets of slits. The length of the beamline is 48 m in total. The detectors consist of five multi-analysing crystal-detector (MAC) arms on a 2ϑ circle, each with Si(111) monochromator (x9), so in total there are 45 separate detectors. Like ID31, the 45 detectors move simultaneously producing 45 high-resolution diffraction patterns in parallel, which can be summed into a single data set.

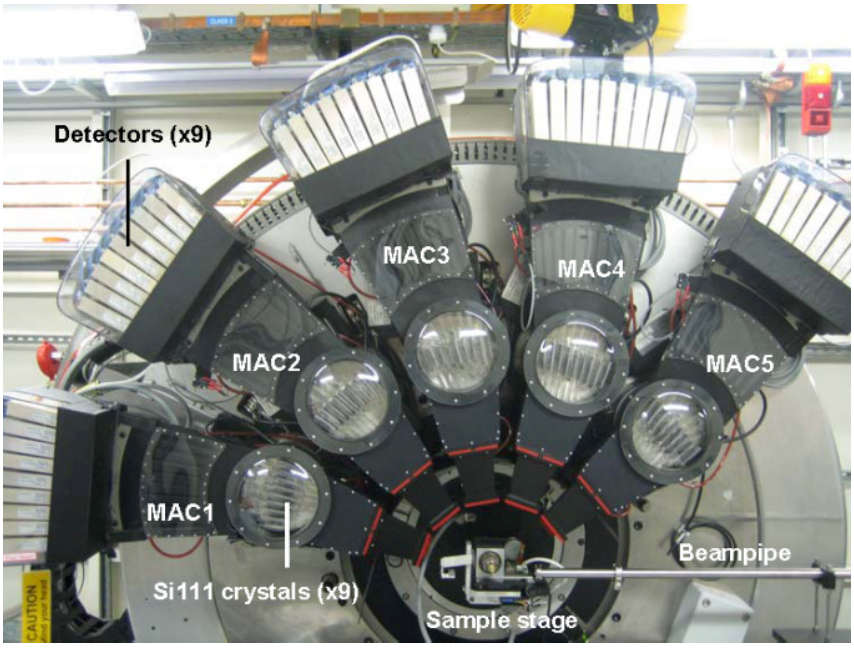

Fig 2.6: Detector system utilised on the I11 beamline.

2.4 Data Analysis – Diffraction

2.4.1 The Rietveld Method

The Rietveld method is an iterative least-squares refinement technique for powder diffraction data that minimises the difference between the observed data points at each 2ϑ and a calculated powder diffraction pattern by adjusting the structural parameters, background coefficients, and profile parameters. The Rietveld method of analysing powder diffraction patterns was first developed for neutron diffraction at fixed wavelength,[10] but was extended later to encompass conventional X-rays[11,12,13] and synchrotron X-ray radiation.[14]

Traditional techniques involve measuring the integrated intensities of individual Bragg reflections, converting them to structure factors and using them to solve or refine structures. This procedure is successful for high symmetry structures where peak overlap is essentially absent; however, more complex low-symmetry structures result in hundreds of Bragg reflections overlapping and it is difficult to decompose the pattern into its individual Bragg reflections.[15] In contrast, the Rietveld method uses the entire powder diffraction pattern, thus overcoming the problem of peak overlap. Data analysed in this thesis using the Rietveld refinement technique were recorded in steps using a fixed increment as the angle is increased. This ensures that overlapping reflection contributions are summative. The calculated intensity, y_c, at position $2\vartheta_i$ in the diffraction pattern can be expressed as:

$$y_c(2\vartheta_i) = y_b(2\vartheta_i) + s\sum_k j_k (LP) A A_s P_k \left|F_k\right|^2 \Phi_k (2\vartheta_i - 2\vartheta_k) \qquad (2.11)$$

In equation 2.11, y_b is the background intensity, s is a scale factor, j_k is the multiplicity factor, LP are the Lorentz and polarisation factors, A is the transmission

coefficient, A_s is an asymmetry correction factor, P_k is the preferred orientation correction and F_k is the structure factor. The last component of the intensity calculation, $\Phi_k(2\vartheta_i - 2\vartheta_k)$ is a reference to the peak shape profile function. The difference between the calculated and observed patterns is known as the residual function (M). The Rietveld refinement technique seeks to minimise the residual function by adjusting the calculated pattern.

$$M = \sum_{2\vartheta_i} w_i (y_o(2\vartheta_i) - y_c(2\vartheta_i))^2 \qquad (2.12)$$

where $y_o(2\vartheta_i)$ is the observed intensity at position $2\vartheta_i$, w_i is a statistical weighting function. The minimisation of the residual function is carried out over the whole diffraction pattern. As the intensity measured at each step is considered a statistically independent observation, a weighting scheme of the form below is used:

$$w_i = \frac{1}{y_o^t(2\vartheta_i)} \qquad (2.13)$$

In equation 2.13, $y_o^t(2\vartheta_i)$ is the total intensity measured, which is the sum of the observed intensity, $y_o(2\vartheta_i)$, and the background intensity, $y_b(2\vartheta_i)$, at position $2\vartheta_i$.

2.4.1.1 Peak shape determination

Empirically the peak shape profile can be modelled by a simple Gaussian profile function; however, in an actual experiment sample and instrument factors mean that more complex peak shape functions are required. Several functions have been used to describe the peak shape.[11,12,13] Young and Wiles suggested that combined Gaussian and Lorentzian functions,[16] such as pseudo-Voigt and Pearson VII functions were the most suitable, and suggest functions such as:

$$pV: \quad \Omega(2\vartheta) = \eta \cdot L(2\vartheta, H_L) + (1-\eta).G(2\vartheta, H_G) \qquad (2.14)$$

$$G: \quad G(2\vartheta) = \frac{2}{H_G}\left[\frac{\ln 2}{\pi}\right]^{\frac{1}{2}} \exp\left(\frac{-4\ln 2}{H_G^2}(2\vartheta - 2\vartheta_h)^2\right) \qquad (2.15)$$

$$L: \quad L(2\vartheta) = \frac{2}{\pi H_L}\left[1 + \frac{4(\sqrt{2}-1)}{H_L^2}(2\vartheta - 2\vartheta_h)^2\right]^{-1} \qquad (2.16)$$

where η is the mixing parameter, which defines the ratio of the peak shape between a Gaussian (where η = 0) and a Lorentzian (where η = 1) function. H_G and H_L are their respective full widths at half maximum (FWHM). Also is has been shown that the width of the Gaussian and Lorentzian components, H_G and H_L, show distinct variation with scattering angle:

$$G: \quad H_G = \left[U\tan^2\vartheta + V\tan\vartheta + W + \frac{P}{\cos^2\vartheta}\right]^{\frac{1}{2}} \qquad (2.17)$$

$$L: \quad H_L = X\tan\vartheta + \frac{Y}{\cos\vartheta} \qquad (2.18)$$

where U, V, W, X, and Y are refinable peak shape parameters.

Improvements in the basic pseudo-Voigt model are needed is many cases as it assumes peaks are symmetrical about the nominal Bragg peak positions; for instance, the basic peak shape can be not symmetric due to axial divergence of the X-ray beam. This effect is exacerbated at low angles as the peaks observed in X-ray diffraction in this region are generally more intense. Most Rietveld refinement programs include a refinable semi-empirical asymmetry correction term to model this anomaly. For the case of the GSAS suite for Rietveld refinements (PC version), two refinable parameters, *S/L* and *H/L*, are incorporated into the profile function.[17] It is necessary to refine both variables *S*/*L* and *H*/*L* simultaneously.

Finally, the peak shape can be strongly influenced by sample effects that cause peak shape broadening. Two more parameters can be utilised for the exact description of the peak shape function. The first is an anisotropy coefficient, *stec*, involved in the Lorentzian broadening of the peaks, while the second parameter corresponds to strain broadening effects, *ptec*. Both *stec* and *ptec* parameters have been incorporated into the profile functions of GSAS suite. In my case, refining these two extra parameters did not afford a better description of the peak shape, therefore they were omitted.

2.4.1.2 Background determination

The observed intensity at each equidistant point in the diffraction profile is a combination of the Bragg intensity resulting from the sample and the background. There is a variety of sample and instrumental conditions contributing to the background which include fluorescence, detector noise, contribution from disordered and amorphous phases, scattering of X-rays by air, diffractometer slits and the choice of sample holder. As my samples were contained in glass capillaries, there was a large contribution to the background from the amorphous glass. The easiest solution for modelling the background is to select several baseline points in the pattern and apply a linear interpolation between these points. This technique is useful early in the refinement procedure as many parameters are initially incorrect, therefore refining functions such as the background too early can hinder the convergence process.

The most common representation of the background is by a polynomial function whose coefficients are variables in the refinement:

$$y_b(2\vartheta_i) = \sum_n b_n [2\vartheta_i]^n \qquad (2.19)$$

In equation 2.19, b_n are refinable background parameters and $2\vartheta_i$ is expressed in radians. Determining the background parameters is an important step in the Rietveld refinement technique and needs to be performed accurately. In poorly resolved patterns, the background parameters tend to correlate with other parameters, predominantly the temperature factors. The extraction of accurate background parameters further increases in complexity at higher 2ϑ angles due to the low intensity and excessive peak overlap.

2.4.1.3 Accuracy of the refinement model

The Rietveld method is predominantly used as a structural refinement technique for fine-tuning an initially proposed starting structural model. After completion of the Rietveld refinement iterations, the agreement between observed and calculated diffraction profiles can be deliberated via careful examination of the *R*-factors. In GSAS, the *R*-factors are listed in the *.LST file.

One of the more mathematically meaningful *R*-factors is the weighted profile one, R_{wp}, which is the appropriate value to quote when data are collected over a series of incrementing angular steps, as the error associated with each intensity value is not constant but varies as a function of the number of individual counts:

$$R_{wp} = \left(\frac{\sum_{2\vartheta_i} w_i \left| y_o(2\vartheta_i) - y_c(2\vartheta_i) \right|^2}{\sum_{2\vartheta_i} w_i \left| y_o(2\vartheta_i) \right|^2} \right)^{\frac{1}{2}} \qquad (2.20)$$

An additional reliability *R*-factor can be defined when the profile is not weighted, R_p, and is defined as:

$$R_{\mathrm{p}} = \left(\frac{\sum_{2\vartheta_{\mathrm{i}}} \left| y_{\mathrm{o}}(2\vartheta_{\mathrm{i}}) - y_{\mathrm{c}}(2\vartheta_{\mathrm{i}}) \right|}{\sum_{2\vartheta_{\mathrm{i}}} \left| y_{\mathrm{o}}(2\vartheta_{\mathrm{i}}) \right|} \right) \tag{2.21}$$

The *expected R*-factor that takes into account the statistical quality of the data and the number of variables used in the refinement and predicts the theoretical minimum achievable is defined as:

$$R_{\mathrm{exp}} = \left(\frac{(N - P + C)}{\sum_{2\vartheta_{\mathrm{i}}} w_{\mathrm{i}} \left[y_{\mathrm{o}}(2\vartheta_{\mathrm{i}}) \right]^2} \right) \tag{2.22}$$

where *N* is the number of observations, *P* is number of refinable parameters and *C* is number of constraints used. The fit can be monitored by the agreement χ^2 factor which approaches 1 when the agreement between observed and calculated profiles is perfect.

$$\chi^2 = \left(\frac{R_{\mathrm{wp}}}{R_{\mathrm{exp}}} \right)^2 = \frac{\sum_{2\vartheta_{\mathrm{i}}} \left| y_{\mathrm{o}}(2\vartheta_{\mathrm{i}}) - y_{\mathrm{c}}(2\vartheta_{\mathrm{i}}) \right|^2}{(N - P + C)} \tag{2.23}$$

A value of $\chi^2 < 1$ generally indicates that there are more parameters in the model than justifiable by the quality of the data.

2.4.2 Le Bail pattern decomposition technique

The Le Bail pattern decomposition technique is used to refine X-ray powder diffraction data in the absence of a known structural model. Only the crystal symmetry and approximate cell parameters need to be specified in the course of this analysis.[18] The calculated intensity, y_c at every point *i* of the profile is given by the equation:

$$y_c(2\vartheta_i) = B_i + \sum_{k=k_1}^{k_2} I_k \cdot \Omega_{ik} \qquad (2.24)$$

where B_i is the background intensity at point *i*, Ω_{ik} and I_k are the peak-shape function and the integrated intensity, respectively, of reflection *k* at point *i*. Initially the peak intensities are assigned arbitrarily and then refined simultaneously with other parameters such as the peak-shape, zero-point and lattice constants. While this technique does provide any structural information, it can be invaluable in obtaining preliminary information about crystal symmetry and lattice metrics that can be then fed into a proper Rietveld refinement procedure.

2.4.3 Refinement Software, GSAS and EXPGUI

GSAS (General Structure Analysis System) is a comprehensive collection of over fifty individual programs (wrote in the FORTRAN language) that can be used for the refinement of structural models to both X-ray and neutron diffraction data. Additionally, the GSAS package can be employed in the refinement of both single crystal and powder diffraction data for either single wavelength or time of flight protocols, as well as data from a mixture of phases, each with their own individual refinable parameters.

At the heart of the GSAS software suite is the experiment editor EXPEDT. The EXPEDT program is operated through navigating a series of options, where the user is prompted to select a function highlighted by a single letter in the text. The GSAS program can become overly sophisticated as you may need to transcend six or more dialogue options to find the relevant option, and the required format for user input is not always clear. Similarly it is hard to view various options and refinement parameters in the experiment file simultaneously. EXPGUI provides a basic GUI alternative to the dialogue options of EXPEDT. The program is able to invoke the relevant programs and options available within the GSAS suite; however, it is not comprehensive and therefore does not offer all the options available within EXPEDIT, but EXPGUI provides many common options available in GSAS. Since EXPGUI and EXPEDT can be used interchangeably, use of EXPGUI does not prevent access to any capabilities within GSAS.[19]

2.5 Magnetism

The term magnetism is used to describe how materials respond on a microscopic level when placed in an external field. Their behaviour can be categorised into different types of response such as paramagnetic, diamagnetic, antiferromagnetic or ferromagnetic. The characterisation of a material can be achieved by measuring how the

magnetisation changes with respect to temperature or the strength of an applied magnetic field. The magnetisation (M) is defined as the magnetic moment per unit volume acquired by a substance when subjected to a magnetic field of strength H. The magnetisation is proportional to H and can be expressed as:

$$M = \chi H \tag{2.25}$$

Both M and H are measured in identical units; therefore χ is dimensionless and known as, the volume magnetic susceptibility. In the *cgs* (centimetres grams seconds) system, the unit of the magnetisation is emu (electromagnetic unit) and the units of the susceptibility are given in emu cm^{-3}. The susceptibility is also defined by referring to mass or number of moles in the material, which leads to units of emu g^{-1} or emu mol^{-1}, respectively.

The magnetic flux density (B) is related to the applied field strength and the magnetisation by the expression:

$$B = \mu_0(H + M) = \mu_0(1 + \chi)H \tag{2.26}$$

where μ_0 is the magnetic permeability of free space. The magnetic flux density can be thought of as the number of magnetic flux lines permeating the material; this increases if M adds to H ($\chi > 0$); however, it decreases if M opposes H ($\chi < 0$). Materials for which χ is positive are referred to as paramagnetic and those for which χ is negative as diamagnetic.

Magnetic measurements are usually performed as a function of temperature ($M(T)$) and/or applied field ($M(H)$). Typical $M(T)$ plots for different types of magnetism are shown in Fig. 2.7.

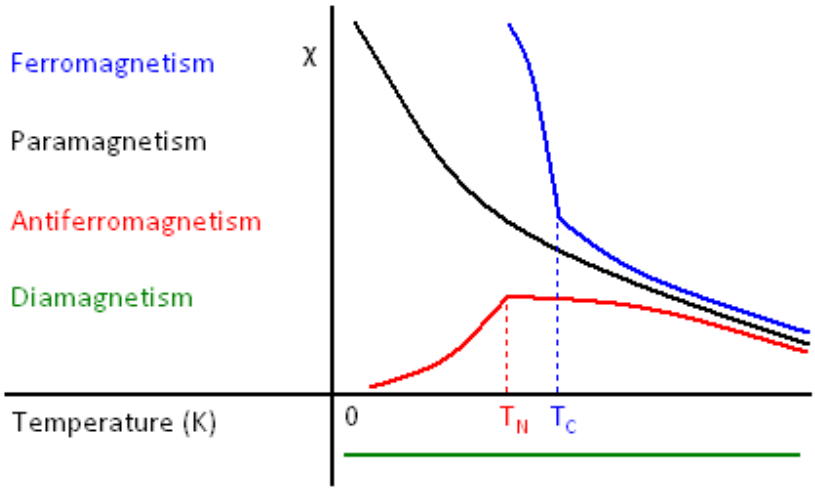

Fig 2.7: Plot of χ vs *T* curves for the different type of magnetic behaviour.

M(*T*) measurements can be performed at a variety of applied fields typically ranging from low-fields such as 10 G over a narrow temperature range in order to observe hysteresis behaviour in the temperature dependence, to high-fields such as 5 Tesla (50,000 G) over a broad range of temperatures to determine the type of magnetism exhibited by the material. Low-field temperature dependent measurements are divided into two categories, zero-field-cooled (ZFC) and field-cooled (FC). In ZFC measurements, the material is cooled down to the lowest measurement temperature, and then the desired weak magnetic field is applied before the magnetisation is measured as a function of temperature. In FC measurements, the protocol is identical except the material is cooled under the desired weak magnetic field. These measurements are useful to determine the temperature range over which the magnetic changes in a system are irreversible.

M(*H*) procedures are known as hysteresis loops and involve increasing the field in stepwise increments to a maximum positive field, followed by a stepwise decrease to maximum negative field and finally a return to a state of zero applied field. In the case of ferromagnetic materials hysteresis is observed below the Curie temperature; in the paramagnetic region there is no hysteresis.

2.5.1 Paramagnetism

Curie-type paramagnetism is the simplest form of magnetic behaviour. It arises from partial alignment of unpaired electron spins, when under the influence of an applied magnetic field. Spins generally align in a material with unpaired electrons; however, these effects are counteracted by a randomisation of the spins due to the thermal energy. The paramagnetic behaviour can be explained using the Curie law, which describes the temperature dependence of the susceptibility:

$$\chi(T) = \frac{C}{T} \qquad (2.27)$$

where *C* is the material-specific Curie constant. From a rearrangement of equation 2.27, a plot of $1/\chi$ against *T* (Fig 2.8) suggests that the plot for a paramagnetic material will be a straight line that passes through the origin with a slope of $1/C$.

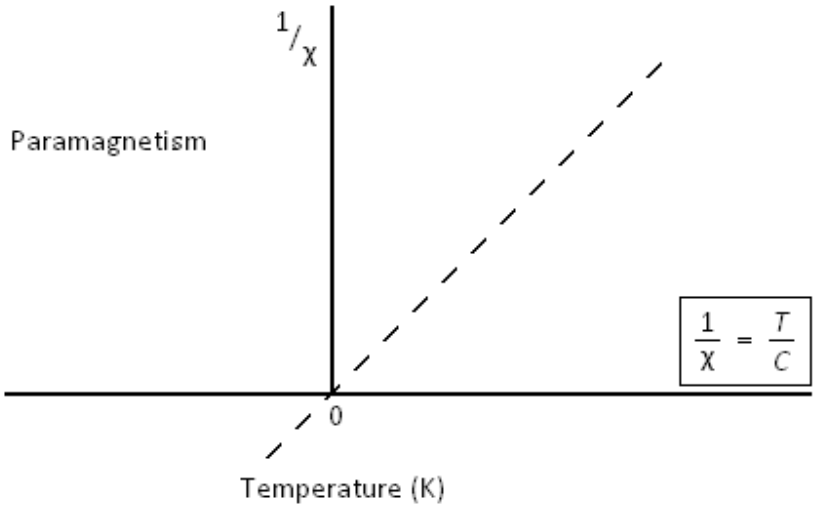

Fig 2.8: Plot of $1/\chi$ vs *T* for a Curie paramagnetic material

The molar Curie constant gives information on the effective magnetic moment in the material and it is defined as:

$$\chi_m = \frac{C_m}{T} = \frac{N_A p_{eff}^2 \mu_B^2}{3K_B T} \qquad (2.28)$$

where χ_m is the molar susceptibility, N_A is Avogadro's number, p_{eff} is the effective magnetic moment, μ_B is the Bohr magneton and K_B is Boltzmann's constant.

2.5.2 Ferromagnetism and Antiferromagnetism

Often materials can demonstrate spontaneous magnetisation effects due to strong intrinsic interactions between the magnetic moments of neighbouring atoms or molecules, thus forming magnetically ordered states at low temperatures. As a result of these interactions, the magnetic moments can align parallel or anti-parallel to one another, leading to ferromagnetism and antiferromagnetism, respectively. The magnetic behaviour above the ordering temperature can explained this time using the Curie-Weiss law, which describes the temperature dependence of the susceptibility for systems with ferromagnetic and antiferromagnetic interactions:

$$\chi(T) = \frac{C}{T - \vartheta} \qquad (2.29)$$

where ϑ is known as the Weiss temperature and is characteristic of the substance, and can be obtained from the x-axis intercept of a plot of $1/\chi$ against T (Fig 2.9). When ϑ is positive the moments are aligned parallel with one another and the material is ferromagnetic below the *Curie temperature*, T_C (Fig 2.9, $\vartheta > 0$). Conversely, when ϑ is negative the

moments are aligned anti-parallel and the material is antiferromagnetic, below the *Néel temperature*, T_N (Fig 2.9, $\vartheta < 0$)

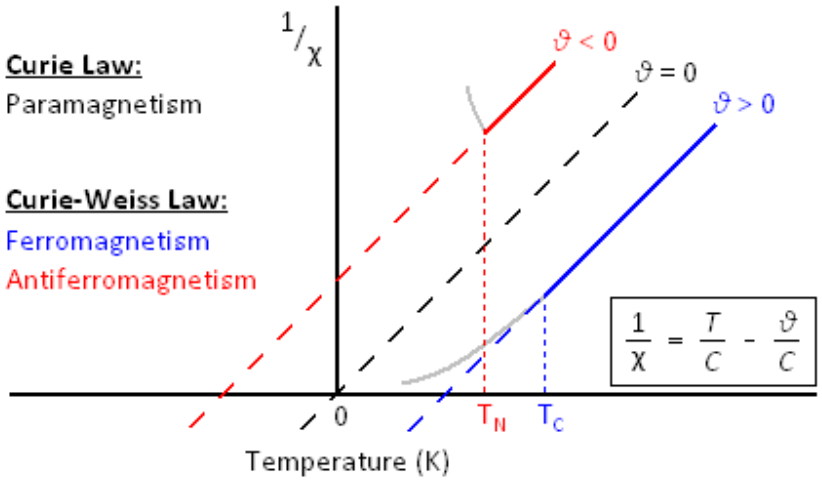

Fig 2.9: Plot of $1/\chi$ vs T for various magnetic systems

Above the Curie and Néel temperature, materials behave like paramagnets and are best described by equation 2.29, this should be re-written depending on the behaviour below T_C and T_N as following:

Ferromagnetism: $$\chi(T) = \frac{C}{T - T_C} \qquad (2.30)$$

Antiferromagnetism: $$\chi(T) = \frac{C}{T + T_N} \qquad (2.31)$$

2.5.3 Diamagnetism

In most cases a diamagnetic contribution arises from the paired core electrons, the value of which is extremely small and negative. This contribution is vastly out-weighed by

other effects such as paramagnetism due to the presence of unpaired electrons; however, very large values of diamagnetism can arise in the case of superconducting materials. It is worth noting that diamagnets repel external magnetic fields. A simple way to visualise this is to think of a magnetic field composed of flux lines. The density of these lines is proportional to the field (*B*). A diamagnet will push out these magnetic flux lines, while a paramagnet will pull them in.

2.5.4 Superconductivity

The magnetic properties of superconductors are very unique and complex. Superconductors are characterised by exactly zero electrical resistance but very importantly by the exclusion of the interior magnetic field (the Meissner effect). In addition, an electrical current flowing through a superconducting material will persist indefinitely with no power source.

The resistivity of a metallic conductor decreases with temperature; however, because of defects and impurities the resistivity never actually reaches a minimum, even at absolute zero. In contrast, the resistivity of a superconductor drops abruptly to zero when cooled below its “critical temperature”, which is material dependent.

When a superconductor is placed into a weak magnetic field, *H*, the field penetrates only to a shallow depth which is called the "London penetration depth". This is the Meissner effect and is a defining characteristic of superconductivity. The Meissner effect is not to be confused with Lenz' Law which states that when a perfect conductor is subjected to an internal magnetic field an equal and opposite magnetic field is induced. The Meissner effect begins to break down under increasingly large applied magnetic fields. Superconductors are divided broadly into two classes depending how this breakdown occurs. In *type-I* superconductors the superconducting state is abruptly destroyed above a certain applied critical field, H_c. In *type-II* superconductors increasing

the applied field strength above H_{c1} leads to a mixed state where an increasing amount of magnetic flux penetrates the material. At the second critical field, H_{c2} the superconductivity is destroyed and the normal metallic state recovered.

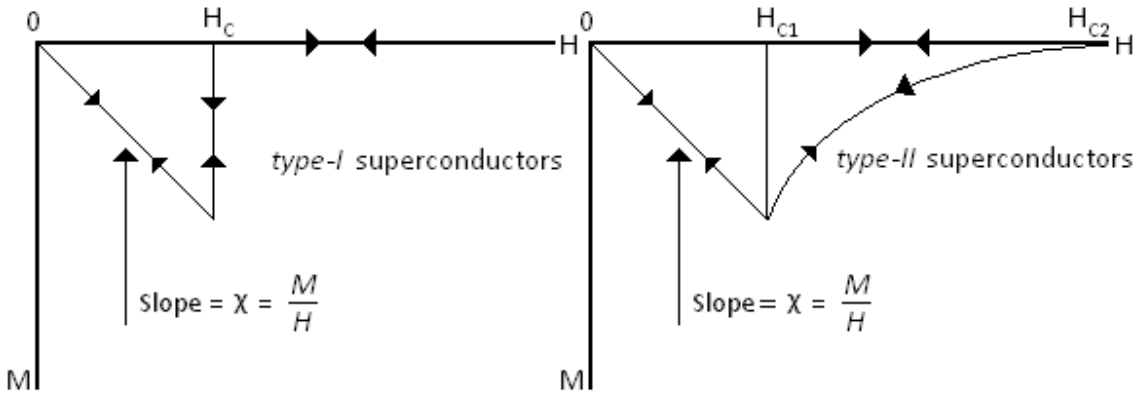

Fig 2.10: Magnetic behaviour as a function of field for type-I and type-II superconductors

The characteristic superconducting transition temperature (T_c) can be measured by following the temperature dependence of the magnetisation in a low applied magnetic field typically of a few Oe. T_c is defined as the temperature where the diamagnetic response is suppressed and the paramagnetic behaviour of the metallic state is recovered.

The most obvious commercial property of superconductivity is the observation of zero electrical resistance, one of the simplest ways to measure this phenomenon is through d.c. magnetisation measurements. Below T_c, persistent currents on the surface of the superconducting material expel all magnetic flux, i.e. it is a perfect diamagnet. In measurements conducted in this thesis we utilise two types of d.c. magnetisation measurements, field-cooled (FC) and zero-field-cooled (ZFC). ZFC, cooling the superconductor in zero applied magnetic field and measuring the magnetisation on warming, below T_c the superconductor displays perfect diamagnetism. FC, cooling in a weak magnetic field through T_c followed by measurement on warming, magnetic flux

present inside the sample above T_c is trapped inside by the shielding currents on the surface during cooling. In terms of flux expulsion, the FC susceptibility is still diamagnetic but at a much reduced in magnitude when compared to the ZFC susceptibility. This hysteresis of the diamagnetic susceptibility below T_c is known as the Meissner effect and is definitive proof of superconductivity. Below (Fig 2.11) shows the typical response of a superconductor to ZFC and FC susceptibility measurements.

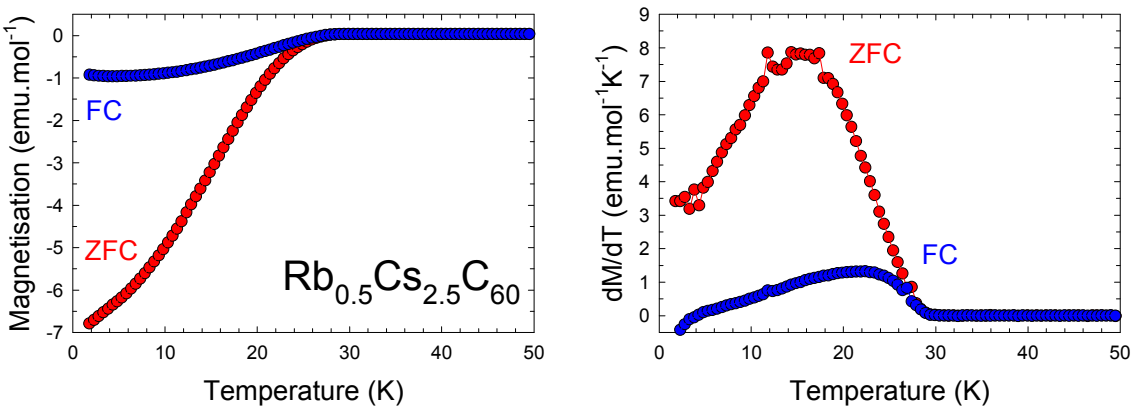

Fig 2.11: Typical FC and ZFC measurements for an A_3C_{60} type II superconductor

2.5.6 BCS Theory

The superconducting transition temperature also shows a dependence on the atomic mass of an element. One of the earliest documented cases is the isotope effect exhibited by mercury, Hg.[20,21] This dependence of the T_c with isotopic mass was the first direct evidence for interaction between the electrons and the lattice. This supported the BCS theory of lattice coupling of electron pairs.

In 1957, John Bardeen, Leon Cooper, and Robert Schrieffer (BCS) proposed a theory that explained the origins of superconductivity.[22] The basis of their theory stems from an earlier discovery by Cooper who showed that at sufficiently low temperatures the

ground state of a material is unstable with respect to the formation of 'bound' pairs of electrons close to the Fermi level.[23] The maximum strength of the e^--e^- interaction is the phonon energy, $\hbar\omega_D \approx 0.01\text{-}0.02eV$, which shows that only a small fraction of the electrons can be paired. These bound electrons are known collectively as Cooper pairs and have opposing spins and momentum, furthermore due to the Pauli exclusion principle, all pairs act as Bosons having the momentum $\vec{P} = 0$ and occupy the same quantum state, the BCS ground state.

At low temperatures in a typical crystalline material an electron within the cation lattice can distort the lattice around it, creating a pocket of increased positive charge density. A second electron some distance away (~ 100nm) in the lattice is then attracted to this pocket of increased charge density, without feeling the Coulomb repulsion of the first electron. Therefore it can be said that, electrons are indirectly attracted to one another and hence the formation of a cooper pair. There are a lot of Cooper pairs in a superconductor; they overlap strongly forming a highly collective "Boson condensate". Breaking just of one pair results in a changing of energies of the remaining Cooper pairs, therefore pairs retain this ordered structure while moving through the crystal lattice. Each pair becomes locked into its position with others pairs and as a result no random scattering of electron pairs occur. Thus, the collective behaviour of "Boson condensate" is a crucial property of superconductivity. Zero resistivity may be defined as the absence of electron scattering; hence the superconductor now demonstrates zero resistivity.

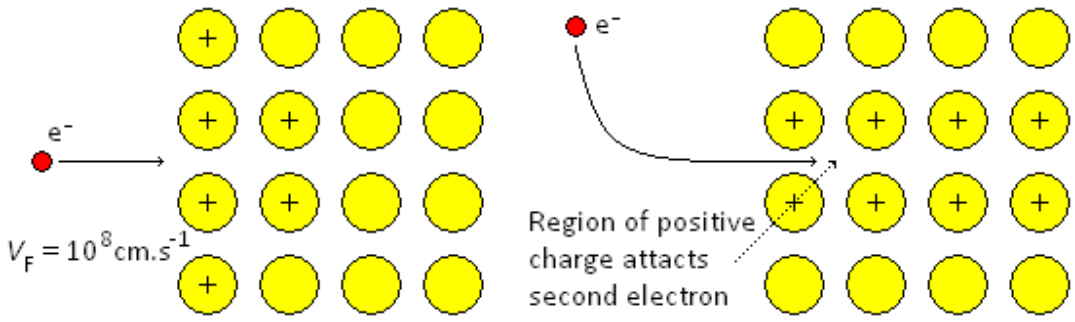

Fig 2.12: Schematic representation of the movement of a Cooper pair.

2.5.6 Superconducting fraction and transition temperature

For the results contained in this thesis the superconducting (shielding) fraction of a material is calculated from the ZFC magnetisation data using the formula:

$$\text{SC Fraction}(\%) = \left(\frac{4\pi \rho \Delta_{mom}}{H m} \right) \times 100 \qquad (2.32)$$

where ρ (g.cm^{-3}) is the density of the material, Δ_{mom} (emu) is the modulus of the change in the long moment from the paramagnetic to the superconducting state, H (Oe) is the magnetic field strength, and *m* (g) is the mass of the material.

T_c is defined as the first temperature point for which dM/dT begins to increase. In some cases there were two distinct upturns in the dM/dT function, the actual T_c is defined as the value of the upturn associated with the main superconducting fraction. In many cases there was a small upturn to higher T_c; however, the size of the superconducting fraction associated with this is trace.

2.5.7 SQUID Magnetometer

The Magnetic Property Measurement System (MPMS5) is designed for studying and determining accurately the magnetic properties of a sample over a temperature range between 1.8 and 400 K and over a range of applied magnetic fields between 0 and 5 Tesla. The MPMS (Fig 2.13) is composed of several different parts, some housing superconducting components. At the centre of the magnetic moment detection system is a SQUID (Superconducting Quantum Interference Device) detector. The MPMS control software can be employed to subtract datasets, thus allowing background subtraction so that sample responses can be studied even in the presence of significant background

contributions. After measuring for extend periods at high magnetic fields, there may be a remnant magnetic field present upon zeroing the field for subsequent low field measurements. This residual drift can be reset using a degaussing procedure which oscillates the magnetic field from a positive magnetic field to a negative magnetic field and gradually reduces amplitude of oscillation. After the degaussing procedure, the superconducting magnet can be also reset; this involves heating the superconducting windings in the magnet above their T_c for 5 seconds before quenching them back into the He reservoir.

Fig 2.13: The MPMS5 SQUID magnetometer: schematic diagram of MPMS probe with blow up of superconducting solenoid detector coil (right).[24]

The sample chamber is located inside the superconducting detection coils and is maintained at a low temperature using helium gas. If moisture or air contaminate the sample space, the SQUID magnetometer needs to be warmed to room temperature so a rigorous pumping procedure can be performed. The sample is attached to the edge of a rigid straight sample rod using Kapton tape, which is non-magnetic and resistant to the low temperatures experienced inside the SQUID, before being lowered into the sample space. The Sample Handling System controls the vertical motion of the rod during data acquisition. Measurements are performed by moving a sample in a series of discrete steps

through the superconducting detection coils, which are connected to the SQUID input coil with superconducting wires (Fig 2.14).

As the sample moves through the second-derivative coil, it causes a perturbation in the magnetic flux within the detection coils. The SQUID is a device that can function as a highly linear and sensitive current-to-voltage converter. The voltage variations are taken at discrete points along the superconducting coil and the integration of the area under the voltage vs position plot gives a highly accurate measurement of the magnetic moment resulting from the sample. This measurement is typically repeated three times and an average is taken along with the associated error. Comparing the errors against the magnitude of the measured signal allows determination of the precision of the observed effects.

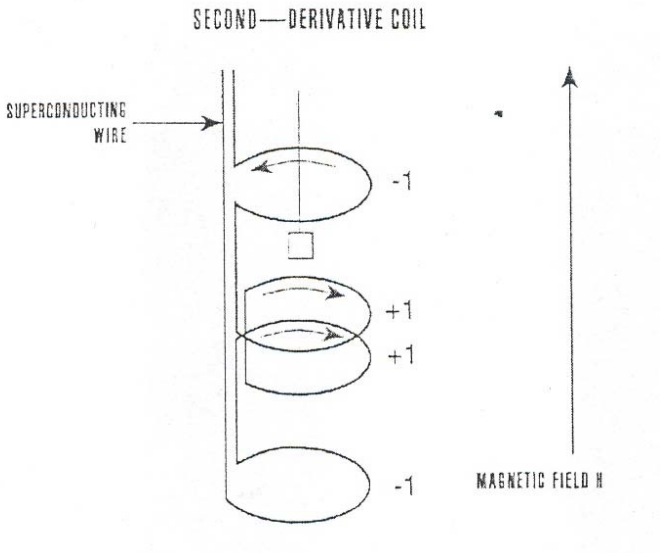

Fig 2.14: Configuration of the second-derivative coil.[25]

2.5.8 High Pressure Magnetic Measurements

High pressure magnetic measurements were carried out using the “easyLab Mcell 10”.

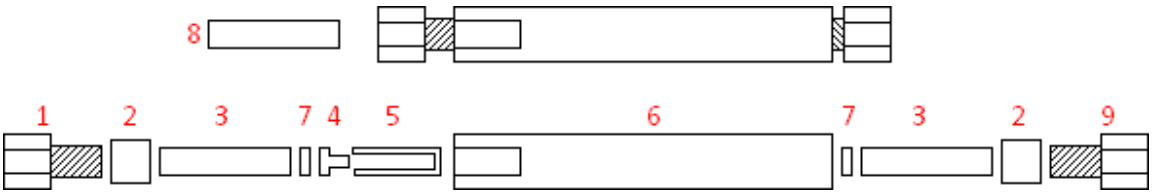

Fig 2.15: easyLab Mcell 10 General Assembly drawing, 1 - Upper lock nut. 2 - Ceramic piston cap. 3 - Ceramic piston. 4 - PTFE plug. 5 - PTFE cap. 6 - Pressure cell body. 7 - Anti-extension ring. 8 - Tungsten-Carbide piston. 9 - Lower lock nut

When assembling the cell, great care must be taken to ensure the channel of the Mcell10 body is clean from dust or remaining debris from previous measurements. The cell is then assembled (see Fig 2.15); during this process the contents of the cell must be correctly/tightly packed. Also the order and orientation of components are extremely important, so that the background is consistent with the actual measurement.

Before anything is loaded into the PTFE cap a small coil of Sn wire is added as a manometer as the temperature dependence of the superconducting transition temperature at different pressure stages is known accurately for Sn. Using a syringe and dispenser, pressure transmitting oil is dispensed into the PTFE cap. It is important to avoid air bubbles at this stage inside the PTFE cap. The oil inside the cell acts as a pressure transmitting medium, so that magnetic measurements can be carried out whilst the sample is under pressure. The PTFE capsule is then closed using a PTFE plug.

When closing the cell, the upper-lock nut is tightened by hand and its distance from the main body of the cell is measured using a Vernier calliper. This value is then recorded onto the loading sheet. The loading sheet shows the user if the cell will be

overtightened at a subsequent pressurisation. Overtightening can permanently damage the high pressure cell.

The assembled cell is then placed into the hydraulic press (Mpress). During the pressurisation process, the WC piston compresses the components of the cell. This allows the upper locking nut to be tightened. At specific pressure points of the Mpress the locking nut is tightened until a resistance is felt (it cannot be tightened anymore). Values are recorded in the loading sheet. Measurements can be made during both increasing and releasing pressure.

Before the measurements are carried out a background measurement is performed with an empty assembly, in that I mean the components, the transition medium and the Sn manometer are assembled with no sample present. ZFC and FC background measurements are ran over the exact temperature range of the forthcoming experiment, with precisely the same field. Also the background measurements are ran using 2 different sized PTFE plug's. This is to emulate the background contribution of the cell at low and high pressures. It is worth noting that centering the loaded sample under weak fields can be a difficult task, in order to ensure the position of the sample in the coils at the mean position is consistent, the transport is first centred using a ferromagnetic material such as Ni, and then one can accurately measure the length of the rod with the attached high pressure cell, from there small adjustments can be made using the SQUIDs software to make the sample height more precise (an accuracy of 0.1 mm can be achieved).

2.6 References

[1] Atkins. P. W., *Physical Chemistry 6th ED*., Oxford University Press, **2001**

[2] Hahn T., *International tables for crystallography, Vol. A, Space group symmetry*, Reidel D., Publishing Company **1983**

[3] Ashcroft N. W., Mermin N. D., *Solid State Physics*, Holt-Saunders, **1976**

[4] Giacovazzo C., *Fundamentals of Crystallography*, Oxford University Press, **1994**

[5] Freund A., *Neutron and Synchrotron Radiation for Condensed Matter Studies*, **1993**, Springer-Verlag, Vol.1, Chap. 3

[6] http://www.esrf.eu/UsersAndScience/Experiments/Beamlines

[7] Masson O., Dooryhée E., Cheary R. W., Fitch A. N. *Mater. Sci. Forum* **2001**, 300, 378-381

[8] Wright J., Vaughan G., Fitch A., *IUCr Computing Commission Newsletter* **2003**, No. 1, p. 92

[9] http://www.diamond.ac.uk/dms/Images/news/Media-images/3D-model-of-the-machine/

[10] Rietveld H. M. *J. Appl. Cryst*. **1969**, 2, 65-71

[11] Young R. A., Mackie R. E., Von-Dreele R. B. *J. Appl. Cryst*. **1977**, 10, 262-269

[12] Albinati A., Willis B. T. M. *J. Appl. Cryst*. **1982**, 15, 361-374

[13] Thomson P., Cox D. E., Hastings J. B. *J. Appl. Cryst*. **1984**, 20, 79-83

[14] Hastings J. B., Thomlinson W., Cox D. E. *J. Appl. Cryst*. **1984**, 17, 85-95

[15] Cheetham A. K., Taylor J. C. *Solid State Chem.* **1977**, 21, 253-275

[16] Young R. A., Wiles D. B. *J. Appl. Cryst.* **1982**, 15, 430-438

[17] Larsen A. C., Von Dreele R. B. *GSAS software, Los Alamos National Laboratory Report LAUR* **1994**, 86-748

[18] LeBail A., Duroy H., Fourquet J. L. *Mater. Res. Bull.* **1988**, 23, 447-452

[19] Toby B. H. *J. Appl. Cryst*. **2001**, 34, 210-213

[20] Maxwell E. *Phys. Rev*. **1950**, 78, 477

[21] Reynolds C. A., Serin B., Wright W. H., Nesbitt L. B. *Phys. Rev*. **1950**, 78, 487

[22] Bardeen L., Cooper L. N., Schrieffer J. R. *Phys. Rev.* **1957**, 108, 1175-1204

[23] Cooper L. N. *Phys. Rev.* **1956**, 104, 1189-1190

[24] MPMS5 instruction manual, electronic copy.

Chapter 3

$Rb_xCs_{3-x}C_{60}$ solid solutions – FCC-rich compositions

3.1 Introduction

In superconducting merohedrally disordered $Fm\bar{3}m$ A_3C_{60} systems, it has been widely reported that T_c increases monotonically with interfulleride separation distance.[1,2,3,4,5] As Cs^+ is the largest alkali metal cation, Cs_3C_{60} is a key material in this family; however, the isolation of FCC Cs_3C_{60} has proven difficult as direct synthesis by thermal combination of Cs and C_{60} in gas–solid or solid–solid reactions has been unsuccessful.[6] The lack of success of traditional solid state synthetic methods can be attributed to the disproportionation reaction of Cs_3C_{60} to give the thermodynamically stable Cs_1C_{60} and Cs_4C_{60} phases. This is driven by the fact that the tetrahedral cavity in the FCC structure is too small to accommodate large cations such as Cs^+. Combining Cs and C_{60} to make Cs_3C_{60} met with moderate success when metal alloys such as CsHg were employed;[7] however, the shielding fraction of the resulting product was <1% and the obtained samples were poorly crystalline and of unknown structure.

In 1995, Palstra *et al.* reported a solution-based low-temperature synthetic technique for producing Cs_3C_{60} in reasonable quantities.[8] The method involved reducing C_{60} with Cs dissolved in liquid ammonia, followed by vacuum removal of ammonia, and annealing at temperatures of 150^{o}C. Their report indicated that the phase responsible for superconductivity, which was induced by pressure was either body-centred cubic, body-centred tetragonal or orthorhombic in symmetry; however, none of the studies proved anything conclusively as the samples were of poor quality.[9,10]

Along similar lines, work by Dahlke *et al.* utilised a similar low-temperature synthesis technique to isolate the series of compounds $A_xCs_{3-x}C_{60}$ [where A is either Rb ($0.3 \leq x \leq 1$) or K ($0.3 \leq x \leq 1$)].[11] The annealing protocols and solvent utilised appeared to favour the formation of the FCC phase; however, sample crystallinity was again poor. In this work, the largest lattice parameter obtained was a = 14.6925(4) Å for a sample with nominal composition $Rb_{0.32}Cs_{2.68}C_{60}$. Reducing further the nominal rubidium content in the samples in order to achieve larger interfulleride separations

led only to smaller fractions of the FCC phase and no increase in the unit cell volume. Theoretically the estimated lattice constant for the FCC phase should reach a maximum of 14.76 Å for Cs_3C_{60}. In addition to this, T_c decreased with increasing FCC lattice volume, e.g. T_c was lower in $Rb_{0.32}Cs_{2.68}C_{60}$ than that in $K_{0.74}Cs_{2.26}C_{60}$. Fig 3.1 summarises the results of earlier studies on the superconducting FCC A_3C_{60} systems. It clearly shows the monotonic increase in T_c with increasing C_{60} nearest neighbour distances together with the anomalous behaviour of the Dahlke *et al.*'s systems at large interfullerene separations.

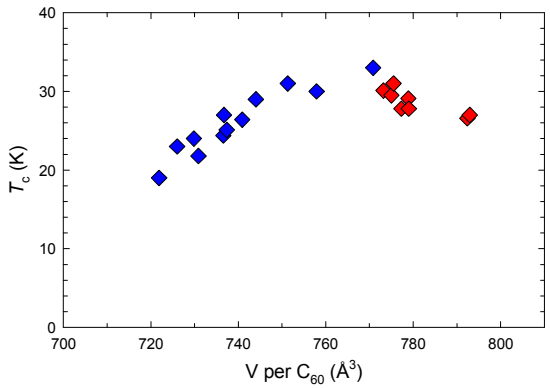

Material	T_c	Volume / C_{60} (A^3)
Li_2CsC_{60}	0	703.8(9)
Na_2CsC_{60}	12	705.9(3)
K_3C_{60}	19	721.9(3)
K_2CsC_{60}	24	729.8(5)
KRb_2C_{60}	27	734.6(5)
Rb_3C_{60}	29	744.0(5)
Rb_2CsC_{60}	31	751.3(3)
$RbCs_2C_{60}$	33	770.9(4)

Fig 3.1: Superconducting transition temperature for selected A_3C_{60} superconductors plotted as a function of the FCC unit cell volume (at room temperature) per C_{60}. Blue diamonds represent literature T_c values, red diamonds represent those for the $Rb_xCs_{3-x}C_{60}$ materials synthesised by Dahlke *et al.*[11]

In the pursuit of methods that produce expanded materials with higher superconducting volume fractions and enhanced crystallinity, new solvents such as methylamine have been utilised.[12,13,14] Precursor samples with cations and solvent molecules distributed homogeneously at the nanoscale are promising candidates to obtain expanded fullerides upon subsequent mild annealing. Recently a comprehensive study of Cs_3C_{60} was performed by Ganin *et al.*[15] utilising methylamine as a solvent. This work showed that the obtained Cs_3C_{60} material following this route was not superconducting; however, application of pressure induced an insulator-metal transition and a superconducting phase with a transition temperature of 38 K and a shielding fraction of 68% was obtained at ~0.7 GPa. The material synthesised comprised three crystalline phases with the majority A15 phase responsible for the

high T_c of 38 K. The two minority phases identified had FCC and body-centred orthorhombic (BCO) structures (Fig. 3.2). Using density functional theory, the electronic properties of the two key polymorphs, A15 and FCC, were compared as a function of unit cell volume.[16] It was found that the A15 phase displays both a substantially broader bandwidth for the partially occupied t_{1u} band and a larger density-of-states at the Fermi level. This result was traced to differences in the nature of the inter-anion overlap in the A15 and FCC structures, showing that the A15 Cs_3C_{60} phase is not simply another superconducting fulleride, albeit with a very high T_c; it is in fact the parent member of an electronically distinct class of fulleride superconductors.

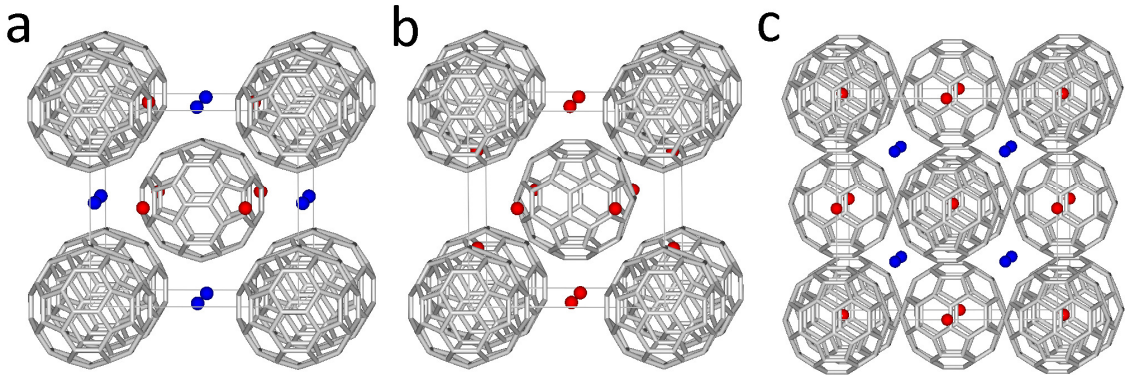

Fig 3.2: **a**, BCO unit cell (space group *Immm*). **b**, A15 unit cell (space group *Pm* $\bar{3}$ *n*). **c**, FCC unit cell (space group *Fm* $\bar{3}$ *m*) of Cs_3C_{60}. In **a** and **b**, one unique orientation of the C_{60}^{3-} anions is present, whereas in **c** two orientations related by 90° rotation about [100] occur in a disordered manner; only one of these orientations is shown for clarity. The Cs^+ ions are shown as red and blue spheres in **a** to signify symmetry-inequivalent positions in the unit cell.

No studies undertaken so far have been able to isolate and fully characterise the FCC phase at high Cs doping levels. Also previous research into FCC-rich $Rb_xCs_{3-x}C_{60}$ derivatives was unable to determine unambiguously how T_c varies with cell volume for these expanded fullerides. Given the important results obtained for the expanded A15 phase of Cs_3C_{60}, the question naturally arises whether it is possible to isolate its FCC analogue and in addition to produce a series of solid solutions $Rb_xCs_{3-x}C_{60}$ and, if yes, what will be their electronic and conducting properties at ambient and elevated

pressures. This would extend significantly the scope of recent research on fulleride superconductivity and provide key information on the pressure dependence of the competing electronic states and of T_c at very large separations (Fig. 3.1). One of the goals of this research investigation has been to attempt to study the properties of the A15 and FCC phases by utilising chemical pressure (partial Rb doping), instead of physical pressure. Presented in this chapter is a solution-based study of a series of "FCC-rich" compounds with nominal composition $Rb_xCs_{3-x}C_{60}$ ($0.0 \leq x \leq 0.5$), prepared using ammonia (NH_3) as the solvent.

3.2 Experimental Methods

3.2.1 Preparation of $Rb_xCs_{3-x}C_{60}$ ($0.0 \leq x \leq 0.5$) – ammonia as the solvent medium

Prior to the experiments, NH_3 was rigorously dried by condensation onto sodium at -72^oC, stirring at RT for 12 hrs, and subsequent distillation into a separate but dimensionally identical reaction vessel (Fig. 3.3). Both vessels were linked using a glass adapter and the joints connecting the glassware were Young's adaptors (ball and socket mechanism) - typical ground glass sockets cannot cope with the high pressures experienced during ammonia transfer. Bulldog clips aided in keeping the joints air-tight. O-rings between the joints were coated in Teflon as ammonia will dissolve the unprotected rubber. In order to transfer ammonia between reaction vessels, both need to be cooled using solid CO_2/ethanol baths (-72^oC). The bath surrounding the NH_3 containing vessel was lowered slowly so that NH_3 can evaporate from the surface and condense into the second vessel (containing the Na metal). The resulting mixture was blue in colour due to the presence of solvated electrons. The vessel was sealed and allowed to settle at room temperature overnight under constant stirring. Re-distillation of the ammonia leaves behind a mixture of sodium, sodium oxide and other trace impurities, which are neutralised safely using isopropanol. The ammonia is now of high enough purity to be used in synthesis.

All samples and precursors synthesised are highly air sensitive, so great care is taken to ensure the sample environment is meticulously clean, dry and air free. C_{60} (MER corporation, super gold grade, >99.9% purity) was ground inside the glove box (O_2 < 0.1 ppm, H_2O < 0.9 ppm) and degassed overnight at 200^{o}C under dynamic vacuum; this procedure was repeated twice. Reaction mixtures of stiochiometric amounts of Rb (99.95% purity Aldrich), Cs (99.95% purity Aldrich) and C_{60} were placed into a glass vessel along with a magnetic stirring bar. The vessel was then removed from the glove box and evacuated at first to low pressures of 10^{-2} Torr using a rotary pump and finally to 10^{-5} Torr with a turbomolecular pump for 1-2 hours. The reaction vessel is then linked to the vessel containing the purified ammonia using the before described procedure. Both are cooled using the solid CO_2/ethanol baths so that 60 ml of ammonia can be transferred. The reaction mixture was red due to the presence of $(C_{60})^{3-}$ anion. The vessel was sealed and allowed to settle at room temperature for 1 hour under constant stirring.

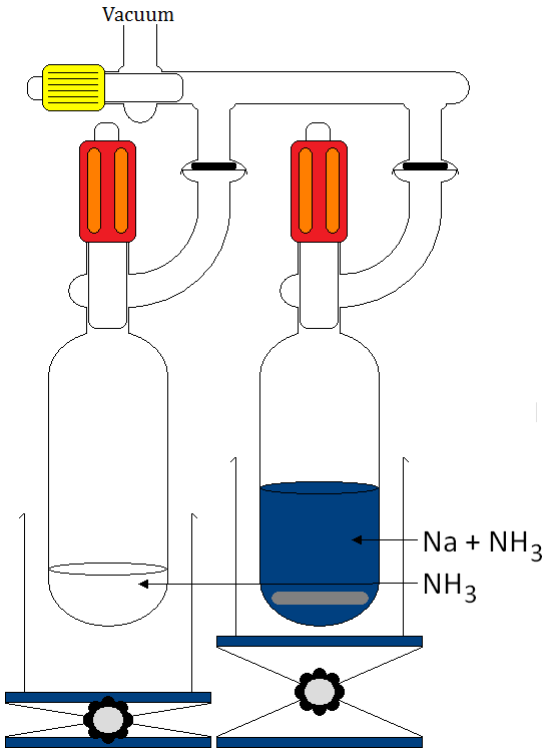

Fig 3.3: Apparatus used for distillation of ammonia during the synthesis of the $Rb_xCs_{3-x}C_{60}$ compounds.

Following re-condensation, the NH_3 liquid was sealed and preserved for subsequent synthesis. The product was evacuated at first to low pressures of 10^{-2} Torr using a rotary pump and then to 10^{-5} Torr with a molecular pump for 3-4 hours to remove any residual ammonia. Finally, the precursor was annealed for 16 hours at 120°C under dynamic vacuum.

The product was removed from the reaction vessel inside the glove box, then ground using a mortar and pestle, and pelletised (8 mm diameter) before being loaded into a tantalum cell. The Ta cell was then sealed inside a glass tube under a small pressure of He gas (400 Torr), and then placed inside a furnace pre-heated to 400°C. Intermediate grindings of the sample were performed on a weekly basis in order to improve the homogeneity and obtain crystalline samples.

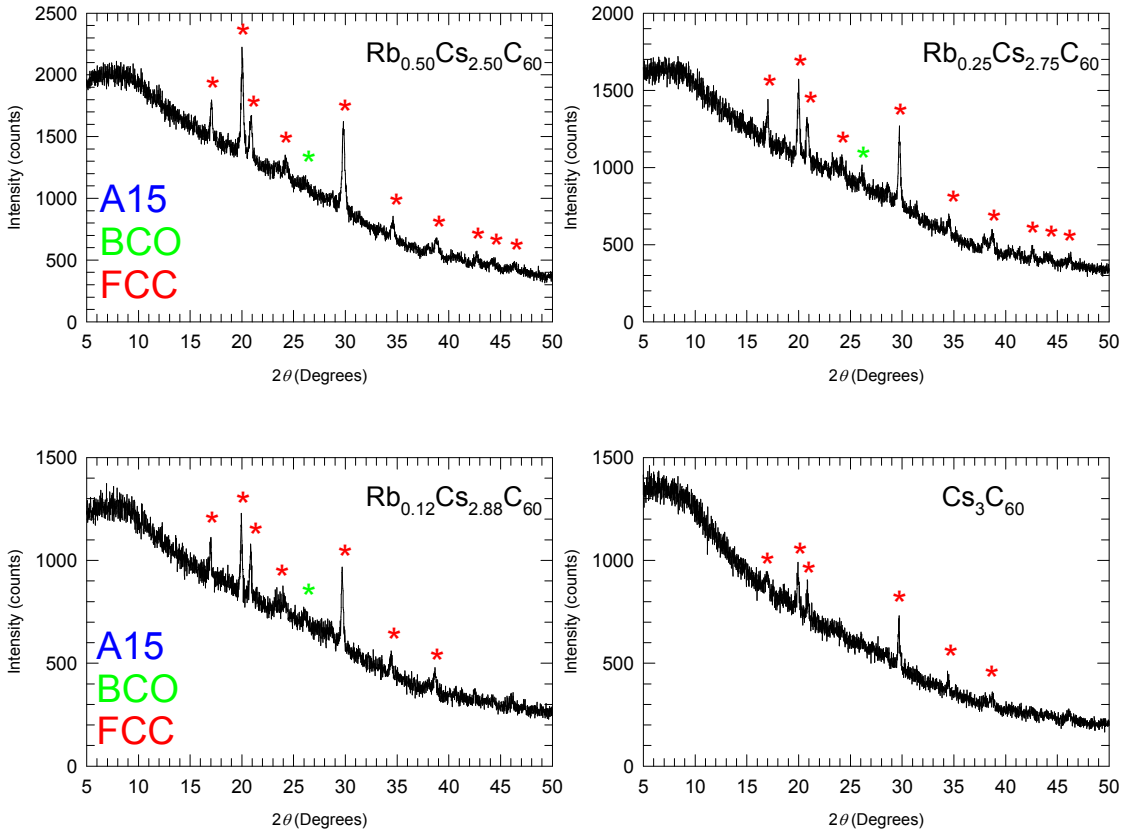

Fig 3.4: X-ray diffraction profiles of the "FCC rich" samples $Rb_xCs_{3-x}C_{60}$ ($0.0 \leq x \leq 0.5$) collected with the Siemens D5000 powder diffractometer (Cu-K_α radiation) in capillary mode at room temperature. Red and green asterisks mark the FCC and BCO diffraction peaks, respectively.

By sealing the sample in small glass capillaries under Ar atmosphere, the reaction products were follow quantitatively after each grinding, by collecting data at room temperature with the Siemens D5000 X-ray powder diffractometer (λ = 1.5406 Å). 12 hr scans were recorded over a 2θ angular range of 5-50^{o} with a step size of 0.015^{o}. The diffraction patterns obtained for $Rb_xCs_{3-x}C_{60}$ ($0.0 \leq x \leq 0.5$) samples are shown in Fig 3.4. The D5000 data provide a preliminary assessment of the success of the synthetic procedures. The Bragg reflections due to the FCC phase are easily identifiable and simple LeBail refinements were performed in order to approximate the sample composition. It can be seen that the majority phase in all cases is the FCC, while a minor contribution from the BCO is also observed; however, no A15 phase is detectable at this signal-to-noise.

The quantities of starting materials used during synthesis are listed in Table 3.1. The accuracy of the balance inside the glovebox was ±1 mg. The volume of solvent was measured by adding 60 ml of water to the vessel prior to the experiment and marking the level on the exterior. As mentioned previously, intermediate grindings were performed on the samples on a weekly basis.

Table 3.1: Masses and volumes of the starting materials used in the synthesis of "FCC rich" $Rb_xCs_{3-x}C_{60}$ ($0.0 \leq x \leq 0.5$) samples. The precursor mass was after evacuation of NH_3 and removal of the precursor from the surface of the glass vessel. Final product mass was after all annealing protocols.

Sample ID	Nominal *x*	Moles of Rb (mmol)	Moles of Cs (mmol)	Moles of C_{60} (mmol)	Vol of NH_3 (ml)	Mass of Precursor (mg)	Mass of Product (mg)
MTM158_4	0.50	0.105	0.527	0.208	60	190	137
MTM159_3	0.25	0.059	0.647	0.232	60	217	162
MTM160_3	0.12	0.035	0.843	0.293	60	286	226
MTM161_3	0.00	--	0.504	0.168	60	162	111

Table 3.2: Summary of annealing protocols of the $Rb_xCs_{3-x}C_{60}$ samples produced using NH_3 as a solvent.

Sample ID	Nominal *x*	Annealing Protocol Timeframe
MTM158_4	0.50	1 week at 400°C + 1 week at 400°C + 1 week at 400°C
MTM159_3	0.25	1 week at 400°C + 1 week at 400°C
MTM160_3	0.12	1 week at 400°C + 1 week at 400°C
MTM161_3	0.00	1 week at 400°C + 1 week at 400°C

3.3 Synchrotron X-ray Diffraction Studies

Small amounts (3-6 mg) of each sample were sealed in 0.5 mm glass capillaries under 300 Torr of He gas. Room temperature and low temperature data were collected for each sample at two different synchrotron facilities, ESRF and Diamond. On beamline ID31 at the ESRF, data were collected in the 2θ range 5 to 30° in continuous scanning mode and re-binned from 2 to 25° in a step size of 0.003°. Room temperature data were collected outside the cryostat with the sample spinning (3000 rpm). Spinning the sample helps to eliminate any preferred orientation effects. For collecting low temperature data on ID31, the sample was remounted inside a continuous flow liquid He cryostat, and cooled at a rate of 5 K/min to 5 K. The sample was also spun during low temperature data acquisition, but at a much slower rate due to instrumental restrictions (1000 rpm).

On beamline I11 at Diamond, data were collected in the 2θ range 3 to 142° in continuous scanning mode and re-binned from 5 to 50° in a step size of 0.003°. Room temperature data were again collected outside the cryostat. For the low temperature measurements, the sample was cooled to 12 K. There was an issue with the quality of the background during data collection at Diamond that at these early stages of operation was attributed to the air conditioning unit.

When collecting data at ID31 the wavelengths were 0.39988(4) Å and 0.39991(7) Å, while the X-ray wavelength at Diamond was 0.8260280(1) Å. Analysis of the data was performed using the GSAS diffraction suite equipped with the EXPGUI interface. For all refinements, when a change of inter-fullerene separation distance was observed, the fullerene molecule dimensions were kept constrained.

3.4 $Rb_xCs_{3-x}C_{60}$ – Synchrotron XRD at room temperature

Detailed below is the methodical process used to determine the best refinement model. As all samples were multiphase the first logical step was to refine the model using fixed nominal Rb doping levels for each phase identified in the diffraction profiles; this basically meant that Rb was distributed equally throughout all observed phases. It is noted at this point that the unit cell volume and the phase fractions of each phase were more or less independent of the refinement model utilised throughout. The issues which immediately became apparent in the $Rb_xCs_{3-x}C_{60}$ series was that the unit cell volume of the A15 (1631(1) to 1632.0(1) $Å^3$, less than 0.1% variation) and BCO (1657.9(2) to 1662.1(1) $Å^3$, approximately 0.3% variation) components varied only slightly as the nominal Cs content increased, and with no consistent pattern. In contrast, the unit cell volume of the FCC phase increased systematically, from 3018.5(1) to 3213.0(1) $Å^3$, approximately a 6% variation across the series. This led to the tentative conclusion that the Rb co-doped into the sample may reside preferentially (or exclusively) in the FCC phase.

Therefore, in the subsequent refinement strategy, Rb was assumed to be present exclusively in the FCC component, while the stoichiometries of the A15 and BCO phases were kept fixed as Cs_3C_{60} and Cs_4C_{60}, respectively in agreement with earlier work.[15] As there are two symmetry-inequivalent cation positions in the unit cell of the FCC phase, the total occupancy of Rb and Cs in each site was fixed to 1.0; however, their relative ratio was allowed to refine. However, the stoichiometries derived by employing this structural model grossly overestimated the amount of Rb

present in each material. For example, a *refined* FCC stoichiometry of $Rb_{0.86(2)}Cs_{2.14(2)}C_{60}$ was obtained for sample MTM158_4 (nominal stoichiometry $Rb_{0.50}Cs_{2.50}C_{60}$), while the maximum *calculated* Rb content based on the quantities initially added and amount of the phase was $Rb_{0.62}Cs_{2.38}C_{60}$. The discrepancy is exacerbated further for sample MTM160_3 (nominal stoichiometry $Rb_{0.12}Cs_{2.88}C_{60}$) – refined composition $Rb_{0.76(2)}Cs_{2.24(2)}C_{60}$, calculated $Rb_{0.18(2)}Cs_{2.72(2)}C_{60}$, a more than four times overestimation of the amount or Rb. A model was then tested by fixing the amount of Rb present in the FCC phase to the maximum calculated value and the site occupancies to 1.0, while the Rb occupancy was allowed to refine unrestricted across both the T_d and the O_h cavities. The obtained results were again unsatisfactory as for every sample the occupancies of the O_h cavity were Rb < 0.0 and Cs > 1.0.

Further test structural models were constructed after considering sample MP002 (stoichiometry Rb_2CsC_{60}) – detailed refinements can be found in the subsequent *section 3.4.1*. Consider partial substitution of Rb by Cs in the parent material Rb_3C_{60} to afford Rb_2CsC_{60}, logically the larger Cs^+ cation will reside exclusively in the larger octahedral cavity and the smaller Rb^+ cation in the smaller T_d cavity. Further Cs substitution towards the $RbCs_2C_{60}$ and Cs_3C_{60} compositions would then involve introducing the additional Cs^+ amount into the smaller T_d, while the O_h site remains fully occupied by Cs^+ only. Therefore the refinement strategy was further modified so that occupancy of the O_h cavity was entirely by Cs^+ and the T_d cavity was a disordered Rb^+/Cs^+ mixture whose total occupancy was fixed to 1.0, while the relative Rb^+/Cs^+ ratio was allowed to refine. However, once more this led to an overestimation of the total Rb content in the samples.

The breakthrough came when the X-ray form factors of the Rb^+/Cs^+ cations were correctly accounted for at each wavelength by including the anomalous contributions to them. As the focus was on small occupancy discrepancies for the metal cations, the *f'* and *f''* corrections for Rb^+/Cs^+ cations at the wavelengths λ = 0.39988(4) Å and λ = 0.826028(1) Å were included. The program Dispano was used to calculate these wavelength dependent parameters λ = 0.39988(4) Å; Cs: *f'*=-1.921, *f''*=0.758; Rb: *f'*=0.156, *f''*=1.116, and λ = 0.826028(1) Å; Cs: *f'*=-0.438, *f''*=2.784; Rb: *f'*=-3.959, *f''*=0.520. This immediately improved the consistency of the refinement results.

Very importantly the occupancies of the cation sites in the FCC phase became meaningful and refinable. In the final refinement iterations the Rb^+ content was fixed to the maximum *calculated* value and placed exclusively in the tetrahedral site. Additionally Cs^+ was placed into this site and its occupancy refined without restriction. If the total occupancy of the fixed Rb plus refined Cs came close to 1.0, then the structural model could be accepted as being correct both chemically (as it conforms to the hypotheses discussed in the earlier paragraph) and mathematically (by the goodness of fit).

3.4.1 Rb_2CsC_{60} (sample MP002_3) at room temperature

Rietveld refinements were performed using the space group $Fm\bar{3}m$ (merohedrally disordered FCC model). As discussed previously, there are two non-equivalent cation sites in the FCC unit cell, one site is octahedral in symmetry and the other tetrahedral. The site multiplicities are in the ratio 2 T_d : 1 O_h. It is known explicitly that the void of the octahedral cavity is much larger than the void of the tetrahedral one and that the size of Cs^+ is larger than that of Rb^+. So for Rb_2CsC_{60} it is reasonable to assume that Rb^+ can be preferentially placed into the T_d site, while the larger Cs^+ resides in the larger O_h site.

In order to test the validity of this site occupation assumption, two refinement models were used. The first conformed to the above described situation of Rb being placed exclusively into the T_d site (cation ordered model). The second model included a constraint that the Rb and Cs total content was constant; however, the relative amount of Rb and Cs in each site was allowed to refine (cation disordered model).

Refinement 1: Cation ordered model

The refined parameters for the FCC (space group $Fm\bar{3}m$) Rb_2CsC_{60} phase obtained from the Rietveld analysis of the synchrotron X-ray powder diffraction data at ambient temperature are shown in Table 3.3. Estimated errors in the last digits are given in parentheses. The weighted profile and expected *R*-factors are R_{wp} = 8.22% and R_{exp} = 6.28%. The values of the lattice constant and unit cell volume are: a = 14.45190(7) Å, V = 3018.51(1) $Å^3$. The fractional occupancy, *N*, of Cs(1) in the octahedral and Rb(1) in the tetrahedral cavities were allowed to vary, converging to values around 1, resulting in a nominal stoichiometry of $Rb_{1.956(6)}Cs_{0.968(3)}C_{60}$. It is also worth noting that the very large isotropic temperature factor of the Cs(1) atom residing in the octahedral hole is a common feature of all known FCC A_3C_{60} phases.

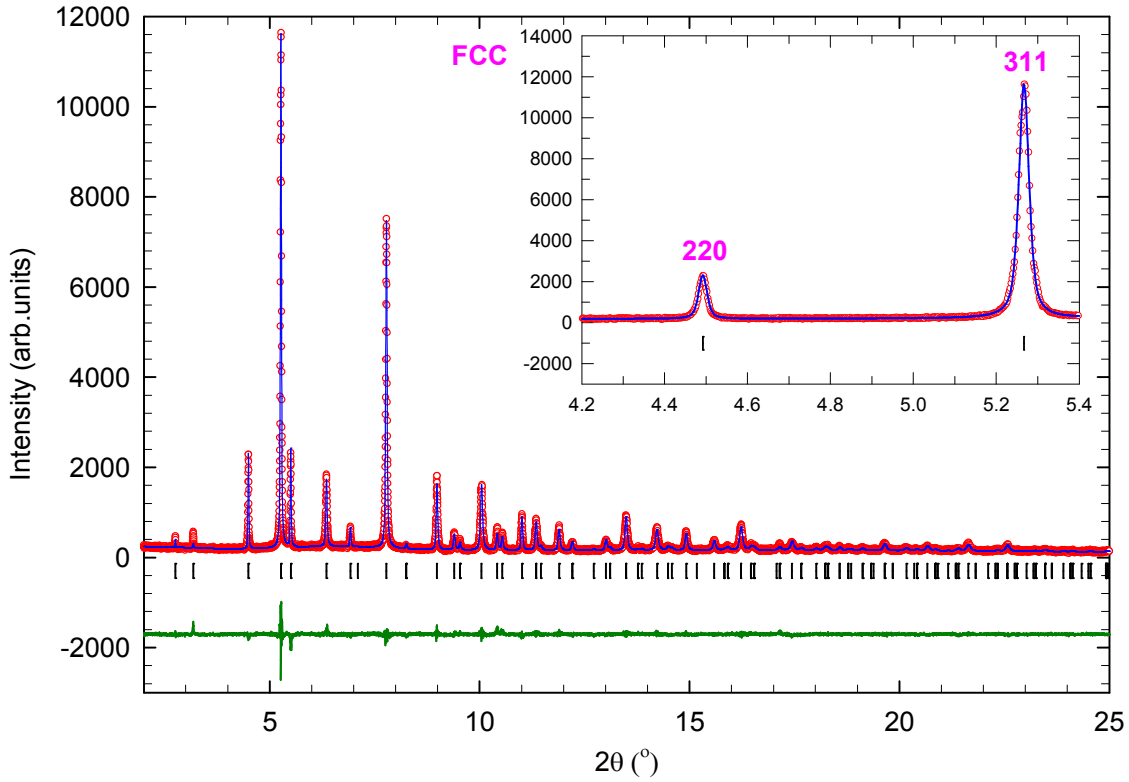

Fig 3.5: Observed (open red circles) and calculated (blue line) data of the room temperature synchrotron powder X-ray diffraction pattern for Rb_2CsC_{60} using the cation ordered model. The bars represent the positions of the Bragg reflections for the FCC phase. Zero point error = 0.00676(3)°, λ = 0.39988(4) Å.

Table 3.3: Results of the single-phase Rietveld refinement of FCC Rb_2CsC_{60} (cation ordered model).

	x/a	*y/b*	*z/c*	*N*	B_{Iso}(Å^2)
Rb(1)	0.25	0.25	0.25	0.978(3)	1.29(4)
Cs(1)	0.5	0.5	0.5	0.968(3)	5.67(7)
C(1)	0	0.0495	0.2490	0.5	0.96(8)
C(2)	0.2140	0.0774	0.1004	0.5	0.96(8)
C(3)	0.1737	0.1514	0.0496	0.5	0.96(8)

Refinement 2: Cation disordered model

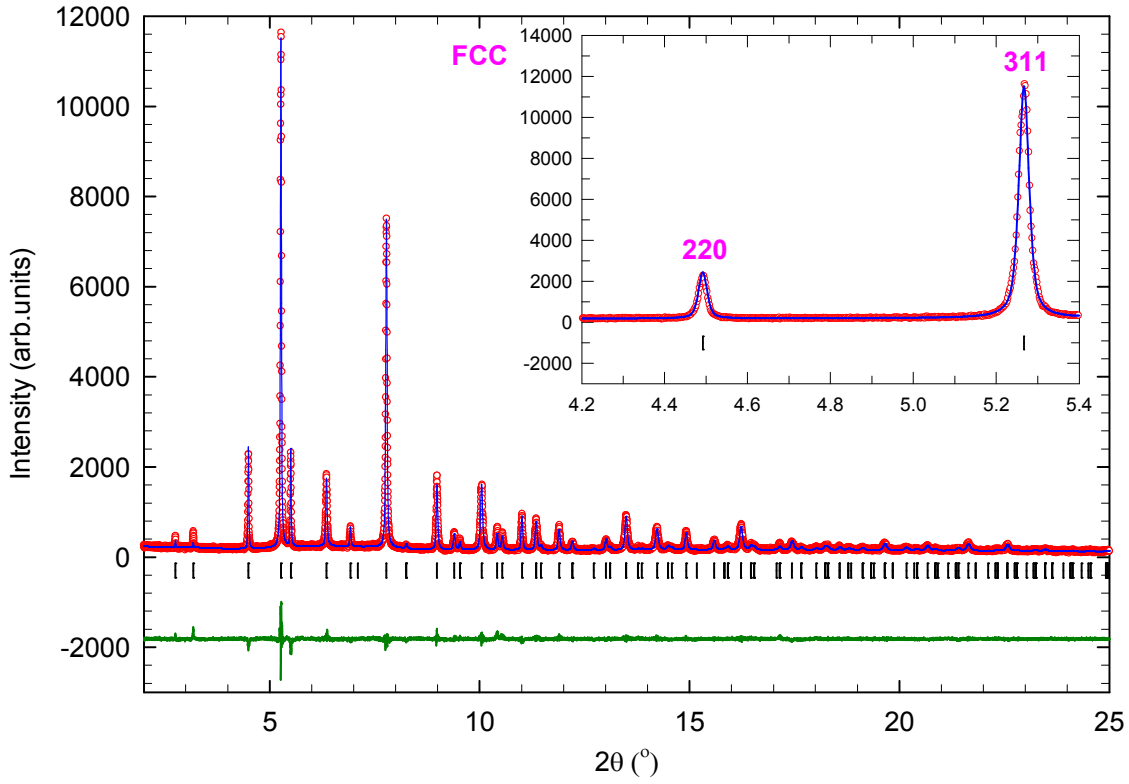

Fig 3.6: Observed (open red circles) and calculated (blue line) data of the room temperature synchrotron powder X-ray diffraction pattern for Rb_2CsC_{60} using the cation disordered model. The bars represent the positions of the Bragg reflections for the FCC phase. Zero point error = 0.00675(3)°, λ = 0.39988(4) Å

Refined parameters for the FCC (space group $Fm\bar{3}m$) Rb_2CsC_{60} phase obtained from the Rietveld refinement of the synchrotron X-ray powder diffraction data at ambient temperature for the cation disordered model are shown in Table 3.4. The weighted profile and expected *R*-factors are R_{wp} = 8.27% and R_{exp} = 6.28%. The values of the lattice constant and unit cell volume are: a = 14.45197(7) Å, V = 3018.43(5) $Å^3$. The fractional occupancy, *N*, of the octahedral and tetrahedral cavity was fixed at 1, and the Rb and Cs content of each site was allowed to vary, resulting in a nominal stoichiometry of $[Rb_{1.972(8)}Cs_{0.028(8)}]_T[Rb_{0.027(7)}Cs_{0.973(7)}]_OC_{60}$. Once again a very large isotropic temperature factor is obtained for the cations residing in the octahedral hole.

Table 3.4: Results of the single-phase Rietveld refinement of FCC Rb_2CsC_{60} (cation disordered model).

	x/a	*y/b*	*z/c*	*N*	B_{Iso}(Å^2)
Rb(1)	0.25	0.25	0.25	0.986(4)	1.41(4)
Cs(1)	0.25	0.25	0.25	0.014(4)	1.41(4)
Rb(2)	0.5	0.5	0.5	0.027(7)	5.81(7)
Cs(2)	0.5	0.5	0.5	0.973(7)	5.81(7)
C(1)	0	0.0495	0.2490	0.5	0.50(6)
C(2)	0.2140	0.0774	0.1004	0.5	0.50(6)
C(3)	0.1737	0.1514	0.0496	0.5	0.50(6)

From the above refinements it can be seen that the overall agreement factors differ little between the two models with R_{wp} being marginally better for the cation ordered model. There is little difference when the disordered model is utilised with the relative amount of cross cavity occupation being extremely small. The conclusion is that the cation ordered model is an excellent description of the crystal structure of Rb_2CsC_{60}.

3.4.2 $Rb_xCs_{3-x}C_{60}$ ($0.0 \leq x \leq 0.5$) at room temperature

Refined parameters for the majority FCC (space group $Fm\bar{3}m$), minority A15 (space group $Pm\bar{3}n$) and minority BCO (space group $Immm$) phases are shown below in the tables within this subsection. First Table 3.5 includes an overall summary, showing key refinement parameters and results, and then each sample is given a more detailed description. A two-phase Rietveld refinement of the synchrotron X-ray powder diffraction data of sample MTM158_4 was undertaken as there was no A15 phase present. The tabulated results for the three remaining samples: MTM159_3, MTM160_3 and MTM161_3 are from three-phase Rietveld refinements. The refinement strategy was exactly as described earlier and the fractional occupancies, *N*, of the Cs(1) and Cs(2) atoms were allowed to vary, converging to values where the total occupancy of the two unique sites [T_d: Cs(1) + Rb(1) and O_h: Cs(2)] were close to 1. In the final stages of the Rietveld refinements, *N* was fixed for Rb to the value given by the amount of Rb added initially. Occasionally the temperature factors for the minority phases have refined to negative values, the cause of this has not been identified. The fractions of the co-existing minority A15 and BCO phases are also included; the stoichiometries of the two minority phases were not refined but kept fixed at Cs_3C_{60} and Cs_4C_{60} for the A15 and BCO phases, respectively.

Table 3.5: Summary results of the Rietveld refinements of the diffraction data of the series $Rb_xCs_{3-x}C_{60}$ ($0.0 \leq x \leq 0.5$) at room temperature.

Parameter	*MTM158_4*	*MTM159_3*	*MTM160_3*	*MTM161_3*
Nominal x	0.50	0.25	0.12	0
R_{wp} **(%)**	6.01	6.20	7.33	5.05
R_{exp} **(%)**	5.23	5.86	6.83	3.71
χ^2	1.072	1.029	1.036	1.167
λ (Å)	0.39988(4)	0.39988(4)	0.39988(4)	0.39988(4)
A15 (%)	0	2.9(2)	5.8(1)	18.1(1)
BCO (%)	19.5(2)	32.0(2)	30.1(2)	33.7(1)
FCC (%)	80.5(1)	65.1(2)	64.1(2)	48.2(1)

A15 *a* (Å)	--	11.771(3)	11.773(1)	11.7736(3)
A15 *V* (Å^3)	--	1631(1)	1631.6(5)	1632.0(1)
BCO cell (Å)	*a* = 11.953(1) *b* = 12.163(1) *c* = 11.4034(9)	*a* = 11.961(1) *b* = 12.163(1) *c* = 11.4119(9)	*a* = 11.951(1) *b* = 12.159(1) *c* = 11.4258(8)	*a* = 11.9632(8) *b* = 12.1603(7) *c* = 11.4254(5)
BCO *V* (Å^3)	1657.9(2)	1660.1(2)	1660.3(2)	1662.1(1)
FCC *a* (Å)	14.6613(2)	14.7009(2)	14.7243(2)	14.75607(7)
FCC *V* (Å^3)	3151.5(1)	3177.1(1)	3192.3(1)	3213.01(5)
Refined FCC stoichiometry	$Rb_{0.62}Cs_{2.36(1)}C_{60}$	$Rb_{0.37}Cs_{2.59(1)}C_{60}$	$Rb_{0.18}Cs_{2.80(1)}C_{60}$	$Cs_{2.99(1)}C_{60}$

Sample MTM158_4 at room temperature

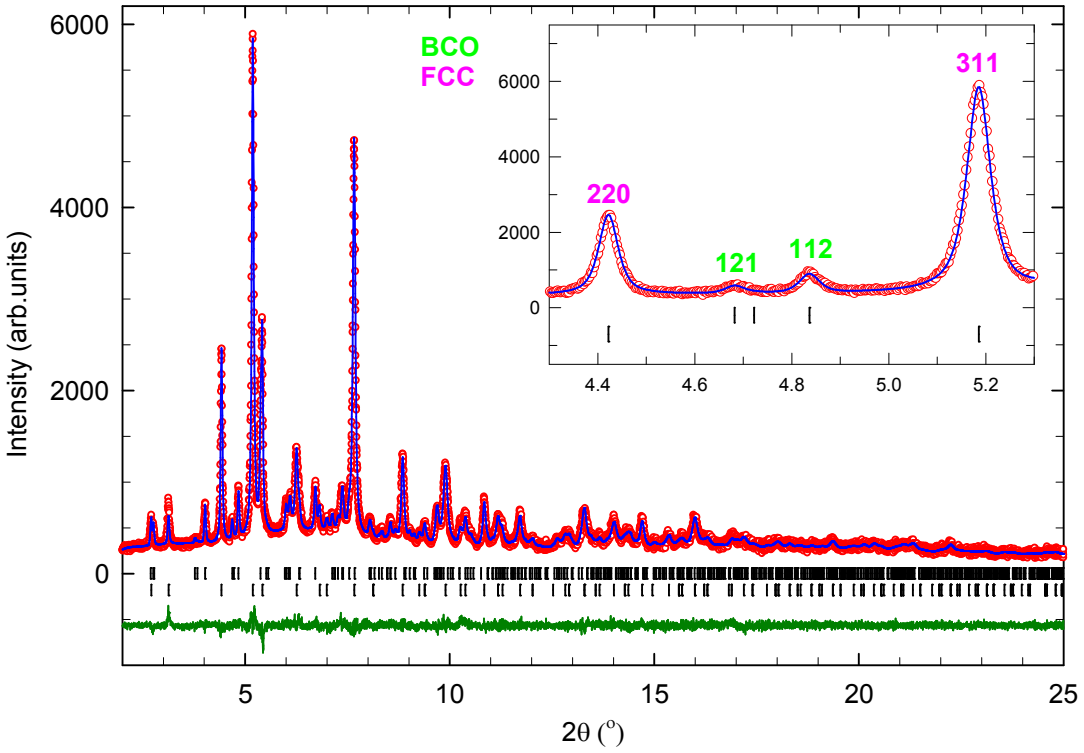

Fig 3.7: Observed (open red circles) and calculated (blue line) data of the room temperature synchrotron powder X-ray diffraction pattern for the sample with nominal composition $Rb_{0.50}Cs_{2.50}C_{60}$. The upper bars represent the positions of the Bragg reflections of the BCO phase and the lower ones of the FCC phase. The wavelength was λ = 0.39988(4) Å.

Table 3.6: Results of the room temperature two-phase Rietveld refinement of the Rb containing FCC phase in the sample with overall nominal composition $Rb_{0.50}Cs_{2.50}C_{60}$ (MTM158_4).

	x/a	*y/b*	*z/c*	*N*	B_{Iso}(Å^2)
Cs(1)	0.25	0.25	0.25	0.681(3)	1.78(7)
Rb(1)	0.25	0.25	0.25	0.309	1.78(7)
Cs(2)	0.5	0.5	0.5	0.992(4)	8.5(2)
C(1)	0	0.0488	0.2455	0.5	0.7(1)
C(2)	0.2110	0.0763	0.0990	0.5	0.7(1)
C(3)	0.1712	0.1492	0.0489	0.5	0.7(1)

Table 3.7: Results of the room temperature two-phase Rietveld refinement of the Cs_4C_{60} BCO phase in the sample with overall nominal composition $Rb_{0.50}Cs_{2.50}C_{60}$ (MTM158_4).

	x/a	*y/b*	*z/c*	*N*	B_{Iso}(Å^2)
Cs(1)	0.2041	0.5	0	1	1.7(2)
Cs(2)	0	0.2540	0.5	1	1.7(2)
C(1)	0	0.2871	0.0627	1	-1.1(4)
C(2)	0.0590	0	0.3020	1	-1.1(4)
C(3)	0.2913	0.0585	0	1	-1.1(4)
C(4)	0.0973	0.2505	0.1254	1	-1.1(4)
C(5)	0.1198	0.0951	0.2660	1	-1.1(4)
C(6)	0.2540	0.1172	0.1028	1	-1.1(4)
C(7)	0.1916	0.2141	0.0638	1	-1.1(4)
C(8)	0.0604	0.1924	0.2275	1	-1.1(4)
C(9)	0.2187	0.0586	0.2032	1	-1.1(4)

It is noted that the A15 phase is absent in this relatively high Rb containing sample, providing a lower Cs limit (or unit cell volume per C_{60}) for its stability range. The refined occupancies of Cs and Rb in the tetrahedral site of the FCC majority phase (phase fraction ~80%) are Cs = 0.681(3) and Rb = 0.309 (total N = 0.990(3)), while the refined Cs occupancy in the octahedral site is 0.992(4) (Table 3.6). The resulting stoichiometry is $Rb_{0.62}Cs_{2.36(1)}C_{60}$ implying full occupation of the cation sites and an oxidation state for C_{60} close to -3.

Sample MTM159_3 at room temperature:

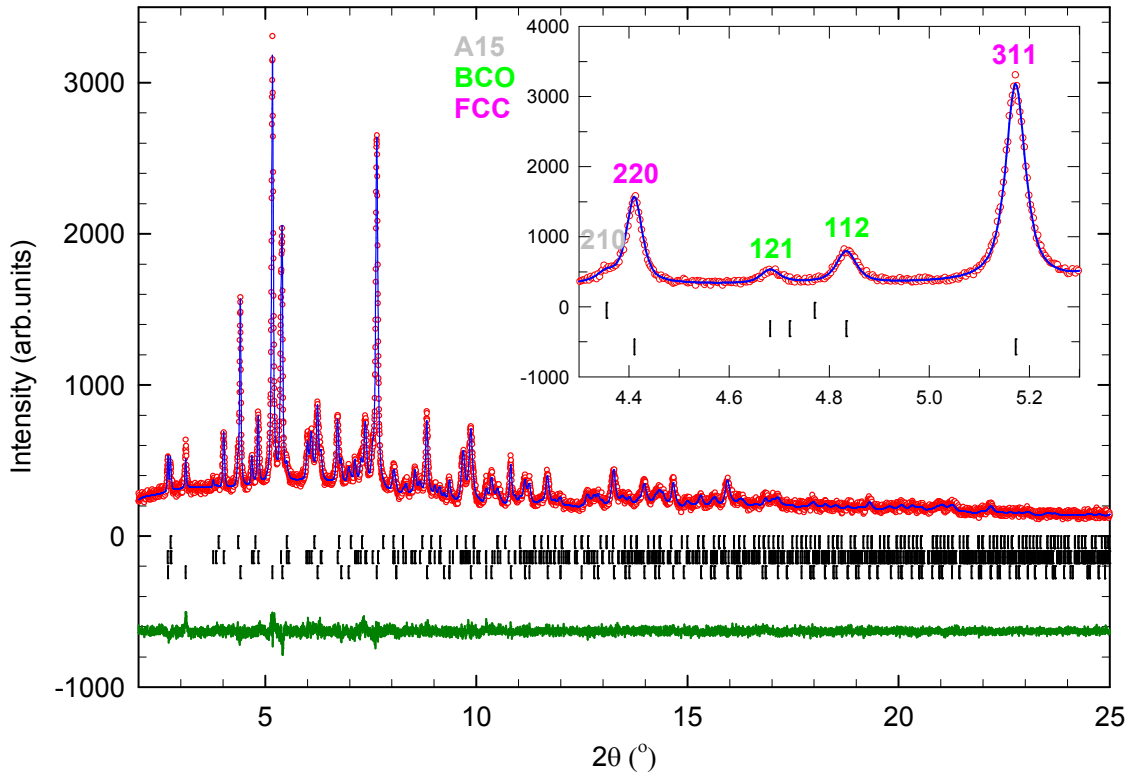

Fig 3.8: Observed (open red circles) and calculated (blue line) data of the room temperature synchrotron powder X-ray diffraction pattern for the sample with nominal composition $Rb_{0.25}Cs_{2.75}C_{60}$. The upper bars represent the positions of the Bragg reflections of the A15 phase, the middle ones of the BCO phase and the lower ones of the FCC phase. The wavelength is λ = 0.39988(4) Å.

Table 3.8: Results of the room temperature three-phase Rietveld refinement of the Rb containing FCC phase in the sample with overall nominal composition $Rb_{0.25}Cs_{2.75}C_{60}$ (MTM159_3).

	x/a	*y/b*	*z/c*	*N*	B_{iso}(Å^2)
Cs(1)	0.25	0.25	0.25	0.795(4)	1.43(8)
Rb(1)	0.25	0.25	0.25	0.186	1.43(8)
Cs(2)	0.5	0.5	0.5	0.995(6)	9.6(2)
C(1)	0	0.0487	0.2448	0.5	0.7(2)
C(2)	0.2104	0.0761	0.0987	0.5	0.7(2)
C(3)	0.1708	0.1488	0.0488	0.5	0.7(2)

Table 3.9: Results of the room temperature three-phase Rietveld refinement of the Cs_4C_{60} BCO phase in the sample with overall nominal composition $Rb_{0.25}Cs_{2.75}C_{60}$ (MTM159_3).

	x/a	*y/b*	*z/c*	*N*	B_{Iso}(Å^2)
Cs(1)	0.2040	0.5	0	1	1.7(2)
Cs(2)	0	0.2541	0.5	1	1.7(2)
C(1)	0	0.2871	0.0626	1	-1.0(4)
C(2)	0.0590	0	0.3018	1	-1.0(4)
C(3)	0.2911	0.0585	0	1	-1.0(4)
C(4)	0.0972	0.2506	0.1253	1	-1.0(4)
C(5)	0.1198	0.0951	0.2658	1	-1.0(4)
C(6)	0.2538	0.1172	0.1028	1	-1.0(4)
C(7)	0.1914	0.2141	0.0638	1	-1.0(4)
C(8)	0.0604	0.1924	0.2274	1	-1.0(4)
C(9)	0.2186	0.0586	0.2030	1	-1.0(4)

Table 3.10: Results of the room temperature three-phase Rietveld refinement of the Cs_3C_{60} A15 phase in the sample with overall nominal composition $Rb_{0.25}Cs_{2.75}C_{60}$ (MTM159_3).

	x/a	*y/b*	*z/c*	*N*	B_{Iso}(Å^2)
Cs(1)	0.25	0.5	0	1	7(2)
C(1)	0	0.2968	0.0610	1	-4(1)
C(2)	0.1210	0.0997	0.2548	1	-4(1)
C(3)	0.0621	0.2003	0.2209	1	-4(1)

The refined occupancies of Cs and Rb in the tetrahedral site of the FCC phase are Cs = 0.795(4) and Rb = 0.186 (total N = 0.981(4)), while the refined Cs occupancy in the octahedral site is 0.995(6) (Table 3.8). The resulting stoichiometry is $Rb_{0.37}Cs_{2.59(1)}C_{60}$ again implying full occupation of the cation sites and an oxidation state for C_{60} close to -3. A small fraction (~2.9%) of the A15 phase appears for the first time, implying the increased stability of this polymorph at increased Cs contents (unit cell volumes). This is accompanied by a decrease in the FCC phase fraction to ~65%.

Sample MTM160_3 at room temperature:

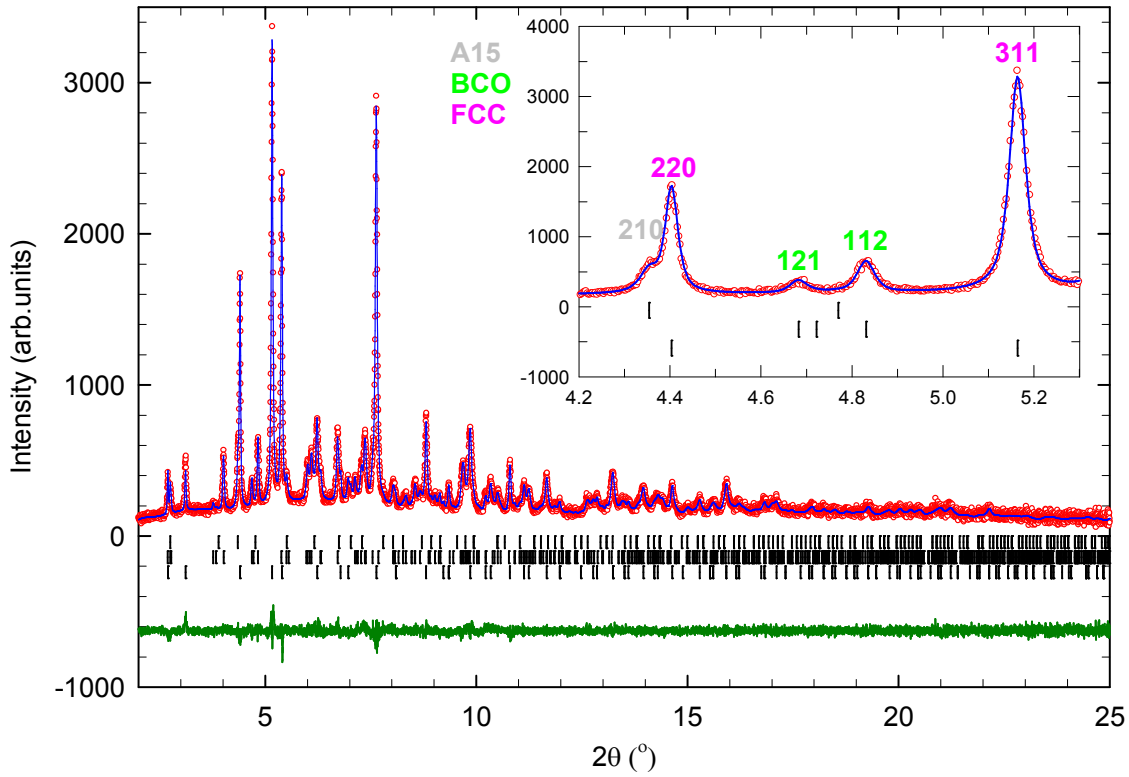

Fig 3.9: Observed (open red circles) and calculated (blue line) data of the room temperature synchrotron powder X-ray diffraction pattern for the sample with nominal composition $Rb_{0.12}Cs_{2.88}C_{60}$. The upper bars represent the positions of the Bragg reflections of the A15 phase, the middle ones of the BCO phase and the lower ones of the FCC phase. The wavelength is λ = 0.39988(4) Å.

Table 3.11: Results of the room temperature three-phase Rietveld refinement of the Rb containing FCC phase in the sample with overall nominal composition $Rb_{0.12}Cs_{2.88}C_{60}$ (MTM160_3).

	x/a	*y/b*	*z/c*	*N*	B_{Iso}(Å^2)
Cs(1)	0.25	0.25	0.25	0.904(4)	1.76(8)
Rb(1)	0.25	0.25	0.25	0.091	1.76(8)
Cs(2)	0.5	0.5	0.5	0.995(5)	10.0(2)
C(1)	0	0.0462	0.2444	0.5	0.6(2)
C(2)	0.2101	0.0760	0.0986	0.5	0.6(2)
C(3)	0.1705	0.1486	0.0487	0.5	0.6(2)

Table 3.12: Results of the room temperature three-phase Rietveld refinement of the Cs_4C_{60} BCO phase in the sample with overall nominal composition $Rb_{0.12}Cs_{2.88}C_{60}$ (MTM160_3).

	x/a	*y/b*	*z/c*	*N*	B_{Iso}(Å^2)
Cs(1)	0.2042	0.5	0	1	1.1(1)
Cs(2)	0	0.2542	0.5	1	1.1(1)
C(1)	0	0.2871	0.0626	1	-1.6(3)
C(2)	0.0590	0	0.3014	1	-1.6(3)
C(3)	0.2913	0.0585	0	1	-1.6(3)
C(4)	0.0973	0.2507	0.1254	1	-1.6(3)
C(5)	0.1198	0.0951	0.2658	1	-1.6(3)
C(6)	0.2539	0.1172	0.1026	1	-1.6(3)
C(7)	0.1916	0.2142	0.0637	1	-1.6(3)
C(8)	0.0604	0.1925	0.2271	1	-1.6(3)
C(9)	0.2187	0.0586	0.2028	1	-1.6(3)

Table 3.13: Results of the room temperature three-phase Rietveld refinement of the Cs_3C_{60} A15 phase in the sample with overall nominal composition $Rb_{0.12}Cs_{2.88}C_{60}$ (MTM160_3).

	x/a	*y/b*	*z/c*	*N*	B_{Iso}(Å^2)
Cs(1)	0.25	0.5	0	1	5.5(8)
C(1)	0	0.2968	0.0610	1	-4(1)
C(2)	0.1210	0.0997	0.2548	1	-4(1)
C(3)	0.0621	0.2003	0.2209	1	-4(1)

The refined occupancies of Cs and Rb in the tetrahedral site of the FCC phase (fraction ~ 64%) are Cs = 0.904(4) and Rb = 0.091 (total *N* = 0.995(4)), while the refined Cs occupancy in the octahedral site is 0.995(5) (Table 3.11). The resulting stoichiometry is $Rb_{0.18}Cs_{2.80(1)}C_{60}$ again implying full occupation of the cation sites and an oxidation state for C_{60} close to -3. The fraction (~5.8%) of the A15 phase increases slightly as the Cs content (unit cell volume) increases further.

Sample MTM161_3 at room temperature:

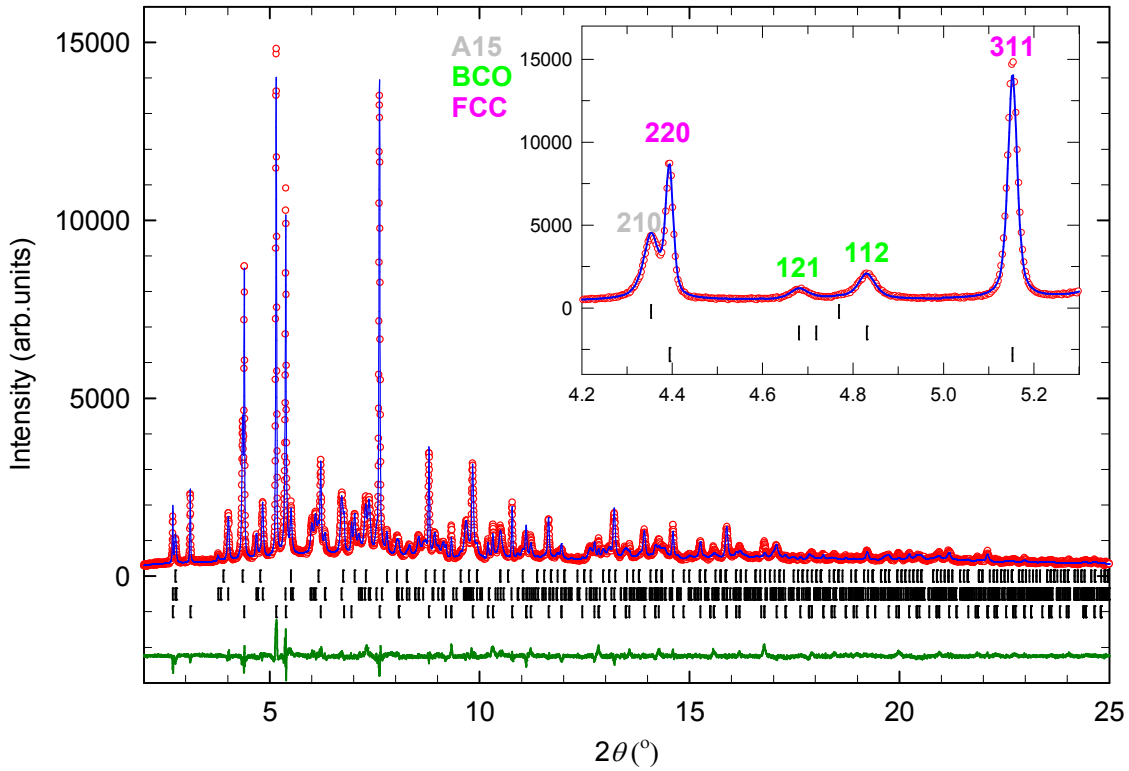

Fig 3.10: Observed (open red circles) and calculated (blue line) data of the room temperature synchrotron powder X-ray diffraction pattern for the sample with nominal composition Cs_3C_{60}. The upper bars represent the positions of the Bragg reflections of the A15 phase, the middle ones of the BCO phase and the lower ones of the FCC phase. The wavelength is λ = 0.39988(4) Å.

Table 3.14: Results of the room temperature three-phase Rietveld refinement of the Cs_3C_{60} FCC phase in the sample with overall nominal composition Cs_3C_{60} (MTM161_3).

	x/a	*y/b*	*z/c*	*N*	B_{iso}(Å^2)
Cs(1)	0.25	0.25	0.25	1.007(3)	1.98(4)
Cs(2)	0.5	0.5	0.5	0.979(4)	10.7(1)
C(1)	0	0.0485	0.2440	0.5	0.8(1)
C(2)	0.2096	0.0758	0.0983	0.5	0.8(1)
C(3)	0.1701	0.1483	0.0486	0.5	0.8(1)

Table 3.15: Results of the room temperature three-phase Rietveld refinement of the Cs_4C_{60} BCO phase in the sample with overall nominal composition Cs_3C_{60} (MTM161_3).

	x/a	*y/b*	*z/c*	*N*	B_{Iso}(Å^2)
Cs(1)	0.2039	0.5	0	1	1.46(9)
Cs(2)	0	0.2541	0.5	1	1.46(9)
C(1)	0	0.2872	0.0626	1	-0.7(2)
C(2)	0.0590	0	0.3014	1	-0.7(2)
C(3)	0.2911	0.0585	0	1	-0.7(2)
C(4)	0.0972	0.2506	0.1251	1	-0.7(2)
C(5)	0.1197	0.0951	0.2654	1	-0.7(2)
C(6)	0.2537	0.1173	0.1026	1	-0.7(2)
C(7)	0.1914	0.2142	0.0637	1	-0.7(2)
C(8)	0.0604	0.1925	0.2271	1	-0.7(2)
C(9)	0.2185	0.0586	0.2028	1	-0.7(2)

Table 3.16: Results of the room temperature three-phase Rietveld refinement of the Cs_3C_{60} A15 phase in the sample with overall nominal composition Cs_3C_{60} (MTM161_3).

	x/a	*y/b*	*z/c*	*N*	B_{Iso}(Å^2)
Cs(1)	0.25	0.5	0	1	2.7(1)
C(1)	0	0.2967	0.0609	1	-0.7(3)
C(2)	0.1210	0.0997	0.2548	1	-0.7(3)
C(3)	0.0620	0.2003	0.2209	1	-0.7(3)

The refined occupancies of Cs in the tetrahedral and octahedral sites of the FCC phase are 1.007(3) and 0.979(4) (Table 3.14). The resulting stoichiometry is $Cs_{2.99(1)}C_{60}$ again implying full occupation of the cation sites and an oxidation state for C_{60} close to -3. The fraction (~18%) of the A15 phase has increased further while the FCC phase fraction decreases to ~48%. Nonetheless it must be stressed that, following the synthetic route devised here, this is the first time that the crystalline FCC Cs_3C_{60} phase (invariably reported in the past as a non-existent phase) has been synthesised at such high phase fraction.

3.4.3 Summary – structural properties of the FCC $Rb_xCs_{3-x}C_{60}$ series at room temperature

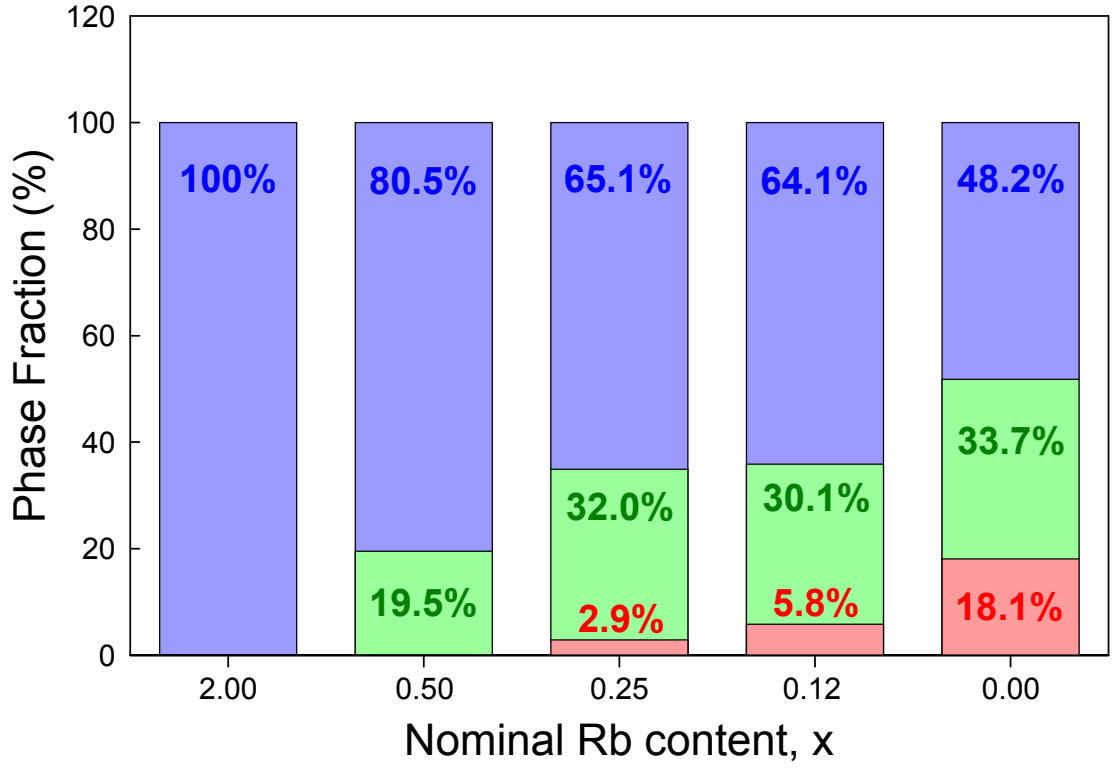

Fig 3.11: Variation of the fractions of the three polymorphs for the series of samples, $Rb_xCs_{3-x}C_{60}$. Red filling represents the A15, green the BCO and blue the FCC phase.

The Rb_2CsC_{60} sample was synthesised using conventional solid-solid reaction techniques and, in agreement with earlier work, it is single phase and exclusively FCC-structured. As the amount of co-intercalated Cs increases, the relative stability of the FCC phase decreases, while formation of the BCO and A15 polymorphs begins to be favoured. For the NH_3-solvent synthesised Cs-rich samples, the reaction conditions were optimised to favour stabilisation of the FCC phase. Such low-temperature solution-based methods were found to lead to a relatively constant amount of the BCO phase. On the other hand, there is an obvious variation in the phase percentage of the A15 and FCC phases – at high Rb doping levels, the FCC phase appears to be completely dominant; however, as the amount of Cs increases until the parent

material Cs_3C_{60} is obtained, the A15 phase fraction, although in minority, becomes significant. These trends are summarised in Fig 3.11. Although a variety of structural models were attempted in the course of the refinements, the observed trends in the volume fractions (Fig 3.11) and the unit cell volume (Fig 3.12) were robust throughout.

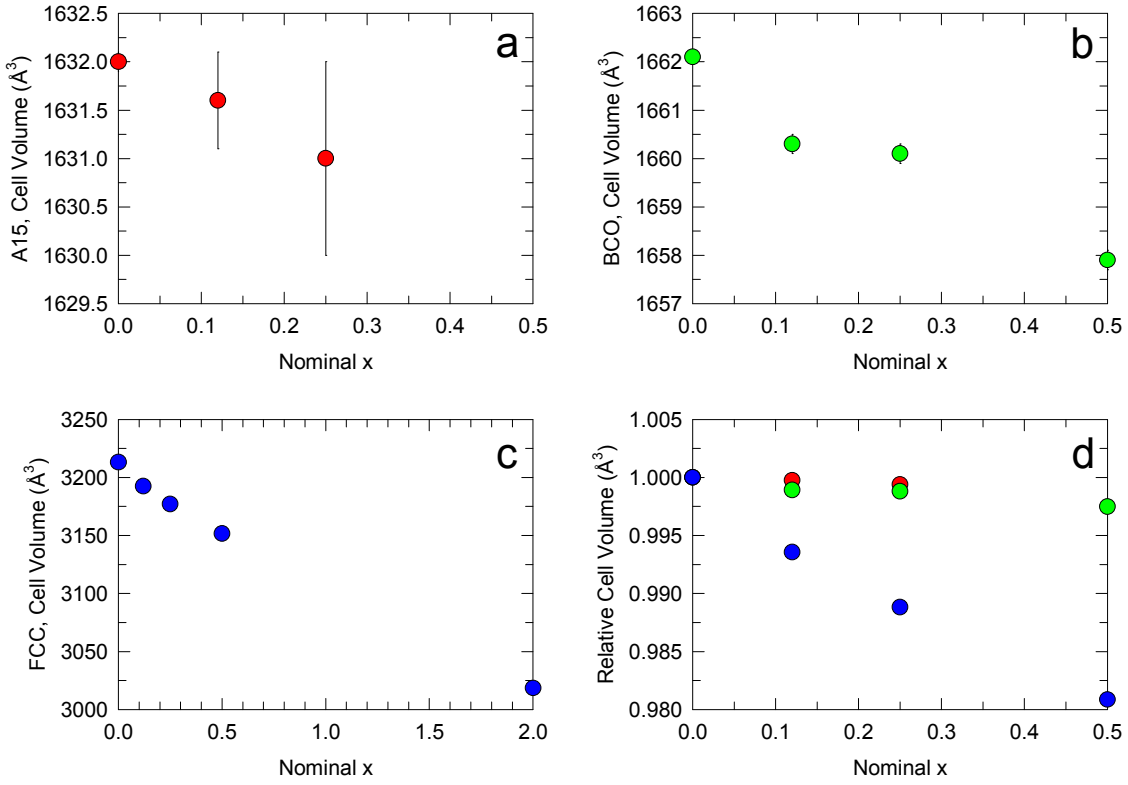

Fig 3.12: Changes in unit cell volume with nominal Rb content *x* in the $Rb_xCs_{3-x}C_{60}$ series. Panels **a** , **b**, **c** show the corresponding evolution for the A15, BCO and FCC phase, respectively. Panel **d** depicts the evolution of normalised unit cell volume for all three phases.

Fig 3.12 shows the unit cell volume changes across the $Rb_xCs_{3-x}C_{60}$ series. It is immediately apparent that for the BCO and A15 phases, there is little variation, V/C_{60} is unaffected by the Rb doping level and no solid solution formation is observed. Therefore, in our final refinement model the compositions were fixed as Cs_3C_{60} and Cs_4C_{60} for the A15 and BCO phases respectively, which is in agreement with the literature findings for the analysis of A15-rich samples.[15] In contrast, the unit cell volume of the FCC phase is very sensitive to the Rb doping level *x* and decreases

monotonically with increasing *x*, implying the formation of a solid $Rb_xCs_{3-x}C_{60}$ solution and obeying Vegard's law. Given the relative sizes of the tetrahedral and octahedral interstices in an FCC fullerene sublattice, it is expected that the cell metrics will be determined sensitively by the size of the cations residing in the tetrahedral holes. This is clearly evident in Fig 3.13 where a linear dependence of the unit cell volume on the relative cationic occupancy of the T_d site by Rb and Cs is observed.

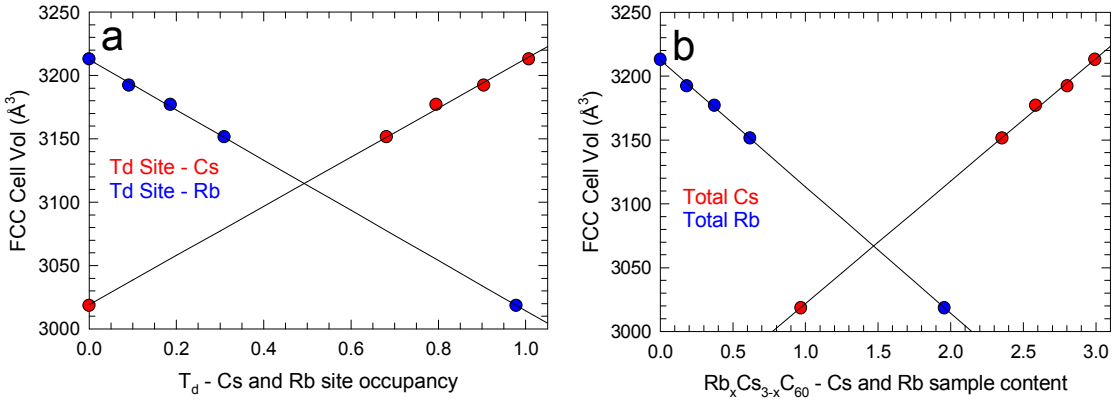

Fig 3.13: Refined unit cell volume of the FCC $Rb_xCs_{3-x}C_{60}$ phases as a function of the site occupancy of the T_d sites by Cs and Rb (**a**) and as a function of the total Cs and Rb content (**b**). (error bars included, but smaller than points).

Finally, it is worth noting that in all room temperature diffraction data refinements, the Cs^+ occupancy of the FCC octahedral cavity was freely refined, always converging to values close to 1.0 – it can be concluded that there is insignificant Rb^+ occupancy of this site. The refinement of the occupancies of the T_d site was more challenging. When refined the values observed were larger than the Rb amount used in the chemical synthesis. Since X-rays are also sensitive to electronic density and not to the identity of the ions, determining partial Cs/Rb occupancy became an ambiguous exercise. Rb was therefore assumed to be exclusive to the T_d site of the FCC phase, the occupancy was calculated based on the quantity initially added and phase fraction of the FCC polymorph. Its value was then fixed and the Cs content of the site to refined.

3.4.4 $Rb_xCs_{3-x}C_{60}$ ($0.0 \leq x \leq 0.5$) at low temperature

Refined parameters at low temperature for the majority FCC (space group $Fm\bar{3}m$), minority A15 (space group $Pm\bar{3}n$) and minority BCO (space group $Immm$) phases are shown below in the tables within this subsection. First Table 3.17 includes an overall summary, showing key refinement parameters and results, and then each sample is given a more detailed description. No phase transitions are observed for any of the samples on cooling, and refinement results obtained are comparable to their room temperature counterparts. Like at room temperature, the temperature factors for the minority phases often refined to negative values, again it must be stressed the cause of this has not been identified. The refinement procedures were identical to those described for the room temperature diffraction data in Section 3.4.2.

Table 3.17: Summary results of the Rietveld refinements of the diffraction data of the series $Rb_xCs_{3-x}C_{60}$ ($0.0 \leq x \leq 0.5$) at low temperature.

Parameter	*MTM158_4*	*MTM159_3*	*MTM160_3*	*MTM161_3*
Nominal x	0.50	0.25	0.12	0
T (K)	5	12	12	12
R_{wp} (%)	4.57	4.98	4.47	4.08
R_{exp} (%)	3.92	2.22	1.37	1.57
χ^2	1.080	1.498	1.806	1.612
λ (Å)	0.39988(4)	0.826028(1)	0.826028(1)	0.826028(1)
A15 (%)	0	2.5(1)	5.2(1)	19.4(1)
BCO (%)	19.5(2)	30.5(2)	29.6(2)	33.8(1)
FCC (%)	80.4(1)	67.0(1)	65.2(2)	46.8(1)
A15 *a* (Å)	--	11.718(2)	11.7201(7)	11.7736(3)
A15 *V* (Å^3)	--	1609.1(6)	1609.9(3)	1632.0(1)

	a = 11.903(2)	a = 11.8864(6)	a = 11.8839(5)	a = 11.8911(5)
BCO cell (Å)	b = 12.121(2)	b = 12.1029(5)	b = 12.1028(4)	b = 12.1015(4)
	c = 11.383(1)	c = 11.3807(4)	c = 11.3977(3)	c = 11.3961(3)
BCO V (Å^3)	1642.3(2)	1637.22(9)	1639.32(8)	1639.91(6)
FCC a (Å)	14.6010(2)	14.6178(1)	14.64879(8)	14.67639(4)
FCC V (Å^3)	3112.7(1)	3123.53(6)	3143.44(5)	3161.24(2)
Refined FCC stoichiometry	$Rb_{0.62}Cs_{2.32(2)}C_{60}$	$Rb_{0.37}Cs_{2.54(1)}C_{60}$	$Rb_{0.18}Cs_{2.76(1)}C_{60}$	$Cs_{2.94(1)}C_{60}$

Sample MTM158_4 at 5 K:

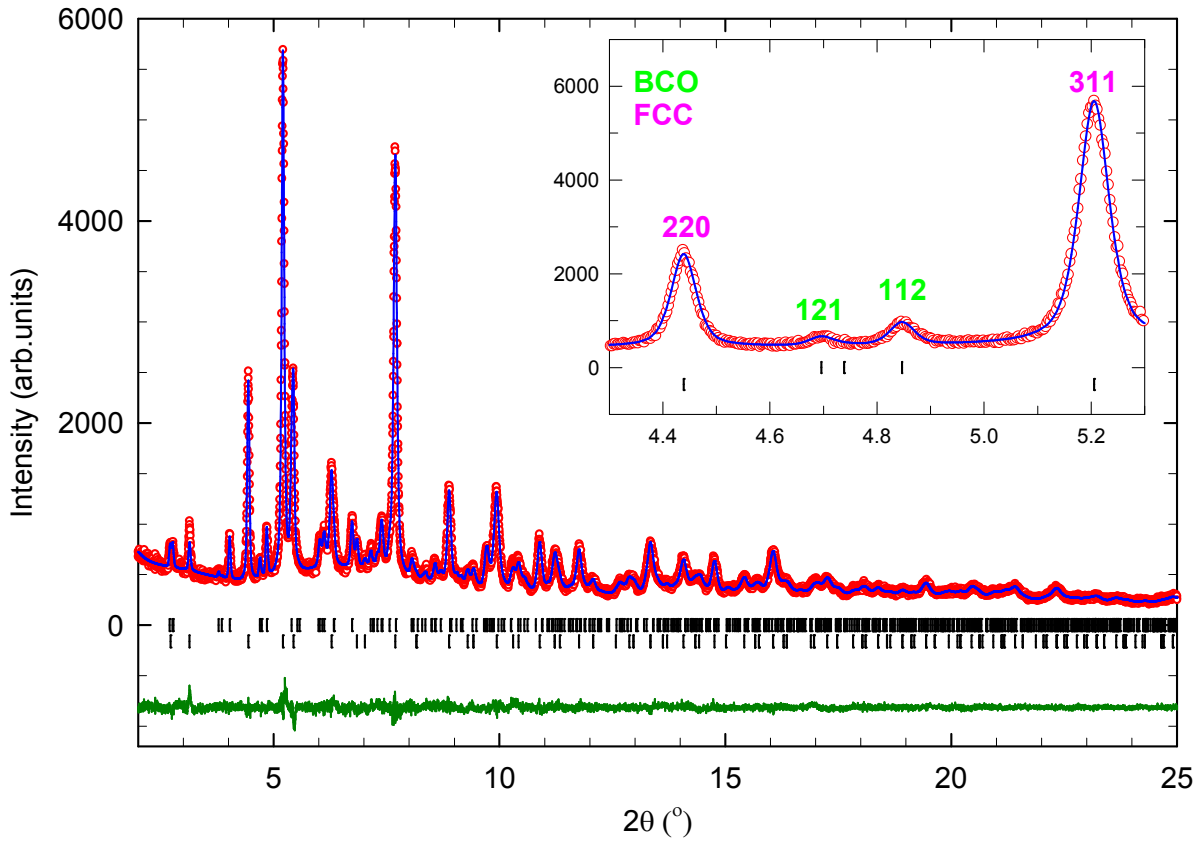

Fig 3.14: Observed (open red circles) and calculated (blue line) data of the 5 K synchrotron powder X-ray diffraction pattern for the sample with nominal composition $Rb_{0.50}Cs_{2.50}C_{60}$. The upper bars represent the positions of the Bragg reflections of the BCO phase and the lower ones of the FCC phase. The wavelength was λ = 0.39988(4) Å.

Table 3.18: Results of the 5 K two-phase Rietveld refinement of the Rb containing FCC phase in the sample with overall nominal composition $Rb_{0.50}Cs_{2.50}C_{60}$ (MTM158_4).

	x/a	*y/b*	*z/c*	*N*	B_{Iso}(Å^2)
Cs(1)	0.25	0.25	0.25	0.664(3)	0.73(5)
Rb(1)	0.25	0.25	0.25	0.309	0.73(5)
Cs(2)	0.5	0.5	0.5	0.987(4)	4.31(9)
C(1)	0	0.0490	0.2465	0.5	0.5(1)
C(2)	0.2119	0.0766	0.0994	0.5	0.5(1)
C(3)	0.1719	0.1498	0.0491	0.5	0.5(1)

Table 3.19: Results of the 5 K two-phase Rietveld refinement of the Cs_4C_{60} BCO phase in the sample with overall nominal composition $Rb_{0.50}Cs_{2.50}C_{60}$ (MTM158_4).

	x/a	*y/b*	*z/c*	*N*	B_{Iso}(Å^2)
Cs(1)	0.2050	0.5	0	1	0.6(2)
Cs(2)	0	0.2550	0.5	1	0.6(2)
C(1)	0	0.2881	0.0628	1	-2.1(3)
C(2)	0.0593	0	0.3025	1	-2.1(3)
C(3)	0.2925	0.0587	0	1	-2.1(3)
C(4)	0.0977	0.2514	0.1256	1	-2.1(3)
C(5)	0.1203	0.0954	0.2664	1	-2.1(3)
C(6)	0.2550	0.1176	0.1030	1	-2.1(3)
C(7)	0.1923	0.2149	0.0639	1	-2.1(3)
C(8)	0.0607	0.1931	0.2279	1	-2.1(3)
C(9)	0.2196	0.0588	0.2035	1	-2.1(3)

The refined occupancies of Cs and Rb in the tetrahedral site of the FCC majority phase (phase fraction ~80%) are Cs = 0.664(3) and Rb = 0.309 (total N = 0.973(3)), while the refined Cs occupancy in the octahedral site is 0.987(4) (Table 3.18). The resulting stoichiometry is $Rb_{0.62}Cs_{2.32(1)}C_{60}$. The refined phase fractions and derived stoichiometry of the FCC phase are in excellent agreement with those obtained at room temperature.

Sample MTM159_3 at 12 K:

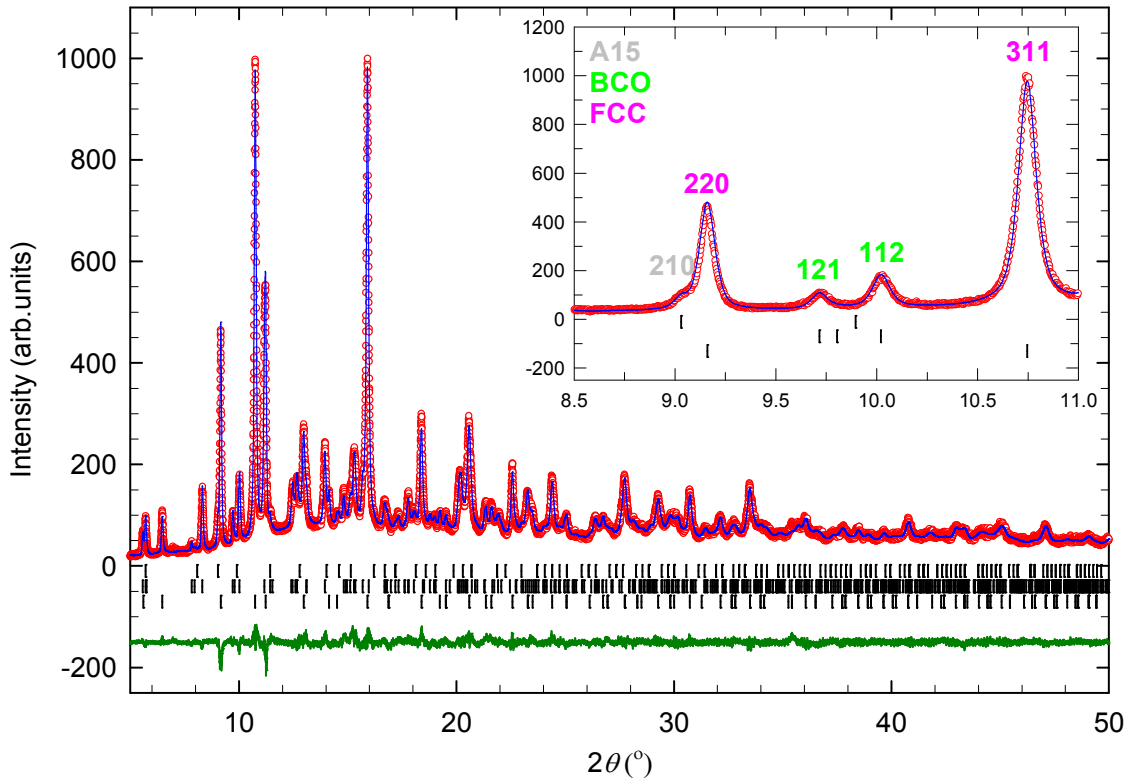

Fig 3.15: Observed (open red circles) and calculated (blue line) data of the 12 K synchrotron powder X-ray diffraction pattern for the sample with nominal composition $Rb_{0.25}Cs_{2.75}C_{60}$. The upper bars represent the positions of the Bragg reflections of the A15 phase, the middle ones of the BCO phase and the lower ones of the FCC phase. The wavelength is λ = 0.826028(1) Å.

Table 3.20: Results of the 12 K three-phase Rietveld refinement of the Rb containing FCC phase in the sample with overall nominal composition $Rb_{0.25}Cs_{2.75}C_{60}$ (MTM159_3).

	x/a	*y/b*	*z/c*	*N*	B_{Iso}(Å^2)
Cs(1)	0.25	0.25	0.25	0.771(2)	0.17(4)
Rb(1)	0.25	0.25	0.25	0.186	0.17(4)
Cs(2)	0.5	0.5	0.5	0.993(4)	3.00(6)
C(1)	0	0.0490	0.2462	0.5	0.17(8)
C(2)	0.2116	0.0765	0.0993	0.5	0.17(8)
C(3)	0.1717	0.1497	0.0490	0.5	0.17(8)

Table 3.21: Results of the 12 K three-phase Rietveld refinement of the Cs_4C_{60} BCO phase in the sample with overall nominal composition $Rb_{0.25}Cs_{2.75}C_{60}$ (MTM159_3).

	x/a	*y/b*	*z/c*	*N*	B_{Iso}(Å^2)
Cs(1)	0.2053	0.5	0	1	-0.10(5)
Cs(2)	0	0.2553	0.5	1	-0.10(5)
C(1)	0	0.2886	0.0628	1	-1.9(1)
C(2)	0.0594	0	0.3026	1	-1.9(1)
C(3)	0.2929	0.0588	0	1	-1.9(1)
C(4)	0.0978	0.2518	0.1256	1	-1.9(1)
C(5)	0.1205	0.0956	0.2665	1	-1.9(1)
C(6)	0.2554	0.1178	0.1031	1	-1.9(1)
C(7)	0.1926	0.2152	0.0639	1	-1.9(1)
C(8)	0.0608	0.1934	0.2280	1	-1.9(1)
C(9)	0.2199	0.0589	0.2036	1	-1.9(1)

Table 3.22: Results of the 12 K three-phase Rietveld refinement of the Cs_3C_{60} A15 phase in the sample with overall nominal composition $Rb_{0.25}Cs_{2.75}C_{60}$ (MTM159_3).

	x/a	*y/b*	*z/c*	*N*	B_{Iso}(Å^2)
Cs(1)	0.25	0.5	0	1	5.0(8)
C(1)	0	0.2980	0.0612	1	-6.6(4)
C(2)	0.1215	0.1001	0.2559	1	-6.6(4)
C(3)	0.0623	0.2011	0.2218	1	-6.6(4)

The refined occupancies of Cs and Rb in the tetrahedral site of the FCC phase (phase fraction ~67%) are Cs = 0.771(2) and Rb = 0.186 (total N = 0.957(2)), while the refined Cs occupancy in the octahedral site is 0.993(4) (Table 3.20). The resulting stoichiometry is $Rb_{0.37}Cs_{2.54(1)}C_{60}$. The refined phase fractions and derived stoichiometry of the FCC phase are in excellent agreement with those obtained at room temperature.

Sample MTM160_3 at 12 K:

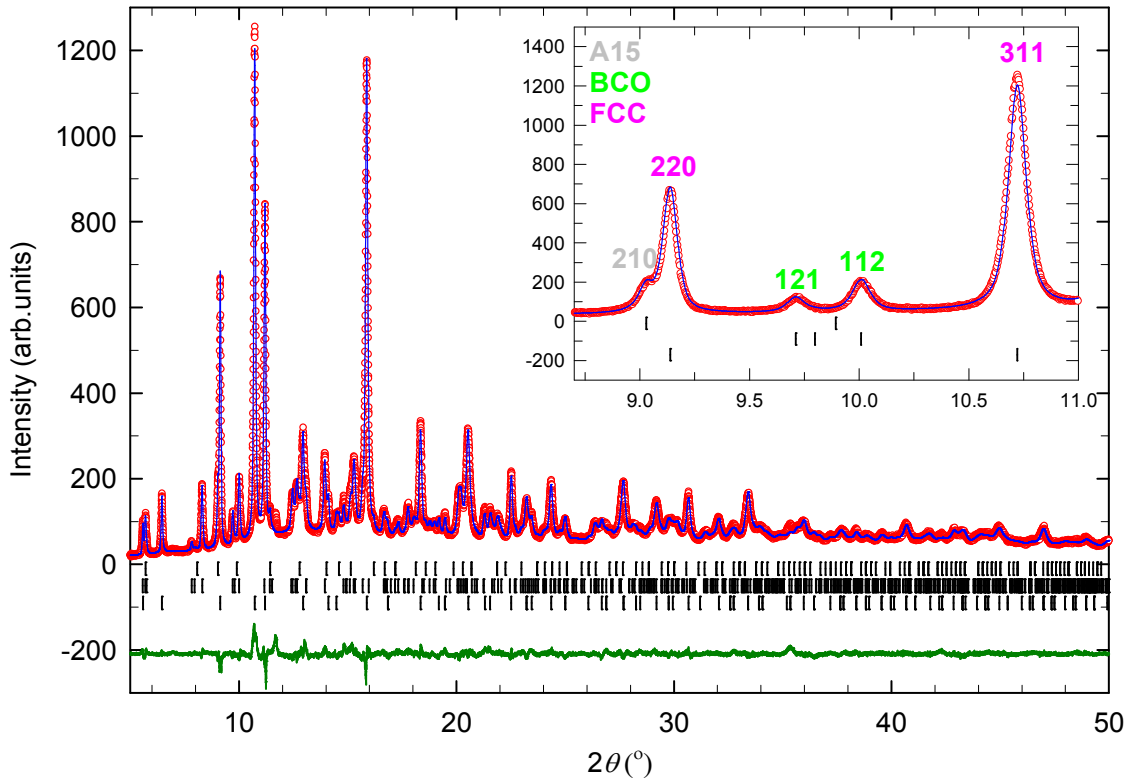

Fig 3.16: Observed (open red circles) and calculated (blue line) data of the 12 K synchrotron powder X-ray diffraction pattern for the sample with nominal composition $Rb_{0.12}Cs_{2.88}C_{60}$. The upper bars represent the positions of the Bragg reflections of the A15 phase, the middle ones of the BCO phase and the lower ones of the FCC phase. The wavelength is λ = 0.826028(1) Å.

Table 3.23: Results of the 12 K three-phase Rietveld refinement of the Rb containing FCC phase in the sample with overall nominal composition $Rb_{0.12}Cs_{2.88}C_{60}$ (MTM160_3).

	x/a	*y/b*	*z/c*	*N*	B_{Iso}(Å^2)
Cs(1)	0.25	0.25	0.25	0.873(2)	0.35(3)
Rb(1)	0.25	0.25	0.25	0.091	0.35(3)
Cs(2)	0.5	0.5	0.5	1.009(4)	4.32(6)
C(1)	0	0.0489	0.2457	0.5	0.11(7)
C(2)	0.2112	0.0763	0.0991	0.5	0.11(7)
C(3)	0.1714	0.1494	0.0489	0.5	0.11(7)

Table 3.24: Results of the 12 K three-phase Rietveld refinement of the Cs_4C_{60} BCO phase in the sample with overall nominal composition $Rb_{0.12}Cs_{2.88}C_{60}$ (MTM160_3).

	x/a	*y/b*	*z/c*	*N*	B_{Iso}(Å^2)
Cs(1)	0.2053	0.5	0	1	0.36(5)
Cs(2)	0	0.2553	0.5	1	0.36(5)
C(1)	0	0.2886	0.0627	1	-1.4(1)
C(2)	0.0594	0	0.3021	1	-1.4(1)
C(3)	0.2930	0.0588	0	1	-1.4(1)
C(4)	0.0978	0.2518	0.1254	1	-1.4(1)
C(5)	0.1205	0.0956	0.2661	1	-1.4(1)
C(6)	0.2554	0.1178	0.1029	1	-1.4(1)
C(7)	0.1927	0.2152	0.0638	1	-1.4(1)
C(8)	0.0608	0.1934	0.2276	1	-1.4(1)
C(9)	0.2200	0.0589	0.2033	1	-1.4(1)

Table 3.25: Results of the 12 K three-phase Rietveld refinement of the Cs_3C_{60} A15 phase in the sample with overall nominal composition $Rb_{0.12}Cs_{2.88}C_{60}$ (MTM160_3).

	x/a	*y/b*	*z/c*	*N*	B_{Iso}(Å^2)
Cs(1)	0.25	0.5	0	1	2.9(2)
C(1)	0	0.2981	0.0612	1	-4.8(2)
C(2)	0.1215	0.1001	0.2560	1	-4.8(2)
C(3)	0.0623	0.2012	0.2219	1	-4.8(2)

The refined occupancies of Cs and Rb in the tetrahedral site of the FCC phase (phase fraction ~65%) are Cs = 0.873(2) and Rb = 0.091 (total N = 0.964(2)), while the refined Cs occupancy in the octahedral site is 1.009(4) (Table 3.23). The resulting stoichiometry is $Rb_{0.18}Cs_{2.76(1)}C_{60}$. The refined phase fractions and derived stoichiometry of the FCC phase are in excellent agreement with those obtained at room temperature.

Sample MTM161_3 at 12 K:

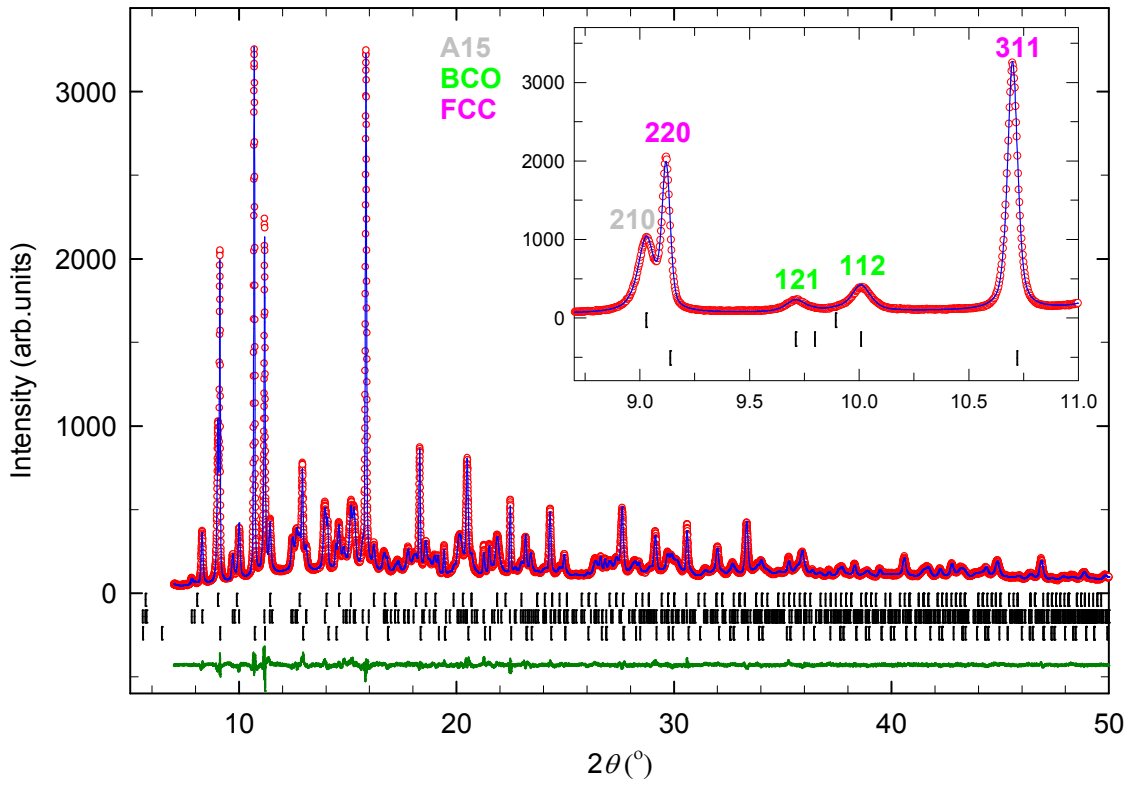

Fig 3.17: Observed (open red circles) and calculated (blue line) data of the 12 K synchrotron powder X-ray diffraction pattern for the sample with nominal composition Cs_3C_{60}. The upper bars represent the positions of the Bragg reflections of the A15 phase, the middle ones of the BCO phase and the lower ones of the FCC phase. The wavelength is λ = 0.826028(1) Å.

Table 3.26: Results of the 12 K three-phase Rietveld refinement of the Rb containing FCC phase in the sample with overall nominal composition Cs_3C_{60} (MTM161_3).

	x/a	*y/b*	*z/c*	*N*	B_{Iso}(Å^2)
Cs(1)	0.25	0.25	0.25	0.969(2)	0.47(2)
Cs(2)	0.5	0.5	0.5	0.998(3)	4.22(5)
C(1)	0	0.0488	0.2452	0.5	0.21(6)
C(2)	0.2108	0.0762	0.0989	0.5	0.21(6)
C(3)	0.1710	0.1491	0.0488	0.5	0.21(6)

Table 3.27: Results of the 12 K three-phase Rietveld refinement of the Cs_4C_{60} BCO phase in the sample with overall nominal composition Cs_3C_{60} (MTM161_3).

	x/a	*y/b*	*z/c*	*N*	B_{Iso}(Å^2)
Cs(1)	0.2052	0.5	0	1	0.31(4)
Cs(2)	0	0.2554	0.5	1	0.31(4)
C(1)	0	0.2886	0.0627	1	-1.4(1)
C(2)	0.0593	0	0.3022	1	-1.4(1)
C(3)	0.2928	0.0588	0	1	-1.4(1)
C(4)	0.0978	0.2518	0.1255	1	-1.4(1)
C(5)	0.1205	0.0956	0.2661	1	-1.4(1)
C(6)	0.2553	0.1178	0.1029	1	-1.4(1)
C(7)	0.1925	0.2152	0.0638	1	-1.4(1)
C(8)	0.0607	0.1934	0.2277	1	-1.4(1)
C(9)	0.2198	0.0589	0.2033	1	-1.4(1)

Table 3.28: Results of the 12 K three-phase Rietveld refinement of the Cs_3C_{60} A15 phase in the sample with overall nominal composition Cs_3C_{60} (MTM161_3).

	x/a	*y/b*	*z/c*	*N*	B_{Iso}(Å^2)
Cs(1)	0.25	0.5	0	1	0.97(4)
C(1)	0	0.2981	0.0612	1	-1.0(1)
C(2)	0.1216	0.1001	0.2560	1	-1.0(1)
C(3)	0.0623	0.2012	0.2219	1	-1.0(1)

The refined occupancies of Cs in the tetrahedral and octahedral sites of the FCC phase (phase fraction ~47%) are 0.969(2) and 0.998(3) (Table 3.26). The resulting stoichiometry is $Cs_{2.94(1)}C_{60}$.

3.4.5 Summary – structural properties of the FCC $Rb_xCs_{3-x}C_{60}$ series at low temperature

The results of the low temperature refinements are in excellent agreement to those of obtained at room temperature. The phase percentage of each structural polymorph refines values comparable to those obtained at room temperature (Fig 3.18), and at the same time, the FCC phase shows the same variation of cell volume with nominal x at both high and low temperatures (Fig 3.19).

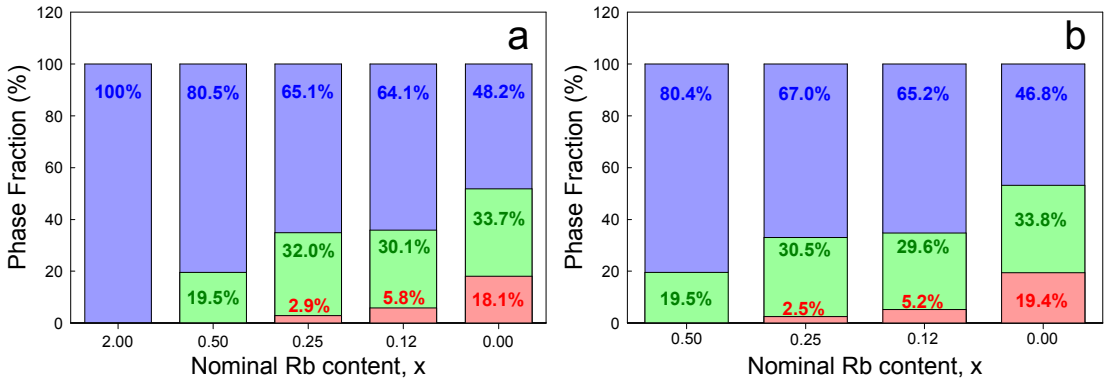

Fig 3.18: Variation of the fractions of the three polymorphs for the series of samples, $Rb_xCs_{3-x}C_{60}$ (**a**) at room temperature and (**b**) at 5 or 12 K. Red filling represents the A15, green the BCO and blue the FCC phase.

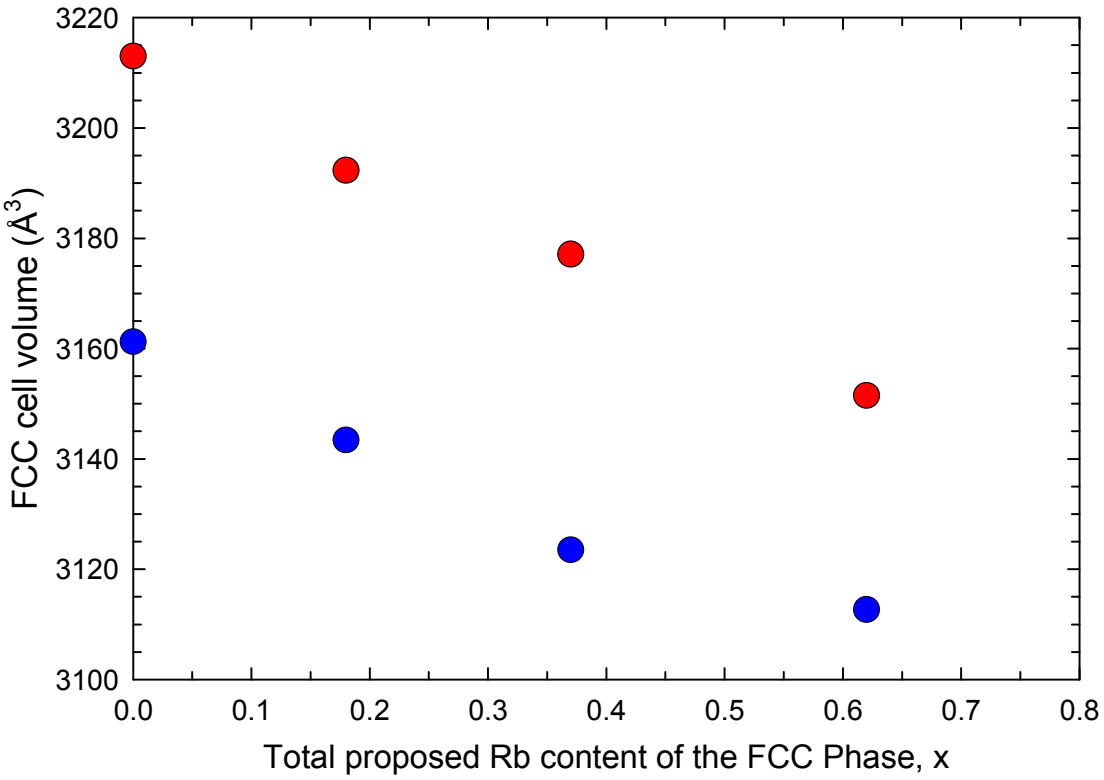

Fig 3.19: Unit cell volume changes of the FCC phase for the series $Rb_xCs_{3-x}C_{60}$ as a function of the Rb^+ content of the T_d site at room temperature (red circles) and at 5 or 12 K (blue circles).

The variation of the unit cell volume trend shows unequivocally from both high and low temperature data that for the FCC-rich $Rb_xCs_{3-x}C_{60}$ series of samples, Rb is doped exclusively into the T_d site of the FCC structure. The refined occupancy of the Rb content of the T_d site suggests that modelling the A15 (Cs_3C_{60}) and BCO (Cs_4C_{60}) phases as exclusively Cs^+ intercalated phases was a valid assumption.

3.5 Magnetic properties

The electronic properties of the FCC-rich $Rb_xCs_{3-x}C_{60}$ materials were followed at both ambient and elevated pressures by zero-field-cooled (ZFC) and field-cooled (FC) magnetisation measurements at a field of 20 Oe. Data were collected first at ambient pressure in order to characterise the evolution of the electronic properties with the

change in the Rb content (chemical pressure effects). These measurements were then extended to high pressures in order to follow the response of each sample upon the application of external pressure. In this way, the electronic behaviour as a function of unit cell volume could be followed over a broad range of unit cell volumes. Earlier high pressure structural work (using beamline BL10XU at SPring-8, Japan) on A15-rich Cs_3C_{60} has established the compressibility (κ) of the three polymorphs at ambient temperature.[15] For the FCC Cs_3C_{60} phase, $\kappa = dV/dP = 19(1)$ Å^3 kbar^{-1}. In the absence of comparable data being available for the Rb co-intercalated samples, this value of the compressibility (via equation (3.1) which is applicable for the low-pressure range of the present experiments) is employed to approximately estimate the unit cell volume, *V*, at each pressure for all the studied FCC-rich $Rb_xCs_{3-x}C_{60}$ samples.

$$V(\text{Å}^3) = V_0(\text{Å}^3) - P(\text{kbar}) \times \kappa(\text{Å}^3\text{kbar}^{-1}) \qquad (3.1)$$

where V_0 is the ambient pressure unit cell volume of the FCC phase. As a result, the observed pressure-dependent superconducting responses of the FCC phases are related directly to changes in the volume occupied per fulleride anion. The superconducting phase fractions at all pressures were calculated exclusively using *equation 2.33* that is derived in *section 2.5.6*.

3.5.1 Ambient Pressure, Low-Field ZFC-FC measurements

A small amount of material was loaded into a quartz tube inside the glove box. The sample and its containing vessel are then removed and sealed under 300 mbar of He gas using a vacuum manifold. The thin quartz tubes contain a very thin partition so that the sealed powders can be correctly centred inside the SQUID magnetometer. The powder was also transferred using a small glass disposable funnel; this ensures that no material is near the sealing point of the vessel. The quartz tubes were specifically designed for SQUID magnetometry measurements of air sensitive materials due to their ergonomic design and negligible background contribution. The samples were

introduced into the MPMS5 at 100 K under zero applied field. The sample space is then cooled at a slow rate to the base temperature of 1.8 K (zero-field-cooled, ZFC). Cooling too quickly may lead to unstable temperature readings as the sample and containing tube are not allowed to equilibrate. When stable at 1.8 K, a field of 20 Oe was applied and the magnetic response was measured as a function of temperature from 1.8 to 50 K at a rate of 0.25 K/min in a step size of 0.5 K. Using the same cooling protocol as previously, the sample was cooled back to base temperature (with the field still applied). Field-cooled (FC) measurements were recorded on warming back to 50 K.

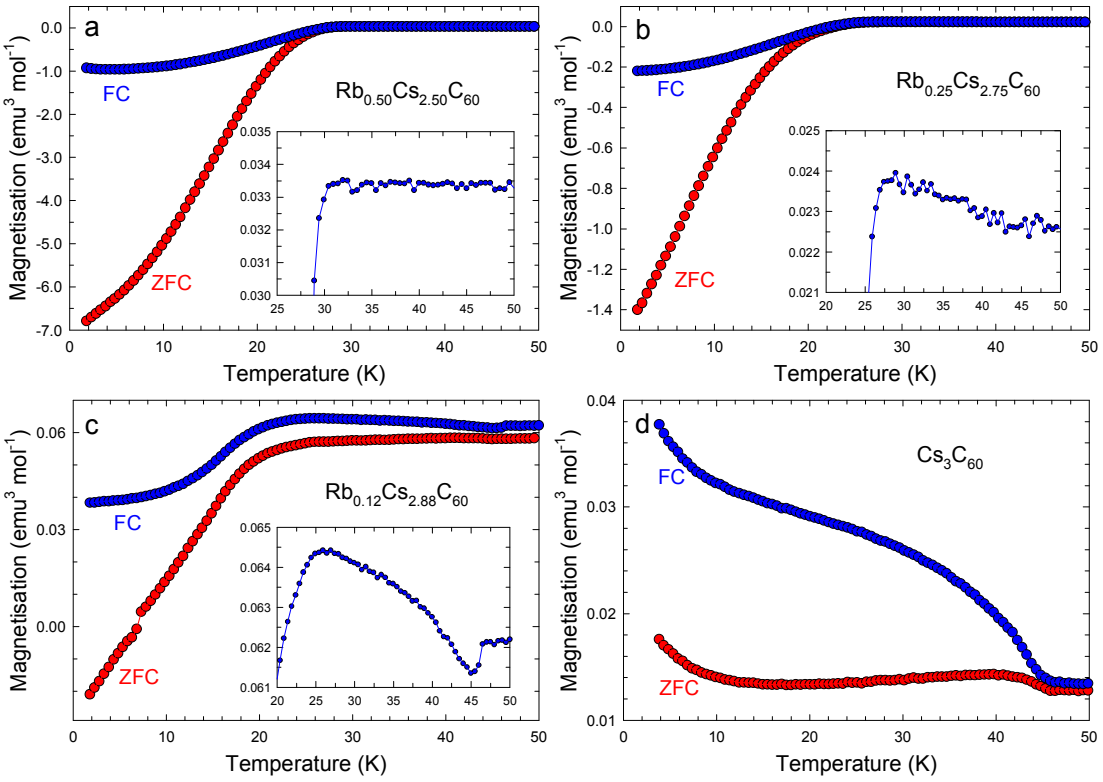

Fig 3.20: Temperature dependence of the ambient pressure ZFC/FC DC magnetisation (20 Oe) for the series of compounds, $Rb_xCs_{3-x}C_{60}$. Red circles are ZFC data and blue circles are FC data. **a:** x = 0.50, $Rb_{0.50}Cs_{2.50}C_{60}$, 21 mg. **b:** x = 0.25, $Rb_{0.25}Cs_{2.75}C_{60}$, 15 mg. **c:** x = 0.12, $Rb_{0.12}Cs_{2.88}C_{60}$, 20 mg. **d:** x = 0.00, Cs_3C_{60}, 21 mg. Insets in **a**, **b** and **c** show expanded versions of each FC M(T) plot near the potential onset of spontaneous magnetisation.

Fig 3.20 collects together all ZFC/FC data for the four samples studied. The evolution of the magnetic properties with decreasing Rb content is immediately

evident. Bulk superconductivity is observed for the sample with nominal Rb content of x = 0.5 with an onset superconducting transition temperature, T_c (seen in both FC and ZFC data, confirming the Meissner effect) of 28.9 K and a superconducting fraction of 20.0%. As the Rb content decreases, T_c decreases to 26.2 K (x = 0.25) and 25.6 K (x = 0.12). At the same time, the superconducting fraction also sharply decreases to 3.0% and 0.2%, respectively. Finally, the Cs_3C_{60} sample is not superconducting at ambient pressure.

The FC data are also instructive in terms of the magnetic response of the various compositions. Fig. 3.20(d) shows the appearance of a small spontaneous magnetisation appearing at around 46 K for the Cs_3C_{60} sample. Its magnitude is in excellent agreement with what is expected for the 18% A15 fraction present in this material - as shown in ref. 17 and discussed further in chapter 4, the A15 phase is a canted antiferromagnet with an ambient pressure T_N of 46 K. In agreement with such an assignment, it is noted that the magnitude of the spontaneous magnetisation decreases as the amount of the A15 phase decreases and compositions with increased Rb content are produced (Fig. 3.20(b) and (c)). Furthermore, it is absent in the sample with x = 0.5 in which no A15 phase is found by the synchrotron XRD measurements. The present data therefore argue strongly that the diamagnetic response (due to superconductivity) is associated with the FCC polymorphs, while the magnetic response with the residual A15 phases.

3.6 High Pressure, Low Field ZFC-FC measurements

For high pressure SQUID measurements, the chosen sample was loaded into the high pressure Mcell whose characteristics are detailed in *section 2.5.8*. Prior to each experiment, a background measurement was run with the empty Mcell under exactly the same measurement protocol. Following background subtraction, the magnetic response of the sample can be obtained. Inside the glovebox, approximately 20 mg of the chosen sample were loaded into the cell, which was tightened by hand as

the sample is air sensitive. During the Mcell's transfer from glovebox to SQUID, all required measurements, such as the height of the upper-locking-net (needs to be checked initially to ensure the cell is tightly packed), were done very efficiently and quickly to ensure survival of the sample as it was generally unknown how air tight the seals of the containing vessel were in each case.

The Mcell is loaded into the SQUID at room temperature and cooled at a slow rate of 3 K per minute to a temperature of 10 K under an applied field of 20 Oe (field-cooled, FC) – this ensures no adverse temperature gradients that may lead to deformations of the cell. The sample was centred in the SQUID so that the cell is in exactly the same position with respect to the background measurement. This is done by measuring the SQUID response and adjusting the height of the transport rod. The sample was centred at this specific temperature for two reasons: The Sn manometer (used to measure cell pressure) is still paramagnetic at this temperature, and the sample should be superconducting so the signal should be strong. If the sample could not be centred at this temperature, T is lowered further to 4.2 K. After the sample is centred, the SQUID is cooled to the base temperature of 1.8 K with the field still on (field-cooled, FC). The magnetic response was again measured as a function of temperature from 1.8 to 50 K at a rate of 0.25 K/min in a step size of 0.5 K. Using the same cooling protocol as before, the sample was cooled back to base temperature under zero applied field (zero-field-cooled, ZFC). The field was then turned back on to 20 Oe and a ZFC measurement was recorded on warming back to 50 K. Finally, an additional set of measurements were performed between 3.8 and 3.2 K with a temperature step size of 0.05 K at an applied field of 10 Oe so that the T_c of the Sn manometer can be accurately measured, thus enabling precise calibration of the cell pressure.

After each measurement, the magnetometer is warmed slowly to room temperature. The pressure cell is only removed from the SQUID after it has been left at room temperature for approximately 30 minutes. After that the pressure of the cell is adjusted mechanically by using the MPress. Sample measurements were typically performed for MPress pressures between hand-tight (0 PSI) to 1000 PSI in steps of 250 PSI. Measurements were also performed upon pressure release back to ambient.

3.6.1 $Rb_{0.50}Cs_{2.50}C_{60}$ (MTM158_4)

The detailed XRD analysis has unambiguously shown that the $Rb_{0.50}Cs_{2.50}C_{60}$ sample does not contain any of the A15 polymorph with the FCC polymorph being the majority (~80%) phase. Given that it has been established that the BCO minority phase is not superconducting,[17] the observation of bulk superconductivity at 28.9 K (superconducting fraction 20.0%) even at ambient pressure should be associated with the FCC phase. Upon application of external pressure, the superconducting fraction increases monotonically and reaches a value of 61.6% at 1.02 GPa – the highest pressure of the present experiments (Fig. 3.21(f)). At the same time, the superconducting transition temperature first increases reaching a maximum of 31.8 K at 0.46 GPa and then decreases upon further pressurisation – at 1.02 GPa, T_c is 27.8 K (Fig. 3.21(e)). This trend is reversible as when the pressure is released, there is no observable hysteresis in the T_c(P) curve. The observed superconductivity dome with increasing pressure differs from the behaviour observed for A_3C_{60} fullerides with smaller lattice constants but is reminiscent of the behaviour of A15 Cs_3C_{60}.

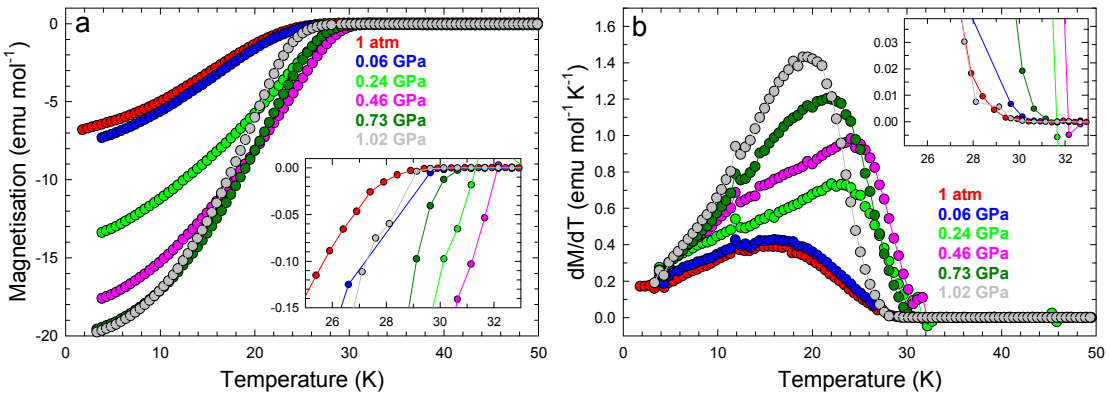

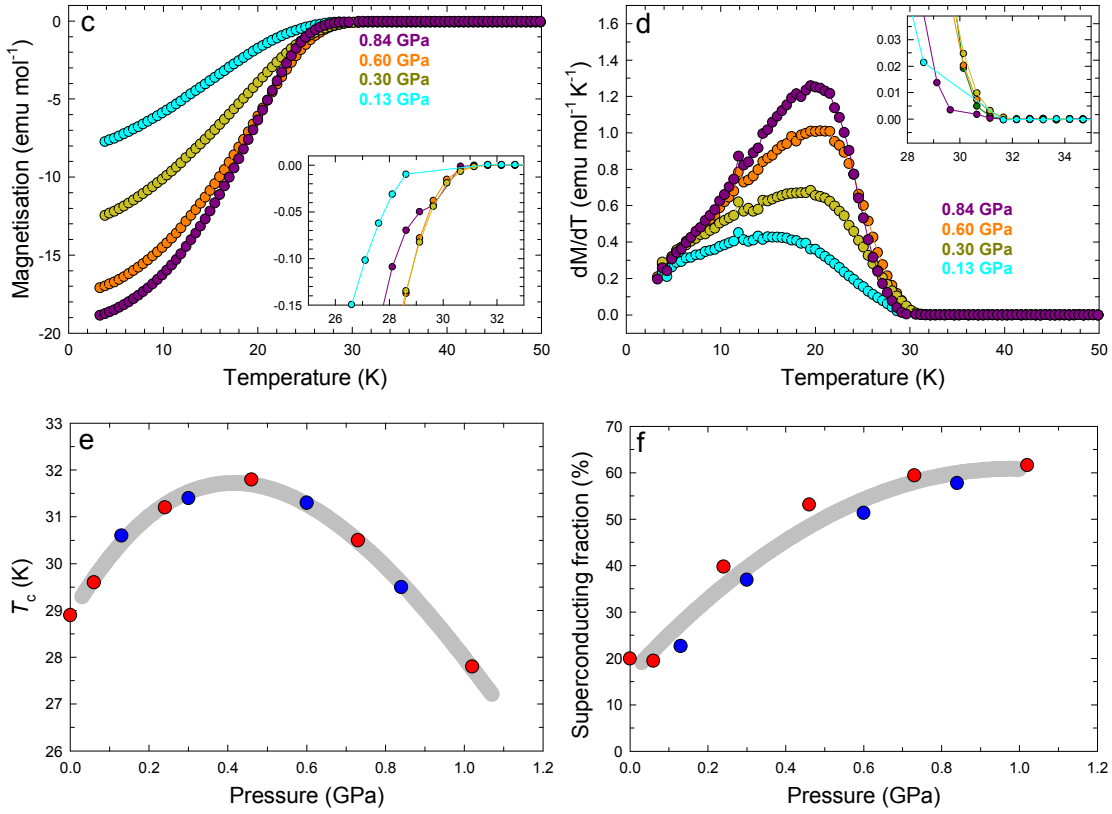

Fig 3.21: High pressure magnetic measurements (ZFC) for the $Rb_{0.50}Cs_{2.50}C_{60}$ sample at an applied field of 20 Oe (19 mg). **a,b:** Magnetisation, M and first derivative of the magnetisation, dM/dT as a function of temperature upon pressurisation. **c,d:** Magnetisation, M and first derivative of the magnetisation, dM/dT as a function of temperature upon pressure release. The insets of **a**, **b**, **c** and **d** show expanded versions of the plots near the onset of the superconducting transition. **e,f:** Transition temperature, T_c and superconducting fraction as a function of pressure; the grey lines are guides-to-the-eye. Red (blue) circles indicate increasing (decreasing) pressure values.

3.6.2 $Rb_{0.25}Cs_{2.75}C_{60}$ (MTM159_3)

A similar trend is revealed by the high P magnetic measurements for the $Rb_{0.25}Cs_{2.75}C_{60}$ sample. This composition is dominated by the FCC component (~65%) but contains a very small fraction (~3%) of the competing A15 polymorph whose magnetic signature was barely visible in the ambient P FC magnetisation measurements (Fig. 3.20(b)). This sample showed a small superconducting fraction of 3.0% in the ZFC measurements at ambient pressure. This increased rapidly to 51.0%

when the sample was pressed to 1.04 GPa (Fig. 3.22(f)). At the same time, the superconducting transition temperature first increases reaching a maximum of 33.9 K at 0.50 GPa and then decreases upon further pressurisation – at 1.04 GPa, T_c is 31.8 K (Fig. 3.22(e)) – in a similar way to that observed for the $Rb_{0.50}Cs_{2.50}C_{60}$ sample. Given the bulk nature of the superconducting state at high P, this electronic state is once again attributed to the FCC polymorph. Once again, the observed trends are fully reversible upon pressure release. Careful examination of the high P magnetisation data shows some evidence for trace superconductivity with a somewhat higher T_c that can be attributed to the minority A15 phase; however, the transition temperature is impossible to define as it is lost in the signal-to-noise ratio of the data.

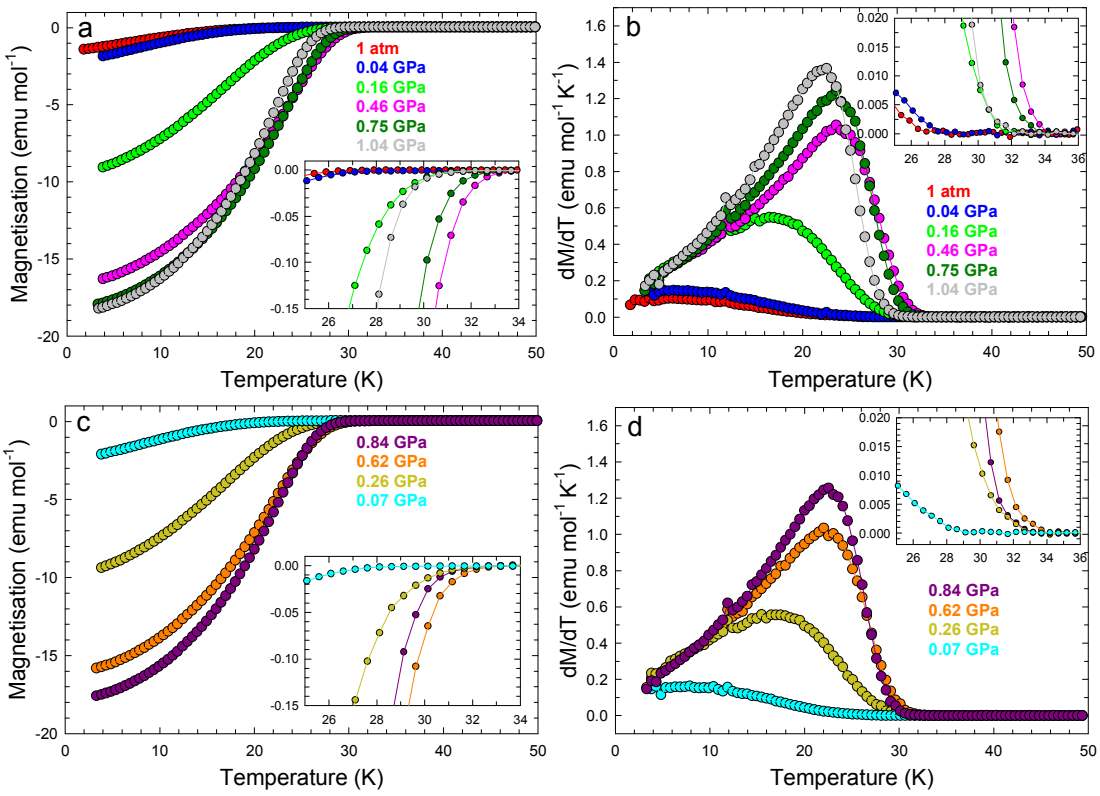

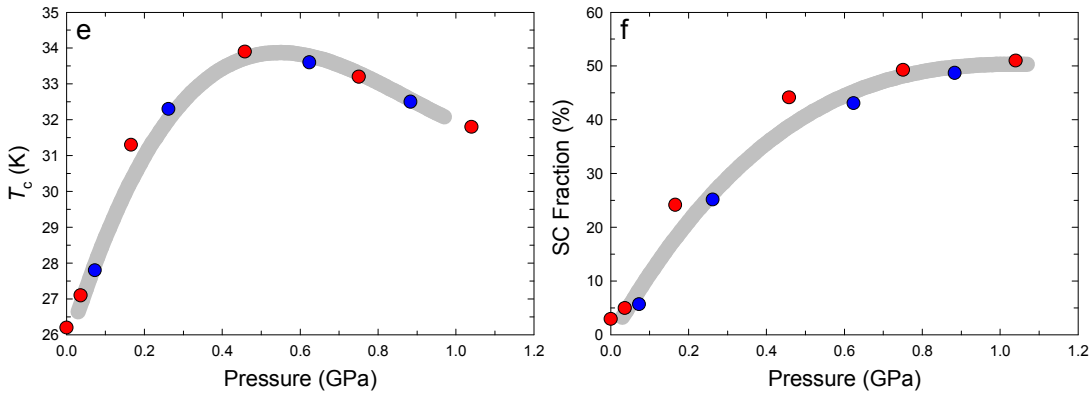

Fig 3.22: High pressure magnetic measurements (ZFC) for the $Rb_{0.25}Cs_{2.75}C_{60}$ sample at an applied field of 20 Oe (19 mg). **a,b:** Magnetisation, M and first derivative of the magnetisation, dM/dT as a function of temperature upon pressurisation. **c,d:** Magnetisation, M and first derivative of the magnetisation, dM/dT as a function of temperature upon pressure release. The insets of **a**, **b**, **c** and **d** show expanded versions of the plots near the onset of the superconducting transition. **e,f:** Transition temperature, T_c and superconducting fraction as a function of pressure; the grey lines are guides-to-the-eye. Red (blue) circles indicate increasing (decreasing) pressure values.

3.6.3 $Rb_{0.12}Cs_{2.88}C_{60}$ (MTM160_3)

The trend already established by the first two samples continues in the high P magnetic measurements for the $Rb_{0.12}Cs_{2.88}C_{60}$ sample. This composition is again dominated by the FCC component (~64%) but contains a slightly larger fraction (~6%) of the competing A15 polymorph whose magnetic signature was better defined in the ambient P FC magnetisation measurements (Fig. 3.20(c)). This sample with a further expanded interfullerene separation showed only trace superconductivity – a tiny superconducting fraction of <0.2% in the ZFC measurements at ambient pressure. This increased rapidly to 46.1% when the sample was gradually pressed to 1.04 GPa, signifying the crossover to bulk superconductivity at high pressure (Fig. 3.23(f)). At the same time, the superconducting transition temperature first increases reaching a maximum of 35.2 K at 0.46 GPa and then decreases upon further pressurisation – at 1.04 GPa, T_c is 33.2 K (Fig. 3.23(e)) – in a similar way to that observed for the $Rb_{0.50}Cs_{2.50}C_{60}$ and $Rb_{0.25}Cs_{2.75}C_{60}$ samples. Given the bulk nature of the superconducting state at high P, this electronic state is once again attributed to the

FCC polymorph. Once again, the observed trends are fully reversible upon pressure release.

As there is a somewhat larger proportion of the A15 polymorph present, its canted antiferromagnetic response is clearly evident in the low pressure FC magnetisation data (Fig 3.23(g)). As the pressure increases, the antiferromagnetic state of the A15 polymorph is suppressed as its own transition to superconductivity occurs (insets of Fig 3.23(b) and (d)). This effect is fully reversible. A weak superconducting response which shows a maximum T_c of 38.0 K at 0.67 GPa (Fig 3.23(e)) is therefore attributed to this minority A15 phase and is in excellent accord with the earlier reported data on A15 Cs_3C_{60}.

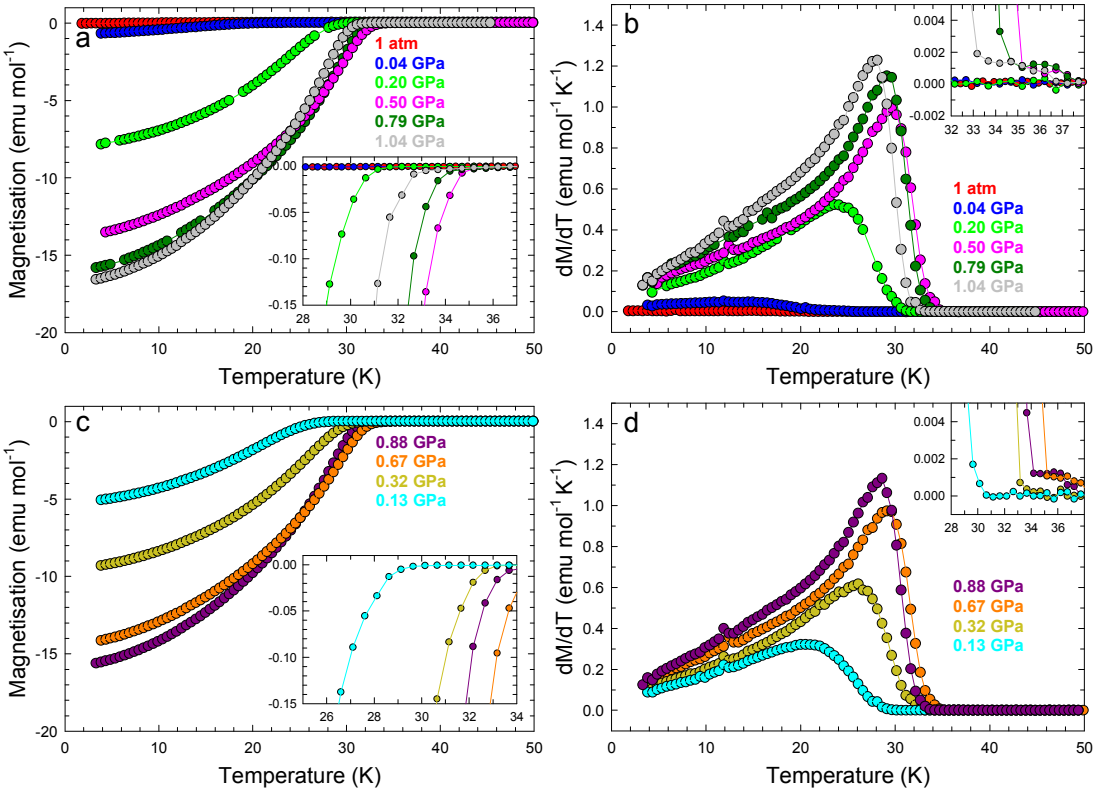

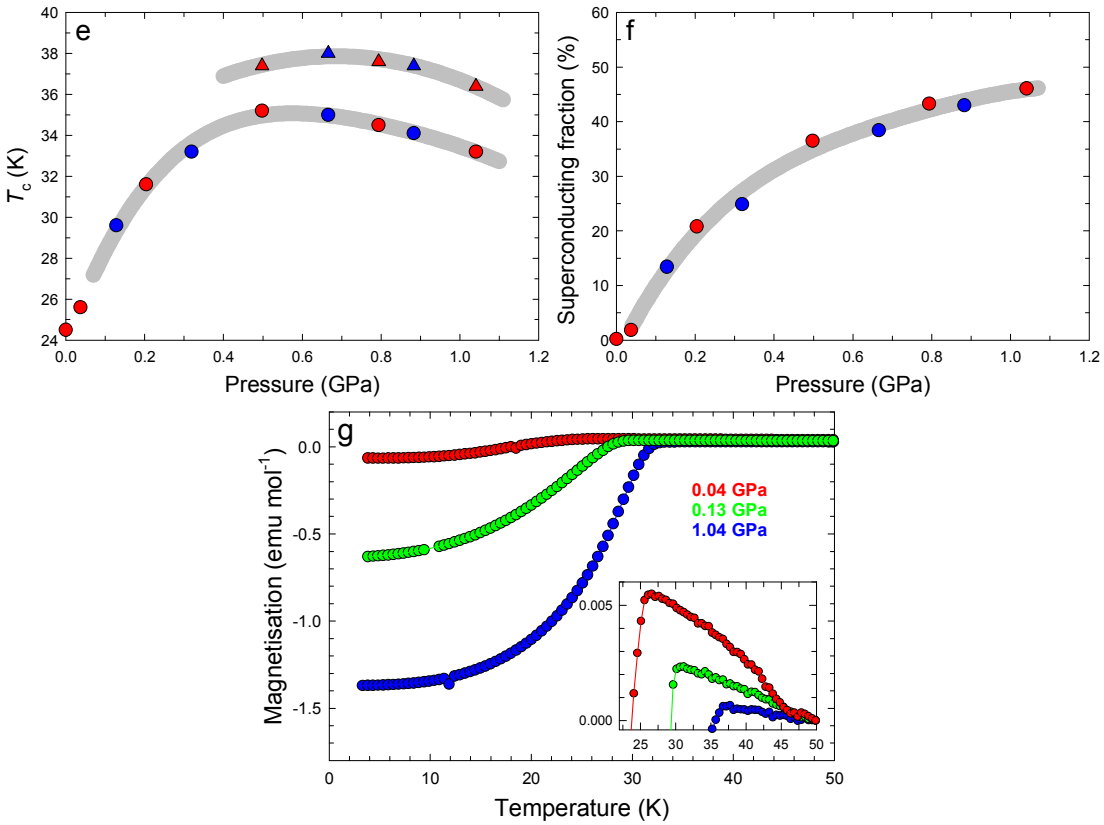

Fig 3.23: High pressure magnetic measurements (ZFC) for the $Rb_{0.12}Cs_{2.88}C_{60}$ sample at an applied field of 20 Oe (21 mg). **a,b:** Magnetisation, M and first derivative of the magnetisation, dM/dT as a function of temperature upon pressurisation. **c,d:** Magnetisation, M and first derivative of the magnetisation, dM/dT as a function of temperature upon pressure release. The insets of **a**, **b**, **c** and **d** show expanded versions of the plots near the onset of the superconducting transition. **e,f:** Transition temperature, T_c (circles/triangles represent data for the FCC/A15 phases) and superconducting fraction as a function of pressure; the grey lines are guides-to-the-eye. Red (blue) circles indicate increasing (decreasing) pressure values. **g:** FC magnetisation measurements (20 Oe) as a function of pressure. The inset shows an expanded region of the plot near the onset of the ferromagnetic transition.

3.6.4 Cs_3C_{60} (MTM161_3)

The final sample studied as a function of pressure in this series is that with composition Cs_3C_{60}. This sample has again as a dominant component the FCC polymorph (~47%) but contains a significant fraction (~19%) of the competing A15 polymorph. The magnetic signature of the latter (T_N = 46 K) is clearly evident in the ambient P FC magnetisation measurements (Fig. 3.20(d)). Nonetheless at the time of

this work, this sample is unique as it represents the first opportunity to directly compare its electronic properties to those of the very well studied analogue, A15-structured Cs_3C_{60}. This sample represents the most expanded fulleride lattice available while retaining the important FCC structure. The further increase in interfullerene separation resulted in the complete suppression of superconductivity – not even trace superconductivity is present in the ZFC measurements at ambient pressure. Therefore the electronic state of FCC Cs_3C_{60} is comparable to that of A15 Cs_3C_{60}. Nonetheless, an immediately obvious difference is the absence of any magnetic signature associated with the majority FCC phase. On the other hand, a similar response to that of the A15 phase is encountered upon pressurisation. A non-superconducting-to-superconducting phase transition occurs upon the application of a very moderate pressure of 0.22 GPa whereupon superconductivity emerges with a T_c of 30.2 K and a superconducting fraction of 12.0 % (Fig. 3.24(e) and (f)). A notable point here is that the critical temperature for the onset of superconductivity is smaller than that observed for A15 Cs_3C_{60} (Fig. 3.24(h)).[17] The superconducting fraction increases rapidly to 40.3% when the sample was gradually pressed to 0.97 GPa (Fig. 3.24(f)). At the same time, the superconducting transition temperature once more first increases reaching a maximum of 35.7 K at 0.73 GPa and then decreases upon further pressurisation – at 0.97 GPa, T_c is 35.1 K (Fig. 3.24(e)) – in a similar way to that observed for both the $Rb_xCs_{3-x}C_{60}$ samples and A15 Cs_3C_{60}. The maximum T_c achieved in the FCC fulleride family is smaller than that of the A15 phase at 38 K. Once again, the observed trends are fully reversible upon pressure release.

The significantly larger proportion of the A15 polymorph present allows a better definition of both its canted antiferromagnetic response and its transition to the superconducting state (Fig 3.24(g) and insets of Fig. 3.24(b) and (d)). A second superconducting transition which reaches a maximum T_c of 38.0 K at 0.73 GPa (Fig 3.24(e)) is therefore attributed to the co-existing minority A15 phase and is in excellent accord with the earlier reported data on A15 Cs_3C_{60}.[15,16,17]

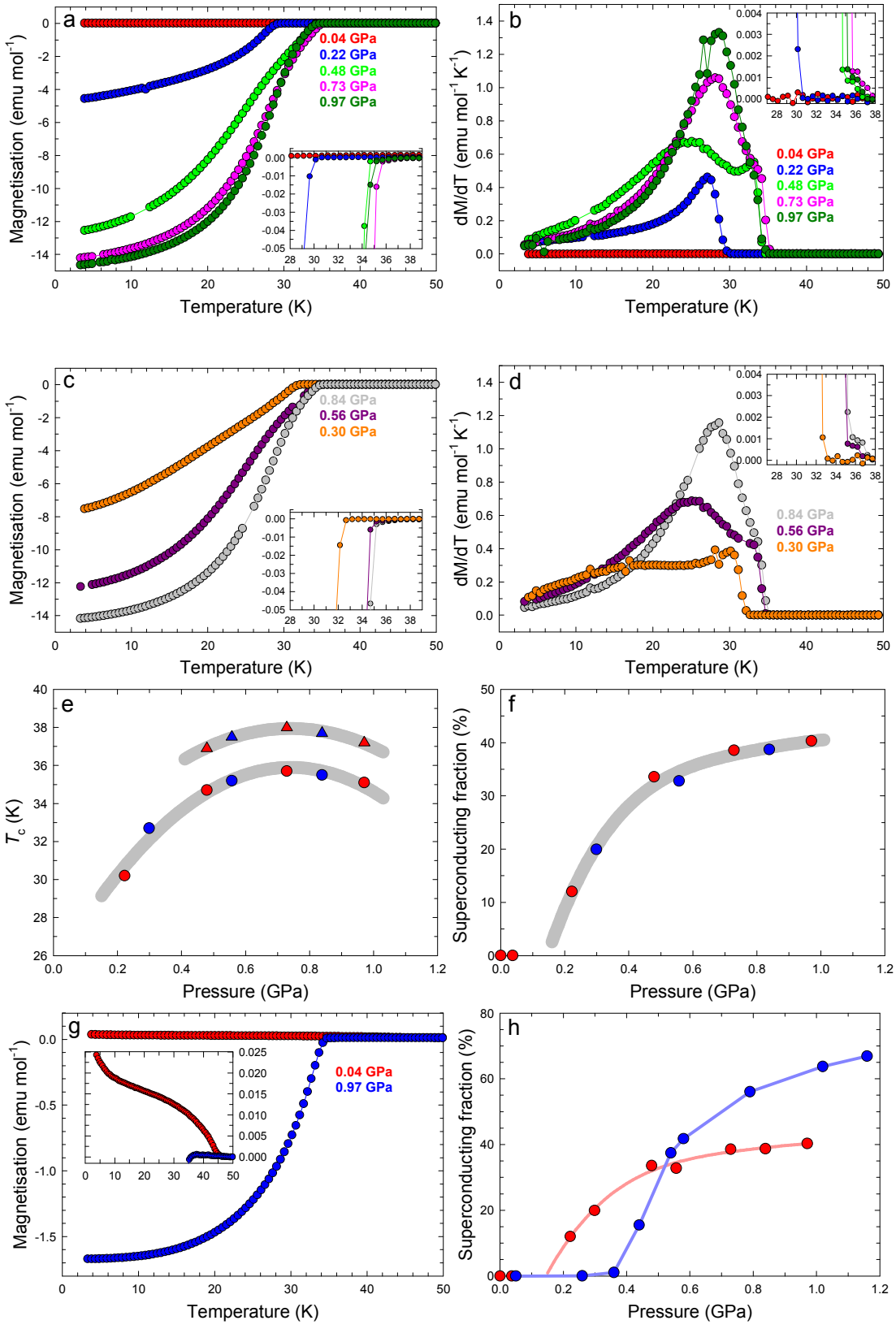

Fig 3.24: High pressure magnetic measurements (ZFC) for the Cs_3C_{60} sample at an applied field of 20 Oe (20 mg). **a,b:** Magnetisation, M and first derivative of the magnetisation, dM/dT as a function of temperature upon pressurisation. **c,d:** Magnetisation, M and first derivative of the magnetisation, dM/dT as a function of temperature upon pressure release. The insets of **a**, **b**, **c** and **d** show expanded

versions of the plots near the onset of the superconducting transition. **e,f:** Transition temperature, T_c (circles/triangles represent data for the FCC/A15 phases) and superconducting fraction as a function of pressure; the grey lines are guides-to-the-eye. Red (blue) circles indicate increasing (decreasing) pressure values. **g:** FC magnetisation measurements (20 Oe) as a function of pressure. The inset shows an expanded region of the plot near the onset of the ferromagnetic transition. **h:** Superconducting fraction as a function of pressure for Cs_3C_{60} materials, red circles indicate sample MTM161_3 FCC-rich, blue circles literature data from A15-rich Cs_3C_{60}.[17] The respective colour lines are guides-to-the-eye.

3.6.5 Summary – superconductivity in the FCC $Rb_xCs_{3-x}C_{60}$ series

One of the most important conclusions of the present work is illustrated in Fig. 3.25, which collects together the evolution of the superconducting fraction in the $Rb_xCs_{3-x}C_{60}$ series as a function of both Rb content *x* and applied pressure *P*. Cs_3C_{60} is not superconducting at ambient pressure but as the Rb doping level increases, a transition to a superconducting state occurs as the unit cell volume of the FCC phase is reduced – at the same time, the ambient *P* superconducting fraction is rapidly enhanced. This clearly demonstrates the effect of chemical pressure resulting from the co-intercalation of the smaller Rb cation. Additionally, as the applied pressure is increased the unit cell volume of the FCC phase is reduced and the superconducting fraction for all samples increases parabolically and eventually saturates. In the case of non-superconducting Cs_3C_{60}, very moderate pressure is enough to switch on superconductivity.

At low chemical and physical pressures the electron repulsion energy (*U*) associated with the half-filled t_{1u} orbitals of the superconducting phases dominate and therefore the materials are insulating. *U* can be considered a molecular quantity, therefore maintaining its value across structural families. The bandwidth (*W*) of both the A15 and FCC superconducting phases is regulated by effective overlap interaction between neighbouring C_{60}^{3-} anions. The bandwidth is larger for the A15-favoured phase as the C_{60}^{3-} anions meet hexagon-to-hexagon, whereas the FCC phase they are almost C-C to C-C only. Therefore application of either chemical of physical pressure increases the effective overlap between adjacent C_{60}^{3-} anions and consequently

increases *W*. Usually the metal-insulator (M-I) transition occurs when $U \approx W$ (e.g. cuprates), but the 3-fold degeneracy of the frontier t_{1u} orbital's raises the critical ratio to; FCC $U \approx 2.3W$ and A15 $U \approx 1.3W$ (as *U* is constant *W* is larger at the M-I transition of the A15 phase). It can be concluded that application of either chemical or physical pressure can drive the transition to the superconducting state by increasing the bandwidth *W* and therefore driving the system below the critical value of the (*U*/*W*) ratio for the Mott-Hubbard M-I transition.

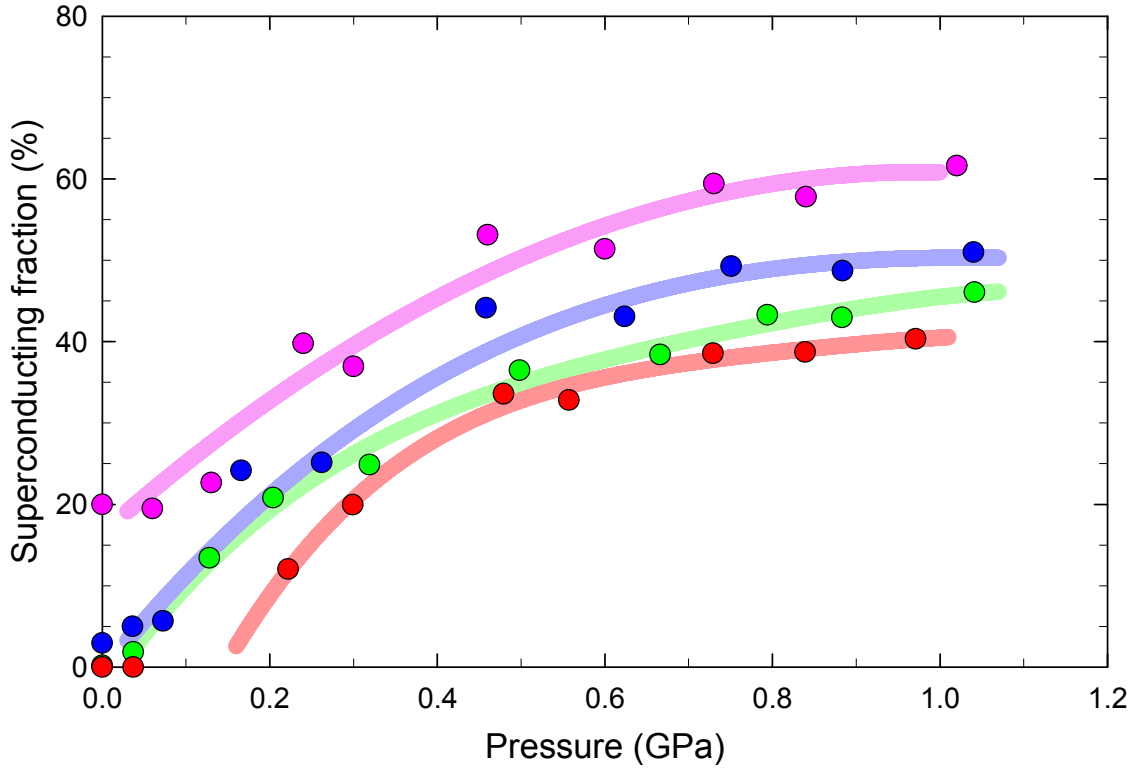

Fig 3.25: Superconducting fraction as a function of pressure for the FCC-structured $Rb_xCs_{3-x}C_{60}$ samples. Pink circles represent x = 0.62, blue x = 0.37, green x = 0.18, and red x = 0. The values of the Rb content are those obtained by the Rietveld refinements of the synchrotron X-ray powder diffraction data. The respective colour lines are guides-to-the-eye.

The second important conclusion which arises from these measurements is the pressure response of the electronic properties of the FCC phase as a function of applied pressure and Rb content, summarised in Fig. 3.26. Pressurisation leads to

superconductivity domes for each individual sample with the maximum T_c of each dome increasing with increasing Cs content (i.e. with increasing unit cell size). At the same time, the pressure at which the maximum T_c occurs shifts to higher values again with increasing Cs content.

In order to convert Fig. 3.26 to one where the same microscopic parameter is utilised as a probe of the electronic properties, equation 3.1 was employed to produce Fig. 3.27 where T_c is now shown as a function of unit cell volume per C_{60} unit. This directly probes the interfullerene separation which essentially is the key parameter which controls the bandwidth, W and therefore for fixed Hubbard U (a molecular C_{60} property), it controls the metal/insulator properties of the materials.

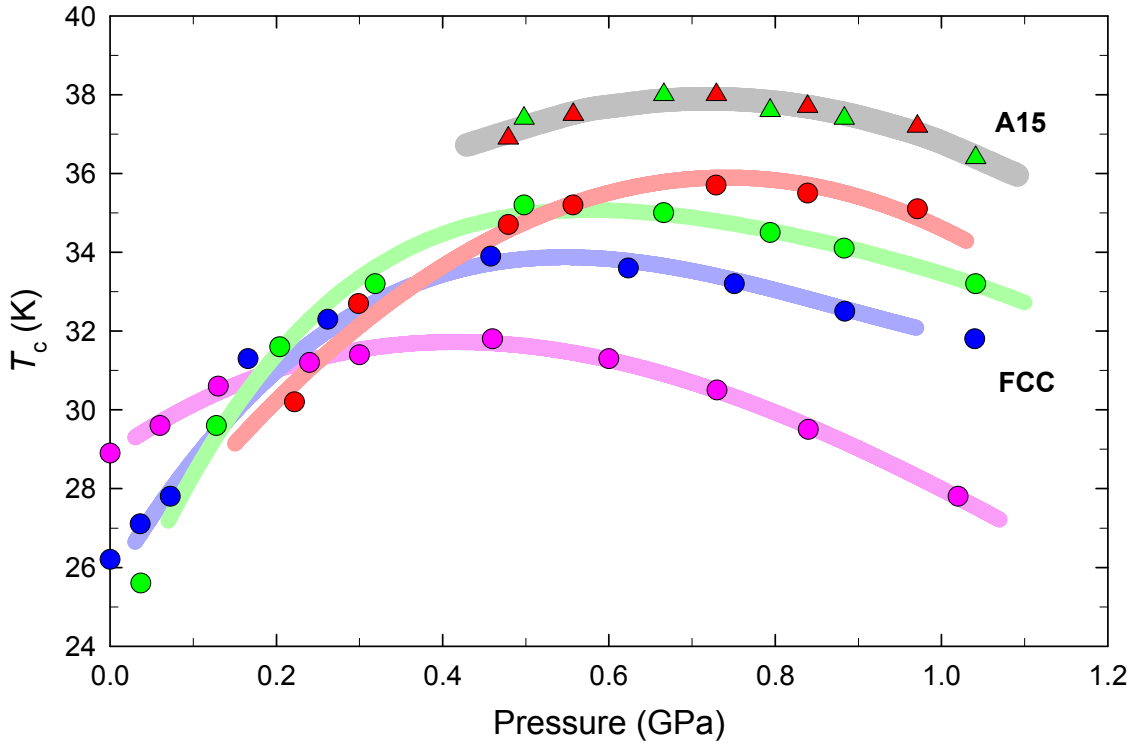

Fig 3.26: Superconducting transition temperature (T_c) as a function of pressure for the FCC-structured $Rb_xCs_{3-x}C_{60}$ samples and for A15-structured Cs_3C_{60}. Pink colour represents x = 0.62, blue x = 0.37, green x = 0.18, and red x = 0. Circles represent data for the FCC phases, triangles the A15 Cs_3C_{60} phase. The values of the Rb content are those obtained by the Rietveld refinements of the synchrotron X-ray powder diffraction data. The respective colour lines are guides-to-the-eye. A single grey line is used as a guide-for-the-eye for all A15 samples as they have a fixed Cs_3C_{60} stoichiometry.

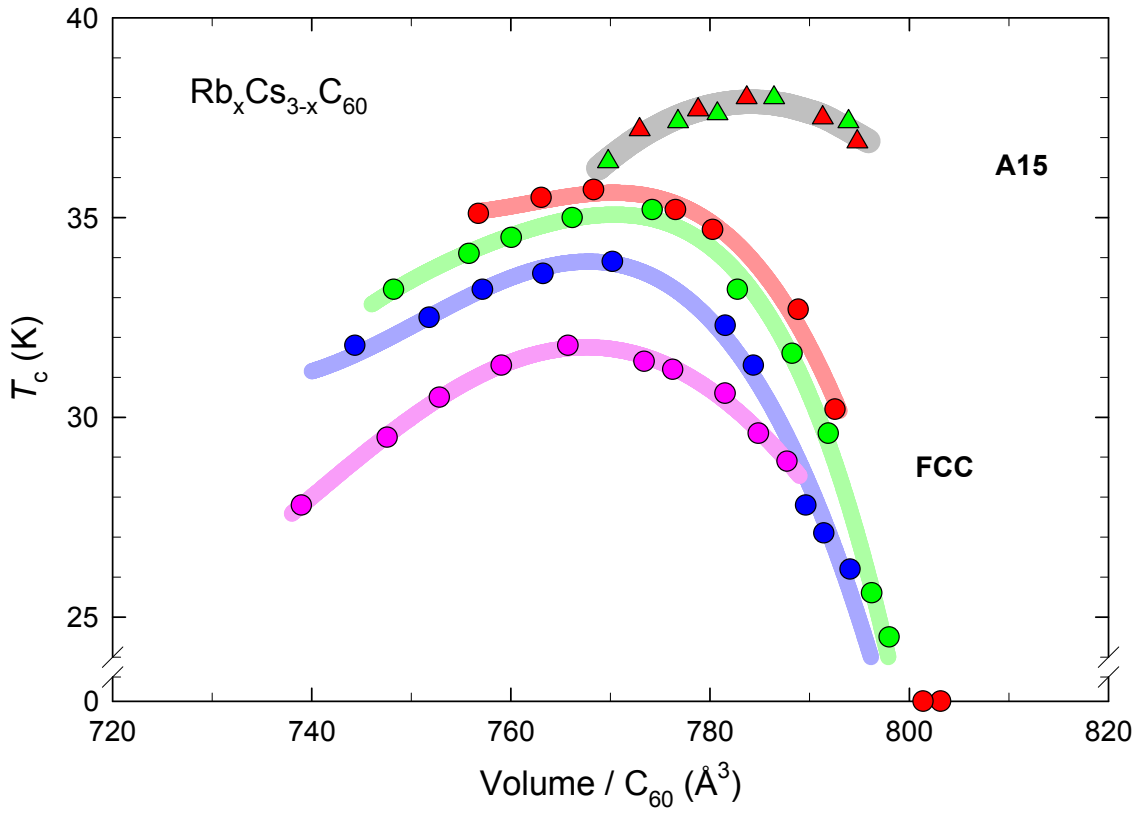

Fig 3.27: Superconducting transition temperature (T_c) as a function of room temperature unit cell volume occupied per C_{60} molecule for the FCC-structured $Rb_xCs_{3-x}C_{60}$ samples and for A15-structured Cs_3C_{60}. Pink colour represents x = 0.62, blue x = 0.37, green x = 0.18, and red x = 0. Circles represent data for the FCC phases, triangles the A15 Cs_3C_{60} phase. The values of the Rb content are those obtained by the Rietveld refinements of the synchrotron X-ray powder diffraction data. The respective colour lines are guides-to-the-eye. A single grey line is used as a guide-for-the-eye for all A15 samples as they have a fixed Cs_3C_{60} stoichiometry.

Fig 3.27 clearly summarises the global response of the FCC family of materials to changes in C_{60} interfullerene separation induced by either chemical or physical pressure. It is immediately apparent that for the same chemical composition (i.e. Cs_3C_{60}) of the two different polymorphs, the T_c(V) domes do not map onto each other. The FCC phase has a lower T_c and the onset of the M-I transition occurs at a smaller value of V/C_{60}. This is presumably related to the differing intermolecular overlaps between the two structural families and is in agreement with the results of theoretical calculations which find a larger density-of-states at the Fermi level at the same interfullerene separation for the A15 family.[16] What is however also immediately

evident and is extremely intriguing is that the $T_c(V)$ domes of the FCC isostructural $Rb_xCs_{3-x}C_{60}$ series are also shifted from each other in both T_c and V/C_{60} space. Namely, they are not superimposable with T_c(max) and V/C_{60}(max) both shifting to higher values with decreasing Rb content. This is at present surprising as within a rigid band picture and for a fixed band filling, it is expected that the electronic and superconducting properties will be controlled entirely by the magnitude of the bandwidth, W. Therefore the present results call for additional subtleties controlling the properties of these FCC phases. A possible candidate for the non-rigid-band behaviour observed and the Rb-specific control of the electronic properties may be the increased positional disorder associated with the occupation of the same interstitial site by ions of differing ionic size (Rb^+ versus Cs^+).

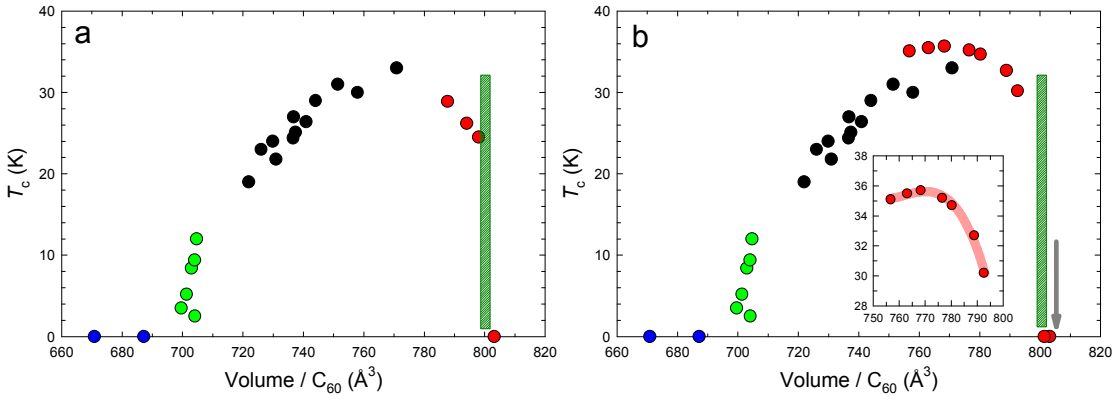

Fig 3.28: Superconducting transition temperature (T_c) as a function of room temperature unit cell volume occupied per C_{60} molecule for the FCC-structured materials. Red circles in (**a**) represent ambient pressure data for the FCC-structured $Rb_xCs_{3-x}C_{60}$ samples. Red circles in (**b**) represent FCC-Cs_3C_{60} as a function of pressure (also displayed as an expanded version in inset). Blue circles indicate Li_2CsC_{60}, green circles simple cubic materials, and black circles FCC-structured materials from the literature. The green shaded region in (**a**, **b)** shows the metal-insulator (M-I) transition region for the FCC-structured materials, and the grey arrow in (**b**) marks the M-I transition in A15 Cs_3C_{60}.

To put into context the data shown in Fig 3.27, the findings were plotted alongside the literature data for the $T_c(V)$ dependence of the FCC series away from the metal-insulator transition (Fig 3.28). In comparison to the BCC-structured polymorph

(A15 phase), there is clearly a shift observed in the onset of the M-I transition to a smaller value of V/C_{60} for the FCC family. From the ambient pressure data in Fig 3.28(a), the presence of the M-I transition at ambient pressure at a critical value of V/C_{60} ~800.6 Å^3 can be identified. The pressure dependence of the T_c for FCC Cs_3C_{60} is instead shown in Fig 3.28(b). The resulting maximum T_c of 35.7 K is the largest reported for the FCC polymorph, and the observed superconductivity dome is reminiscent of the T_c behaviour of the high-T_c copper oxides as they are chemically doped to cross the Mott–Hubbard M-I transition. The FCC Cs_3C_{60} polymorph is able to cross the M-I phase boundary while retaining the triple degeneracy of the t_{1u} levels. This is a unique experimental feature among C_{60}^{3-} fulleride phases and places stringent constraints on theories of superconductivity in these materials.

3.7 Conclusions

Previous studies of the merohedrally disordered $Fm\bar{3}m$ A_3C_{60} (where A is a mixture of K, Rb and Cs) systems had established a monotonic dependence of T_c on unit cell volume.[1,2,3,4,5] As Cs^+ is the largest alkali metal cation, Cs_3C_{60} is a key material in this family in order to establish the universality of this relationship at large interfullerene separations. However, the isolation of FCC Cs_3C_{60} has proven difficult as direct synthesis by thermal combination of Cs and C_{60} in gas–solid or solid–solid reactions has been unsuccessful over the last 20 years.[6] There has been no literature evidence of the successful synthesis of crystalline systems with lattice size larger than $RbCs_2C_{60}$ by traditional solid state synthetic methods.

The low-temperature solution-based work by Dahlke *et al.*[11] of FCC-rich $Rb_xCs_{3-x}C_{60}$ polymorphs have yielded interesting results; however, in terms of unit cell size they were unable to advance beyond a lattice parameter of a = 14.6925(4) Å for a sample with nominal composition $Rb_{0.32}Cs_{2.65}C_{60}$. Very importantly, the samples suffered from poor crystallinity making unambiguous conclusions of chemical composition by diffraction techniques very problematic.

Investigations in this area in collaboration with the University of Liverpool[13,14,15,16,17] initiated studies where methylamine was employed as a solvent. This work was successful for the first time in obtaining crystalline Cs_3C_{60} phases which were not superconducting at ambient pressure; however, application of pressure induced an insulator-metal transition and a superconducting phase followed with a transition temperature of 38 K and a shielding fraction of 68% at ~0.7 GPa. The material synthesised comprised of three crystalline phases with the majority phase responsible for the high T_c of 38 K adopting A15 symmetry. The two minority phases identified crystallised with the FCC and BCO structures.

So to define this work in terms of the related investigations: work by Dahlke *et al.* on $Rb_xCs_{3-x}C_{60}$ systems utilising ammonia as the solvent produced inconsistent results on FCC-rich systems, while work by Ganin, Takabayashi *et al.* on Cs_3C_{60} utilising methylamine as the solvent produced a three-phase material. However, the FCC phase was in minority and of poorly crystalline nature. In order to explore the possibility of synthesising FCC-rich samples, ammonia was utilised as the solvent coupled with higher annealing temperatures.

This chapter details the successful synthesis of crystalline FCC-rich $Rb_xCs_{3-x}C_{60}$ (nominal composition, x = 0.50, 0.25, 0.12, 0.00) systems. Like the earlier methylamine solvent route, the obtained products were typically three-phase crystalline materials; however, a reproducible route that led to products where the majority phase was FCC-structured has been discovered for the first time. During the course of the investigation a crystalline Cs_3C_{60} FCC phase has been produced with a lattice parameter of 14.75607(7) Å.

The non-superconducting BCO phase (space group *Immm*) accounted for 20-35% of each material synthesised – its composition was modelled to be entirely Cs_4C_{60}. This is an insulating phase and had no bearing on the results presented.

As the doping level of Rb increases in $Rb_xCs_{3-x}C_{60}$, observed in the Rietveld refinements of the synchrotron XRD data is a reduction in the proportion of the A15 phase present in the multiphase compositions – when the nominal Rb content approaches x = 0.50, no evidence of the presence of the A15 polymorph is found. This

is also reflected in the magnetisation measurements. In the ZFC results for the Cs_3C_{60} sample, there is evidence of two superconducting transitions arising from the A15 and FCC phases, respectively. As the Rb doping level is reduced, the contribution of the higher transition (arising from the A15 phase) to the magnetisation is suppressed and disappears for the samples with nominal stoichiometries, $Rb_{0.50}Cs_{2.50}C_{60}$ and $Rb_{0.25}Cs_{2.75}C_{60}$. As well as being superconducting at high P, the A15 phase also exhibits an antiferromagnetic insulating (AFI) ground state at low P that manifests itself as a small positive spontaneous magnetisation observable in low-field FC measurements. The amount of the A15 phase is directly proportional to the magnitude of the spontaneous magnetisation and again decreases as the Rb content increases. The origin of the A15 state is described in more detail in the introduction of *chapter 4*. In terms of both the diffraction and magnetic measurements, the composition of the A15 component appears more or less invariant with changes in the nominal composition. If one considers the diffraction measurements, the variation of the unit cell volume is less than 0.1% across the investigated compounds. In addition, the superconducting transition temperature dependence on volume occupied per C_{60} for samples with nominal stoichiometries, $Rb_{0.12}Cs_{2.88}C_{60}$ and Cs_3C_{60} is identical. Therefore a single Cs_3C_{60} composition with no Rb co-intercalation is entirely consistent with all the results. In the subsequent chapter attempts to co-intercalate Rb into the A15 Cs_3C_{60} polymorph are discussed.

On the other hand, the FCC component of the $Rb_xCs_{3-x}C_{60}$ samples investigated shows a sensitive variation in properties as the doping level of Rb varies. The first structural conclusion is to deduce the location of the Rb co-dopant in the FCC structure. From initial refinements of the Rb_2CsC_{60} sample it was concluded that Rb^+ cation resided entirely in the smaller tetrahedral cavity (T_d) of the FCC unit cell. As the size of the T_d cavity is much smaller than either the Rb^+ or the Cs^+ cation size, a large variation was observed in the unit cell volume in the FCC phase with changing composition. Detailed Rietveld refinements of high-quality diffraction data led to the conclusion that Rb^+ exists essentially exclusively in the FCC phase. Difficulties arose during Rietveld refinements of data from samples containing mixed cation occupancy as it is challenging to account for the ratio of the cationic mixture and the occurrence

of partial occupancy. The final structural model consistent with all diffraction data involved Rb being exclusively resident in the T_d sites. The model gave convincing results that made sense both structurally and chemically.

Unlike the A15 polymorph, whose magnetic properties appear invariant with changes in Rb content (and consistent with our conclusion of line phase formation under the present synthetic conditions), the FCC phase shows a large variation in the superconducting transition temperature with changing the doping level of Rb. Our systematic studies have established that the ambient pressure electronic state of FCC Cs_3C_{60} is non-superconducting and non-magnetic – the latter is consistent with the frustrated topology associated with the FCC crystal structure. However, in analogy with the A15-structured analogue, it also undergoes an insulator-to-metal transition upon pressurisation with superconductivity appearing at a lower pressure onset than for the A15 phase. The similarity also extends to the T_c vs P response – as pressure increases and the intermolecular separation decreases, T_c initially increases, reaches a maximum and then begins to decrease. Notably the maximum T_c at 35 K is lower than that of the A15 phase. As the Rb content increases, an insulator-to-metal transition also occurs as a result of chemical pressure and superconductivity gradually emerges even at ambient pressure. However, all $Rb_xCs_{3-x}C_{60}$ compositions show a similar superconductivity dome but with the maximum T_c and the pressure where the dome occurs decreasing monotonically with increasing Rb content. While the differences in the T_c versus V response of the two Cs_3C_{60} polymorphs (FCC, A15) can be traced to their differing electronic structures, the systematically varying T_c versus V domes of the $Rb_xCs_{3-x}C_{60}$ ($x \neq 0$) compositions apparently reflect Rb-specific effects of the electronic properties. Such effects are not anticipated by rigid band theories and possibly reflect the importance of cation positional disorder effects.

3.8 References

[1] Fleming R. M., Ramirez A. P., Rosseinsky M. J., Murphy D. W., Haddon R. C., Zahurak S. M., Makhija A. V. *Nature* **1991**, 352, 787-788

[2] Sparn G., Thompson J. D., Huang S. M., Kaner R. B., Diederich F., Whetten R. L., Gruner G., Holczer K. *Science* **1991**, 252, 1829-1831

[3] Zhou O., Vaughan G. B. M., Zhu Q., Fischer J. E., Heiney P. A., Coustel N., McCauley J. P., Smith A. B. *Science* **1992**, 255, 833-835

[4] Chen C. C., Kelty S. P., Lieber C. M. *Science* **1991**, 253, 886-888

[5] Movshovich R., Thompson J. D., Chen C. C., Lieber C. M. *Phys. Rev. B* **1994**, 49, 3619-3621

[6] Zhou O., Cox D. E. *J. Phys. Chem. Solids* **1992**, 53, 1373–1390

[7] Kelty S. P., Che. C. C., Lieber C. M. *Nature* **1991**, 352, 223–225

[8] Palstra T. T. M., Zhou 0., Iwasa Y., Sulewski P. E., Fleming R. M., Zegarski B. R. *Solid State Commun.* **1995**, 93, 327–330

[9] Messaoudi A., Conard J., Setton R., Beguin F. *Chem. Phys. Lett*. **1993**, 202, 506–508

[10] Fujiki S., Kubozono Y., Emura S., Takabayashi Y., Kashino S., Fujiwara A., Ishii K., Suematsu H., Murakami Y., Iwasa Y., Mitani T., Ogata H. *Phys. Rev. B* **2000**, 62, 5366–5369

[11] Dahlke P., Denning M. S., Henry P. F., Rosseinsky M. J. *J. Am. Chem. Soc.* **2000**, 122, 12352-12361

[12] Cooke S., Glenis S., Chen X., Lin C. L., Labes M. M. *J. Mater. Chem*. **1996**, 6, 1-3

[13] Ganin. A. Y., Takabayashi. Y., Bridges. C. A., Khimyak. Y. Z., Margadonna. S., Prassides. K., Rosseinsky. M. J., *J. Am. Chem. Soc*. 128, **2006**, 14784–14785

[14] Takabayashi T., Ganin A. Y., Rosseinsky M. J., Prassides K. *Chem. Commun*. **2007**, 870–872

[15] Ganin A. Y., Takabayashi T., Khimyak Y. Z., Margadonna S., Tamai A., Rosseinsky M. J., Prassides K. *Nature Materials* **2008**, 7, 367-371

[16] Darling G. R., Ganin A. Y., Rosseinsky M. J., Takabayashi Y., Prassides K. *Phys. Rev. Lett.* **2008**, 101, 136404-136408

[17] Takabayashi Y., Ganin A. Y., Jeglic P., Arcon D., Takano T., Iwasa Y., Ohishi Y., Takata M., Takeshita N., Prassides K., Rosseinsky M. J. *Science* **2009**, 232, 1585-1590

Chapter 4

$Rb_xCs_{3-x}C_{60}$ solid solutions – A15-rich compositions

4.1 Introduction

In this chapter results of a study on the series of multiphase compounds with nominal composition $Rb_xCs_{3-x}C_{60}$ ($0.0 \leq x \leq 0.5$) will be presented. Now the synthetic protocol is optimised that the materials are rich in the A15 polymorph. Two sets of solid solutions were synthesised and structurally and electronically characterised: (i) "FCC rich" ones by utilising ammonia (NH_3) as a solvent (*chapter 3*) and (ii) "A15 rich" by utilising methylamine ($MeNH_2$) as the solvent medium. As already stated in *chapter 3*, the A15 Cs_3C_{60} phase is a second polymorph, which is structurally and electronically different from its FCC counterpart.

The A15 Cs_3C_{60} phase (BCC structured) was first unambiguously synthesised and characterised by Ganin *et al*[1] using methylamine ($MeNH_2$) as the solvent in a solution-based low-temperature synthetic procedure. Annealing temperatures utilised during the synthesis were generally low (not higher than 150-180°C), as higher temperatures appear to promote the formation of the FCC and BCO phases. The solvent employed is also a crucial factor that determines which phase is produced preferentially. As described in *chapter 3,* the FCC phase is preferentially formed when NH_3 is used as the solvent while $MeNH_2$ favours the formation of the A15 phase. The earlier work showed that Cs_3C_{60} obtained following this route was not superconducting at ambient pressure; however, application of pressure induced a metal-insulator transition and a superconducting phase with a transition temperature of 38 K and a shielding fraction of 68% was obtained at ~0.7 GPa. The material synthesised comprised three crystalline phases with the majority A15 phase responsible for the high T_c of 38 K. The two minority phases identified had FCC and body-centred-orthorhombic (BCO) structures; in *chapter 3* the highest definitive T_c for the FCC phase of 35.7 K was recorded. The structures of all three polymorphs are shown in Fig 4.1.

Using density functional theory, the electronic properties of the two key Cs_3C_{60} polymorphs, A15 and FCC, were compared as a function of unit cell volume.[2] It was found that the A15 phase displays both a substantially wider width for the partially

occupied t_{1u} band and a larger density-of-states at the Fermi level. This result was traced to differences between the nature of the inter-anion overlap in the A15 and FCC structures, showing that the A15 Cs_3C_{60} phase is not simply another superconducting fulleride, albeit with a very high T_c; it rather represents the parent member of an electronically distinct class of fulleride superconductors that have different properties from those of their FCC antecedents.

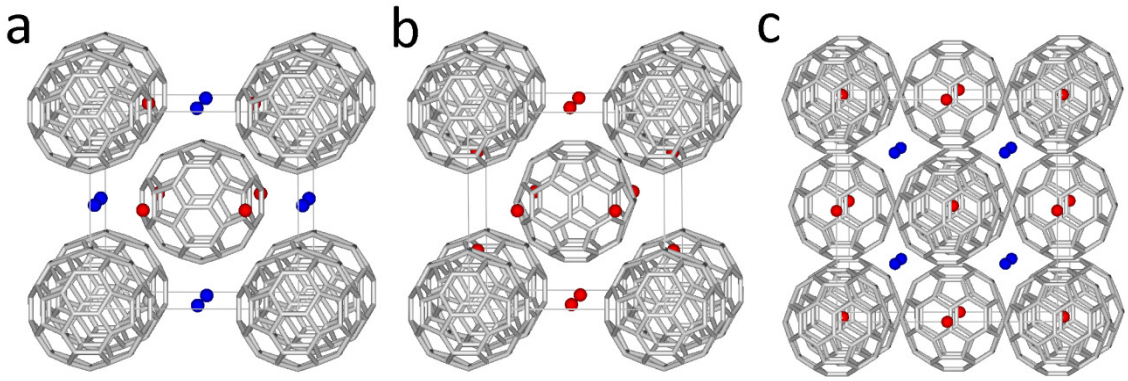

Fig 4.1: a, BCO unit cell (space group *Immm*). **b**, A15 unit cell (space group *Pm* $\bar{3}$ *n*). **c**, FCC unit cell (space group *Fm* $\bar{3}$ *m*) of Cs_3C_{60}. In **a** and **b**, one unique orientation of the C_{60}^{3-} anions is present, whereas in **c** two orientations related by 90° rotation about [100] occur in a disordered manner; only one of these orientations is shown for clarity. The Cs^+ ions are shown as red and blue spheres in (**a)** to signify symmetry-inequivalent positions in the unit cell.

Aside from the pressure-induced superconducting response, it has also been found that samples rich in the A15 phase exhibit an antiferromagnetic (AFM) transition on cooling below T_N = 46 K at ambient pressure. In addition, a small spontaneous magnetisation is observed at exactly the same temperature in low-field-cooled measurements (Fig 4.3) implying that that the ground state at ambient pressure is that of a canted antiferromagnet.[3]

The antiferromagnetic state of the A15 phase is a BCC-based structure type bipartite lattice. As a result this BCC-structured material can support an antiferromagnetic state with no frustration. The small spontaneous magnetisation occurs due to a small canting of the spins. Considering the BCC structural model of Fig

4.2, this implies that the spins of nearest neighbour C_{60} units are not precisely aligned in an opposite way, *i.e.* their alignment is at a small angle of misalignment, and hence a weakly ordered ferromagnetic state can be observed. Examination of many batches of multiphase samples has shown that the strength of the signal is proportional to the amount of A15 phase present in the material. It is then interesting to note that the FCC structure represents a frustrated topology for the development of antiferromagnetic order - the tetrahedral coordination of nearest neighbour C_{60} units cannot support an anti-ferromagnetic ground state (Fig 4.2). The FCC phase therefore remains paramagnetic as observed in our measurements of $Rb_{0.50}Cs_{2.50}C_{60}$ in *chapter 3*, which has no A15 phase present (there is no evidence for antiferromagnetic order at T_N above the pressure-induced T_c.

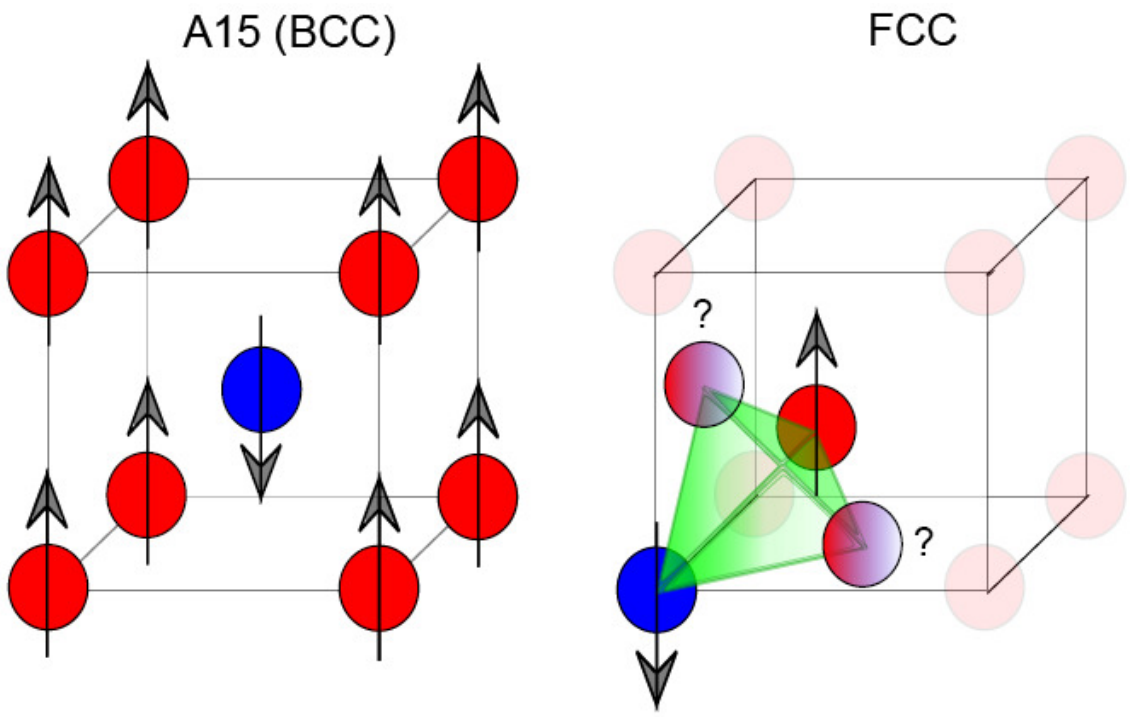

Fig 4.2: BCC- and FCC-based packing. Blue and red spheres represent C_{60}^{3-} anions, the arrows represent the magnetic moments of each unit and their direction indicates their antiparallel alignment in the antiferromagnetic state relationship. The spheres that are both red and blue have an unidentified (frustrated) spin direction.

The electronic phase diagram of the parent A15 Cs_3C_{60} phase under the influence of external pressure has already been mapped out (Fig 4.3).[3] The aim behind the results presented in this section of the thesis is to attempt to investigate the possibility of whether a distinct family A15-structured materials could be synthesised. This would allow us to probe in detail the metal-insulator transition by producing A15-rich samples with a reduced cell volume after doping with a smaller cation (replacing Cs^+ with Rb^+).

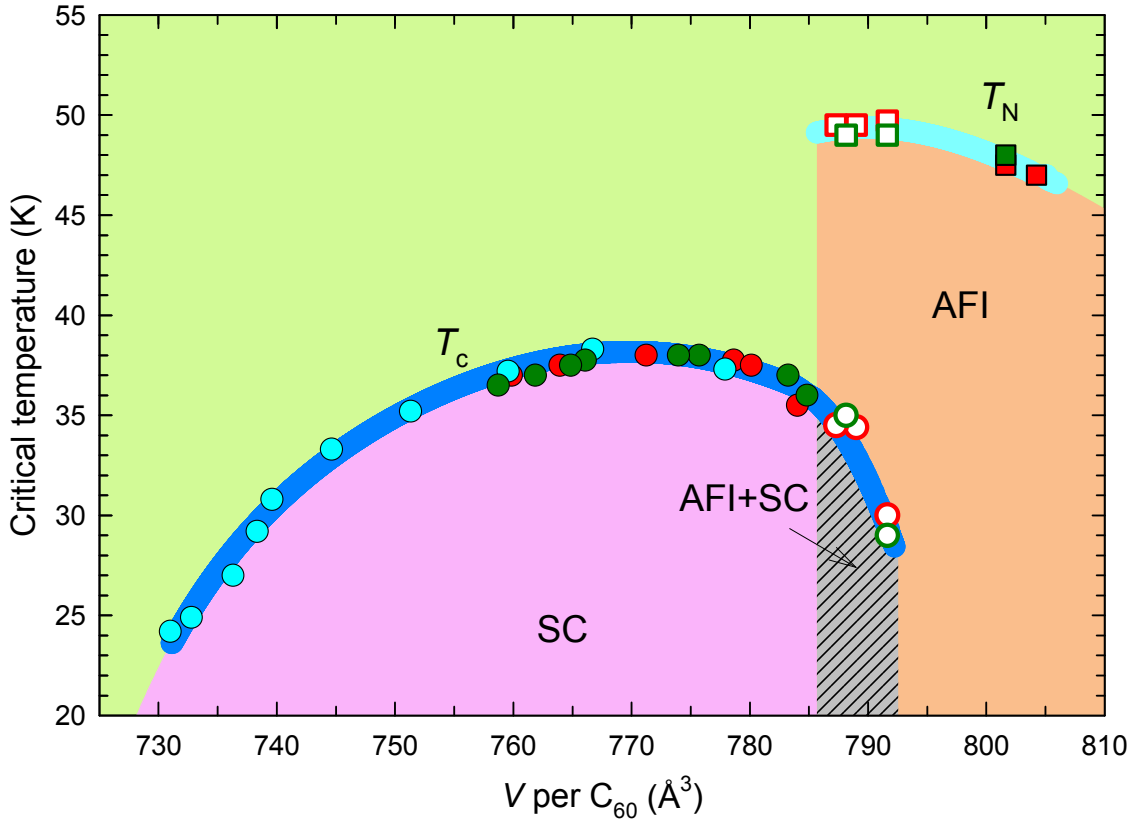

Fig 4.3: Electronic phase diagram of A15 Cs_3C_{60}, showing the evolution of the Néel temperature, T_N (squares) and the superconducting transition temperature, T_c (circles), and thus the isosymmetric transition from the ambient-pressure AFI state to the high-pressure superconducting state as a function of volume occupied per fulleride anion, V, at 14.6 K for A15 Cs_3C_{60}. Different symbol colours represent data obtained for different sample batches. Open symbols represent data in the AFI-superconductor coexistence regime.[3]

4.2 Experimental Methods

4.2.1 Preparation of $Rb_xCs_{3-x}C_{60}$ ($0.0 \leq x \leq 0.5$) – methylamine as the solvent medium

The samples studied in this section were prepared by a visiting colleague Manolis Tzirakis, aided by the candidate and Professor Prassides. The sample preparation procedures were analogous to those for the FCC-rich samples with the following variations.

The boiling point of NH_3 is −33^{o}C, while the boiling point of $MeNH_2$ is -6^{o}C. Therefore as $MeNH_2$ is less volatile than NH_3, transferring it between vessels is a less hazardous but slower (lower pressure) procedure; however, $MeNH_2$ is extremely flammable, so it must be handled with extreme care. In comparison to the NH_3 prepared samples, the annealing procedures were significantly different. Generally, the samples were annealed at 100^{o}C under dynamic vacuum until the pressure reached 10^{-5} Torr (not time dependent). The remaining products were sealed in 12-mm glass ampoules under a partial pressure of He (ca. 500 Torr), then annealed at 180^{o}C (heating rate 2^{o}C/min, cooling rate 5^{o}C/min) for 48 hrs.

Some of the samples were synthesised using a Cs/Rb (5:1) alloy as the source of alkali metals to be intercalated. The alloy was pre-prepared in the glovebox by mixing 530 mg (3.988 mmol) of Cs and 68 mg (0.796 mmol) of Rb. This helps to minimise the error associated with weighing small quantities of Rb metal. The alloy is a liquid at room temperature and therefore it needed syringing into the reaction vessel.

By sealing the sample in small glass capillaries under an Ar atmosphere, the progress of the reactions were followed by collecting data with the Siemens D5000 X-ray powder diffractometer (λ = 1.5406 Å). The diffraction patterns obtained for the synthesised $Rb_xCs_{3-x}C_{60}$ ($0.0 \leq x \leq 0.5$) samples are shown Fig 4.4. Sample MT003 was used to investigate the difference between annealing the samples as a free flowing powder and as a compacted pellet (8 mm diameter).

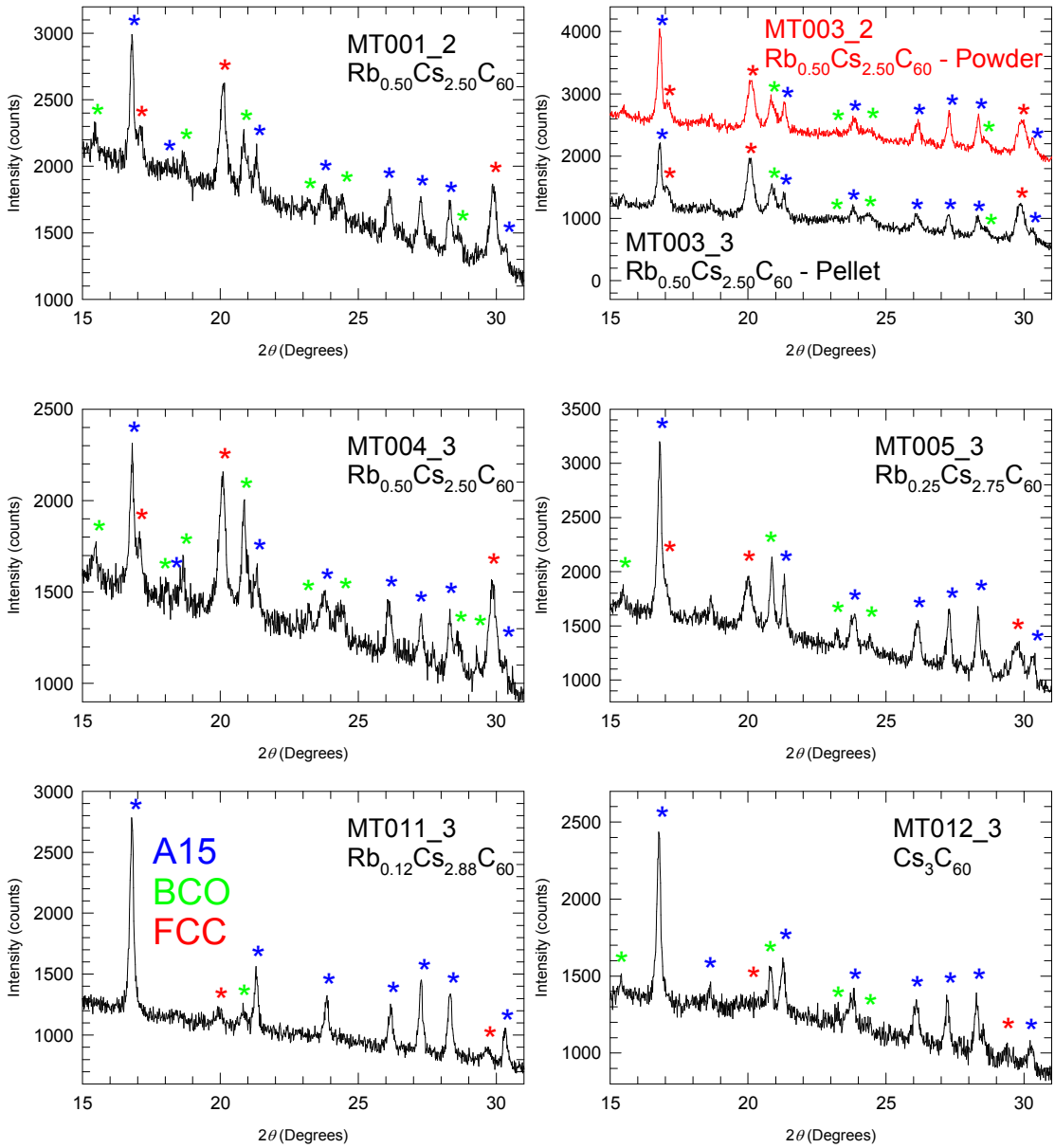

Fig 4.4: X-ray diffraction profiles of the "A15-rich" samples $Rb_xCs_{3-x}C_{60}$ ($0.0 \leq x \leq 0.5$) collected with the Siemens D5000 powder diffractometer (Cu-K_α radiation) in capillary mode at room temperature. Blue, red and green asterisks mark the A15, FCC and BCO diffraction peaks, respectively.

A qualitative summary of the results could be obtained from the D5000 data. Expected phases are easily identified and simple Le Bail refinements could be performed in order to check roughly sample constitution; however, the signal-to-noise is quite poor so minor phases are often not identified. It can be seen from Fig 4.4 that as the Rb content is reduced the amount of A15 phase increases, and consequently the

FCC phase is suppressed. In a qualitative comparison to the samples described in chapter 3, it is clear that the synthetic protocol enhances the A15 phase content in the present multiphase assemblages. Both sets of samples appear to contain small but observable amounts of the competing BCO phase.

The quantities of starting materials used during synthesis are listed in Table 4.1. The accuracy of the balance inside the glovebox is ±1 mg. The volume of solvent was measured by adding 80 ml of water to the vessel prior to the experiment and marking the level on the exterior. As the aim was to enhance the A15 phase content, the samples were annealed at only 180^{o}C for 48 hrs with no intermediate grindings. Mass discrepancy between precursor and product is attributed to making capillaries during intermediate grindings.

Table 4.1: Masses and volumes of the starting materials used in the synthesis of "A15 rich" $Rb_xCs_{3-x}C_{60}$ ($0.0 \leq x \leq 1.0$) samples. The precursor mass was after evacuation of $MeNH_2$ and removal of the precursor from the surface of the glass vessel. Final product mass was after all annealing protocols.

Sample ID	Nominal *x*	Moles of Rb (mmol)	Moles of Cs (mmol)	Moles of C_{60} (mmol)	Vol of $MeNH_2$ (ml)	Mass of Precursor (mg)	Mass of Product (mg)
MT001_2	0.50	0.105	0.527	0.208	80	217	202
MT002_4	1.00	0.208	0.416	0.208	80	194	168
MT003_2	0.50	0.163	0.815	0.347	80	280	100
MT003_3	0.50	0.163	0.815	0.347	80	280	100
MT004_3	0.50	0.063	0.314	0.069	80	45	35
MT005_1	0.25	0.058	0.640	0.232	80	210	210
MT011_3	0.12	0.024	0.593	0.208	80	195	147
MT012_3	0.00	--	0.459	0.168	80	162	111

4.3 Synchrotron X-ray Diffraction Studies

Small amounts (3-6 mg) of each sample were sealed in 0.5-mm glass capillaries under 300 Torr of He gas. Room temperature and low temperature data were collected for each sample at two different synchrotron facilities, ID31 and Diamond. On ID31, data were collected in the 2θ range 5-30^{o} in continuous scanning mode and re-binned from 2 to 25^{o} in a step size of 0.003^{o}. Room temperature data were collected outside the cryostat with the sample spinning (3000 rpm). Spinning the sample helps to eliminate any preferred orientation effects. For collecting low temperature data on ID31, the sample was remounted inside a continuous flow liquid He cryostat, and cooled at a rate of 5 K/min to 5 K. The sample was also rotating during low temperature data acquisition, but at a much slower rate due to instrumental restrictions (1000 rpm).

At Diamond, data were collected in the 2θ range 3-142^{o} in continuous scanning mode and re-binned from 5 to 50^{o} in a step size of 0.003^{o}. Room temperature data were again collected outside the cryostat. For the low temperature measurements, the sample was cooled to 12 K. There was an issue with the quality of the background during data collection at Diamond that at these early stages of operation was attributed to the air conditioning unit.

When collecting data on ID31 (ESRF) the X-ray wavelength was 0.39988(4) Å, while the wavelength on I11 (Diamond) was 0.8260280(1) Å. Analysis of the data was performed using the GSAS diffraction suite equipped with the EXPGUI interface.[4,5] For all refinements, when a change of inter-fullerene separation distance was observed, the fullerene molecule dimensions were kept constrained.

4.4 $Rb_xCs_{3-x}C_{60}$ – Synchrotron XRD at room temperature

In a similar approach to the procedure employed for the samples produced using the ammonia solvent, a methodical process was used to determine the best refinement model for samples created when $MeNH_2$ was the solvent medium. There are two initial observations that can be made in comparison with the NH_3 solvent route samples. Firstly the majority phase in the present samples is the A15 phase and secondly the crystallinity of the FCC phase is inferior; the latter can be attributed to the lower annealing temperatures utilised during synthesis.

In this section of the thesis two models are presented that were employed in order to probe the structure of the A15 phases.

Earlier work had established characteristics and trends that influenced the models chosen. Initially it was noticed that the unit cell volume of the A15 phase varied only slightly (1630.74(4) to 1633.45(8) $Å^3$, i.e. less than 0.2% variation) as the nominal Cs content increased. In contrast, the unit cell volume of the minority FCC phase increased systematically from 3128.6(2) to 3232.7(4) $Å^3$, an approximate 3.2% variation across the series of samples. So the first model assumes that all the co-doped Rb is incorporated in the FCC phase, and that the A15 phase is exclusively Cs_3C_{60} - this implies that A15 Cs_3C_{60} is a line phase and that a structural family with varying Rb content cannot be obtained. This model appears consistent with previous analysis of the FCC-rich samples. However, as the FCC-phase is a minority and poorly crystalline component, the occupancy of the cation sites cannot be refined reliably. Instead the Cs:Rb ratio of the tetrahedral cavity is determined by calculating the theoretical maximum value of Rb, based on the FCC phase percentage and the amount of Rb reagent used initially in synthesis. Similarly to the previous samples, the non-superconducting BCO phase was again a minority phase (<20%) and its stoichiometry was fixed at Cs_4C_{60}.[1]

The results of this refinement model will then be fed into the second model which will be described in more detail later; however, the rationale behind the model

would be to prove if any Rb is doped into the A15 phase. As the focus is on small occupancy discrepancies for the metal cations, anomalous scattering corrections (*f'* and *f''*) for Rb^+/Cs^+ cations at the wavelengths λ = 0.39988(4) Å and λ = 0.826028(1) Å were included. The program Dispano[6] was used to calculate these wavelength-dependent parameters: λ = 0.39988(4) Å; Cs: *f'*=-1.921, *f''*=0.758; Rb: *f'*=0.156, *f''*=1.116, and λ = 0.826028(1) Å; Cs: *f'*=-0.438, *f''*=2.784; Rb: *f'*=-3.959, *f''*=0.520.

4.4.1 $Rb_xCs_{3-x}C_{60}$ (0.0 ≤ x ≤ 0.5) at room temperature, model 1

Refined parameters for the majority A15 (space group $Pm\bar{3}n$), minority FCC (space group $Fm\bar{3}m$) and minority BCO (space group *Immm*) phases are summarised in the tables within this subsection. Table 4.2 includes an overall summary, showing key refinement parameters and results, and then each sample is given a more detailed description. Three-phase Rietveld refinements of the synchrotron X-ray powder diffraction data of samples with nominal stoichiometry $Rb_xCs_{3-x}C_{60}$; MT001_2 (x = 0.50), MT003_2 (x = 0.50), MT003_3 (x = 0.50), MT005_1 (x = 0.25), MT011_3 (x = 0.12) and MT012_3 (x = 0.00) were undertaken. The refinement strategy was exactly as described earlier and the fractional occupancy, *N*, of the Cs(1) atom in the A15 phase was allowed to vary, converging to a value close to 1. The Rb doped into the sample was positioned entirely into the T_d site of the FCC phase, while the remaining occupancy was modelled as Cs, thus keeping the total occupancy of the T_d site fixed at 1.0. The fractions of the co-existing minority BCO and FCC phases are also listed in Table 4.2; the stoichiometry of the BCO phase was not refined but kept fixed at Cs_4C_{60}, while the stoichiometry of the FCC phase was also fixed, but its value varied based around the Rb doping level.

Table 4.2: Results of the Rietveld refinements of the series $Rb_xCs_{3-x}C_{60}$ ($0.0 \leq x \leq 0.5$) at room temperature, Model 1

Parameter	*MT001_2*	*MT003_2*	*MT003_3*	*MT005_1*	*MT011_3*	*MT012_3*
Nominal x	0.50	0.50	0.50	0.25	0.12	0
R_{wp} (%)	5.00	4.79	6.72	6.66	4.35	3.10
R_{exp} (%)	4.19	3.74	6.36	6.38	2.14	1.01
χ^2	1.092	1.132	1.028	1.022	1.426	1.752
λ (Å)	0.39988(4)	0.39988(4)	0.39988(4)	0.39988(4)	0.826028(1)	0.826028(1)
A15 (%)	28.7(3)	28.0(2)	25.6(2)	42.1(4)	70.4(1)	71.3(1)
BCO (%)	18.7(1)	17.7(1)	18.1(2)	19.4(2)	7.9(1)	5.2(1)
FCC (%)	52.6(1)	54.3(1)	56.3(2)	38.5(3)	21.7(2)	23.5(2)
A15 *a* (Å)	11.7739(1)	11.7705(1)	11.7770(2)	11.7769(1)	11.77319(4)	11.77660(4)
A15 *V* (Å^3)	1632.17(5)	1630.74(4)	1633.45(8)	1633.41(6)	1631.86(2)	1633.28(2)
BCO cell (Å)	*a* = 11.8927(7) *b* = 12.1766(5) *c* = 11.4311(4)	*a* = 11.9061(8) *b* = 12.1790(6) *c* = 11.4182(5)	*a* = 11.895(1) *b* = 12.184(1) *c* = 11.4375(7)	*a* = 11.8953(7) *b* = 12.1732(5) *c* = 11.4479(4)	*a* = 11.873(1) *b* = 12.201(1) *c* = 11.4445(6)	*a* = 11.8953(7) *b* = 12.1732(5) *c* = 11.4479(4)
BCO *V* (Å^3)	1655.34(9)	1655.7(1)	1657.7(2)	1657.70(8)	1658.0(1)	1657.70(8)
FCC *a* (Å)	14.6279(2)	14.6257(3)	14.6412(4)	14.6967(7)	14.7196(4)	14.7862(7)
FCC *V* (Å^3)	3130.0(2)	3128.6(2)	3138.6(2)	3174.3(5)	3189.2(3)	3232.7(4)
Refined A15 stoichiometry	$Cs_{2.84(2)}C_{60}$	$Cs_{2.93(2)}C_{60}$	$Cs_{2.92(3)}C_{60}$	$Cs_{2.92(3)}C_{60}$	$Cs_{2.760(6)}C_{60}$	$Cs_{2.892(6)}C_{60}$
Fixed FCC stoichiometry	$Rb_{0.96}Cs_{2.04}C_{60}$	$Rb_{0.92}Cs_{2.08}C_{60}$	$Rb_{0.88}Cs_{2.12}C_{60}$	$Rb_{0.66}Cs_{2.34}C_{60}$	$Rb_{0.60}Cs_{2.40}C_{60}$	Cs_3C_{60}

Sample MT001_2 at room temperature, model 1:

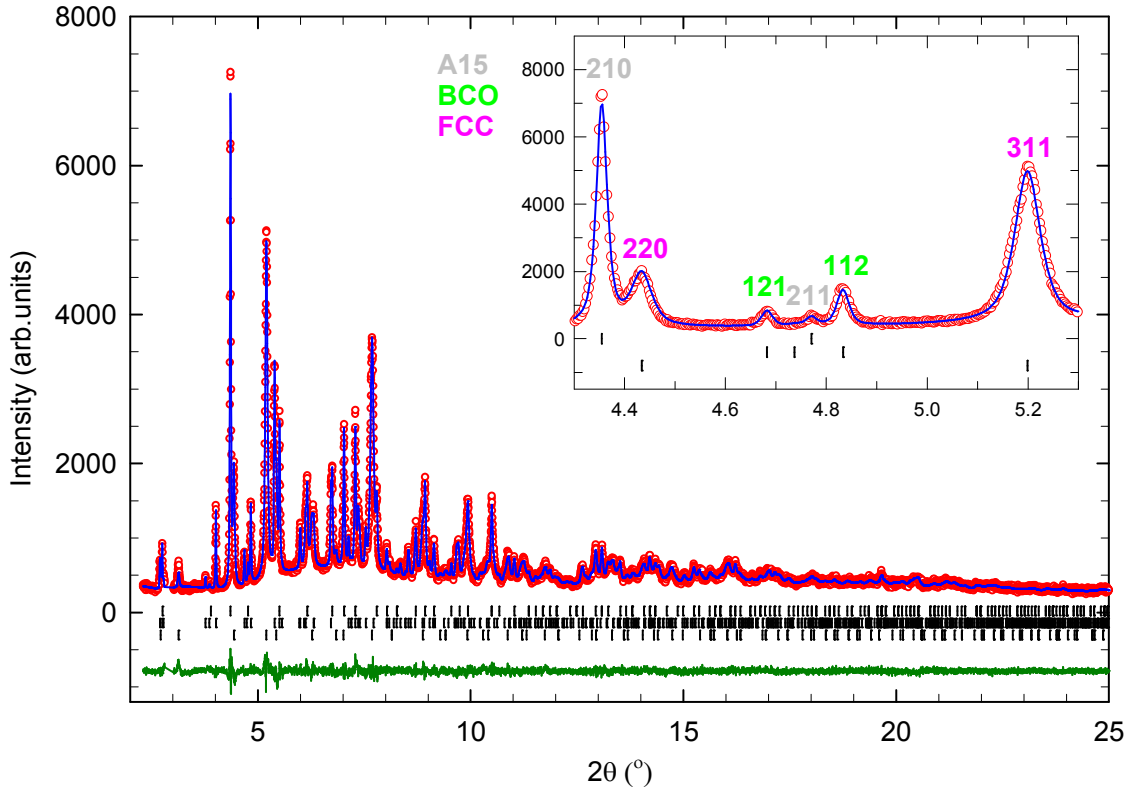

Fig 4.5: Observed (open red circles) and calculated (blue line) data of the room temperature synchrotron powder X-ray diffraction pattern for the sample with nominal composition $Rb_{0.50}Cs_{2.50}C_{60}$ (MT001_2). The upper bars represent the positions of the Bragg reflections of the A15 phase, the middle ones of the BCO phase and the lower ones of the FCC phase. The wavelength is λ = 0.39988(4) Å.

Table 4.3: Results of the room temperature three-phase Rietveld refinement of the Cs_3C_{60} A15 phase in the sample with overall nominal composition $Rb_{0.50}Cs_{2.50}C_{60}$ (MT001_2).

	x/a	*y/b*	*z/c*	*N*	B_{Iso}(Å^2)
Cs(1)	0.25	0.5	0	0.946(7)	2.99(8)
C(1)	0	0.2967	0.0609	1	1.8(3)
C(2)	0.1210	0.0997	0.2548	1	1.8(3)
C(3)	0.0620	0.2002	0.2209	1	1.8(3)

Table 4.4: Results of the room temperature three-phase Rietveld refinement of the Rb-containing FCC phase in the sample with overall nominal composition $Rb_{0.50}Cs_{2.50}C_{60}$ (MT001_2).

	x/a	*y/b*	*z/c*	*N*	B_{Iso}(Å^2)
Cs(1)	0.25	0.25	0.25	0.520	2.18(9)
Rb(1)	0.25	0.25	0.25	0.480	2.18(9)
Cs(2)	0.5	0.5	0.5	1.0	8.9(2)
C(1)	0	0.0489	0.2460	0.5	0.3(1)
C(2)	0.2115	0.0765	0.0992	0.5	0.3(1)
C(3)	0.1716	0.1496	0.0490	0.5	0.3(1)

Table 4.5: Results of the room temperature three-phase Rietveld refinement of the Cs_4C_{60} BCO phase in the sample with overall nominal composition $Rb_{0.50}Cs_{2.50}C_{60}$ (MT001_2).

	x/a	*y/b*	*z/c*	*N*	B_{Iso}(Å^2)
Cs(1)	0.2052	0.5	0	1	2.2(1)
Cs(2)	0	0.2537	0.5	1	2.2(1)
C(1)	0	0.2871	0.0626	1	-0.4(3)
C(2)	0.0593	0	0.3012	1	-0.4(3)
C(3)	0.2928	0.0584	0	1	-0.4(3)
C(4)	0.0978	0.2503	0.1251	1	-0.4(3)
C(5)	0.1205	0.0950	0.2653	1	-0.4(3)
C(6)	0.2553	0.1171	0.1026	1	-0.4(3)
C(7)	0.1925	0.2139	0.0637	1	-0.4(3)
C(8)	0.0607	0.1922	0.2269	1	-0.4(3)
C(9)	0.2198	0.0585	0.2027	1	-0.4(3)

The refined occupancy of Cs in the A15 phase is 0.946(7), resulting in the stoichiometry $Cs_{2.84(2)}C_{60}$ (Table 4.3) and implying nearly full occupation of the cation site and an oxidation state for C_{60} close to -3. A significant fraction of the A15 phase (28.7 %) persists, signifying the increased stability of this polymorph under these reaction conditions. The sample of identical nominal stoichiometry synthesised by the ammonia route showed no A15 phase present.

Sample MT003_2 (Powder) at room temperature, model 1:

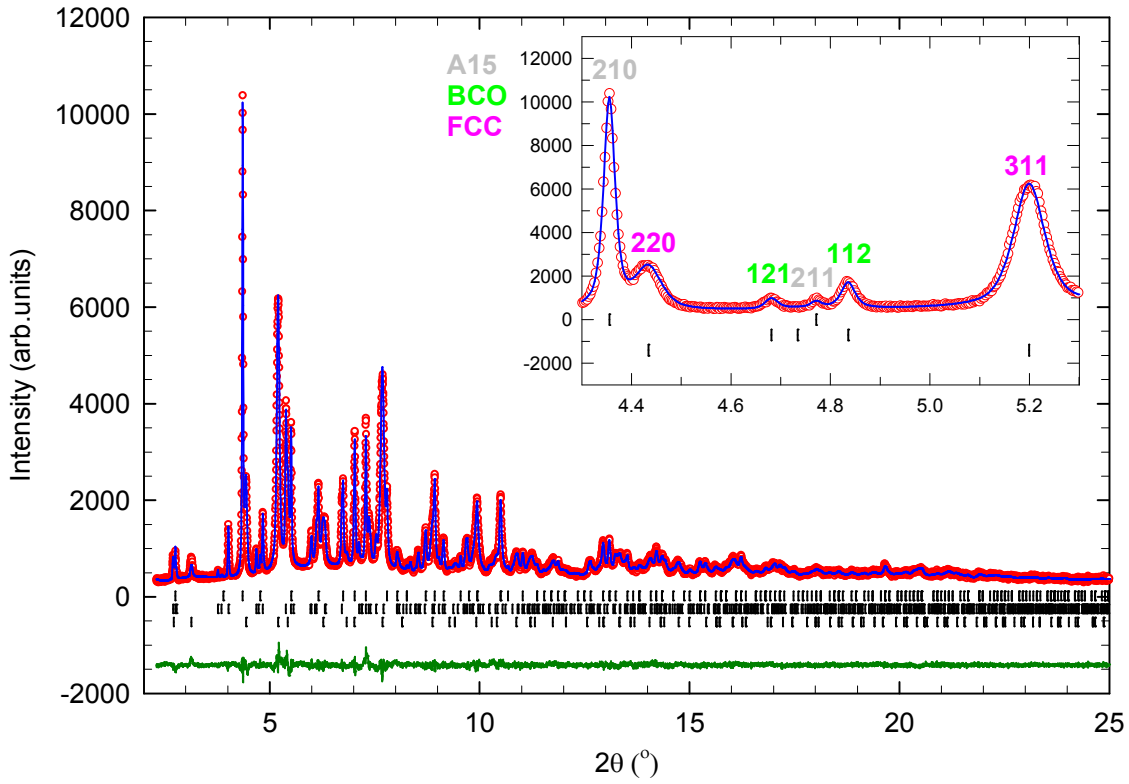

Fig 4.6: Observed (open red circles) and calculated (blue line) data of the room temperature synchrotron powder X-ray diffraction pattern for the sample with nominal composition $Rb_{0.50}Cs_{2.50}C_{60}$ (MT003_2 – Powder). The upper bars represent the positions of the Bragg reflections of the A15 phase, the middle ones of the BCO phase and the lower ones of the FCC phase. The wavelength is λ = 0.39988(4) Å.

Table 4.6: Results of the room temperature three-phase Rietveld refinement of the Cs_3C_{60} A15 phase in the sample with overall nominal composition $Rb_{0.50}Cs_{2.50}C_{60}$ (MT003_2 - Powder).

	x/a	*y/b*	*z/c*	*N*	B_{Iso}(Å^2)
Cs(1)	0.25	0.5	0	0.975(6)	3.01(6)
C(1)	0	0.2968	0.0610	1	1.3(2)
C(2)	0.1210	0.0997	0.2549	1	1.3(2)
C(3)	0.0621	0.2003	0.2209	1	1.3(2)

Table 4.7: Results of the room temperature three-phase Rietveld refinement of the Rb-containing FCC phase in the sample with overall nominal composition $Rb_{0.50}Cs_{2.50}C_{60}$ (MT003_2 - Powder).

	x/a	*y/b*	*z/c*	*N*	B_{Iso}(Å^2)
Cs(1)	0.25	0.25	0.25	0.542	2.30(8)
Rb(1)	0.25	0.25	0.25	0.458	2.30(8)
Cs(2)	0.5	0.5	0.5	1.0	9.8(2)
C(1)	0	0.0489	0.2461	0.5	0.7(1)
C(2)	0.2115	0.0765	0.0992	0.5	0.7(1)
C(3)	0.1716	0.1496	0.0490	0.5	0.7(1)

Table 4.8: Results of the room temperature three-phase Rietveld refinement of the Cs_4C_{60} BCO phase in the sample with overall nominal composition $Rb_{0.50}Cs_{2.50}C_{60}$ (MT003_2 - Powder).

	x/a	*y/b*	*z/c*	*N*	B_{Iso}(Å^2)
Cs(1)	0.2049	0.5	0	1	2.5(1)
Cs(2)	0	0.2537	0.5	1	2.5(1)
C(1)	0	0.2867	0.0626	1	-1.3(3)
C(2)	0.0592	0	0.3016	1	-1.3(3)
C(3)	0.2924	0.0584	0	1	-1.3(3)
C(4)	0.0976	0.2502	0.1252	1	-1.3(3)
C(5)	0.1203	0.0950	0.2656	1	-1.3(3)
C(6)	0.2549	0.1171	0.1027	1	-1.3(3)
C(7)	0.1923	0.2138	0.0637	1	-1.3(3)
C(8)	0.0607	0.1922	0.2272	1	-1.3(3)
C(9)	0.2196	0.0585	0.2029	1	-1.3(3)

The refined occupancy of Cs in the A15 phase is 0.975(6), resulting in the stoichiometry $Cs_{2.93(2)}C_{60}$ (Table 4.6) and implying nearly full occupation of the cation site and an oxidation state for C_{60} close to -3.

Sample MT003_3 (Pellet) at room temperature, model 1:

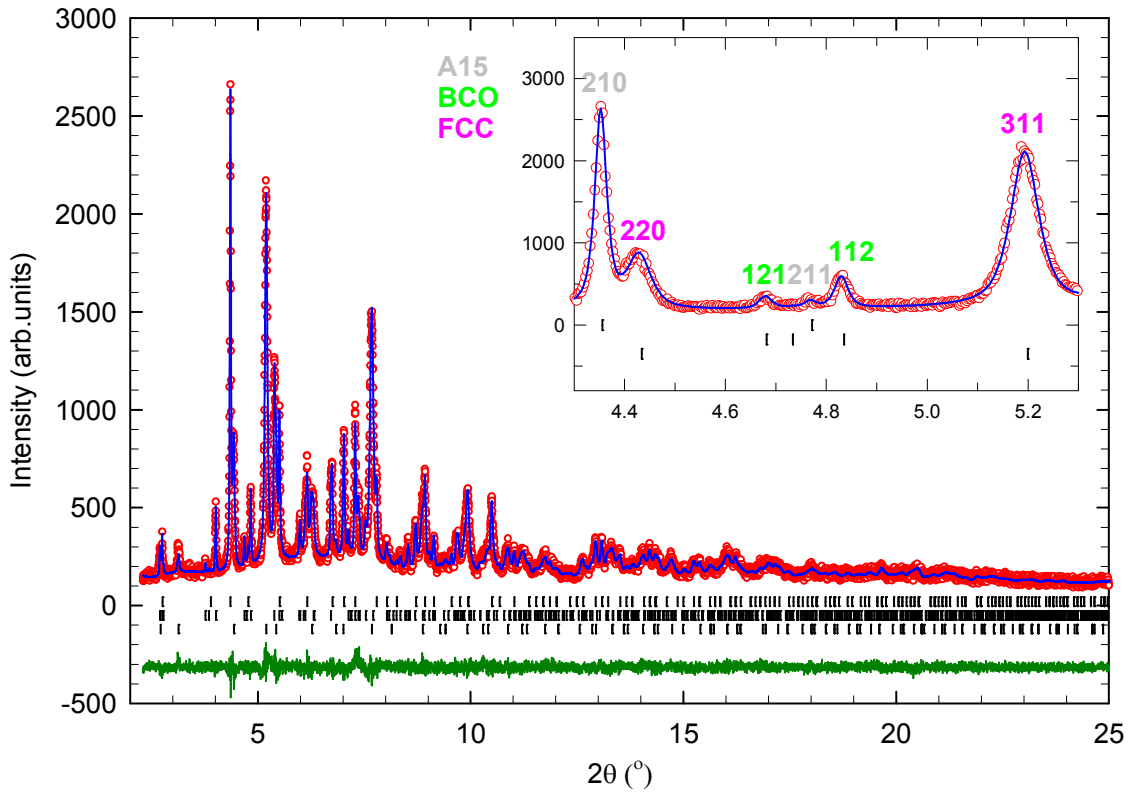

Fig 4.7: Observed (open red circles) and calculated (blue line) data of the room temperature synchrotron powder X-ray diffraction pattern for the sample with nominal composition $Rb_{0.50}Cs_{2.50}C_{60}$ (MT003_3 – pellet). The upper bars represent the positions of the Bragg reflections of the A15 phase, the middle ones of the BCO phase and the lower ones of the FCC phase. The wavelength is λ = 0.39988(4) Å.

Table 4.9: Results of the room temperature three-phase Rietveld refinement of the Cs_3C_{60} A15 phase in the sample with overall nominal composition $Rb_{0.50}Cs_{2.50}C_{60}$ (MT003_3 - Pellet).

	x/a	*y/b*	*z/c*	*N*	B_{Iso}(Å^2)
Cs(1)	0.25	0.5	0	0.974(11)	3.1(1)
C(1)	0	0.2967	0.0609	1	1.4(4)
C(2)	0.1210	0.0996	0.2547	1	1.4(4)
C(3)	0.0620	0.2002	0.2208	1	1.4(4)

Table 4.10: Results of the room temperature three-phase Rietveld refinement of the Rb-containing FCC phase in the sample with overall nominal composition $Rb_{0.50}Cs_{2.50}C_{60}$ (MT003_3 - Pellet).

	x/a	*y/b*	*z/c*	*N*	B_{Iso}(Å^2)
Cs(1)	0.25	0.25	0.25	0.559	2.0(1)
Rb(1)	0.25	0.25	0.25	0.441	2.0(1)
Cs(2)	0.5	0.5	0.5	1.0	9.3(3)
C(1)	0	0.0489	0.2458	0.5	0.3(2)
C(2)	0.2113	0.0764	0.0991	0.5	0.3(2)
C(3)	0.1715	0.1494	0.0490	0.5	0.3(2)

Table 4.11: Results of the room temperature three-phase Rietveld refinement of the Cs_4C_{60} BCO phase in the sample with overall nominal composition $Rb_{0.50}Cs_{2.50}C_{60}$ (MT003_3 - Pellet).

	x/a	*y/b*	*z/c*	*N*	B_{Iso}(Å^2)
Cs(1)	0.2051	0.5	0	1	2.3(2)
Cs(2)	0	0.2536	0.5	1	2.3(2)
C(1)	0	0.2866	0.0625	1	-1.8(4)
C(2)	0.0593	0	0.3011	1	-1.8(4)
C(3)	0.2927	0.0584	0	1	-1.8(4)
C(4)	0.0977	0.2502	0.1250	1	-1.8(4)
C(5)	0.1204	0.0949	0.2652	1	-1.8(4)
C(6)	0.2552	0.1170	0.1025	1	-1.8(4)
C(7)	0.1925	0.2137	0.0636	1	-1.8(4)
C(8)	0.0607	0.1921	0.2268	1	-1.8(4)
C(9)	0.2198	0.0585	0.2026	1	-1.8(4)

The purpose of studying this sample was to investigate whether pelletisation (closer proximity of the grains) influenced the outcome of the reactions. In comparison with the previous powder sample, the phase percentages and cell volumes are very similar signifying the reproducibility of the results and low influence of pelletisation on the reaction outcome. The refined occupancy of Cs in the A15 phase is 0.974(11), resulting in the stoichiometry $Cs_{2.92(3)}C_{60}$ (Table 4.9) and implying nearly full occupation of the cation site and an oxidation state for C_{60} close to -3. In comparison with the previous sample there is only a small shift in phase composition and cell volumes.

Sample MT005_1 at room temperature, model 1:

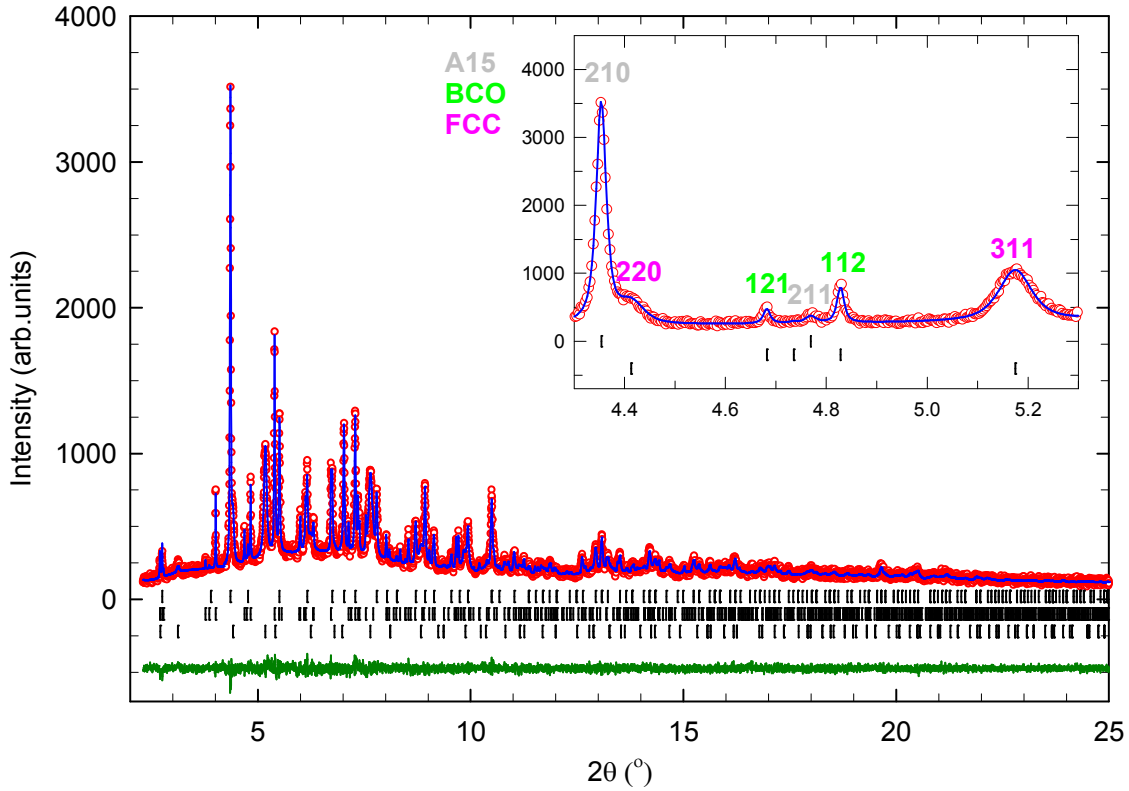

Fig 4.8: Observed (open red circles) and calculated (blue line) data of the room temperature synchrotron powder X-ray diffraction pattern for the sample with nominal composition $Rb_{0.25}Cs_{2.75}C_{60}$. The upper bars represent the positions of the Bragg reflections of the A15 phase, the middle ones of the BCO phase and the lower ones of the FCC phase. The wavelength is λ = 0.39988(4) Å.

Table 4.12: Results of the room temperature three-phase Rietveld refinement of the Cs_3C_{60} A15 phase in the sample with overall nominal composition $Rb_{0.25}Cs_{2.75}C_{60}$ (MT005_1).

	x/a	*y/b*	*z/c*	*N*	B_{Iso}(Å^2)
Cs(1)	0.25	0.5	0	0.974(9)	2.94(9)
C(1)	0	0.2966	0.0609	1	1.3(3)
C(2)	0.1210	0.0996	0.2547	1	1.3(3)
C(3)	0.0620	0.2002	0.2208	1	1.3(3)

Table 4.13: Results of the room temperature three-phase Rietveld refinement of the Rb-containing FCC phase in the sample with overall nominal composition $Rb_{0.25}Cs_{2.75}C_{60}$ (MT005_1).

	x/a	*y/b*	*z/c*	*N*	B_{Iso}(Å^2)
Cs(1)	0.25	0.25	0.25	0.672	2.2(2)
Rb(1)	0.25	0.25	0.25	0.328	2.2(2)
Cs(2)	0.5	0.5	0.5	1.0	11.8(6)
C(1)	0	0.0487	0.2449	0.5	-0.3(4)
C(2)	0.2105	0.0761	0.0987	0.5	-0.3(4)
C(3)	0.1708	0.1489	0.0488	0.5	-0.3(4)

Table 4.14: Results of the room temperature three-phase Rietveld refinement of the Cs_4C_{60} BCO phase in the sample with overall nominal composition $Rb_{0.25}Cs_{2.75}C_{60}$ (MT005_1).

	x/a	*y/b*	*z/c*	*N*	B_{Iso}(Å^2)
Cs(1)	0.2051	0.5	0	1	2.2(2)
Cs(2)	0	0.2539	0.5	1	2.2(2)
C(1)	0	0.2869	0.0624	1	-0.4(4)
C(2)	0.0593	0	0.3008	1	-0.4(4)
C(3)	0.2927	0.0584	0	1	-0.4(4)
C(4)	0.0977	0.2504	0.1249	1	-0.4(4)
C(5)	0.1204	0.0950	0.2649	1	-0.4(4)
C(6)	0.2552	0.1171	0.1024	1	-0.4(4)
C(7)	0.1925	0.2137	0.0636	1	-0.4(4)
C(8)	0.0607	0.1923	0.2267	1	-0.4(4)
C(9)	0.2198	0.0585	0.2024	1	-0.4(4)

Like for the samples produced where NH_3 was used as the solvent, reducing the nominal Rb doping level increases the amount of the A15 phase and consequently reduces the amount of the FCC phase. Additionally, comparing the cell volume and Cs content of the A15 phase, there is little variation between this sample (*vol* = 1633.45(8) Å^3 Cs = 0.974(9)) and the previous one (*vol* = 1633.41(6) Å^3 Cs = 0.975(6)). Therefore it is logical to infer at this stage that Rb is difficult to intercalate controllably into the A15 structure.

Sample MT011_3 at room temperature, model 1:

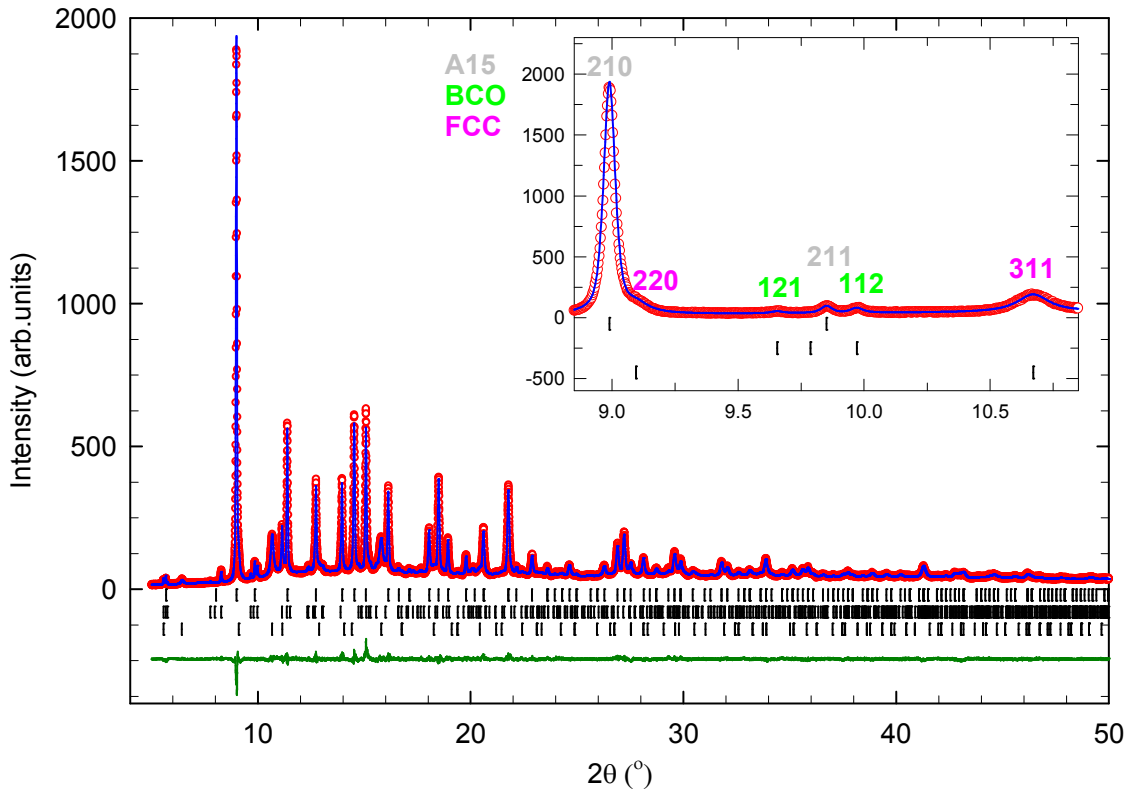

Fig 4.9: Observed (open red circles) and calculated (blue line) data of the room temperature synchrotron powder X-ray diffraction pattern for the sample with nominal composition $Rb_{0.12}Cs_{2.88}C_{60}$. The upper bars represent the positions of the Bragg reflections of the A15 phase, the middle ones of the BCO phase and the lower ones of the FCC phase. The wavelength is λ = 0.826028(1) Å.

Table 4.15: Results of the room temperature three-phase Rietveld refinement of the Cs_3C_{60} A15 phase in the sample with overall nominal composition $Rb_{0.12}Cs_{2.88}C_{60}$ (MT011_3).

	x/a	*y/b*	*z/c*	*N*	B_{Iso}(Å^2)
Cs(1)	0.25	0.5	0	0.920(2)	2.68(2)
C(1)	0	0.2967	0.0610	1	2.29(8)
C(2)	0.1210	0.0997	0.2548	1	2.29(8)
C(3)	0.0621	0.2003	0.2209	1	2.29(8)

Table 4.16: Results of the room temperature three-phase Rietveld refinement of the Rb containing FCC phase in the sample with overall nominal composition $Rb_{0.12}Cs_{2.88}C_{60}$ (MT011_3).

	x/a	*y/b*	*z/c*	*N*	B_{Iso}(Å^2)
Cs(1)	0.25	0.25	0.25	0.699	2.6(2)
Rb(1)	0.25	0.25	0.25	0.301	2.6(2)
Cs(2)	0.5	0.5	0.5	1.0	13.9(4)
C(1)	0	0.0486	0.2445	0.5	2.2(3)
C(2)	0.2102	0.0760	0.0986	0.5	2.2(3)
C(3)	0.1706	0.1487	0.0487	0.5	2.2(3)

Table 4.17: Results of the room temperature three-phase Rietveld refinement of the Cs_4C_{60} BCO phase in the sample with overall nominal composition $Rb_{0.12}Cs_{2.88}C_{60}$ (MT011_3).

	x/a	*y/b*	*z/c*	*N*	B_{Iso}(Å^2)
Cs(1)	0.2055	0.5	0	1	3.2(2)
Cs(2)	0	0.2533	0.5	1	3.2(2)
C(1)	0	0.2862	0.0625	1	1.1(6)
C(2)	0.0594	0	0.3009	1	1.1(6)
C(3)	0.2933	0.0583	0	1	1.1(6)
C(4)	0.0979	0.2498	0.1249	1	1.1(6)
C(5)	0.1207	0.0948	0.2650	1	1.1(6)
C(6)	0.2557	0.1168	0.1025	1	1.1(6)
C(7)	0.1929	0.2135	0.0636	1	1.1(6)
C(8)	0.0608	0.1918	0.2267	1	1.1(6)
C(9)	0.2202	0.0584	0.2024	1	1.1(6)

The refined occupancy of Cs in the A15 component is 0.920(2), resulting in the stoichiometry $Cs_{2.760(6)}C_{6,}$ (Table 4.15) this is lower than results of previous refinements suggesting either con-intercalation of Rb into the T_d cavity or partial occupancy. Again the cell volume of the A15 phase appears invariant to increased Rb doping levels; however, the response of the FCC phase is much more sensitive. Additionally the phase composition of the sample reveals that 70.4(1) % of the majority A15 phase is present, while the amount of the BCO phase is reduced significantly to 7.9(1) %.

Sample MT012_3 at room temperature, model 1:

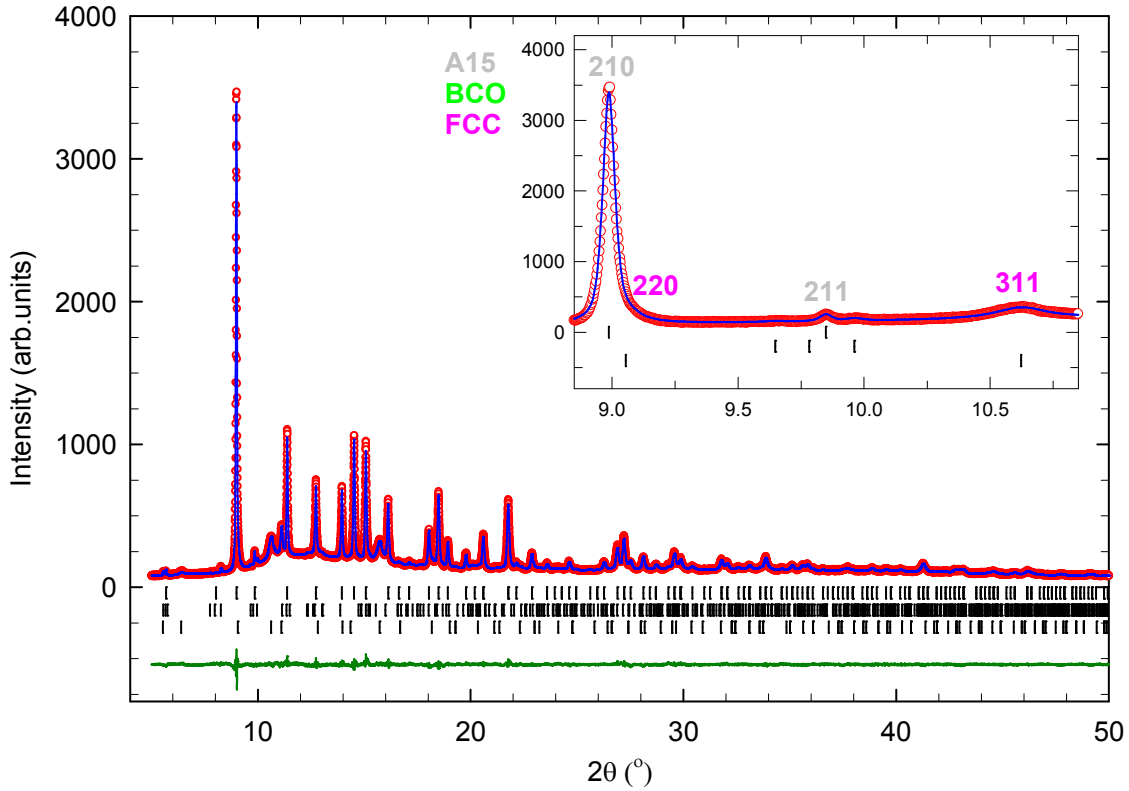

Fig 4.10: Observed (open red circles) and calculated (blue line) data of the room temperature synchrotron powder X-ray diffraction pattern for the sample with nominal composition Cs_3C_{60}. The upper bars represent the positions of the Bragg reflections of the A15 phase, the middle ones of the BCO phase and the lower ones of the FCC phase. The wavelength is λ = 0.826028(1) Å.

Table 4.18: Results of the room temperature three-phase Rietveld refinement of the Cs_3C_{60} A15 phase in the sample with overall nominal composition Cs_3C_{60} (MT012_3).

	x/a	*y/b*	*z/c*	*N*	B_{Iso}(Å^2)
Cs(1)	0.25	0.5	0	0.964(2)	2.93(2)
C(1)	0	0.2967	0.0609	1	1.42(7)
C(2)	0.1210	0.0997	0.2547	1	1.42(7)
C(3)	0.0620	0.2002	0.2208	1	1.42(7)

Table 4.19: Results of the room temperature three-phase Rietveld refinement of the Cs_3C_{60} FCC phase in the sample with overall nominal composition Cs_3C_{60} (MT012_3).

	x/a	*y/b*	*z/c*	*N*	B_{Iso}(Å^2)
Cs(1)	0.25	0.25	0.25	1.0	3.0(2)
Cs(2)	0.5	0.5	0.5	1.0	16.7(5)
C(1)	0	0.0484	0.2434	0.5	-2.6(2)
C(2)	0.2092	0.0756	0.0982	0.5	-2.6(2)
C(3)	0.1698	0.1480	0.0485	0.5	-2.6(2)

Table 4.20: Results of the room temperature three-phase Rietveld refinement of the Cs_4C_{60} BCO phase in the sample with overall nominal composition Cs_3C_{60} (MT012_3).

	x/a	*y/b*	*z/c*	*N*	B_{Iso}(Å^2)
Cs(1)	0.2052	0.5	0	1	2.9(4)
Cs(2)	0	0.2532	0.5	1	2.9(4)
C(1)	0	0.2861	0.0624	1	-2.6(7)
C(2)	0.0593	0	0.3005	1	-2.6(7)
C(3)	0.2928	0.0583	0	1	-2.6(7)
C(4)	0.0978	0.2497	0.1248	1	-2.6(7)
C(5)	0.1205	0.0948	0.2646	1	-2.6(7)
C(6)	0.2553	0.1168	0.1023	1	-2.6(7)
C(7)	0.1925	0.2134	0.0635	1	-2.6(7)
C(8)	0.0607	0.1917	0.2264	1	-2.6(7)
C(9)	0.2198	0.0584	0.2021	1	-2.6(7)

The refined occupancy of Cs in the A15 phase is 0.964(2), resulting in the stoichiometry $Cs_{2.892(6)}C_{60}$ and implying nearly full occupation of the cation site and an oxidation state for C_{60} close to -3. This final sample in the series has a nearly identical phase composition to that of the previous sample (nominal stoichiometry $Rb_{0.12}Cs_{2.88}C_{60}$) in which a very small amount of Rb was used in the synthesis. There is however a significant difference in the composition and cell volume of the FCC phases. The previous sample has FCC stoichiometry and cell volume of $Rb_{0.60}Cs_{2.40}C_{60}$ and *vol* =

3189.2(3) Å^3, respectively, while for the current Cs_3C_{60} sample a unit cell volume of 3232.7(4) Å^3 is found. This huge variation in the volume of the minority phase reinforces the conjecture that Rb enters principally the FCC structure.

4.4.2 Summary – structural properties of the A15 $Rb_xCs_{3-x}C_{60}$ series at room temperature (refinement model 1)

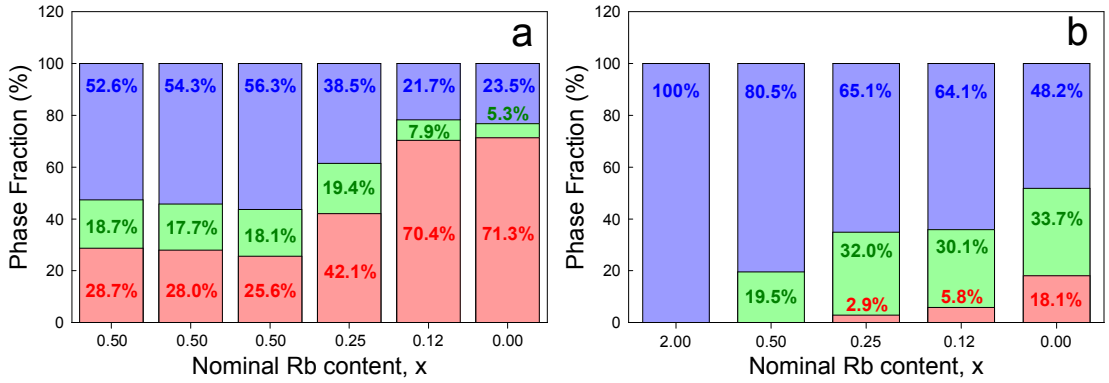

Fig 4.11: Room temperature variation of the fractions of the three polymorphs for the series of samples, $Rb_xCs_{3-x}C_{60}$ (**a**) when methylamine is used as the solvent, and (**b**) where ammonia is used as the solvent. Red filling represents the A15, green the BCO and blue the FCC phase.

Samples MT001_2, MT003_2, MT003_3, MT005_1, MT011_3, and MT012_3 were synthesised using low temperature solution-based reaction techniques, involving $MeNH_2$ as the solvent. Compared to the corresponding NH_3-produced samples, the reactions conditions were comparable except for the annealing temperatures and times. The NH_3-produced samples were annealed at elevated (400^{o}C) temperatures for long periods of time (14 days), whereas cooler temperatures (180^{o}C) and much shorter annealing times (48 hours) were employed for the samples produced when the solvent was $MeNH_2$. These differing reaction conditions lead to differences in the resulting assemblage constitution between samples of the same starting stoichiometry. The first noticeable difference is the crystallinity of the FCC phase - the lower annealing

temperatures lead to reduced crystallinity. This is evident by the broader diffraction peaks observed for the FCC phase.

Both solution-based methods were found to lead to a relatively constant amount of the BCO phase. However, there is an obvious variation in the phase percentage of the A15 and FCC components – at high Rb doping levels, the FCC phase is the major faction (52.6 %); however, as the amount of Cs increases and the parent material Cs_3C_{60} is created, the A15 phase fraction dominates and becomes significant at 71.3 %. These trends are summarised in Fig 4.11. It can be seen that two sets of multiphase materials were successfully synthesised, one rich in the A15 phase and the other rich in the FCC phase. Although a variety of structural models were attempted in the course of the refinements, the observed trends in the volume fractions (Fig 4.12) and the unit cell volume (Fig 4.13) were robust throughout.

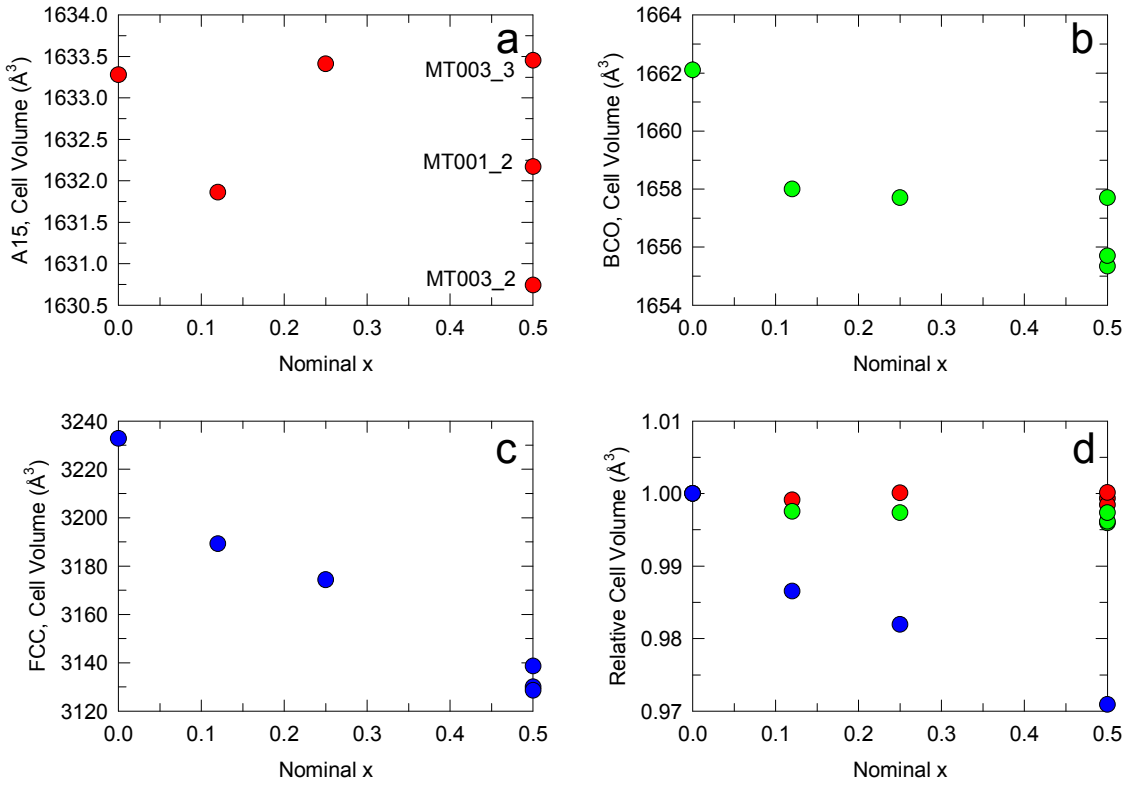

Fig 4.12: Changes in unit cell volume with nominal Rb content, *x* in the $Rb_xCs_{3-x}C_{60}$ series. Panels **a** , **b**, **c** show the corresponding evolution for the A15, BCO, and FCC phase, respectively. Panel **d** depicts the

evolution of normalised unit cell volume for all three phases. (error bars included, but smaller than points).

The unit cell volumes obtained in the final sets of refinements are shown in Fig 4.12, noting that their values are very similar to those obtained in the refinements detailed in section 3. It is immediately apparent that for the BCO and A15 phases, there is little variation; V/C_{60} is unaffected by the Rb doping level and there is no strong evidence for solid solution formation as the starting Rb content varies. Conversely, the unit cell volume of the FCC phase is very sensitive to the Rb doping level *x* and decreases monotonically with increasing *x*, implying the formation of a solid $Rb_xCs_{3-x}C_{60}$ solution and obeying Vegard's law. Due to the small contribution of the BCO phase to each assemblage, the cation occupancy was fixed to be entirely Cs at 1.0.

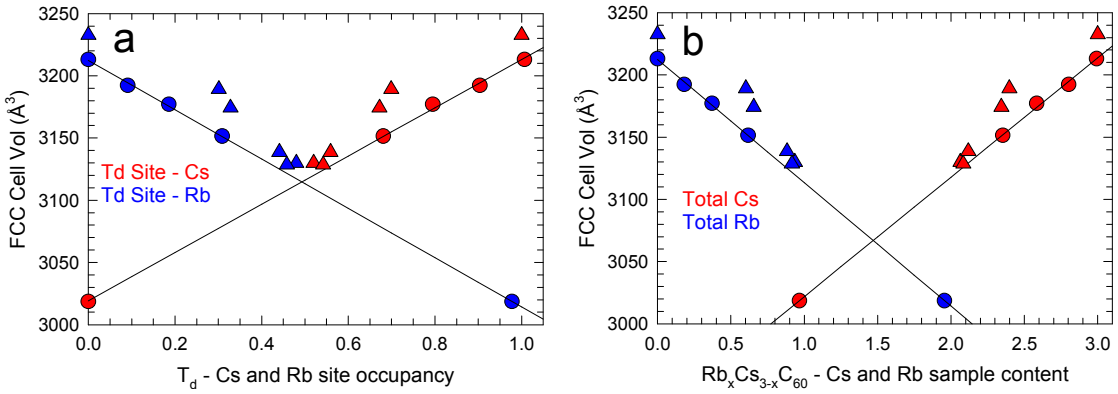

Fig 4.13: Refined unit cell volume of the minority FCC $Rb_xCs_{3-x}C_{60}$ phases as a function of the site occupancy of the T_d sites by Cs and Rb (**a**) and as a function of the total Cs and Rb content (**b**). Blue shapes symbolise the Rb^+ cation, red shapes the Cs^+ cation. Circles represent the FCC results from the FCC-rich $Rb_xCs_{3-x}C_{60}$ samples (chapter 3); triangles represent the FCC results from the A15-rich $Rb_xCs_{3-x}C_{60}$ samples (current chapter). Guide-for-the-eye lines are included for the FCC-rich samples. (error bars included, but smaller than points).

Given the relative sizes of the tetrahedral and octahedral interstices in an FCC fullerene sublattice, the cell metrics are determined sensitively by the size of the

cations residing in the T_d holes. This is clearly evident in Fig 4.13 where a quasi-linear dependence of the unit cell volume on the relative cationic occupancy of the T_d site by Rb and Cs is observed; however, this model appears to be overestimating the amount of Rb present in the FCC phase, suggesting that some co-doping may also exist in the majority A15 phase. This will be the main subject to address in the subsequent parts of this chapter as the model is expanded to test for incorporation of Rb^+ into the distorted tetrahedral site of the A15 phase.

4.4.3 $Rb_xCs_{3-x}C_{60}$ – Refinement model 2

When examining the structural analysis results detailed before, there is one question that immediately arises - should a systematic large lattice reduction for the A15 phase be observed, similar to that unambiguously seen for the FCC phase, if Rb^+ (r = 1.52 Å)[7] is co-intercalated to partially replace Cs^+ (r = 1.67 Å) in the distorted tetrahedral interstices? The radius of C_{60} (r = 5.01 Å) can be used to calculate the tetrahedral cavity size of the BCC structure. For BCC-structured C_{60} (a = 11.75 Å), the cavity size can be calculated as 1.46 Å. This implies that in contrast to what is encountered for the very small tetrahedral holes of FCC-structured C_{60}, Rb^+ fits almost perfectly in size within the A15 available holes. If the lattice constant of FCC Cs_3C_{60} is considered, as the size of Cs^+ is larger than the hole size, the lattice has expanded and the lattice constant is approximately 11.78 Å. Therefore the size of the available interstitial hole is now 1.58 Å, exceeding the magnitude of the Rb ionic radius. These simple calculations imply that the huge dependence of the FCC lattice constant on the amount of Rb content is not necessarily expected to be observed for the A15-structured materials. Therefore can the refinement model be modified to search for accommodation of Rb in the A15 phase?

Difficulties arise when trying to adapt the structural model to incorporate Rb in the A15 phase. The Rb distribution in the overall assemblage cannot accurately be determined, because of the accompanying partial occupancy of the poorly crystalline

FCC phase. The best solution is to attempt to modify the model and see how chemically plausible the results appear.

The earlier results from refinement model 1 imply that the amount of Rb in the FCC phase may have been overestimated. Since the FFC is poorly crystalline and a minority phase, accurate and robust refinement results of the cation occupancies cannot be expected. Therefore an approximation was introduced, by fixing the occupancies in the FCC model. Then the fractional occupancy, N, of the cation site in the A15 structure was fixed at 1.0, while the Cs(1):Rb(2) occupancy ratio of this site was allowed to vary. The remaining Rb was calculated and then added to the T_d site of the FCC phase. Therefore probing the A15 phase for the Rb dopant.

4.4.4 $Rb_xCs_{3-x}C_{60}$ ($0.0 < x \leq 0.5$) at room temperature, model 2

Refined parameters for the majority A15 (space group $Pm\bar{3}n$), minority FCC (space group $Fm\bar{3}m$) and minority BCO (space group *Immm*) phases are shown below in the tables within this subsection. First there is an overall summary, Table 4.21, showing key refinement parameters and results, and then each sample is given a more detailed description. For all structural analyses (samples MT001_2, MT003_2, MT003_3, MT005_1, MT011_3, and MT012_3), three-phase Rietveld refinements of the synchrotron X-ray powder diffraction data at ambient temperature were undertaken.

For the A15 phase, the fractional occupancies, *N*, of the Cs(1) and Rb(1) atoms were allowed to vary; however, the total occupancy of the cation site was fixed at 1.0. The remaining Rb doped into the sample was placed entirely into the T_d site of the minority FCC phase. Due to the broadness of the FCC diffraction peaks, the occupancies of the two non-equivalent cation sites were not refined. The cation stoichiometry for the minority BCO phase was also kept fixed, at Cs_4C_{60}. The phase fractions of each phase are also given.

Table 4.21: Results of the Rietveld refinements of the series $Rb_xCs_{3-x}C_{60}$ ($0.0 \leq x \leq 0.5$) at room temperature, Model 2

Parameter	*MT001_2*	*MT003_2*	*MT003_3*	*MT005_1*	*MT011_3*
Nominal x	0.50	0.50	0.50	0.25	0.12
R_{wp} (%)	5.11	4.76	6.75	6.63	4.57
R_{exp} (%)	4.20	3.75	6.37	6.37	2.10
χ^2	1.103	1.127	1.029	1.020	1.475
λ (Å)	0.39988(4)	0.39988(4)	0.39988(4)	0.39988(4)	0.826028(1)
A15 (%)	28.9(3)	28.0(3)	25.5(4)	42.7(5)	70.9(1)
BCO (%)	18.9(1)	18.2(1)	18.2(2)	19.9(2)	8.0(1)
FCC (%)	52.2(1)	53.9(1)	56.3(1)	37.4(3)	21.1(1)
A15 *a* (Å)	11.7738(1)	11.7705(1)	11.7769(5)	11.7769(1)	11.7731(1)
A15 *V* (Å^3)	1632.10(5)	1630.73(4)	1633.4(2)	1633.41(6)	1631.82(4)
BCO cell (Å)	*a* = 11.8923(7) *b* = 12.1763(6) *c* = 11.4308(4)	*a* = 11.9058(8) *b* = 12.1789(6) *c* = 11.4183(5)	*a* = 11.895(1) *b* = 12.184(1) *c* = 11.4375(9)	*a* = 11.8953(7) *b* = 12.1730(5) *c* = 11.4478(4)	*a* = 11.871(1) *b* = 12.203(1) *c* = 11.4453(7)
BCO *V* (Å^3)	1655.24(9)	1655.7(1)	1657.6(3)	1657.67(8)	1658.0(2)
FCC *a* (Å)	14.6278(3)	14.6258(3)	14.6411(7)	14.6968(7)	14.7203(5)
FCC *V* (Å^3)	3130.0(2)	3128.6(2)	3138.5(4)	3174.5(5)	3189.7(3)
Refined A15 stoichiometry	$Rb_{0.55(7)}Cs_{2.45(7)}C_{60}$	$Rb_{0.22(6)}Cs_{2.78(6)}C_{60}$	$Rb_{0.3(1)}Cs_{2.7(1)}C_{60}$	$Rb_{0.29(9)}Cs_{2.71(9)}C_{60}$	$Rb_{0.39(2)}Cs_{2.61(2)}C_{60}$
Fixed FCC stoichiometry	$Rb_{0.67}Cs_{2.33}C_{60}$	$Rb_{0.80}Cs_{2.20}C_{60}$	$Rb_{0.77}Cs_{2.23}C_{60}$	$Rb_{0.34}Cs_{2.68}C_{60}$	Cs_3C_{60}

Sample MT001_2 at room temperature, model 2:

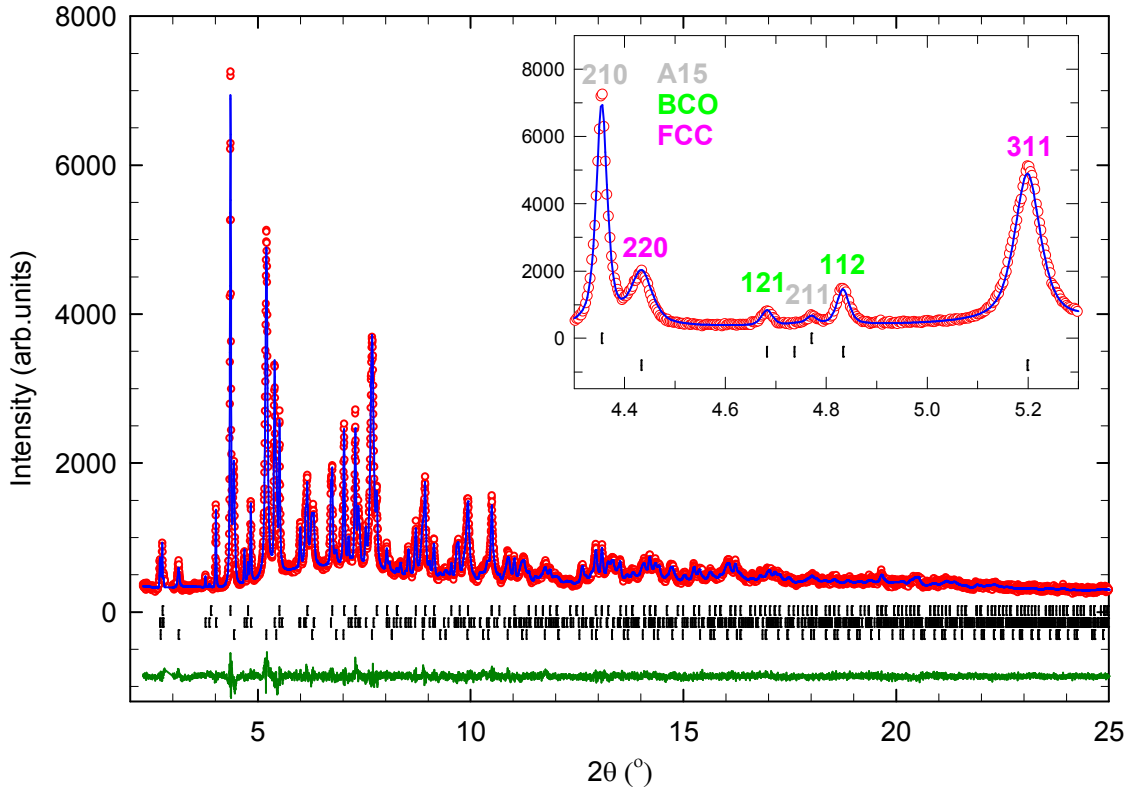

Fig 4.14: Observed (open red circles) and calculated (blue line) data of the room temperature synchrotron powder X-ray diffraction pattern for the sample with nominal composition $Rb_{0.50}Cs_{2.50}C_{60}$ (MT001_2). The upper bars represent the positions of the Bragg reflections of the A15 phase, the middle ones of the BCO phase and the lower ones of the FCC phase. The wavelength is λ = 0.39988(4) Å.

Table 4.22: Results of the room temperature three-phase Rietveld refinement of the Rb-containing A15 phase in the sample with overall nominal composition $Rb_{0.50}Cs_{2.50}C_{60}$ (MT001_2).

	x/a	*y/b*	*z/c*	*N*	B_{Iso}(Å^2)
Cs(1)	0.25	0.5	0	0.816(23)	2.94(8)
Rb(1)	0.25	0.5	0	0.184(23)	2.94(8)
C(1)	0	0.2967	0.0609	1	1.8(3)
C(2)	0.1210	0.0997	0.2548	1	1.8(3)
C(3)	0.0620	0.2002	0.2209	1	1.8(3)

Table 4.23: Results of the room temperature three-phase Rietveld refinement of the Rb-containing FCC phase in the sample with overall nominal composition $Rb_{0.50}Cs_{2.50}C_{60}$ (MT001_2).

	x/a	*y/b*	*z/c*	*N*	B_{Iso}(Å^2)
Cs(1)	0.25	0.25	0.25	0.667	2.9(1)
Rb(1)	0.25	0.25	0.25	0.333	2.9(1)
Cs(2)	0.5	0.5	0.5	1.0	8.4(2)
C(1)	0	0.0489	0.2460	0.5	-0.6(1)
C(2)	0.2115	0.0765	0.0992	0.5	-0.6(1)
C(3)	0.1716	0.1496	0.0490	0.5	-0.6(1)

Table 4.24: Results of the room temperature three-phase Rietveld refinement of the Cs_4C_{60} BCO phase in the sample with overall nominal composition $Rb_{0.50}Cs_{2.50}C_{60}$ (MT001_2).

	x/a	*y/b*	*z/c*	*N*	B_{Iso}(Å^2)
Cs(1)	0.2052	0.5	0	1	2.1(1)
Cs(2)	0	0.2538	0.5	1	2.1(1)
C(1)	0	0.2868	0.0625	1	-0.5(3)
C(2)	0.0593	0	0.3012	1	-0.5(3)
C(3)	0.2928	0.0584	0	1	-0.5(3)
C(4)	0.0978	0.2503	0.1251	1	-0.5(3)
C(5)	0.1204	0.0950	0.2653	1	-0.5(3)
C(6)	0.2552	0.1171	0.1026	1	-0.5(3)
C(7)	0.1925	0.2139	0.0636	1	-0.5(3)
C(8)	0.0607	0.1922	0.2270	1	-0.5(3)
C(9)	0.2198	0.0585	0.2027	1	-0.5(3)

The refined occupancy of Cs and Rb in the A15 phase is Cs = 0.816(23) and Rb = 0.184(23) (Table 4.22), resulting in stoichiometries of $Rb_{0.55(7)}Cs_{2.45(7)}C_{60}$ (A15) and $Rb_{0.67}Cs_{2.33}C_{60}$ (FCC). The accuracy of the model cannot be determined form the first refinement; however, from the results there appears to be Rb intercalated in the A15 phase and still a significant amount in the FCC phase.

Sample MT003_2 (powder) at room temperature, model 2:

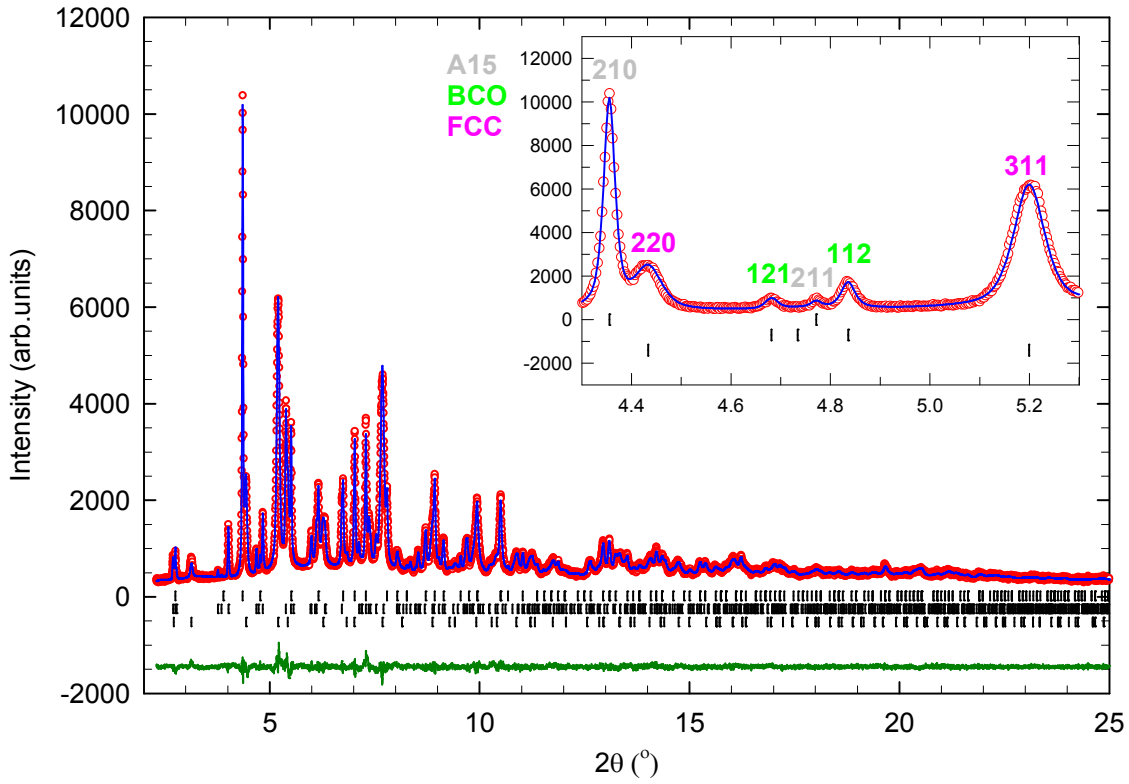

Fig 4.15: Observed (open red circles) and calculated model (blue line) data of the room temperature synchrotron powder X-ray diffraction pattern for the sample with nominal composition $Rb_{0.50}Cs_{2.50}C_{60}$ (MT003_2 - Powder). The upper bars represent the positions of the Bragg reflections of the A15 phase, the middle ones of the BCO phase and the lower ones of the FCC phase. The wavelength is λ = 0.39988(4) Å.

Table 4.25: Results of the room temperature three-phase Rietveld refinement of the Rb-containing A15 phase in the sample with overall nominal composition $Rb_{0.50}Cs_{2.50}C_{60}$ (MT003_2 - Powder).

	x/a	*y/b*	*z/c*	*N*	B_{Iso}(Å^2)
Cs(1)	0.25	0.5	0	0.928(21)	2.96(5)
Rb(1)	0.25	0.5	0	0.072(21)	2.96(5)
C(1)	0	0.2968	0.0610	1	1.2(2)
C(2)	0.1210	0.0997	0.2549	1	1.2(2)
C(3)	0.0621	0.2003	0.2209	1	1.2(2)

Table 4.26: Results of the room temperature three-phase Rietveld refinement of the Rb-containing FCC phase in the sample with overall nominal composition $Rb_{0.50}Cs_{2.50}C_{60}$ (MT003_2 - Powder).

	x/a	*y/b*	*z/c*	*N*	B_{Iso}(Å^2)
Cs(1)	0.25	0.25	0.25	0.598	2.55(8)
Rb(1)	0.25	0.25	0.25	0.402	2.55(8)
Cs(2)	0.5	0.5	0.5	1.0	9.5(2)
C(1)	0	0.0489	0.2461	0.5	0.6(1)
C(2)	0.2115	0.0765	0.0992	0.5	0.6(1)
C(3)	0.1716	0.1496	0.0490	0.5	0.6(1)

Table 4.27: Results of the room temperature three-phase Rietveld refinement of the Cs_4C_{60} BCO phase in the sample with overall nominal composition $Rb_{0.50}Cs_{2.50}C_{60}$ (MT003_2 - Powder).

	x/a	*y/b*	*z/c*	*N*	B_{Iso}(Å^2)
Cs(1)	0.2049	0.5	0	1	2.5(1)
Cs(2)	0	0.2537	0.5	1	2.5(1)
C(1)	0	0.2867	0.0626	1	-1.2(3)
C(2)	0.0593	0	0.3016	1	-1.2(3)
C(3)	0.2924	0.0584	0	1	-1.2(3)
C(4)	0.0976	0.2502	0.1252	1	-1.2(3)
C(5)	0.1203	0.0950	0.2656	1	-1.2(3)
C(6)	0.2550	0.1171	0.1027	1	-1.2(3)
C(7)	0.1923	0.2139	0.0637	1	-1.2(3)
C(8)	0.0607	0.1922	0.2272	1	-1.2(3)
C(9)	0.2196	0.0585	0.2029	1	-1.2(3)

In comparison to sample MT001_2 (nominal stoichiometry, $Rb_{0.50}Cs_{2.50}C_{60}$), a big variation is observed; there appears to be half the amount of Rb intercalated into the A15 phase, MT001_2: Rb(1) = 0.184(23) and MT003_2: Rb(1) = 0.072. It is unclear if this is a "real effect" as the model does not account for the existence of partial occupancies in the cation site, which could severely affect the results.

Sample MT003_3 (pellet) at room temperature, model 2:

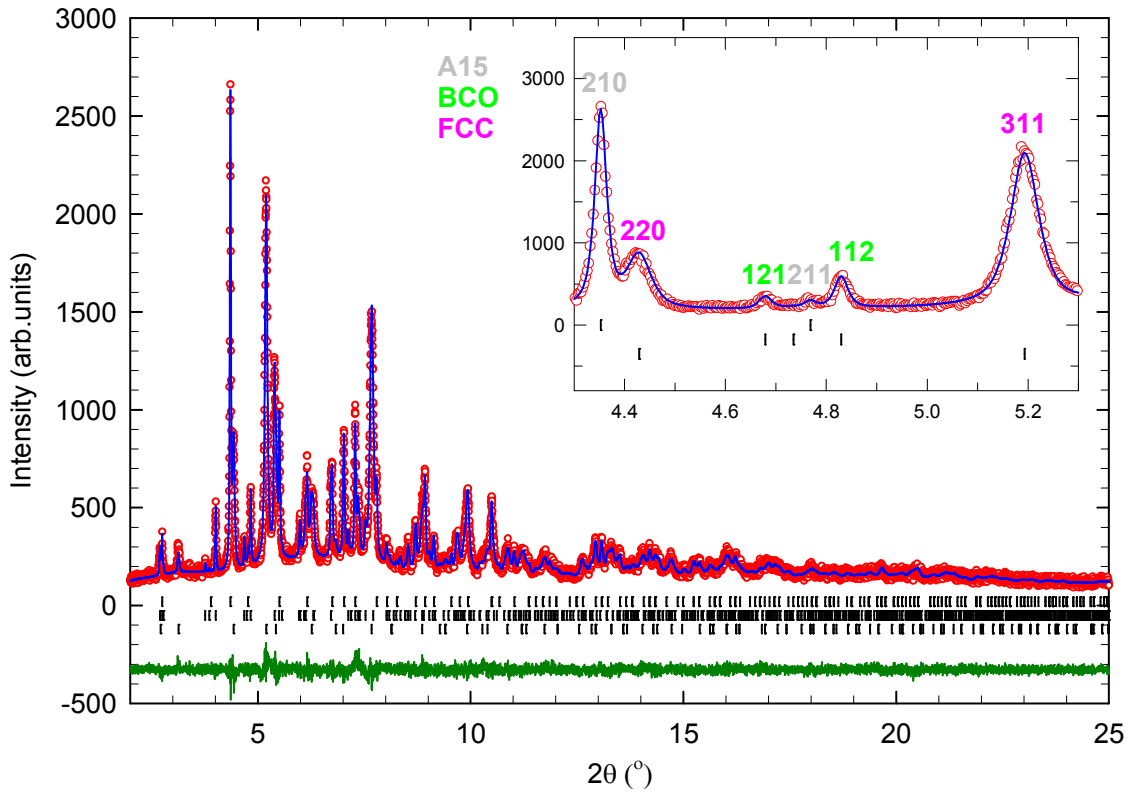

Fig 4.16: Observed (open red circles) and calculated model (blue line) data of the room temperature synchrotron powder X-ray diffraction pattern for the sample with nominal composition $Rb_{0.50}Cs_{2.50}C_{60}$ (MT003_3 - Pellet). The upper bars represent the positions of the Bragg reflections of the A15 phase, the middle ones of the BCO phase and the lower ones of the FCC phase. The wavelength is λ = 0.39988(4) Å.

Table 4.28: Results of the room temperature three-phase Rietveld refinement of the Rb containing A15 phase in the sample with overall nominal composition $Rb_{0.50}Cs_{2.50}C_{60}$ (MT003_3 - Pellet).

	x/a	*y/b*	*z/c*	*N*	B_{Iso}(Å^2)
Cs(1)	0.25	0.5	0	0.911(37)	3.1(1)
Rb(1)	0.25	0.5	0	0.089(37)	3.1(1)
C(1)	0	0.2966	0.0609	1	1.4(4)
C(2)	0.1210	0.0996	0.2547	1	1.4(4)
C(3)	0.0620	0.2002	0.2208	1	1.4(4)

Table 4.29: Results of the room temperature three-phase Rietveld refinement of the Rb containing FCC phase in the sample with overall nominal composition $Rb_{0.50}Cs_{2.50}C_{60}$ (MT003_3 - Pellet).

	x/a	*y/b*	*z/c*	*N*	B_{Iso}(Å^2)
Cs(1)	0.25	0.25	0.25	0.617	2.3(1)
Rb(1)	0.25	0.25	0.25	0.383	2.3(1)
Cs(2)	0.5	0.5	0.5	1.0	9.1(3)
C(1)	0	0.0489	0.2458	0.5	0.3(2)
C(2)	0.2113	0.0764	0.0991	0.5	0.3(2)
C(3)	0.1715	0.1494	0.0490	0.5	0.3(2)

Table 4.30: Results of the room temperature three-phase Rietveld refinement of the Cs_4C_{60} BCO phase in the sample with overall nominal composition $Rb_{0.50}Cs_{2.50}C_{60}$ (MT003_3 - Pellet).

	x/a	*y/b*	*z/c*	*N*	B_{Iso}(Å^2)
Cs(1)	0.2051	0.5	0	1	2.3(2)
Cs(2)	0	0.2536	0.5	1	2.3(2)
C(1)	0	0.2866	0.0625	1	-1.8(4)
C(2)	0.0593	0	0.3011	1	-1.8(4)
C(3)	0.2927	0.0584	0	1	-1.8(4)
C(4)	0.0977	0.2502	0.1250	1	-1.8(4)
C(5)	0.1204	0.0949	0.2652	1	-1.8(4)
C(6)	0.2552	0.1170	0.1025	1	-1.8(4)
C(7)	0.1925	0.2138	0.0636	1	-1.8(4)
C(8)	0.0607	0.1921	0.2268	1	-1.8(4)
C(9)	0.2198	0.0585	0.2026	1	-1.8(4)

The cation distribution of this sample (Cs = 0.911(37), Rb = 0.089(37)) is comparable to the previous one (Cs = 0.928(21), Rb = 0.072(21)); however, they both differ from the first MT001_2 batch (Cs = 0.816(23), Rb = 0.184(23)). In conclusion it can be said that pelletisation prior to annealing at these relatively low temperatures has very little effect on the composition of the product.

Sample MT005_1 at room temperature, model 2:

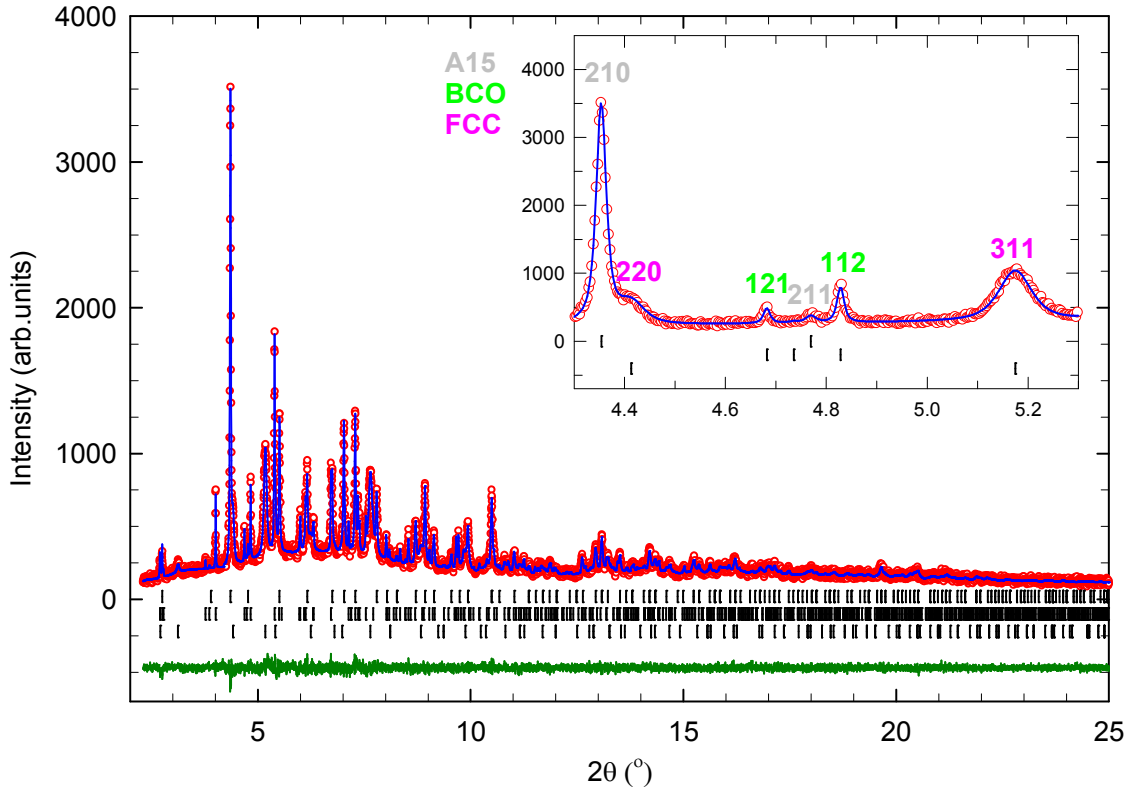

Fig 4.17: Observed (open red circles) and calculated model (blue line) data of the room temperature synchrotron powder X-ray diffraction pattern for the sample with nominal composition $Rb_{0.25}Cs_{2.75}C_{60}$. The upper bars represent the positions of the Bragg reflections of the A15 phase, the middle ones of the BCO phase and the lower ones of the FCC phase. The wavelength is λ = 0.39988(4) Å.

Table 4.31: Results of the room temperature three-phase Rietveld refinement of the Rb containing A15 phase in the sample with overall nominal composition $Rb_{0.25}Cs_{2.75}C_{60}$ (MT005_1).

	x/a	*y/b*	*z/c*	*N*	B_{Iso}(Å^2)
Cs(1)	0.25	0.5	0	0.903(31)	2.94(9)
Rb1)	0.25	0.5	0	0.097(31)	2.94(9)
C(1)	0	0.2966	0.0609	1	1.3(3)
C(2)	0.1210	0.0997	0.2547	1	1.3(3)
C(3)	0.0620	0.2002	0.2208	1	1.3(3)

Table 4.32: Results of the room temperature three-phase Rietveld refinement of the Rb containing FCC phase in the sample with overall nominal composition $Rb_{0.25}Cs_{2.75}C_{60}$ (MT005_1).

	x/a	*y/b*	*z/c*	*N*	B_{Iso}(Å^2)
Cs(1)	0.25	0.25	0.25	0.829	3.2(3)
Rb(1)	0.25	0.25	0.25	0.171	3.2(3)
Cs(2)	0.5	0.5	0.5	1.0	10.8(6)
C(1)	0	0.0487	0.2449	0.5	-0.9(5)
C(2)	0.2105	0.0761	0.0987	0.5	-0.9(5)
C(3)	0.1708	0.1489	0.0488	0.5	-0.9(5)

Table 4.33: Results of the room temperature three-phase Rietveld refinement of the Cs_4C_{60} BCO phase in the sample with overall nominal composition $Rb_{0.25}Cs_{2.75}C_{60}$ (MT005_1).

	x/a	*y/b*	*z/c*	*N*	B_{Iso}(Å^2)
Cs(1)	0.2051	0.5	0	1	2.2(2)
Cs(2)	0	0.2539	0.5	1	2.2(2)
C(1)	0	0.2869	0.0624	1	-0.2(4)
C(2)	0.0593	0	0.3008	1	-0.2(4)
C(3)	0.2927	0.0584	0	1	-0.2(4)
C(4)	0.0977	0.2504	0.1249	1	-0.2(4)
C(5)	0.1204	0.0950	0.2649	1	-0.2(4)
C(6)	0.2552	0.1171	0.1024	1	-0.2(4)
C(7)	0.1925	0.2137	0.0636	1	-0.2(4)
C(8)	0.0607	0.1923	0.2267	1	-0.2(4)
C(9)	0.2198	0.0585	0.2024	1	-0.2(4)

The cation distribution in the A15 phase (Cs = 0.903(31), Rb = 0.097(31)) is comparable to the previous sample with nominal composition $Rb_{0.50}Cs_{2.50}C_{60}$ (Cs = 0.911(37), Rb = 0.089(37)); this is a worrying observation for the validity of the systematics of the current model. It currently appears that if Rb is indeed doped into the A15 structure, it may not correlate with its amount initially added.

Sample MT011_3 at room temperature, model 2:

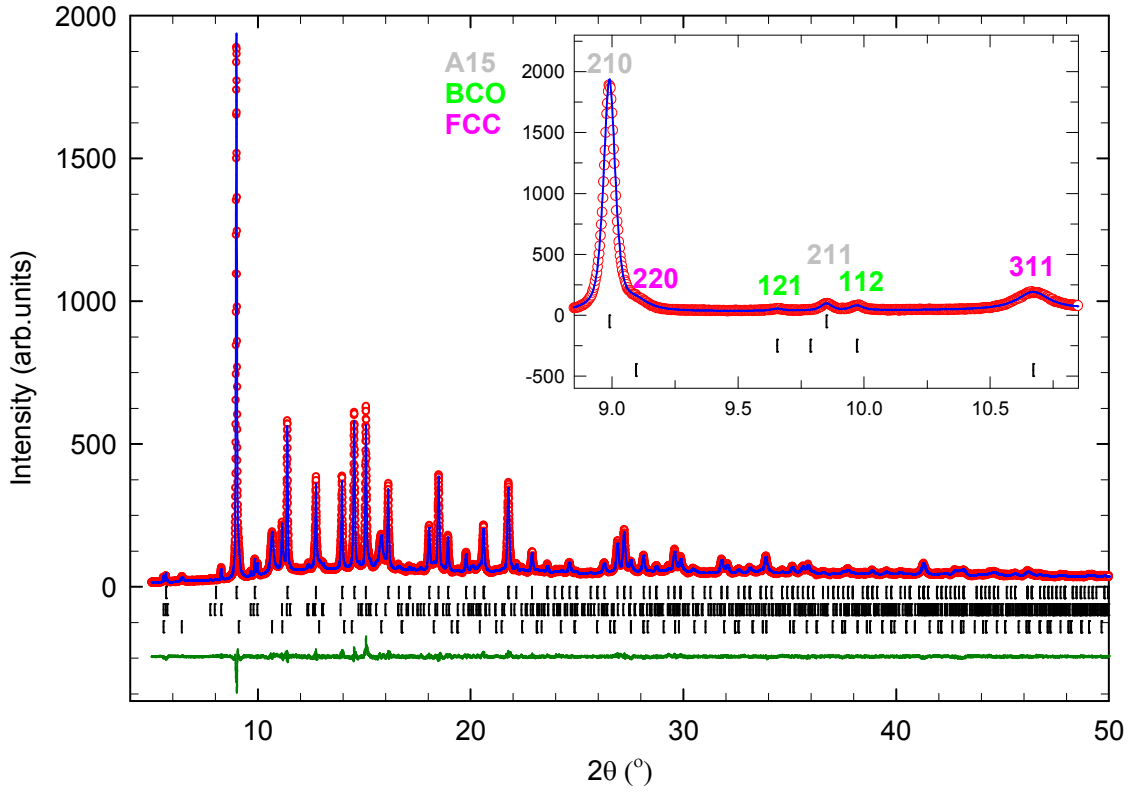

Fig 4.18: Observed (open red circles) and calculated (blue line) data of the room temperature synchrotron powder X-ray diffraction pattern for the sample with nominal composition $Rb_{0.12}Cs_{2.88}C_{60}$. The upper bars represent the positions of the Bragg reflections of the A15 phase, the middle ones of the BCO phase and the lower ones of the FCC phase. The wavelength is λ = 0.826028(1) Å.

Table 4.34: Results of the room temperature three-phase Rietveld refinement of the Cs_3C_{60} A15 phase in the sample with overall nominal composition $Rb_{0.12}Cs_{2.88}C_{60}$ (MT011_3).

	x/a	*y/b*	*z/c*	*N*	B_{Iso}(Å^2)
Cs(1)	0.25	0.5	0	0.871(5)	2.65(2)
Rb(1)	0.25	0.5	0	0.129(5)	2.65(2)
C(1)	0	0.2967	0.0610	1	1.57(7)
C(2)	0.1210	0.0997	0.2548	1	1.57(7)
C(3)	0.0621	0.2003	0.2209	1	1.57(7)

Table 4.35: Results of the room temperature three-phase Rietveld refinement of the Rb-containing FCC phase in the sample with overall nominal composition $Rb_{0.12}Cs_{2.88}C_{60}$ (MT011_3).

	x/a	*y/b*	*z/c*	*N*	B_{Iso}(Å^2)
Cs(1)	0.25	0.25	0.25	1.0	4.0(2)
Rb(1)	0.25	0.25	0.25	0	4.0(2)
Cs(2)	0.5	0.5	0.5	1.0	12.7(4)
C(1)	0	0.0486	0.2445	0.5	-2.1(2)
C(2)	0.2102	0.0760	0.0986	0.5	-2.1(2)
C(3)	0.1706	0.1487	0.0487	0.5	-2.1(2)

Table 4.36: Results of the room temperature three-phase Rietveld refinement of the Cs_4C_{60} BCO phase in the sample with overall nominal composition $Rb_{0.12}Cs_{2.88}C_{60}$ (MT011_3).

	x/a	*y/b*	*z/c*	*N*	B_{Iso}(Å^2)
Cs(1)	0.2055	0.5	0	1	2.1(2)
Cs(2)	0	0.2533	0.5	1	2.1(2)
C(1)	0	0.2862	0.0625	1	-1.8(5)
C(2)	0.0594	0	0.3009	1	-1.8(5)
C(3)	0.2933	0.0583	0	1	-1.8(5)
C(4)	0.0979	0.2498	0.1249	1	-1.8(5)
C(5)	0.1207	0.0948	0.2650	1	-1.8(5)
C(6)	0.2557	0.1168	0.1025	1	-1.8(5)
C(7)	0.1929	0.2135	0.0636	1	-1.8(5)
C(8)	0.0608	0.1918	0.2267	1	-1.8(5)
C(9)	0.2202	0.0584	0.2024	1	-1.8(5)

The simple structural model used appears now to have broken down as the refinement shows the presence of more Rb (0.129(5)) than that added initially. Additionally, the FCC phase should also have some Rb intercalated into it.

4.4.5 Summary – structural properties of the A15 $Rb_xCs_{3-x}C_{60}$ series at room temperature (refinement model 2)

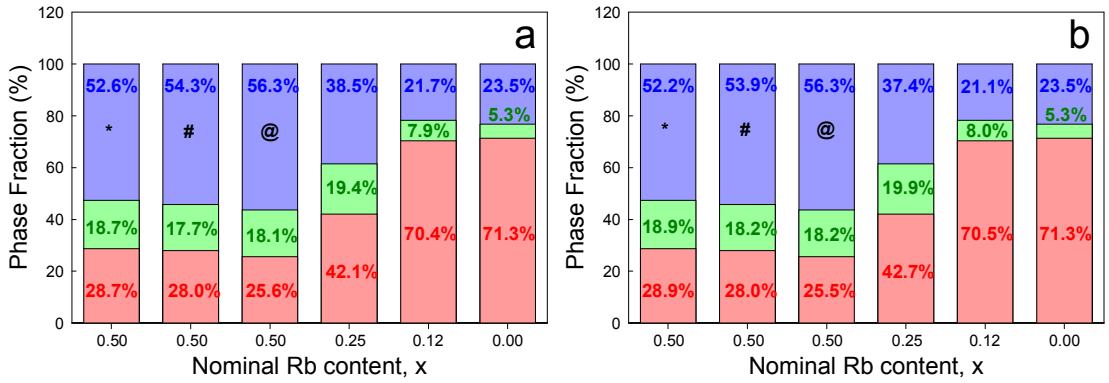

Fig 4.19: Room temperature variation of the fractions of the three polymorphs for the series of samples, $Rb_xCs_{3-x}C_{60}$ (**a**) refinement model 1 where Rb is exclusively incorporated in the FCC phase, and (**b**) refinement model 2 where Rb is distributed in both the FCC and A15 phases. Red filling represents the A15, green the BCO and blue the FCC phase.(* = MT001_2, # = MT003_2 @ = MT003_3)

The first noticeable observation is that the sample phase fractions of models 1 and 2 (Fig 4.19) are comparable; however, the refinement model breaks down at sample MT011_3 (nominal x =0.12) as the refined Rb content of the A15 phase alone is greater than the amount initially added in the course of the synthetic procedure. Additionally, is it known that Rb should also be present in the FCC phase, as the cell volume of sample MT011_3 (nominal stoichiometry $Rb_{0.12}Cs_{2.88}C_{60}$), *vol* = 3189.7(3) $Å^3$, is smaller than that of the parent material Cs_3C_{60} material, *vol* = 3232.7(4) $Å^3$.

The relationship between the refined cell volume and the cation site distribution of Cs and Rb in the A15 phase suggests there is no apparent trend, as summarised in Fig 4.20. The A15 phases only differ in volume across the series by 3 $Å^3$, and even though there may be an insignificant change in cell volume as a result of the fitting of Rb in the distorted tetrahedral sites, a reliable trend from the obtained refinements cannot be found. The difficulty is further exacerbated by the fact that, depending on the synthetic conditions, the relationship between the amount of Rb incorporated into the A15 structure may be not directly related to the nominal stoichiometry of the sample.

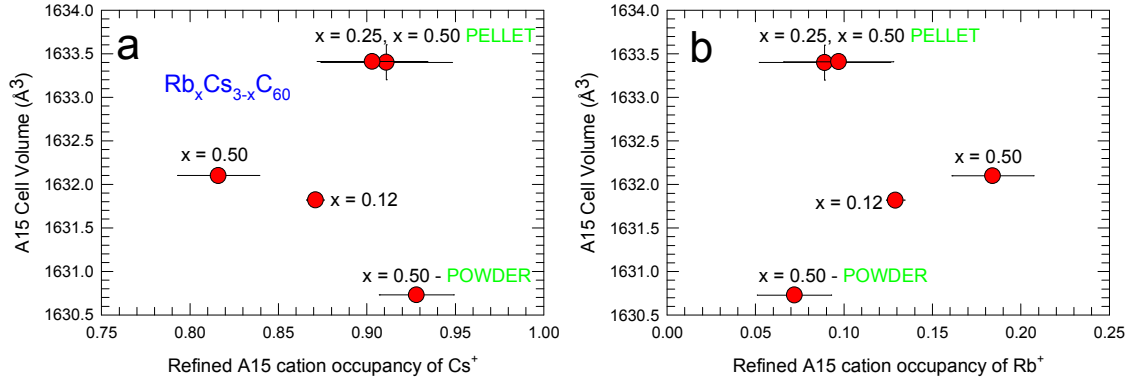

Fig 4.20: Refined A15 cation occupancy of (**a**) Cs^+ and (**b**) Rb^+ against the unit cell volume of the A15 phase for samples of the series $Rb_xCs_{3-x}C_{60}$, Samples are labelled with their nominal stoichiometry.

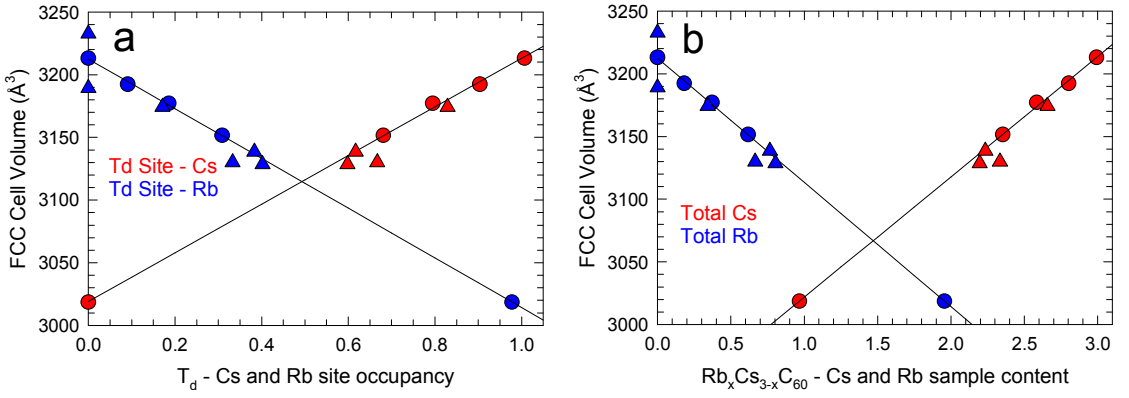

Fig 4.21: Refined unit cell volume of the minority FCC $Rb_xCs_{3-x}C_{60}$ phases as a function of the site occupancy of the T_d sites by Cs and Rb (**a**) and as a function of the total Cs and Rb content (**b**). Blue shapes symbolise the Rb^+ cation, red shapes the Cs^+ cation. Circles represent the FCC phase results from the FCC-rich $Rb_xCs_{3-x}C_{60}$ samples (chapter 3); triangles represent the FCC phase results from the A15-rich $Rb_xCs_{3-x}C_{60}$ samples (current chapter). Guide-for-the-eye lines are included for the FCC-rich samples. (error bars included, but smaller than points).

Fig 4.21 shows how the Rb content of the FCC phase varies with unit cell volume in comparison to the more crystalline NH_3-produced samples. There is a significant improvement in comparison to the results of the earlier refinements with no incorporation of Rb into the A15 phase; however, there is a major problem with the sample with nominal x =0.12, in which far more Rb is found for the A15 phase than what was initially added in the course of the reaction. Also the FCC phase in the

sample with nominal composition Cs_3C_{60} (V = 3232.7(4) Å^3) has a much larger cell volume than its more crystalline counterpart, MTM161_3 (V = 3213.01(5) Å^3 - nominal stoichiometry, Cs_3C_{60}). Therefore this also precludes the possibility of calculating the Rb content of the A15 phase based on the Rb amount present in the FCC phase (e.g. by extrapolation of the linear plot obtained for the FCC-rich samples).

Despite a number of systematic attempts, it has not been possible to determine definitively through powder X-ray diffraction whether a family of $Rb_xCs_{3-x}C_{60}$ materials with the A15 structure can be accessed. On the one hand, there is competition between partial site occupancies and Rb doping. Additionally, the cell volume change may also be insignificant; therefore it is difficult to determine how much of the Cs variation is actually the result of Rb co-doping or of partial occupancy of the cation sites. In order to obtain complementary evidence, an attempt was made to probe the structural evolution of the FCC phase, as an excellent trend has already established between the unit cell volume and Rb doping for the samples where the FCC component is the majority phase. However, additional anomalies were encountered for samples that have low levels of Rb doping and for the parent material Cs_3C_{60}. The results of the magnetic measurements in *section 4.5* were used to attempt to shed more light onto the matter.

4.4.6 $Rb_xCs_{3-x}C_{60}$ ($0.0 \leq x \leq 0.5$) at low temperature, model 1

Refinements of the low-temperature diffraction data were only undertaken using the first refinement model because of the inconsistencies observed for the refinements using the second model at room temperature.

Refined parameters for the majority A15 (space group $Pm\bar{3}n$), minority FCC (space group $Fm\bar{3}m$) and minority BCO (space group *Immm*) phases are shown below in the tables within this subsection. First Table 4.37 includes an overall summary, showing key refinement parameters and results, and then each sample is given a more detailed description. Three-phase Rietveld refinements of the synchrotron X-ray

powder diffraction data of samples with nominal stoichiometry, $Rb_xCs_{3-x}C_{60}$ (MT001_2 (x = 0.50), MT003_2 (x = 0.50), MT003_3(x = 0.50), MT005_1 (x = 0.25), MT011_3 (x = 0.12) and MT012_3 (x = 0.00)) were undertaken. The fractional occupancy, *N*, of the Cs(1) atom in the A15 structure was allowed to vary, converging to a value close to 1. Any Rb doped into the phase assemblage was included entirely into the T_d site of the FCC phase, while the remaining fraction was modelled as Cs, thus keeping the total occupancy of the T_d site fixed at 1.0. The stoichiometry of the BCO phase was not refined but kept again fixed at Cs_4C_{60}, while the stoichiometry of the FCC phase was also fixed.

Table 4.37: Results of the Rietveld refinements of the series $Rb_xCs_{3-x}C_{60}$ ($0.0 \geq x \geq 0.5$) at 5 and 12 K

Parameter	*MT001_2 (5K)*	*MT005_1 (5K)*	*MT011_3 (5K)*	*MT012_3 (12K)*
R_{wp} (%)	3.49	4.06	5.44	3.54
R_{exp} (%)	2.14	3.61	1.02	0.75
χ^2	1.277	1.060	2.309	2.173
λ (Å)	0.39988(4)	0.39988(4)	0.826028(1)	0.826028(1)
A15 (%)	18.9(3)	42.7(3)	73.1(1)	72.6(1)
BCO (%)	19.7(1)	20.1(1)	8.2(1)	5.8(2)
FCC (%)	61.4(1)	37.2(3)	18.8(2)	21.6(2)
A15 *a* (Å)	11.7069(2)	11.7117(1)	11.7227(1)	11.7233(1)
A15 *V* (Å^3)	1604.45(7)	1606.43(4)	1610.97(5)	1611.20(5)
BCO cell (Å)	*a* = 11.8163(5) *b* = 12.1061(4) *c* = 11.3921(3)	*a* = 11.8156(5) *b* = 12.1062(4) *c* = 11.4143(3)	*a* = 11.819(2) *b* = 12.143(2) *c* = 11.4182(9)	*a* = 11.817(3) *b* = 12.141(3) *c* = 11.424(2)
BCO *V* (Å^3)	1629.63(7)	1632.72(6)	1638.7(2)	1639.1(4)
FCC *a* (Å)	14.5404(2)	14.5959(5)	14.6449(7)	14.7086(7)
FCC *V* (Å^3)	3074.2(1)	3109.5(3)	3140.9(4)	3182.1(5)
Refined A15 stoichiometry	$Cs_{2.81(2)}C_{60}$	$Cs_{2.81(2)}C_{60}$	$Cs_{2.80(2)}C_{60}$	$Cs_{2.76(1)}C_{60}$
Fixed FCC stoichiometry	$Rb_{0.82}Cs_{2.18}C_{60}$	$Rb_{0.66}Cs_{2.34}C_{60}$	$Rb_{0.60}Cs_{2.40}C_{60}$	Cs_3C_{60}

Sample MT001_2 at 5K:

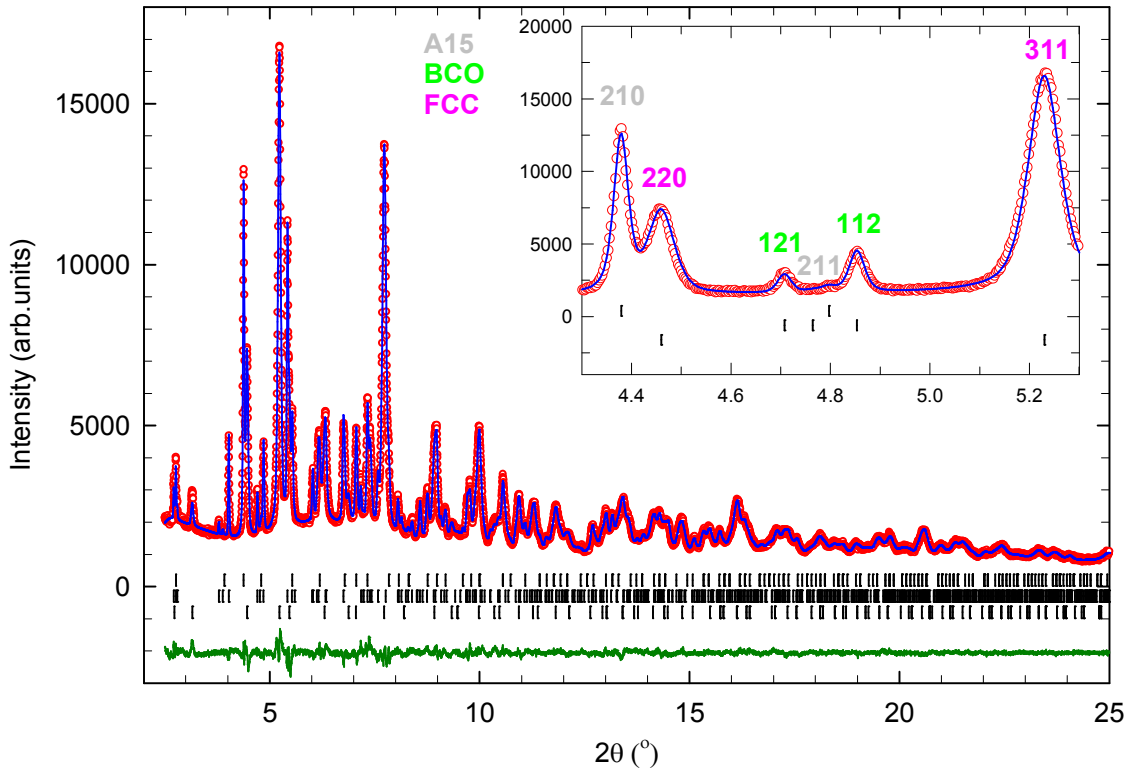

Fig 4.22: Observed (open red circles) and calculated (blue line) data of the 5 K synchrotron powder X-ray diffraction pattern for the sample with nominal composition $Rb_{0.50}Cs_{2.50}C_{60}$. The upper bars represent the positions of the Bragg reflections of the BCO phase and the lower ones of the FCC phase. The wavelength was λ = 0.39988(4) Å.

Table 4.38: Results of the 5 K three-phase Rietveld refinement of the Cs_3C_{60} A15 phase in the sample with overall nominal composition $Rb_{0.50}Cs_{2.50}C_{60}$ (MT001_2).

	x/a	*y/b*	*z/c*	*N*	B_{Iso}(Å^2)
Cs(1)	0.25	0.5	0	0.938(8)	0.43(5)
C(1)	0	0.2980	0.0612	1	0.2(2)
C(2)	0.1215	0.1001	0.2559	1	0.2(2)
C(3)	0.0623	0.2011	0.2218	1	0.2(2)

Table 4.39: Results of the 5 K three-phase Rietveld refinement of the Rb containing FCC phase in the sample with overall nominal composition $Rb_{0.50}Cs_{2.50}C_{60}$ (MT001_2).

	x/a	*y/b*	*z/c*	*N*	B_{Iso}(Å^2)
Cs(1)	0.25	0.25	0.25	0.589	0.71(4)
Rb(1)	0.25	0.25	0.25	0.411	0.71(5)
Cs(2)	0.5	0.5	0.5	1.0	1.11(3)
C(1)	0	0.0490	0.2465	0.5	-0.17(7)
C(2)	0.2119	0.0766	0.0994	0.5	-0.17(7)
C(3)	0.1719	0.1498	0.0491	0.5	-0.17(7)

Table 4.40: Results of the 5 K three-phase Rietveld refinement of the Cs_4C_{60} BCO phase in the sample with overall nominal composition $Rb_{0.50}Cs_{2.50}C_{60}$ (MT001_2).

	x/a	*y/b*	*z/c*	*N*	B_{Iso}(Å^2)
Cs(1)	0.2041	0.5	0	1	-0.13(5)
Cs(2)	0	0.2540	0.5	1	-0.13(5)
C(1)	0	0.2871	0.0627	1	-1.2(2)
C(2)	0.0590	0	0.3020	1	-1.2(2)
C(3)	0.2913	0.0585	0	1	-1.2(2)
C(4)	0.0973	0.2505	0.1254	1	-1.2(2)
C(5)	0.1198	0.0951	0.2660	1	-1.2(2)
C(6)	0.2540	0.1172	0.1028	1	-1.2(2)
C(7)	0.1916	0.2141	0.0638	1	-1.2(2)
C(8)	0.0604	0.1924	0.2275	1	-1.2(2)
C(9)	0.2187	0.0586	0.2032	1	-1.2(2)

The refined occupancy of Cs in the A15 phase is found to be 0.936(6), resulting in a stoichiometry of $Cs_{2.81(2)}C_{60}$ (Table 4.38). There is an irregular discrepancy between the phase percentages of this sample at low and room temperature (the same capillary was used for both). At room temperature the phase fraction of the A15 phase is 28.7(3) % and at low temperature it is 18.9(3) %.

MT005_1 at 5K:

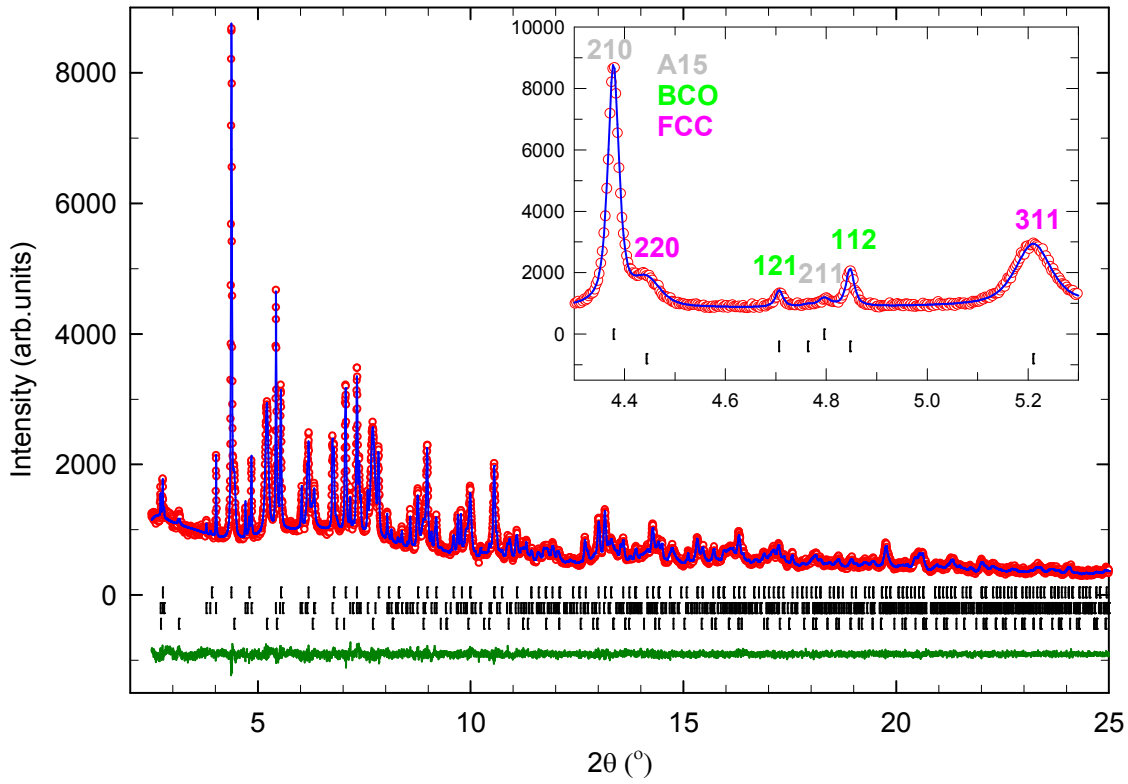

Fig 4.23: Observed (open red circles) and calculated (blue line) data of the 5 K synchrotron powder X-ray diffraction pattern for the sample with nominal composition $Rb_{0.25}Cs_{2.75}C_{60}$. The upper bars represent the positions of the Bragg reflections of the A15 phase, the middle ones of the BCO phase and the lower ones of the FCC phase. The wavelength is λ = 0.39988(4) Å.

Table 4.41: Results of the 5 K three-phase Rietveld refinement of the Cs_3C_{60} A15 phase in the sample with overall nominal composition $Rb_{0.25}Cs_{2.75}C_{60}$ (MT005_1).

	x/a	*y/b*	*z/c*	*N*	B_{Iso}(Å^2)
Cs(1)	0.25	0.5	0	0.936(6)	0.32(4)
C(1)	0	0.2983	0.0613	1	0.7(2)
C(2)	0.1216	0.1002	0.2561	1	0.7(2)
C(3)	0.0624	0.2013	0.2220	1	0.7(2)

Table 4.42: Results of the 5 K three-phase Rietveld refinement of the Rb-containing FCC phase in the sample with overall nominal composition $Rb_{0.25}Cs_{2.75}C_{60}$ (MT005_1).

	x/a	*y/b*	*z/c*	*N*	B_{Iso}(Å^2)
Cs(1)	0.25	0.25	0.25	0.672	0.5(1)
Rb(1)	0.25	0.25	0.25	0.328	0.5(1)
Cs(2)	0.5	0.5	0.5	1.0	2.5(2)
C(1)	0	0.0490	0.2466	0.5	-1.0(2)
C(2)	0.2119	0.0766	0.0994	0.5	-1.0(2)
C(3)	0.1720	0.1499	0.0491	0.5	-1.0(2)

Table 4.43: Results of the 5 K three-phase Rietveld refinement of the Cs_4C_{60} BCO phase in the sample with overall nominal composition $Rb_{0.25}Cs_{2.75}C_{60}$ (MT005_1).

	x/a	*y/b*	*z/c*	*N*	B_{Iso}(Å^2)
Cs(1)	0.2064	0.5	0	1	0.26(8)
Cs(2)	0	0.2553	0.5	1	0.26(8)
C(1)	0	0.2885	0.0626	1	-1.1(2)
C(2)	0.0597	0	0.3017	1	-1.1(2)
C(3)	0.2947	0.0587	0	1	-1.1(2)
C(4)	0.0983	0.2518	0.1253	1	-1.1(2)
C(5)	0.1212	0.0956	0.2657	1	-1.1(2)
C(6)	0.2569	0.1178	0.1027	1	-1.1(2)
C(7)	0.1937	0.2152	0.0637	1	-1.1(2)
C(8)	0.0611	0.1933	0.2273	1	-1.1(2)
C(9)	0.2212	0.0588	0.2030	1	-1.1(2)

The refined stoichiometry of the A15 cation site came to 0.936(6) (Table 4.41). As less Rb is employed in the synthetic procedure, there is a rapid growth of the A15 phase content and suppression of the FCC content. Additionally, the phase quantities are much closer to the room temperature refinements than the previous sample.

MT011_3 at 5 K:

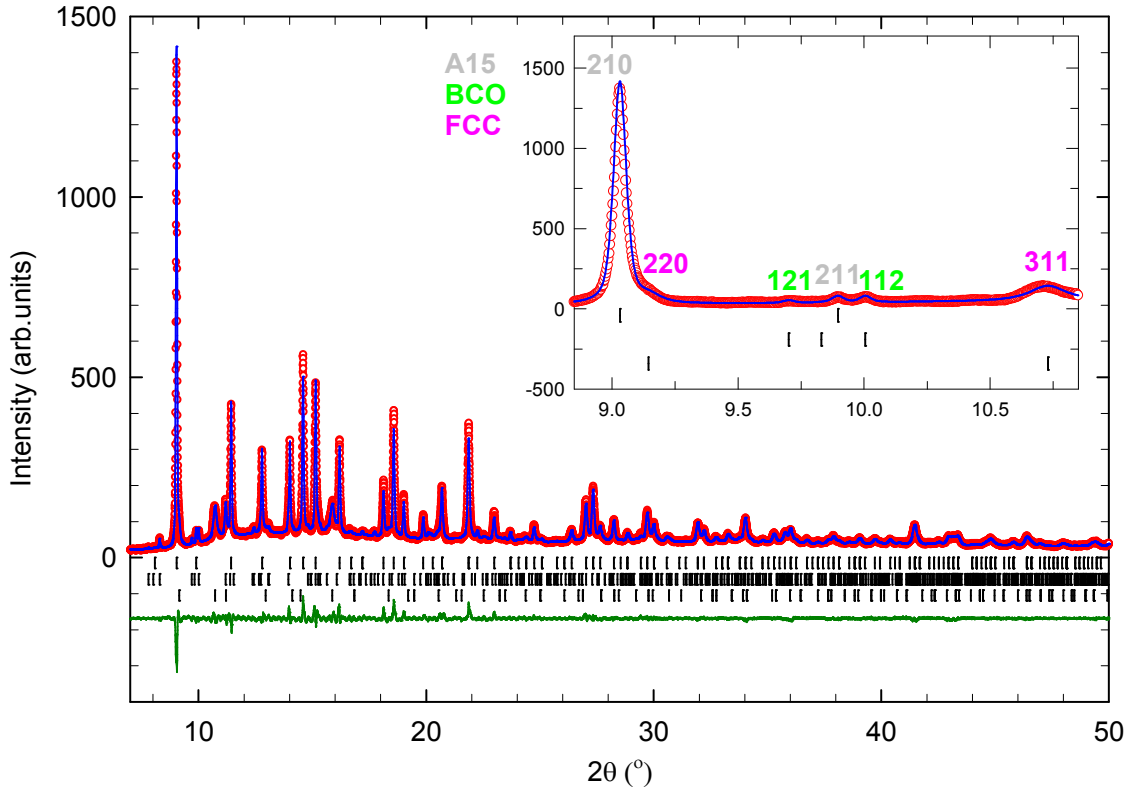

Fig 4.24: Observed (open red circles) and calculated (blue line) data of the 12 K synchrotron powder X-ray diffraction pattern for the sample with nominal composition $Rb_{0.12}Cs_{2.88}C_{60}$. The upper bars represent the positions of the Bragg reflections of the BCO phase and the lower ones of the FCC phase. The wavelength was λ = 0.826028(1) Å.

Table 4.44: Results of the 12 K three-phase Rietveld refinement of the Cs_3C_{60} A15 phase in the sample with overall nominal composition $Rb_{0.12}Cs_{2.88}C_{60}$ (MT011_3).

	x/a	*y/b*	*z/c*	*N*	B_{Iso}(Å^2)
Cs(1)	0.25	0.5	0	0.934(3)	0.67(2)
C(1)	0	0.2981	0.0612	1	1.06(8)
C(2)	0.1215	0.1001	0.2560	1	1.06(8)
C(3)	0.0623	0.2012	0.2219	1	1.06(8)

Table 4.45: Results of the 12 K three-phase Rietveld refinement of the Rb containing FCC phase in the sample with overall nominal composition $Rb_{0.12}Cs_{2.88}C_{60}$ (MT011_3).

	x/a	*y/b*	*z/c*	*N*	B_{Iso}(Å^2)
Cs(1)	0.25	0.25	0.25	0.699	1.0(2)
Rb(1)	0.25	0.25	0.25	0.301	1.0(2)
Cs(2)	0.5	0.5	0.5	1.0	6.4(4)
C(1)	0	0.0489	0.2457	0.5	0.6(4)
C(2)	0.2112	0.0763	0.0991	0.5	0.6(4)
C(3)	0.1714	0.1494	0.0489	0.5	0.6(4)

Table 4.46: Results of the 12 K three-phase Rietveld refinement of the Cs_4C_{60} BCO phase in the sample with overall nominal composition $Rb_{0.12}Cs_{2.88}C_{60}$ (MT011_3).

	x/a	*y/b*	*z/c*	*N*	B_{Iso}(Å^2)
Cs(1)	0.2053	0.5	0	1	1.6(2)
Cs(2)	0	0.2553	0.5	1	1.6(2)
C(1)	0	0.2886	0.0627	1	-1.1(6)
C(2)	0.0594	0	0.3021	1	-1.1(6)
C(3)	0.2930	0.0588	0	1	-1.1(6)
C(4)	0.0978	0.2518	0.1254	1	-1.1(6)
C(5)	0.1205	0.0956	0.2661	1	-1.1(6)
C(6)	0.2554	0.1178	0.1029	1	-1.1(6)
C(7)	0.1927	0.2152	0.0638	1	-1.1(6)
C(8)	0.0608	0.1934	0.2276	1	-1.1(6)
C(9)	0.2200	0.0589	0.2033	1	-1.1(6)

The refined stoichiometry of the A15 cation site in this sample (x = 0.12) came to 0.934(3) (Table 4.44).

MT012_3 at 12 K:

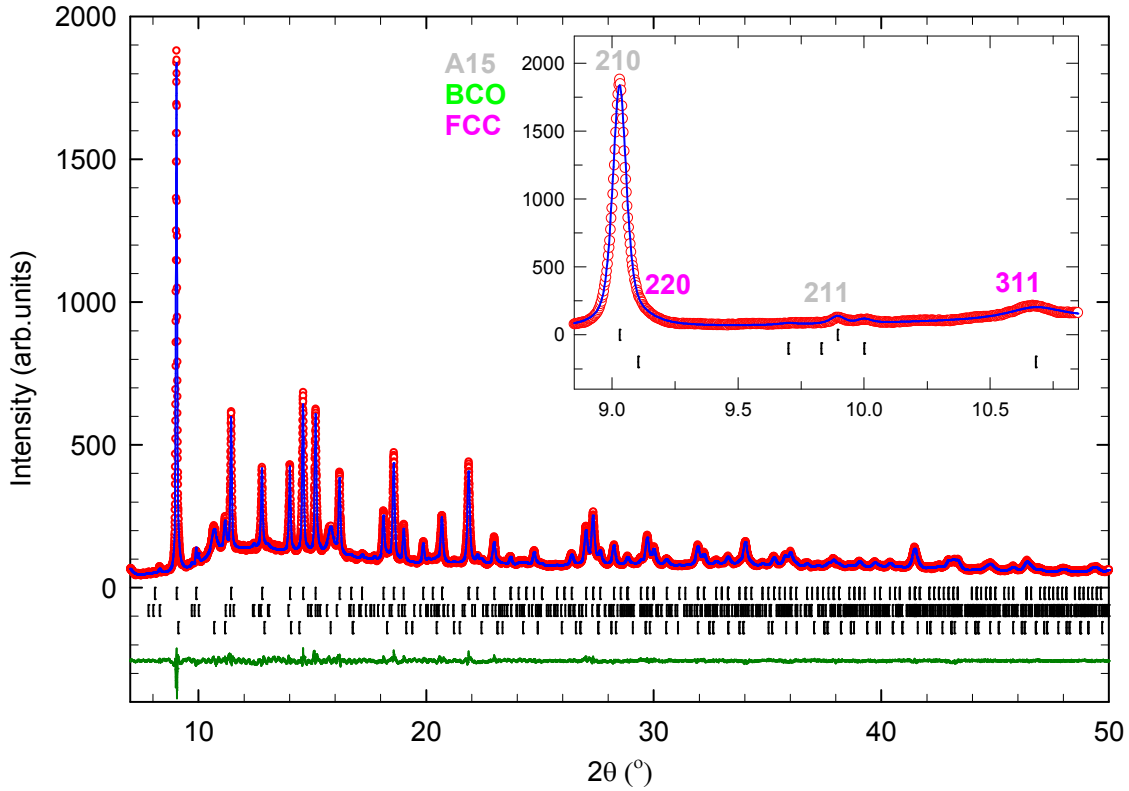

Fig 4.25: Observed (open red circles) and calculated (blue line) data of the 12 K synchrotron powder X-ray diffraction pattern for the sample with nominal composition Cs_3C_{60}. The upper bars represent the positions of the Bragg reflections of the BCO phase and the lower ones of the FCC phase. The wavelength was λ = 0.826028(1) Å.

Table 4.47: Results of the 12 K three-phase Rietveld refinement of the Cs_3C_{60} A15 phase in the sample with overall nominal composition Cs_3C_{60} (MT012_3).

	x/a	*y/b*	*z/c*	*N*	B_{Iso}(Å^2)
Cs(1)	0.25	0.5	0	0.920(3)	0.39(2)
C(1)	0	0.2981	0.0612	1	0.86(6)
C(2)	0.1215	0.1001	0.2559	1	0.86(6)
C(3)	0.0623	0.2011	0.2218	1	0.86(6)

Table 4.48: Results of the 12 K three-phase Rietveld refinement of the Cs_3C_{60} FCC phase in the sample with overall nominal composition Cs_3C_{60} (MT012_3).

	x/a	*y/b*	*z/c*	*N*	B_{Iso}(Å^2)
Cs(1)	0.25	0.25	0.25	1.0	2.8(2)
Cs(2)	0.5	0.5	0.5	1.0	7.2(4)
C(1)	0	0.0487	0.2447	0.5	-0.6(3)
C(2)	0.2103	0.0760	0.0987	0.5	-0.6(3)
C(3)	0.1707	0.1488	0.0487	0.5	-0.6(3)

Table 4.49: Results of the 12 K three-phase Rietveld refinement of the Cs_4C_{60} BCO phase in the sample with overall nominal composition Cs_3C_{60} (MT012_3).

	x/a	*y/b*	*z/c*	*N*	B_{Iso}(Å^2)
Cs(1)	0.2052	0.5	0	1	3.2(5)
Cs(2)	0	0.2554	0.5	1	3.2(5)
C(1)	0	0.2886	0.0627	1	3(1)
C(2)	0.0593	0	0.3022	1	3(1)
C(3)	0.2928	0.0588	0	1	3(1)
C(4)	0.0978	0.2518	0.1255	1	3(1)
C(5)	0.1205	0.0956	0.2661	1	3(1)
C(6)	0.2553	0.1178	0.1029	1	3(1)
C(7)	0.1925	0.2152	0.0638	1	3(1)
C(8)	0.0607	0.1934	0.2277	1	3(1)
C(9)	0.2198	0.0589	0.2033	1	3(1)

The refined stoichiometry of the A15 cation site came to 0.920(3) (Table 4.47). The phase contents are comparable to those obtained at room temperature. The poor crystallinity of the FCC phase persists through the series and the unit cell volume of the phase decreases monotonically as the parent material is doped with more Rb. From these results it seems the main unambiguous conclusion drawn is that all Rb is doped into the FCC phase exclusively.

4.4.7 Summary – structural properties of the FCC-Rich $Rb_xCs_{3-x}C_{60}$ series at low temperature

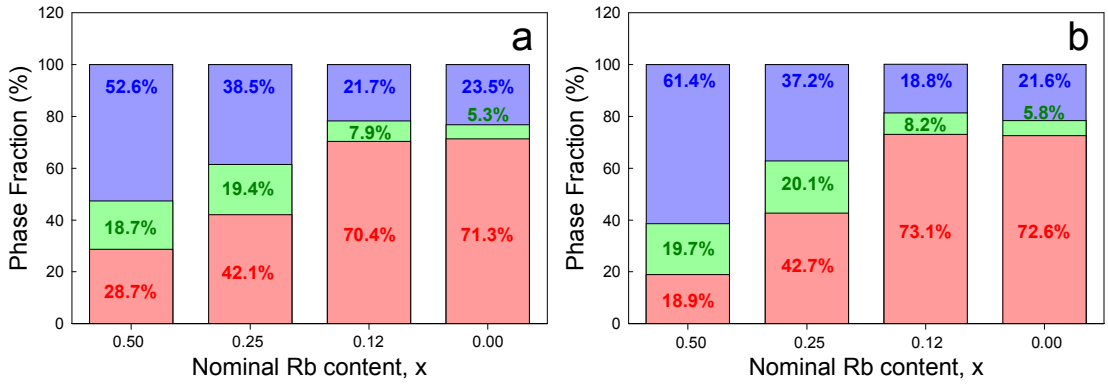

Fig 4.26: Variation of the fractions of the three polymorphs for the series of samples, $Rb_xCs_{3-x}C_{60}$ (**a**) at room temperature and (**b**) at 5 or 12 K. Red filling represents the A15, green the BCO and blue the FCC phase. [only MT001_2 at room temperature for comparison]

The results of the low temperature refinements are comparable to those obtained for the room temperature diffraction data. The room temperature data were all collected at ID31. The low temperature data for samples MT001_2 and MT005_1 was collected at ID31 (5 K) and the low temperature data of MT011_3 and MT012_3 was collected at Diamond (12 K). The phase percentages refined to values comparable to their room temperature equivalents - a summary of the composition of the materials is shown in Fig 4.26. There is a peculiar unexplainable discrepancy for the sample of nominal stoichiometry $Rb_{0.50}Cs_{2.50}C_{60}$, in which the same capillary was measured at both room and low temperatures.

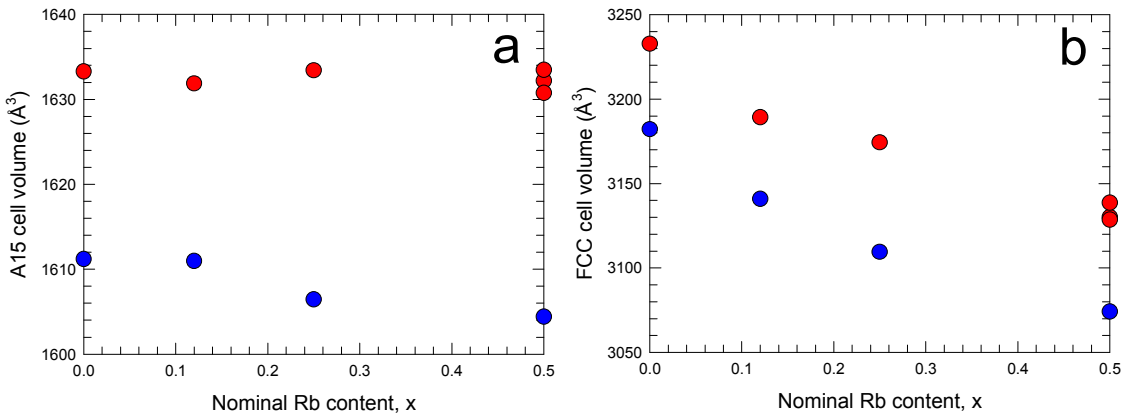

Fig 4.27: Unit cell volume changes of the $Rb_xCs_{3-x}C_{60}$ series at room temperature (red circles) and at 5 or 12 K (blue circles). **a:** Shows the A15 phase. **b:** Shows the FCC phase.

The unit cell volumes for the BCO and A15 phases vary only slightly with changing nominal stoichiometry. The results of the A15 phase refinements shown in Fig 4.27(a) indicate that the A15 phase metrics change very little, while the FCC are very sensitive (Fig 4.27(b)) to changes in the Rb co-dopant level. For the A15 phase, there may still be some Rb intercalated; however, identifying precisely how much Rb is co-doped proved an impossible task, as the volume and site occupancies of the A15 phase show only a small variation at low temperature.

4.5 Magnetic properties

The electronic properties of the A15-rich $Rb_xCs_{3-x}C_{60}$ materials were followed at both ambient and elevated pressures by zero-field-cooled (ZFC) and field-cooled (FC) magnetisation measurements at a field of 20 Oe. Data were collected first at ambient pressure in order to characterise the evolution of the electronic properties with the change in the Rb content (chemical pressure effects). These measurements were then extended to high pressures in order to follow the response of each sample upon the application of physical pressure. In this way, the electronic behaviour as a function of unit cell volume could be followed over a broad range of unit cell volumes. Earlier high

pressure structural work (using beamline BL10XU at SPring-8) on A15-rich Cs_3C_{60} has established the compressibility, κ of the three polymorphs at ambient temperature.[1] For the FCC Cs_3C_{60} phase, $\kappa = dV/dP$ = 19(1) $Å^3$ $kbar^{-1}$, while for the A15 phase, $\kappa = dV/dP$ = 8.9(4) $Å^3$ $kbar^{-1}$. In the absence of comparable data being available for the Rb co-intercalated samples, these values of the compressibility (via equation (4.1)) were employed to estimate approximately the unit cell variation with change in pressure for all the studied A15-rich $Rb_xCs_{3-x}C_{60}$ samples.

$$V(Å^3) = V_0(Å^3) - P(\text{kbar}) \times \kappa(Å^3 \text{kbar}^{-1}) \qquad (4.1)$$

where V_0 is the ambient pressure unit cell volume of the polymorph, and V is the volume estimated at that particular pressure. As a result, the observed pressure-dependent superconducting response of both the A15 and FCC phases were correlated to changes in the volume occupied per fulleride anion. The superconducting phase fractions at all pressures were calculated exclusively using *equation 2.33* that is derived in *section 2.5.6*.

4.5.1 Ambient Pressure, Low Field ZFC-FC measurements

Approximately 20-30 mg of each powder was transferred using a small disposable funnel and placed into a single-use quartz tube inside the glove box. As the tube is sealed using a blow-torch, the funnel ensures that the sealing point of the vessel is clean. The quartz tubes were specifically designed for SQUID magnetometry measurements of air sensitive materials due to their ergonomic design and negligible background contribution. The samples were attached to a long metal rod and loaded into the MPMS5 under zero applied field at 100 K. The MPMS5 was then cooled slowly using a pre-designed sequence to the base temperature of 1.8 K (zero-field-cooled, ZFC). When stable at 1.8 K for at least 10 minutes, a field of 20 Oe was applied and the sample centered. The magnetic response was measured as a function of temperature from 1.8 to 50 K at a rate of 0.25 K/min in a step size of 0.5 K.

With the field still applied, the MPMS5 was cooled back to base temperature. Field-cooled (FC) measurements were then recorded on warming back to 50 K, using the same protocol as previously described.

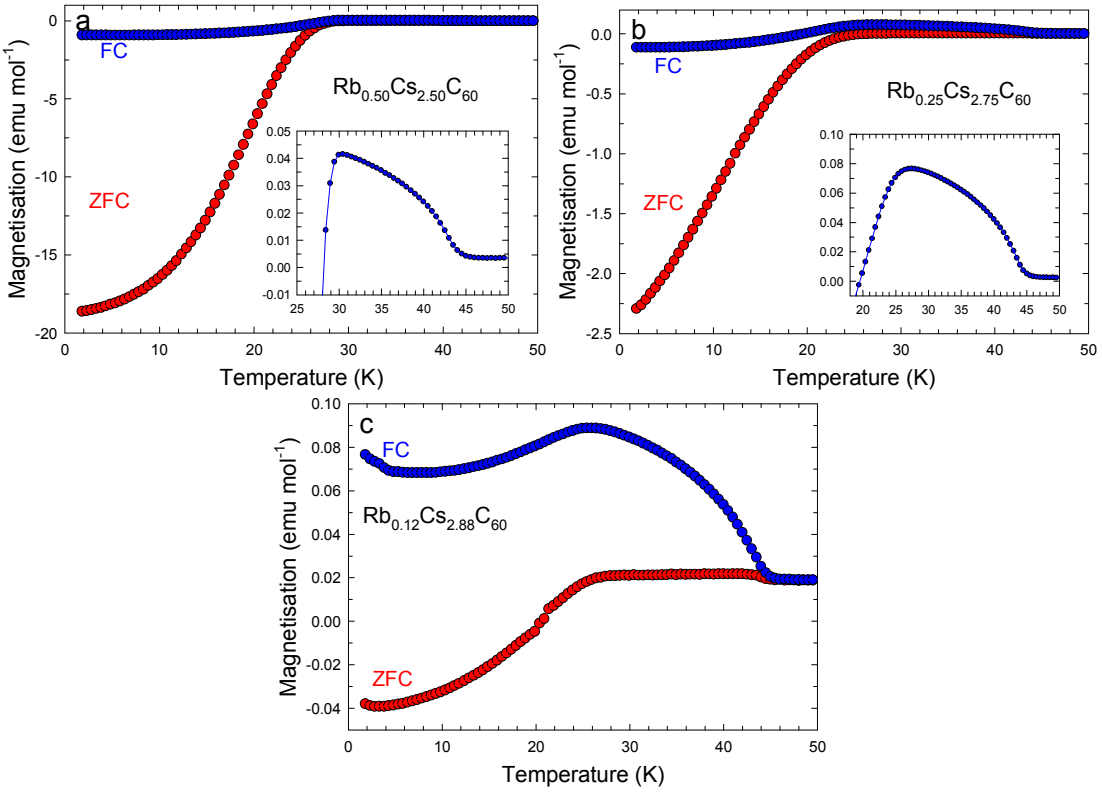

Fig 4.28: Temperature dependence of the ambient pressure ZFC/FC DC magnetisation (20 Oe) for the A15-rich series of compounds, $Rb_xCs_{3-x}C_{60}$. Red circles are ZFC data and blue circles are FC data. **a:** x = 0.50 (MT001_2), $Rb_{0.50}Cs_{2.50}C_{60}$, 23mg. **b:** x = 0.25, $Rb_{0.25}Cs_{2.75}C_{60}$, 22mg. **c:** x = 0.12, $Rb_{0.12}Cs_{2.88}C_{60}$, 21 mg. Insets in **a** and **b** show expanded versions of the FC M(T) plots near the potential onset of spontaneous magnetisation.

Fig 4.28 collects together all ZFC/FC data for the three samples measured. Bulk superconductivity is observed for the sample with nominal Rb content of x = 0.5 with an onset superconducting transition temperature, T_c (seen in both FC and ZFC data, confirming the Meissner effect) of 29.7 K and a superconducting fraction of 39%. As the Rb content decreases, T_c decreases to 27.7 K (x = 0.25) and 26.2 K (x = 0.12). At the

same time, the superconducting fraction also sharply decreases to 5.9% and <0.1%, respectively.

The FC data are also instructive in terms of the magnetic response of the various compositions. Fig. 4.28(c) shows the appearance of a small spontaneous magnetisation appearing at around 46 K for the $Rb_{0.12}Cs_{2.88}C_{60}$ sample. Its magnitude is in excellent agreement with what is expected for the 70% A15 fraction present in this material. The evolution of this spontaneous magnetisation with changing A15 content is summarised in Fig 4.29, where the results from the FCC-rich samples are also included. It can be seen that the magnitude of the spontaneous magnetisation decreases as the amount of the A15 phase decreases.

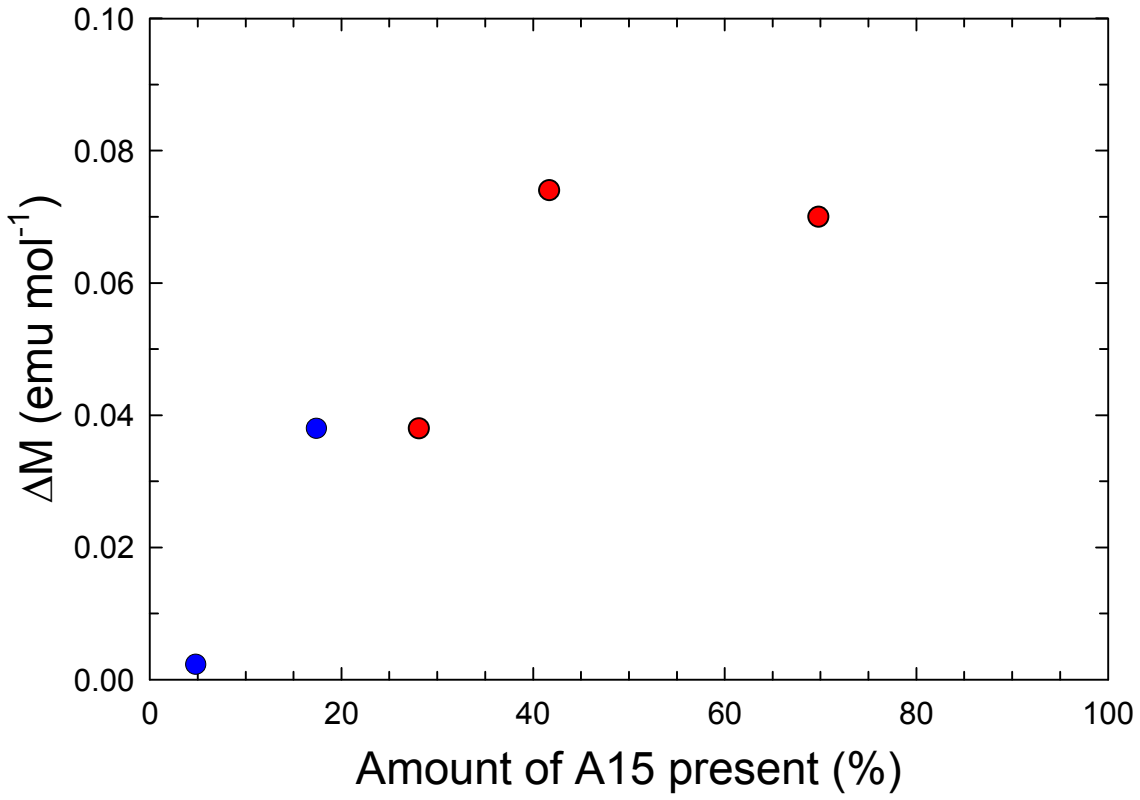

Fig 4.29: Field-cooled spontaneous magnetisation as a function of A15 phase content. FCC-rich samples are represented by blue circles, and A15-rich samples by red circles.

4.6 High Pressure, Low Field ZFC-FC measurements

For the high pressure SQUID measurements, the chosen sample was loaded into the high pressure Mcell whose characteristics are detailed in *section 2.5.8*. Inside the glovebox, the sample was placed into the PTFE cap and the silicon oil pressure transferring medium added via syringe. The cell was then packed in an identical fashion to the background measurement (orientation of components), and the upper-locking nut tightened by hand. A background measurement was performed with an empty Mcell prior to the measurement, so that the background contributions of the cell could be subtracted. In high pressure measurements the background is subtracted on a point-by-point basis, therefore the protocols of both the background and sample measurements must be identical. When removed from the glovebox the cell was transferred quickly to the SQUID, as it was generally unknown how air tight the seals of the containing vessel were in each case.

The Mcell was loaded into the SQUID at room temperature and cooled in stages down to 10 K, under an applied field of 20 Oe (field-cooled, FC), cooling slowly ensures no adverse temperature gradients that may lead to deformations of the cell. Samples were centered at 10 K as the signal was strong and no contributing signal would be observed from the Sn manometer as it is paramagnetic (at this temperature). Additionally, the sample was centred in the SQUID so that the cell is in exactly the same position with respect to the background measurement. If the sample could not be centred at this temperature, *T* is lowered further to 4.2 K (signal should be even stronger). After centering, the SQUID is cooled to the base temperature of 1.8 K with the field still applied (field-cooled, FC). The magnetic response was measured as a function of temperature from 1.8 to 50 K at a rate of 0.25 K/min in a step size of 0.5 K. The field was then switched off and the SQUID cooled back to base temperature. At 1.8 K a field of 20 Oe was applied and the response was again measured from 1.8 to 50 K at a rate of 0.25 K/min in a step size of 0.5 K (zero-field-cooled, ZFC). Finally, an additional set of measurements were performed between 3.8 and 3.2 K with a step

size of 0.05 K at an applied field of 10 Oe so that the the T_c of the Sn manometer can be accurately measured, thus enabling precise calibration of the cell pressure.

After each measurement the SQUID is warmed to room temperature at 5 K per minute. The pressure cell is only removed from the SQUID after it has been allowed to equilibrate at room temperature for approximately 30 minutes. The pressure of the cell was then adjusted mechanically using the MPress. Sample measurements were typically performed for MPress pressures between hand-tight (0 PSI) to 1000 PSI in steps of 250 PSI. Measurements were also performed upon pressure release back to ambient. After each measurement the ceramic components of the cell are checked closely for fractures, and the cell diameter checked for deformations. Typically the ceramic pistons are replaced every 5 measurements.

4.6.1 $Rb_{0.50}Cs_{2.50}C_{60}$ (MT001_2)

Sample MT001_2, nominal stoichiometry $Rb_{0.50}Cs_{2.50}C_{60}$ has a dominant FCC component (~52%) but contains a significant fraction (~29%) of the competing A15 polymorph. The detailed XRD analysis has shown that the FCC component is poorly crystalline. There is a large significant fraction of the A15 polymorph, which allows excellent definition of both its canted antiferromagnetic response and its transition to the superconducting state (Fig 4.30(g) and insets of Fig. 4.30(b) and (d)). Intermediate pressure FC measurements were also taken; the data show that increasing pressure increases marginally T_N. However, at pressures between 0.17 and 0.48 GPa, the AFI state is completely suppressed, Fig 4.30(g).

This sample also shows bulk superconductivity with a T_c of 29.7 K and superconducting fraction of 39% at ambient pressure – this is associated with the FCC phase. Upon application of external pressure, the superconducting fraction increases monotonically and reaches a value of 72 % at 1.00 GPa – the highest pressure of the present experiments (Fig. 4.30(f)). At the same time, the superconducting transition temperature first increases reaching a maximum for the A15 phase of 38.0 K at 0.73

GPa and a maximum for the FCC phase of 31.8 K at 0.48 GPa (Fig. 4.30(e)). These trends are reversible as when the pressure is released, there is no observable hysteresis in the T_c(P) curves. It is noted that the maximum T_c achieved in the FCC polymorph is smaller than that of the A15 phase. The observed superconductivity dome with increasing pressure differs from the behaviour observed for A_3C_{60} fullerides with smaller lattice constants but is reminiscent of the behaviour of A15 Cs_3C_{60}.

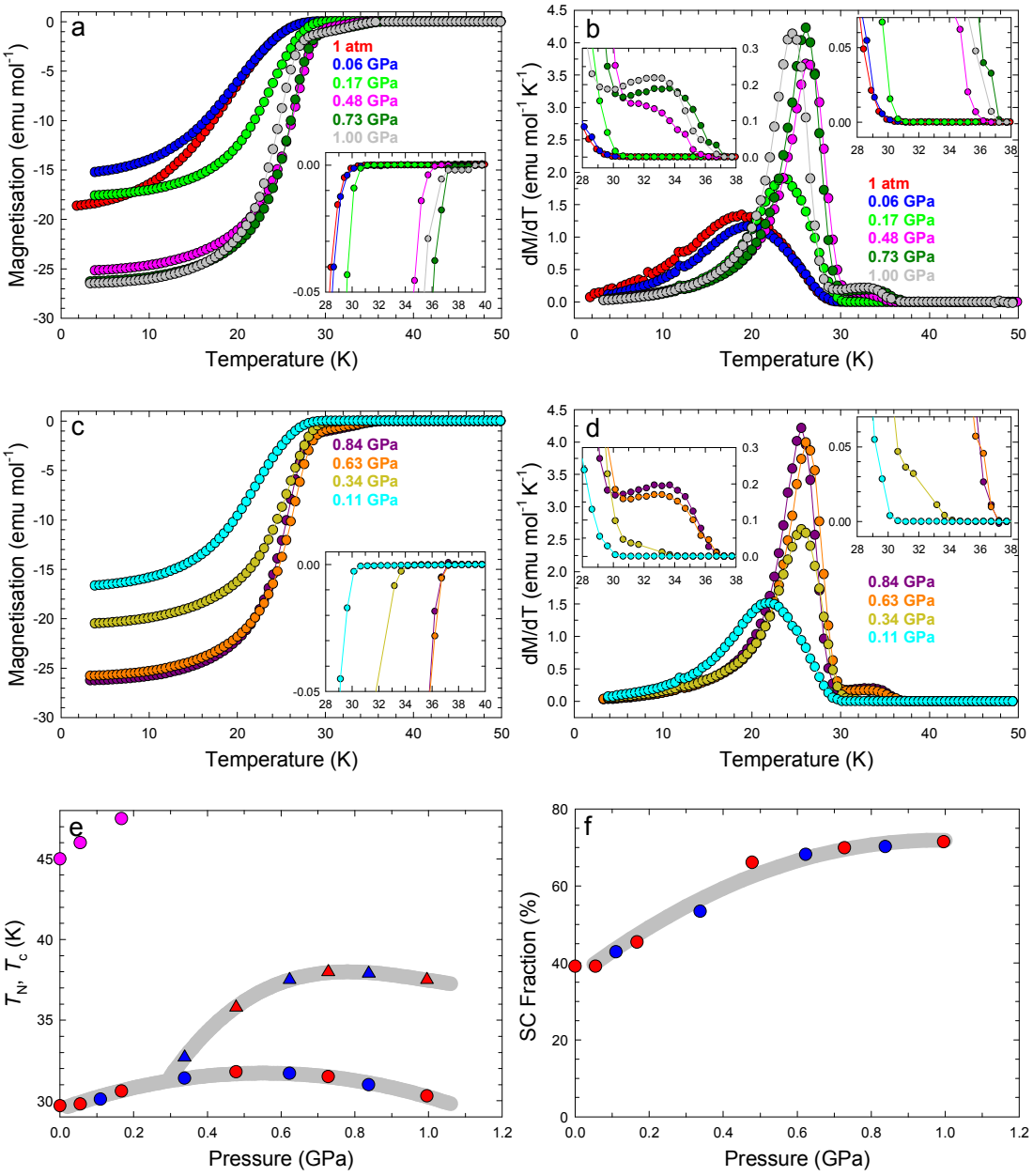

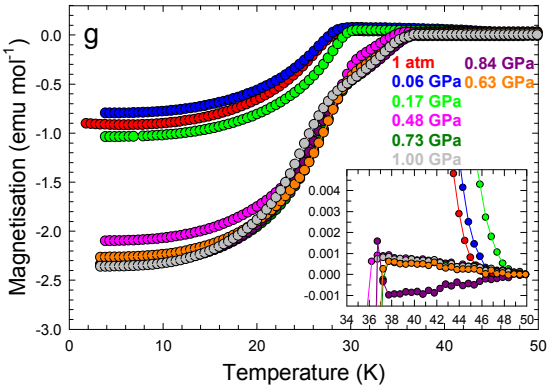

Fig 4.30: High pressure magnetic measurements (ZFC) for the $Rb_{0.50}Cs_{2.50}C_{60}$ sample at an applied field of 20 Oe (19 mg). **a,b:** Magnetisation, M and first derivative of the magnetisation, dM/dT as a function of temperature upon pressurisation. **c,d:** Magnetisation, M and first derivative of the magnetisation, dM/dT as a function of temperature upon pressure release. The insets of **a**, **b**, **c** and **d** show expanded versions of the plots near the onset of the superconducting transition. **e,f:** Transition temperatures, T_N and T_c (circles/triangles represent data for the FCC/A15 phases) and superconducting fraction as a function of pressure; the grey lines are guides-to-the-eye. Red (blue) circles indicate increasing (decreasing) pressure values. Pink markers show the values of T_N. **g:** FC magnetisation measurements (20 Oe) as a function of pressure. The inset shows an expanded region of the plot near the onset of the ferromagnetic transition.

4.6.2 $Rb_{0.25}Cs_{2.75}C_{60}$ (MT005_1)

A similar trend is revealed by the high *P* magnetic measurements for the $Rb_{0.25}Cs_{2.75}C_{60}$ sample. This composition is dominated by the A15 component (~42%) but contains a very significant fraction (~39%) of the competing FCC polymorph whose magnetic signature affords a superconducting fraction of 5.9 % and a T_c of 27.7 K at the ambient *P* ZFC magnetisation measurements (Fig. 4.28(b)). There is a large significant proportion of the A15 polymorph, which allows good definition of both its canted antiferromagnetic response and its transition to the superconducting state (Fig 4.30(g) and insets of Fig. 4.30(b) and (d)). Intermediate pressure FC measurements were again taken with the data showing that increasing pressure leads to an increase in T_N; however, between 0.22 and 0.46 GPa the AFI state is completely suppressed, Fig 4.30(g).

The superconducting fraction increases rapidly from 5.9% to 53.7% when the sample was pressed to 1.07 GPa (Fig. 4.31(f)). At the same time, the superconducting transition temperature first increases reaching a maximum for the A15 phase of 38.1 K at 0.71 GPa and a maximum for the FCC phase of 32.2 K at 0.75 GPa (Fig. 4.31(e)). Once again, these trends are reversible as when the pressure is released, there is no observable hysteresis in the T_c(P) curves.

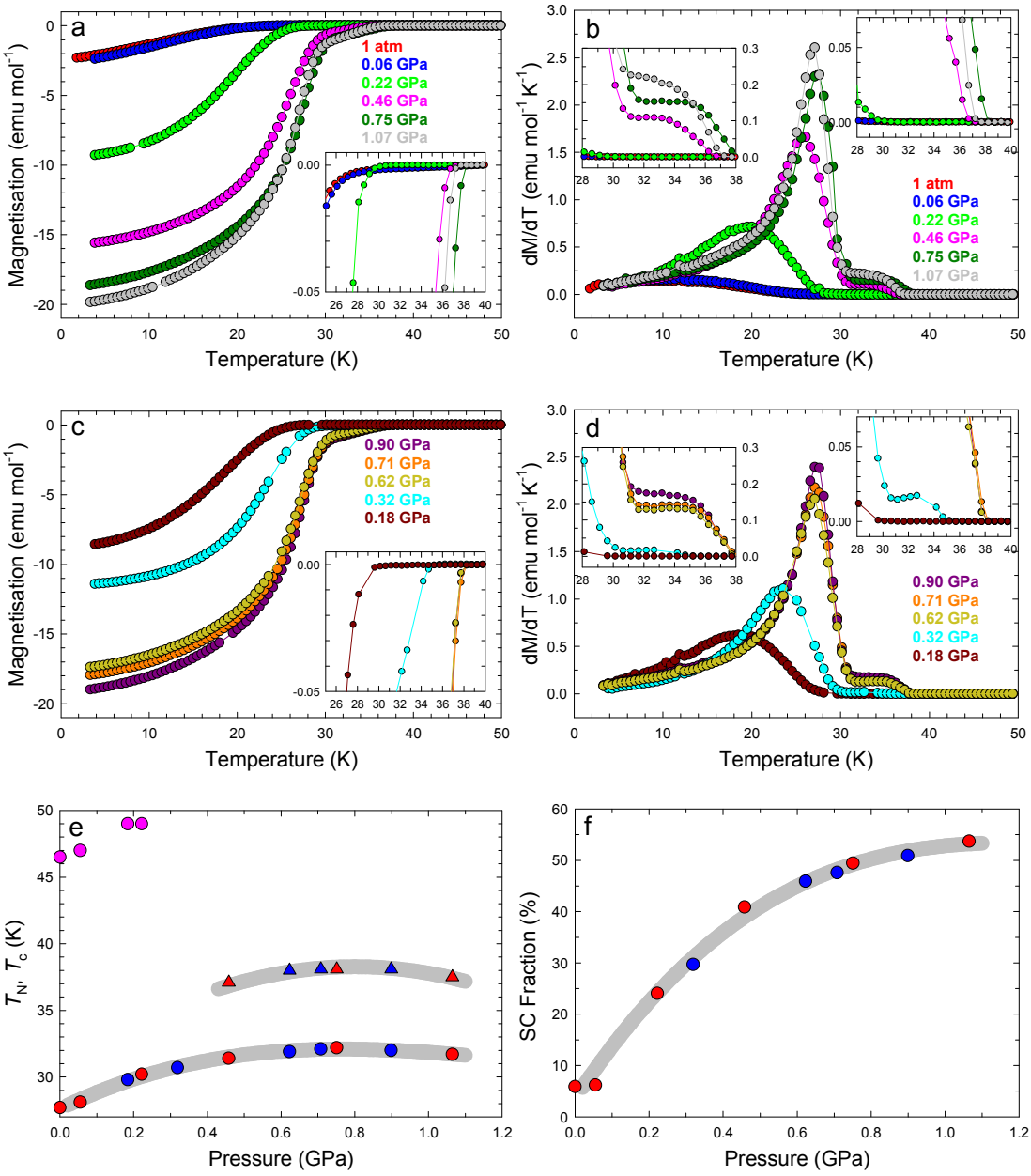

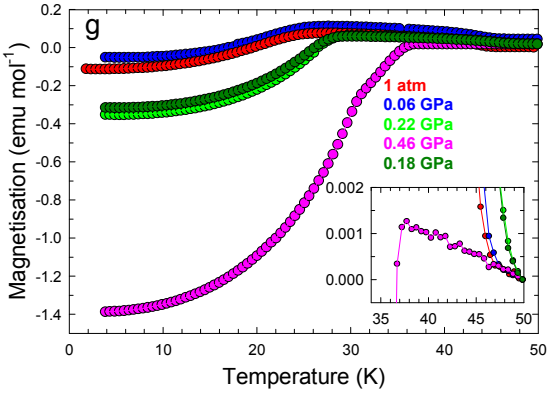

Fig 4.31: High pressure magnetic measurements (ZFC) for the $Rb_{0.25}Cs_{2.75}C_{60}$ sample at an applied field of 20 Oe (19 mg). **a,b:** Magnetisation, M and first derivative of the magnetisation, dM/dT as a function of temperature upon pressurisation. **c,d:** Magnetisation, M and first derivative of the magnetisation, dM/dT as a function of temperature upon pressure release. The insets of **a**, **b**, **c** and **d** show expanded versions of the plots near the onset of the superconducting transition. **e,f:** Transition temperatures, T_N and T_c (circles/triangles represent data for the FCC/A15 phases) and superconducting fraction as a function of pressure; the grey lines are guides-to-the-eye. Red (blue) circles indicate increasing (decreasing) pressure values. Pink markers show the values of T_N. **g:** FC magnetisation measurements (20 Oe) as a function of pressure. The inset shows an expanded region of the plot near the onset of the ferromagnetic transition.

4.6.3 $Rb_{0.12}Cs_{2.88}C_{60}$ (MT011_3)

The final sample studied as a function of pressure in this series is that with nominal composition $Rb_{0.12}Cs_{2.88}C_{60}$. This sample has as a dominant component the A15 polymorph (~70%) but contains a very small fraction (~8%) of the competing FCC polymorph. The magnetic signature of the former (T_N = 46.5 K) is clearly evident in the ambient *P* FC magnetisation measurements (Fig. 4.28(c)). Nonetheless at the time of this work, this sample is unique as it represented the first opportunity to probe the possibility of studying the effects of chemical pressure of the A15-structured Cs_3C_{60}. However, as already established from the X-ray diffraction study the composition of the A15 phase appears to be invariant with Rb co-dopant levels. Since there is again a significant proportion of the A15 polymorph it allows superb definition of both its canted antiferromagnetic response and its transition to the superconducting state (Fig 4.32(g) and insets of Fig. 4.32(b) and (d)). Intermediate pressure FC measurements

were again taken, the trend showing that increasing pressure increases T_N to 49 K; however, between 0.22 and 0.32 GPa, the AFI state is completely suppressed, Fig 4.32(g).

At ambient pressure the superconducting fraction is <0.1 % and when pressed to 0.99 GPa, it rises to 45.6 % (Fig. 4.32(f)). At the same time, T_c first increases reaching a maximum for the A15 phase of 38.2 K at 0.73 GPa and a maximum for the FCC phase of 34.3 K at 0.73 GPa (Fig. 4.31(e)). Once again, these trends are reversible as when the pressure is released, there is no observable hysteresis in the T_c(P) curves.

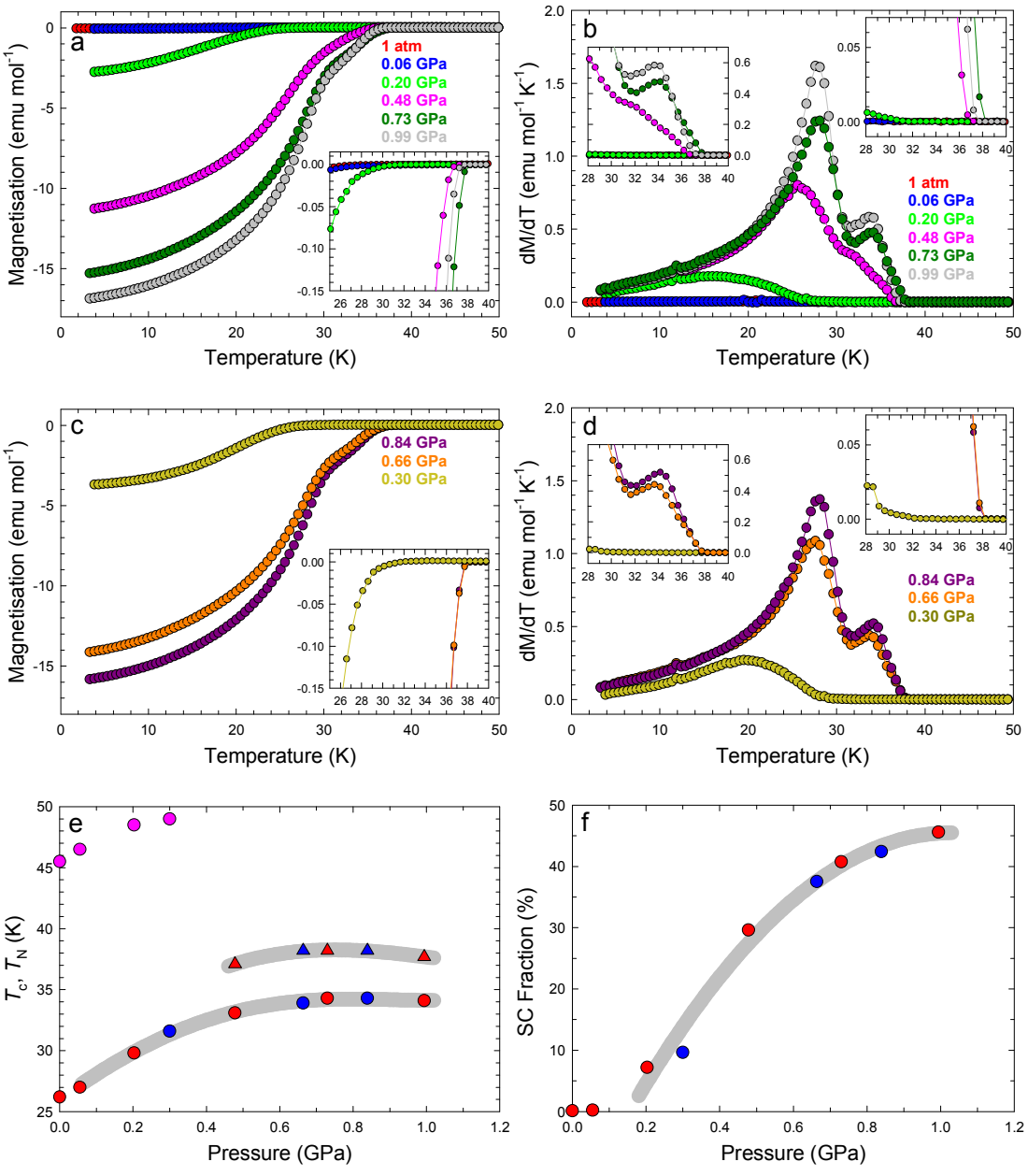

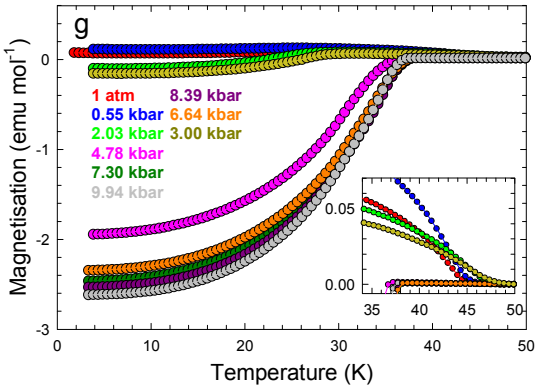

Fig 4.32: High pressure magnetic measurements (ZFC) for the $Rb_{0.12}Cs_{2.88}C_{60}$ sample at an applied field of 20 Oe (19 mg). **a,b:** Magnetisation, M and first derivative of the magnetisation, dM/dT as a function of temperature upon pressurisation. **c,d:** Magnetisation, M and first derivative of the magnetisation, dM/dT as a function of temperature upon pressure release. The insets of **a**, **b**, **c** and **d** show expanded versions of the plots near the onset of the superconducting transition. **e,f:** Transition temperatures, T_N and T_c (circles/triangles represent data for the FCC/A15 phases) and superconducting fraction as a function of pressure; the grey lines are guides-to-the-eye. Red (blue) circles indicate increasing (decreasing) pressure values. Pink markers show the values of T_N. **g:** FC magnetisation measurements (20 Oe) as a function of pressure. The inset shows an expanded region of the plot near the onset of the ferromagnetic transition.

4.6.4 Summary – superconductivity in the A15 $Rb_xCs_{3-x}C_{60}$ series

An important conclusion derived from the results obtained earlier for the FCC-rich samples is upheld in the A15-rich samples and illustrated in Fig. 4.33, which collects together the evolution of the superconducting fraction in the A15-rich $Rb_xCs_{3-x}C_{60}$ series as a function of both Rb content, *x* and applied pressure, *P*. For all samples in this series, the A15 phase is not superconducting at ambient pressure; in contrast, superconductivity is observed for the FCC phase. The superconducting fraction observed in the FCC phases is dependent on the Rb doping level. $Rb_{0.12}Cs_{2.88}C_{60}$ shows signs of trace superconductivity at ambient pressure; as the Rb doping level increases, a transition to a superconducting state occurs as the unit cell volume of the FCC phase is reduced – at the same time, the ambient *P* superconducting fraction is rapidly enhanced. This clearly demonstrates the effect of chemical pressure resulting from the

co-intercalation of the smaller Rb cation in the FCC phase. Additionally, as the applied pressure is increased the unit cell volumes of both superconducting polymorphs are reduced and the superconducting fraction for all samples increases parabolically and eventually saturates. In the case of the A15 phase, very moderate pressure is enough to switch on superconductivity; however, the required pressure is constant across all samples, as the obtained composition of the A15 phase appears to have been insensitive to changing of the Rb amount in the reaction procedures. On the other hand, the FCC phase is sensitive to Rb doping levels; at low Rb doping levels, very moderate pressure is enough to switch on superconductivity. Therefore it can be said that for both polymorphs the application of either chemical or physical pressure can drive the transition to the superconducting state by increasing the bandwidth W and therefore driving the system below the critical value of the (U/W) ratio for the Mott metal-insulator transition.

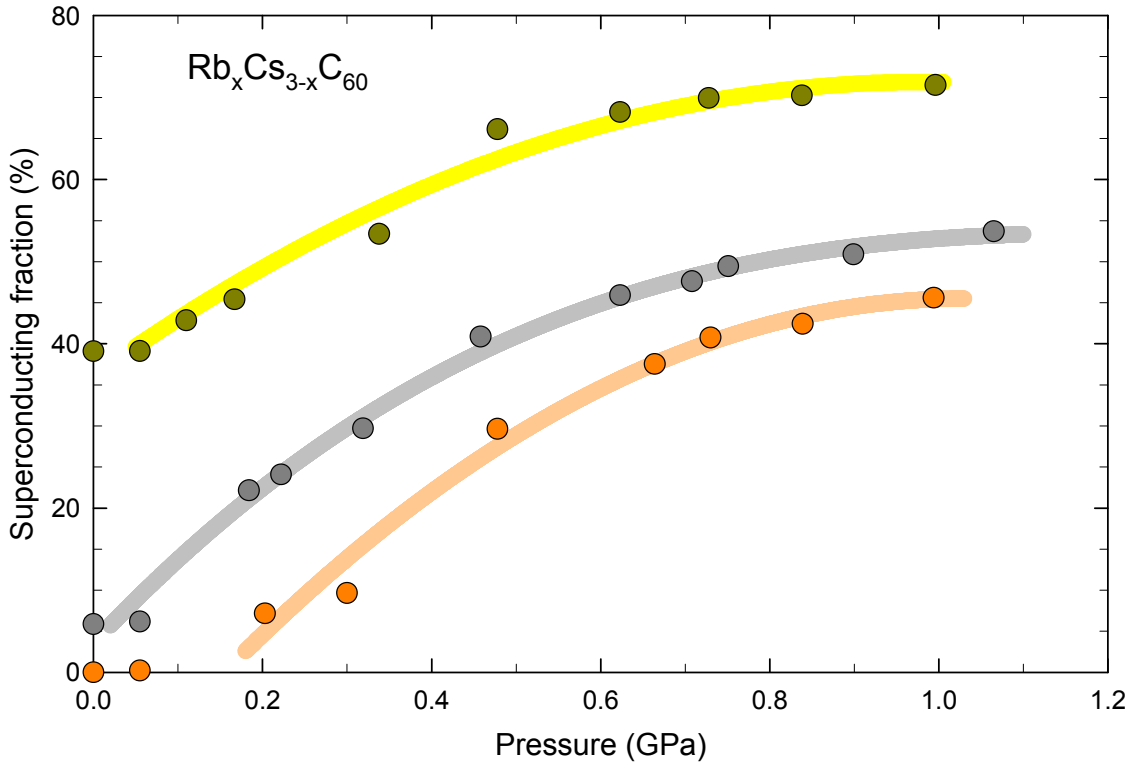

Fig 4.33: Superconducting fraction as a function of pressure for the $Rb_xCs_{3-x}C_{60}$ samples produced with methylamine as the solvent. Dark-yellow circles represent sample MT001_2 (nominal, x = 0.50), grey MT005_1 (nominal, x = 0.25) and orange MT011_3 (nominal, x = 0.12). The respective colour lines are a guide-for-the-eye. [*]

The second important conclusion which arises from these measurements is the pressure response of the electronic properties of the FCC phase as a function of applied pressure and Rb content, summarised in Fig. 4.34. Increasing pressure leads to superconductivity domes for each individual sample with the maximum T_c of each dome increasing with increasing Cs content (i.e. with increasing unit cell size). At the same time, the pressure at which the maximum T_c occurs shifts to higher values again with increasing Cs content. The dominant A15 phase of these phase assemblages does not exhibit the same sensitive response, as already stated. Considering all the structural and magnetic evidence, the conclusion is that the composition is very close to the parent Cs_3C_{60} phase irrespective of the presence of Rb or not in the starting reactant materials.

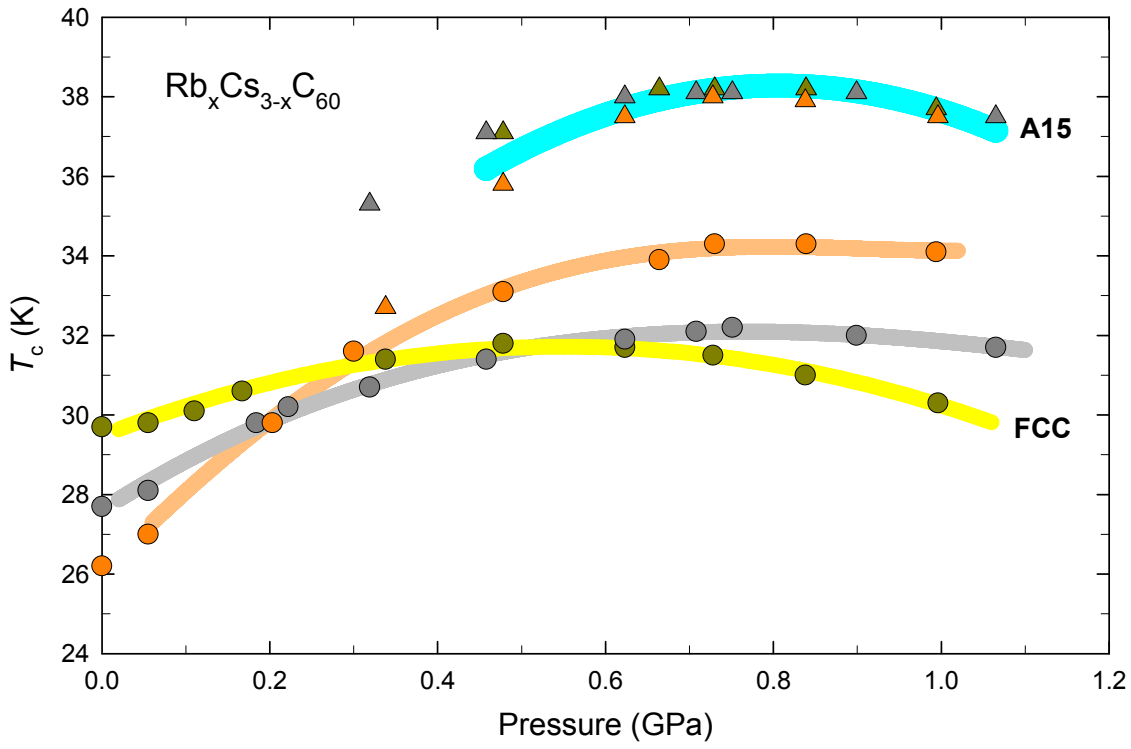

Fig 4.34: Superconducting transition temperature (T_c) as a function of pressure for the FCC $Rb_xCs_{3-x}C_{60}$ phase and for A15 Cs_3C_{60} phase. Dark-yellow colour represents samples of nominal x = 0.50, grey x = 0.25, and orange x = 0.12. Circles represent data for the FCC phases, triangles for the A15 Cs_3C_{60} phase. The respective colour lines are guides-to-the-eye for the FCC polymorph. A single cyan line is used as a guide-for-the-eye for all A15 phases as they have a fixed Cs_3C_{60} stoichiometry.

In order to convert Fig. 4.34 to one where the same microscopic parameter is utilised as a probe of the electronic properties, equation 4.1 was employed to produce Fig. 4.35, where T_c is now shown as a function of unit cell volume per C_{60} unit. This directly probes the interfullerene separation which essentially is the key parameter which controls the bandwidth, W and therefore for fixed Hubbard U (a molecular C_{60} property), it controls the metal/insulator properties of the materials.

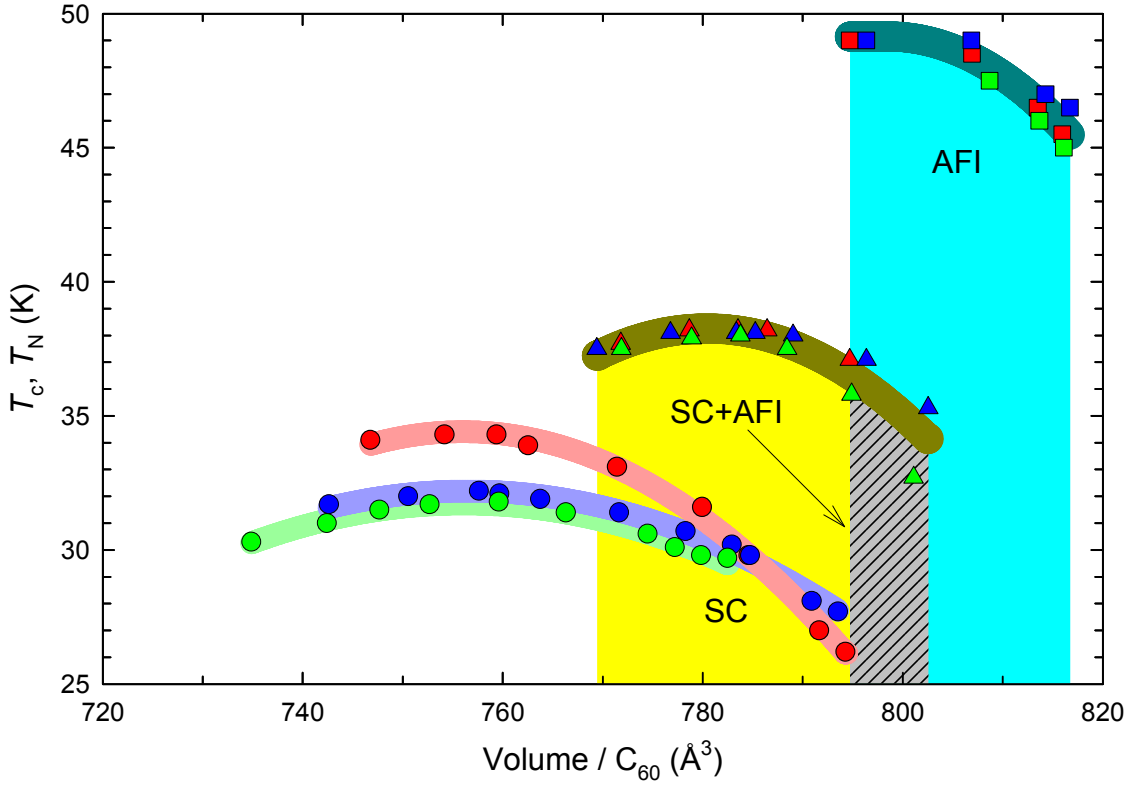

Fig 4.35: Superconducting transition temperature (T_c) and Néel temperature (T_N) as a function of room temperature unit cell volume occupied per C_{60} molecule for the FCC $Rb_xCs_{3-x}C_{60}$ phase and for A15 Cs_3C_{60} phase. Green colour represent samples of nominal x = 0.50, blue x = 0.25, and red x = 0.12. Circles represent T_c data for the FCC phases, triangles T_c data for the A15 Cs_3C_{60} phase and squares T_N data for the A15 Cs_3C_{60}. The respective colour lines are guides-to-the-eye for the FCC polymorph. A single dark-yellow line is used as a guide-for-the-eye for all A15 phases as they have a fixed Cs_3C_{60} stoichiometry.

Fig. 4.35 clearly summarises the global response of A15 Cs_3C_{60} to changes in C_{60} interfullerene separation induced by either chemical or physical pressure. It is

immediately apparent that for the two different polymorphs, the T_c(V) domes do not map onto each other. The FCC phase has a lower T_c and the onset of the M-I transition occurs at a smaller value of V/C_{60}. This is presumably related to the differing intermolecular overlaps between the two structural families and is in agreement with the results of theoretical calculations, which find a larger density-of-states at the Fermi level at the same interfullerene separation for the A15 family. What is however also immediately evident and is extremely intriguing is that the T_c(V) domes of the FCC isostructural $Rb_xCs_{3-x}C_{60}$ series are also shifted from each other in both T_c and V/C_{60} space, confirming our conclusions in our study of the FCC-rich materials. Namely, they are not superimposable with T_c(max) and V/C_{60}(max) both shifting to higher values with decreasing Rb content. This is at present surprising as within a rigid band picture and for a fixed band filling, the electronic and superconducting properties will be controlled entirely by the magnitude of the bandwidth, W. Therefore the present results call for additional subtleties controlling the properties of these FCC phases. A possible candidate for the non-rigid-band behaviour observed and the Rb-specific control of the electronic properties may be the increased positional disorder associated with the occupation of the same interstitial site by ions of differing ionic size (Rb^+ versus Cs^+).

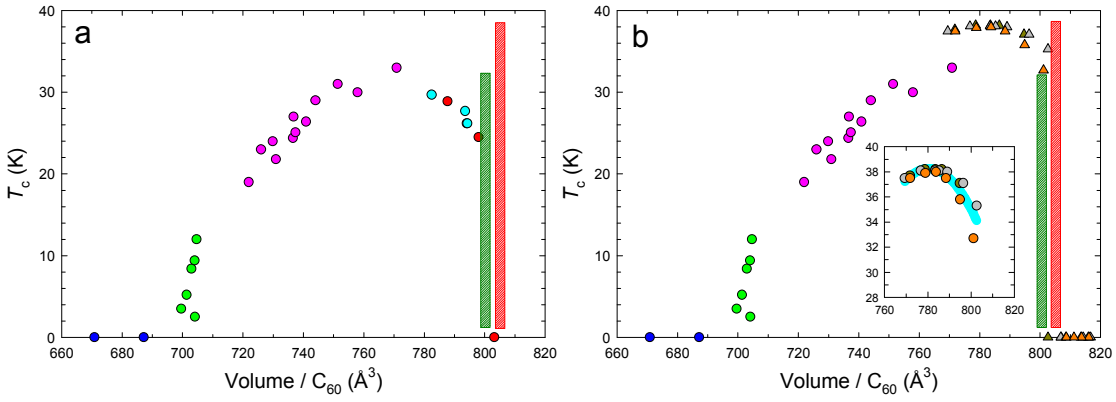

Fig 4.36: Superconducting transition temperature (T_c) as a function of room temperature unit cell volume occupied per C_{60} molecule. (**a**) shows the ambient pressure data for the FCC phase $Rb_xCs_{3-x}C_{60}$ samples, (**b**) shows A15-Cs_3C_{60} as a function of pressure (also displayed in the inset). Blue circles indicate Li_2CsC_{60}, green circles primitive cubic materials, and pink circles FCC-structured materials. Red (cyan) circles in (**a**) represent ambient pressure data for FCC phase in the FCC-rich (A15-rich) $Rb_xCs_{3-x}C_{60}$

samples. Dark-yellow triangles in **b** represent A15 phase of samples of nominal x = 0.50, grey x = 0.25, and orange x = 0.12. The green (red) shaded region in **a**, **b** shows the M-I transition region for the FCC (A15) phase.

To put into context the data contained in Fig 4.35, the findings of both the A15 and FCC-rich materials were plotted alongside the literature data of the FCC series, Fig 4.36. In comparison to the BCC-structured polymorph (A15 phase), there clearly is a shift in the M-I transition to a smaller V/C_{60} for the FCC-structure. From the ambient pressure data in Fig 4.36(a) the presence of the M-I transition is noted as there is a dip in T_c for larger volume FCC A_3C_{60} materials. The pressure dependence of T_c for the majority A15 Cs_3C_{60} phases are shown in Fig 4.36(b). Undoubtedly there is an observed difference in the V onset of the M-I transition between the A15 and FCC polymorphs.

4.7 Conclusions

The results presented in this chapter closely mirror earlier works by Ganin, Takabayashi *et al*,[1,2,3,8] where they demonstrated the isolation of a three-phase material with stoichiometry Cs_3C_{60} that was not superconducting at ambient pressure; however, application of pressure yielded a maximum T_c of 38 K at 0.7 GPa. The majority A15 phase was responsible for the observed high T_c. Samples described in this section display the same physical characteristics. Attempts were made to study the effects of tuning the unit cell volume of the A15 phase by partial substitution of the smaller Rb cation (chemical pressure effects); however, this exercise proved unsuccessful for the A15 phase, which appears resilient to cationic substitution of Cs^+ by Rb^+. As the doping levels of Rb in the reactants were decreased, the A15 phase obtained showed comparable unit cell volumes. In addition, the X-ray powder diffraction measurements implied refined Cs contents of all A15 components close to each other within the error of the refinements. There was some weak evidence that there may be partial occupancy of the cation site, i.e. there may be $Cs^+ + Rb^+$ but the

total occupancy is <1.0. Such a scenario was found impossible to incorporate within a refinable structural model, as the data could simply not relay this information.

The magnetisation data also obtained for this series of samples similarly suggest that the level of change in the cationic site is negligible at best. The maximum T_c and hence its pressure dependence for each sample are more or less superimposable and independent of the Rb levels.

In contrast, the minority FCC phases in the present assemblages changes a great deal with the Rb doping levels. As the Rb doping level is reduced the unit cell volume of the FCC phase decreases in line with the phase fraction and amount of Rb doping. The FCC phases of these materials are in minority and poorly crystalline as the synthetic protocol was optimised to enrich the A15 phase content in the samples; nonetheless, the evolution of this phase was followed in considerable detail obtaining results in good accord with those described in *chapter 3*.

4.8 References

[1] Ganin A. Y., Takabayashi T., Khimyak Y. Z., Margadonna S., Tamai A., Rosseinsky M. J., Prassides K. *Nature Materials* **2008**, 7, 367-371

[2] Darling G. R., Ganin A. Y., Rosseinsky M. J., Takabayashi Y., Prassides K. *Phys. Rev. Lett.* **2008**, 101, 136404-136408

[3] Takabayashi Y., Ganin A. Y., Jeglic P., Arcon D., Takano T., Iwasa Y., Ohishi Y., Takata M., Takeshita N., Prassides K., Rosseinsky M. J. *Science* **2009**, 232, 1585-1590

[4] Larsen A. C., Von Dreele R. B. *GSAS software, Los Alamos National Laboratory Report LAUR* **1994**, 86-748

[5] Toby B. H. *J. Appl. Cryst*. **2001**, 34, 210-213

[6] *LMGP-Suite Suite of Programs for the interpretation of X-ray Experiments, by Jean laugier and Bernard Bochu, ENSP/Laboratoire des Matériaux et du Génie Physique, BP 46. 38042 Saint Martin d'Hères, France. WWW: http://www.inpg.fr/LMGP and http://www.ccp14.ac.uk/tutorial/lmgp/*

[7] Shannon R. D., *Acta Cryst. A* **1976**, 32, 751-767

[8] Takabayashi T., Ganin A. Y., Rosseinsky M. J., Prassides K. *Chem. Commun*. **2007**, 870–872

Chapter 5

The family of quaternary $Na_{2-x}K_xCsC_{60}$ ($0.0 \leq x \leq 2.0$) fulleride superconductors

5.1 Introduction

In superconducting FCC A_3C_{60} systems, it has been widely reported that T_c increases monotonically with interfulleride separation.[1,2,3,4,5] Within the close-packed FCC structure, large high-symmetry cavities exist where smaller atoms, ions or molecules can reside. There are two types of such cavities - one larger for which there are six C_{60} near-neighbours (octahedral cavity, O_h, r = 2.06 Å) and one smaller for which there are only four near- neighbour C_{60} molecules (tetrahedral cavity, T_d, r = 1.12 Å). The separation between the C_{60}^{3-} anions is directly related to the size of the cation inserted into the tetrahedral cavity. Recalling the ionic sizes of Na^+ (r = 0.99 Å), K^+ (r = 1.37 Å), Rb^+ (r = 1.52 Å) and Cs^+ (r = 1.67 Å),[6] it is apparent that the octahedral cation occupancy has little influence on the interfulleride separation (as it is smaller than all), whereas only Na^+ is smaller than the size of the tetrahedral cavity.

If the structural properties of the A_3C_{60} systems are plotted against decreasing unit cell volume, a phase transformation is observed from FCC $Fm\bar{3}m$ structures to orientationally-ordered primitive cubic (space group $Pa\bar{3}$) depending on the identity of the ion residing in the tetrahedral hole. The proceeding text discusses the structure of pristine C_{60} solids and then the ramifications of inserting cations of increasing size into the T_d cavities.

5.1.1 Spherically Disordered A_3C_{60} Fullerides

Diffraction studies of solid C_{60} have shown that at room temperature the C_{60} molecules are translationally ordered but rotationally disordered - this is termed spherically disordered FCC phase (space group $Fm\bar{3}m$).[7] As solid C_{60} is cooled below 260 K, extra Bragg peaks emerge in the diffraction pattern and the structure no longer conforms to an FCC lattice; instead a primitive cubic structure is adopted (space group $Pa\bar{3}$). The C_{60} molecules are now rotationally ordered and can adopt one of two energetically-favourable orientations. The most favourable state involves 98°

anticlockwise rotations of all C_{60} units in the unit cell about their local [111] axes. In this preferred orientation, the electron-rich 6:6 C-C "double" bond of one molecule is facing electron deficient pentagon faces of adjacent molecules. In the somewhat less favourable orientation, the electron rich 6:6 bond is facing the centre of a 6-membered ring on an adjacent molecule.

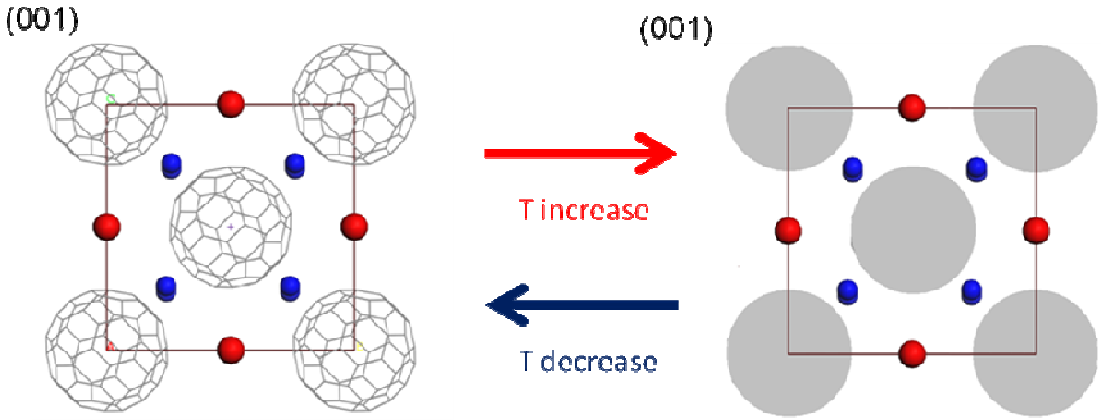

Fig 5.1: Schematic representation of the temperature-induced structural transition from disordered $Fm\bar{3}m$ to orientationally ordered $Pa\bar{3}$ phase of solid C_{60}. Tetrahedral cavities are shown in blue, octahedral cavities in red.

Further cooling below 90 K causes the molecules to freeze resulting in the formation of an orientational glass;[8] the C_{60} molecules no longer have enough energy to flip between the two orientations and the ratio of both remains essentially constant on cooling with 83.5 % existing in the more favourable orientation.

When all the tetrahedral and octahedral cavities are occupied ($2*T_d + 1*O_h$) in an FCC structure the stoichiometry of the resulting compound is A_3C_{60}. When small cations are placed in the tetrahedral holes, as in Na_2CsC_{60}, the C_{60} molecules are still able to rotate freely.[9] Thus at high temperatures, such fullerides are isosymmetrical with pristine C_{60} and adopt an orientationally disordered $Fm\bar{3}m$ structure. On cooling, once again an ordering transition occurs and the low temperature structure is primitive cubic ($Pa\bar{3}$).

5.1.2 *Merohedrally Disordered A_3C_{60} Fullerides*

When the cations occupying the T_d voids are larger than the size of the hole, the C_{60} molecules are no longer able to rotate freely even at high temperatures. The adopted FCC structure incorporates merohedrally disordered C_{60} units frozen into two orientations (in a ratio of 1:1) that are related by a 90° rotation about the unit cell axes.

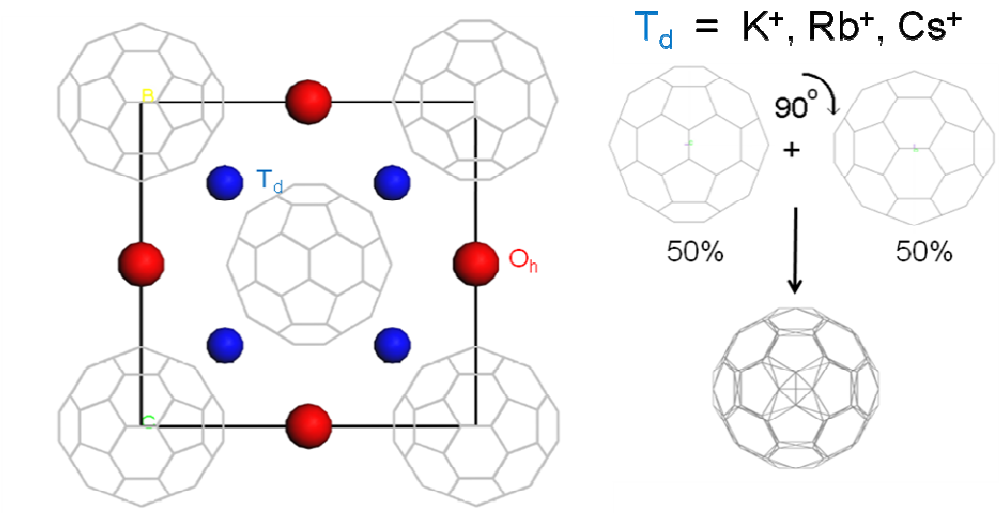

Fig 5.2: Representation of the merohedrally disordered *Fm* $\bar{3}$ *m* structural model adopted by fullerides with large cations in the T_d cavities of a FCC A_3C_{60} structure.

The crystal structure of these materials at high temperature is still FCC; however, the C_{60} molecules are unable to rotate freely due to sterical repulsive interactions, and show no structural transition on cooling to low temperatures. Compounds such as K_2CsC_{60} adopt the merohedrally disordered model,[10] and so do other expanded fullerides like K_3C_{60},[11] Rb_3C_{60} and Rb_2CsC_{60}.[12,13] In these materials the size of the K and Rb cations is larger than that of the tetrahedral void.

5.1.3 Purpose of Present Study

In merohedrally disordered FCC fullerides, the superconducting T_c varies in an established monotonic way with no differences demonstrated by the application of either physical or chemical pressure.[14] However, when smaller ions (Na^+) occupy the tetrahedral interstices, the situation appears to be much more complicated.[8]

The metastable primitive cubic family $Na_2Rb_{1-x}Cs_xC_{60}$ ($1 \leq x \leq 0$) has been of great interest as it displays a much steeper rate of change of T_c with interfullerene spacing[15] than the merohedrally disordered $Fm\bar{3}m$ systems. At the same time, magnetic susceptibility measurements at high pressure on Na_2CsC_{60}[16] have led to the conclusion that the effect of physical[15] and chemical[17] pressure on the superconducting properties of the $Pa\bar{3}$ phases is not identical with that of chemical pressure; in the latter case, T_c is suppressed much faster than when physical pressure is applied (Fig 5.3).

This particular series of quaternary $Na_{2-x}K_xCsC_{60}$ fullerides were chosen for a further detailed investigation because the two parent tertiary fulleride materials, Na_2CsC_{60} and K_2CsC_{60}, adopt different structures. Due to the smaller Na cation in the T_d cavity in Na_2CsC_{60}, this adopts the orientationally ordered $Pa\bar{3}$ structure at low temperature; conversely, K_2CsC_{60} crystallises with the merohedrally disordered $Fm\bar{3}m$ structure. The intention was to explore the synthesis of solid solutions between the parent Na_2CsC_{60} and K_2CsC_{60} phases and therefore to probe in detail the crossover between merohedral disorder and orientational order of the C_{60} units. If one were successful to synthesise $Pa\bar{3}$-type $Na_{2-x}K_xCsC_{60}$ materials whose interfullerene separation was larger than that in the parent Na_2CsC_{60}, one might be able to exploit the larger $T_c(a)$ slope (Fig 5.3) in this family to obtain fullerides with very high T_c. In addition, it will be important to investigate any effects the cooling protocol may have on the structural and magnetic properties of these materials, which straddle the $Pa\bar{3}$ to merohedral $Fm\bar{3}m$ transition region.

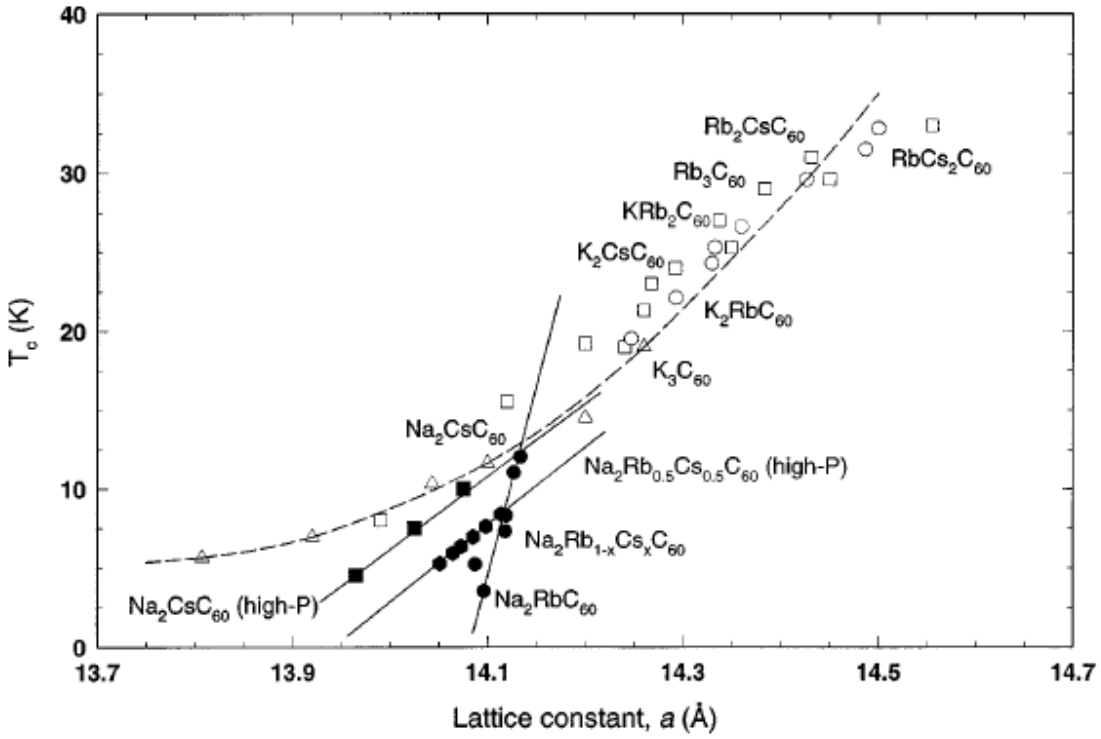

Fig 5.3: Relationship between the superconducting transition temperature, T_c and the cubic lattice constants, a of fulleride salts. Open (Solid) symbols are experimental measurements on fulleride salts with the $Fm\bar{3}m$ ($Pa\bar{3}$) structure at both ambient and elevated pressures. Circles represent ambient pressure data, while elevated pressure experiments are indicated by squares for Na_2CsC_{60} and hexagons for $Na_2Rb_{0.5}Cs_{0.5}C60$. The dotted line shows the predicted T_c values from local density approximation (LDA) calculations given the unit cell parameter. The straight lines are guides to the eye.[14]

5.2 Experimental Methods

5.2.1 Preparation of the precursor, K_6C_{60}

All samples and precursors synthesised are highly air sensitive, so great care is taken to ensure the sample environment is meticulously clean, dry and air free. C_{60} (MER corporation, super gold grade, >99.9% purity) was ground inside the glove box (O_2 < 0.1 ppm, H_2O < 0.9 ppm) and degassed overnight at 200^oC under dynamic vacuum; this procedure was repeated twice. Single-phase K_6C_{60} was prepared by direct

reaction of C_{60} powder with a stoichiometric amount of K (99.95% purity Aldrich). First 30 mg of K (0.767 mmol) was placed into the bottom of a small clean dry tantalum (Ta) cell (diameter 5 mm), followed by the addition of 92 mg of a free-flowing C_{60} (0.128 mmol) powder. The Ta cell was then loaded into a glass tube (diameter 12 mm), removed from the glove box, evacuated, and then sealed under a small pressure of He gas (300 Torr). Finally the reaction mixture was placed in a furnace at room temperature and heated to 250^{o}C at a rate of 5^{o}C/min so that it could be annealed for 17 hours. After the annealing period, the furnace was switched off and was allowed to cool to room temperature.

The precursor was removed from the reaction vessel inside the glove box, then ground using a mortar and pestle, and pelletised before being loaded into a larger Ta cell. The Ta cell was then sealed inside a glass tube under a small pressure of He gas (400 Torr). The pelletised product was annealed for a further period of 48 + 48 hrs at 300^{o}C (identical ramp and cooling rates as above) with one intermediate grinding. Intermediate grindings are essential in order to improve the homogeneity and to obtain single-phase crystalline samples.

Sealing the sample in small glass capillaries under Ar atmosphere, facilitated the study of the reaction products after each grinding, by collecting data with the Siemens D5000 X-ray powder diffractometer (λ = 1.5406 Å) - 2 hr scans over a 2ϑ angular range of 5-40^{o} with a step size of 0.015(6)^{o}. The D5000 data provide a preliminary assessment of the success of the synthetic procedures. The Bragg reflections due to K_6C_{60} are easily identifiable and simple LeBail refinements (space group = $Im\bar{3}$; a = 11.356(1) Å) were performed in order to check the sample composition. In early precursors it can be seen that pure C_{60} is still present meaning the sample was not completely homogeneous, hence the increased annealing time and temperature after intermediate grindings.

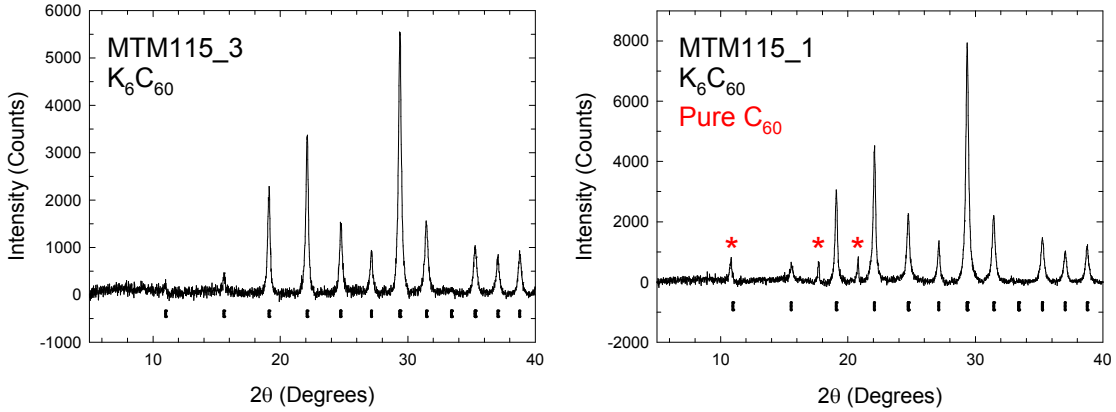

Fig 5.4: X-ray diffraction profiles of K_6C_{60} collected with the Siemens D5000 powder diffractometer (Cu-K_α radiation) in capillary mode at room temperature (background subtracted). Pure C_{60} peaks are identified by using red asterisks.

K_6C_{60} was synthesised for use as a reactant in reactions to produce low K doped ($x < 0.2$) $Na_{2-x}K_xCsC_{60}$ materials. The reasoning behind this is that there will be less uncertainty in weighing K_6C_{60} over pure K. Another added benefit is that it is a lot easier to handle than pure the metal. Additionally, Cs_6C_{60} was synthesised for use as a reactant in the synthesis of the low K-doped materials. Aside from having the same benefits as K_6C_{60}, It also meant that they could be mixed thoroughly prior to annealing, thus aiding in producing homogenous materials.

5.2.2 Preparation of the precursor, Cs_6C_{60}

Single-phase Cs_6C_{60} was prepared by direct reaction of C_{60} powder with excess Cs (99.95% purity Aldrich). Using a narrow glass funnel, 100 mg of C_{60} (0.139 mmol) were placed into the bottom of a glass tube (12 mm diameter). 200 mg of Cs (1.505 mmol) was weighed and placed into a small glass capsule (7 mm diameter); this was then lowered into the glass tube; however, it was stopped 15 cm from the bottom by a narrowing of the tube (in one place), thus some distance was created between the reactants. Into the base of the capsule small grooves were etched so that when

subsequently evacuated, the argon gas can escape. The glass tube was removed from the glove box, evacuated, and then sealed under a small pressure of He gas (300 Torr). Finally the reaction mixture was placed in a 3-zone furnace at room temperature and a pre-designated sequence was run.

The furnace and reaction vessel was setup in such a way that the reaction proceeds via convection currents that will be created by a temperature gradient in the furnace between the two reactants. Cs is at the hotter end of the vessel, and thus when vapourised, it will travel to the cooler end, where the C_{60} resides.

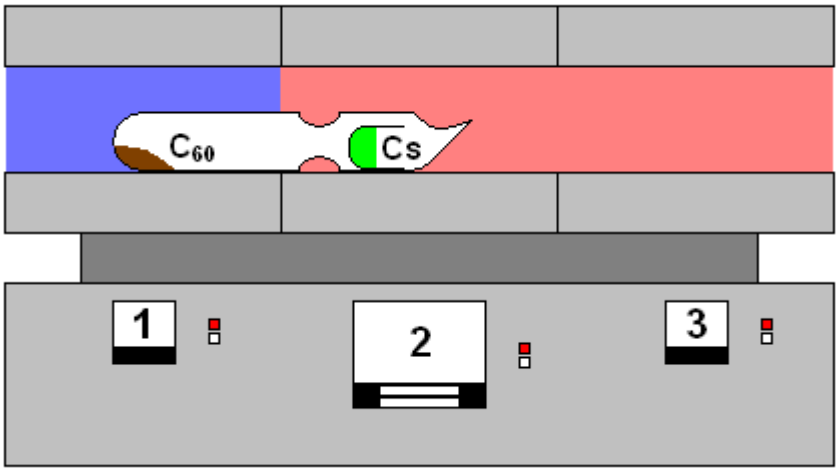

Fig 5.5: Furnace setup for the reaction of excess Cs with C_{60} to produce Cs_6C_{60}. The top of the furnace is cylindrical and the diagram is a cross-section of this area. Temperature controller 1 was set to 330°C, 2 and was 3 were set to 350°C.

The ramp rate of the furnace was set to 2°C/min and the temperature gradient was established before 350°C was achieved. The reactants were annealed for 3 days and then the vessel was cooled to room temperature at the same rate it was heated, whilst reversing the temperature gradient so that when the unreacted Cs condensed, it was away from the newly formed Cs_6C_{60}. As it is easier to maintain a higher temperature in the centre of the furnace, part 3 was set as the cooler zone during

cooling and the position of the vessel adjusted according (without needing to remove it).

In order to make a saturated sample this process was repeated once more; however, at the step where C_{60} was placed at the bottom of the tube, the Cs_6C_{60} isolated from the original experiment was used in its place.

Sealing the sample in small glass capillaries under Ar atmosphere, aided the study of the reaction products after each grinding, by collecting data with the Siemens D5000 X-ray powder diffractometer (λ = 1.5406 Å) - 2 hr scans over a 2θ angular range of 5-40^o with a step size of 0.015(6)^o. The D5000 data provide a preliminary assessment of the success of the synthetic procedure. The Bragg reflections due to Cs_6C_{60} are easily identifiable and simple LeBail refinements (space group = $Im\bar{3}$; a = 11.778(4) Å) were performed in order to check the sample composition.

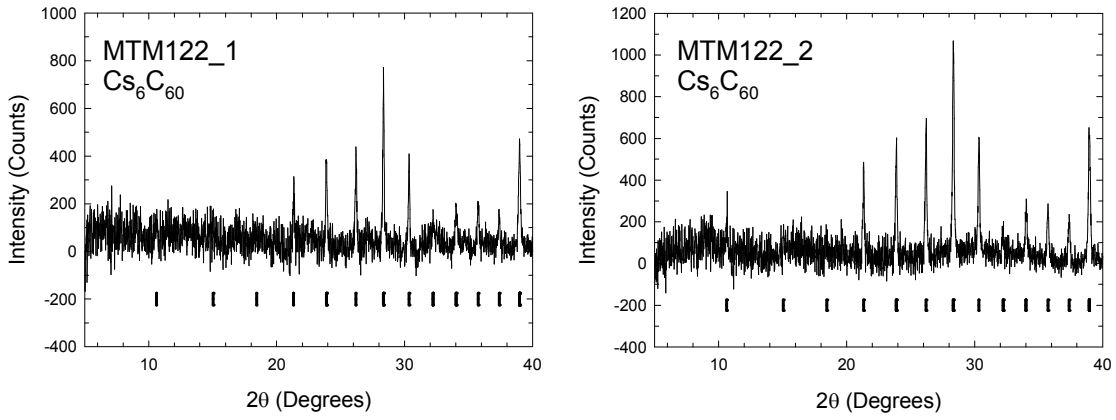

Fig 5.6: X-ray diffraction profiles of Cs_6C_{60} collected with the Siemens D5000 powder diffractometer (Cu-K_α radiation) in capillary mode at room temperature (background subtracted).

5.2.3 Preparation of the $Na_{2-x}K_xCsC_{60}$ ($0.2 < x \leq 2.0$) solid solutions

Crystalline $Na_{2-x}K_xCsC_{60}$ materials were prepared by direct reaction of C_{60} (MER corporation, super gold grade, >99.9% purity) powder with a stoichiometric amount of K (99.95% purity Aldrich), Na (99.95% purity Aldrich) and Cs (99.95% purity Aldrich). First the desired amount of metals (Table 5.1) were placed into the bottom of a clean dry tantalum (Ta) cell (diameter 5 mm) in order of decreasing RMM (first Cs, then K, finally Na). If any metals were stuck around the rim of the Ta cell, the cell was heated to 80^{o}C to melt the metals so that they can flow to the bottom. Secondly the required amount of degassed C_{60} was poured into the cell. The Ta cell was then loaded into a glass tube (diameter 12 mm), removed from the glove box, evacuated, and then sealed under a small pressure of He gas (300 Torr). Finally the reaction mixture was placed in a furnace at room temperature followed by a specific annealing protocol. The samples were annealed initially at 200^{o}C for 3 hours, 300^{o}C for 18 hours and 350^{o}C for 3 days. The ramp rates were 5^{o}C/min and after the annealing period the furnace was switched off to allow it to cool to room temperature.

The initial annealing procedure does not produce a homogeneous material; its purpose is to make a precursor that can be pelletised for further annealing at higher temperatures. The precursor was removed from the reaction vessel inside the glove box, then ground using a mortar and pestle, and pelletised before being loaded into a larger Ta cell. The Ta cell was then sealed inside a glass tube under a small pressure of He gas (400 Torr). The pelletised product was annealed for a further period of 7 + 7 days at 430^{o}C (identical ramp and cooling rates as above) with one intermediate grinding. The furnace used to anneal the samples at 430^{o}C was never switched off, therefore the samples were placed into and removed using tongs and quenched to ambient temperature.

By sealing the sample in small glass capillaries under an Ar atmosphere, the reaction products were inspected quantitatively after each grinding, by collecting data with the Siemens D5000 X-ray powder diffractometer (λ = 1.5406 Å) - 2 hr scans over a 2θ angular range of 5-40^{o} with a step size of 0.015(6)^{o}.

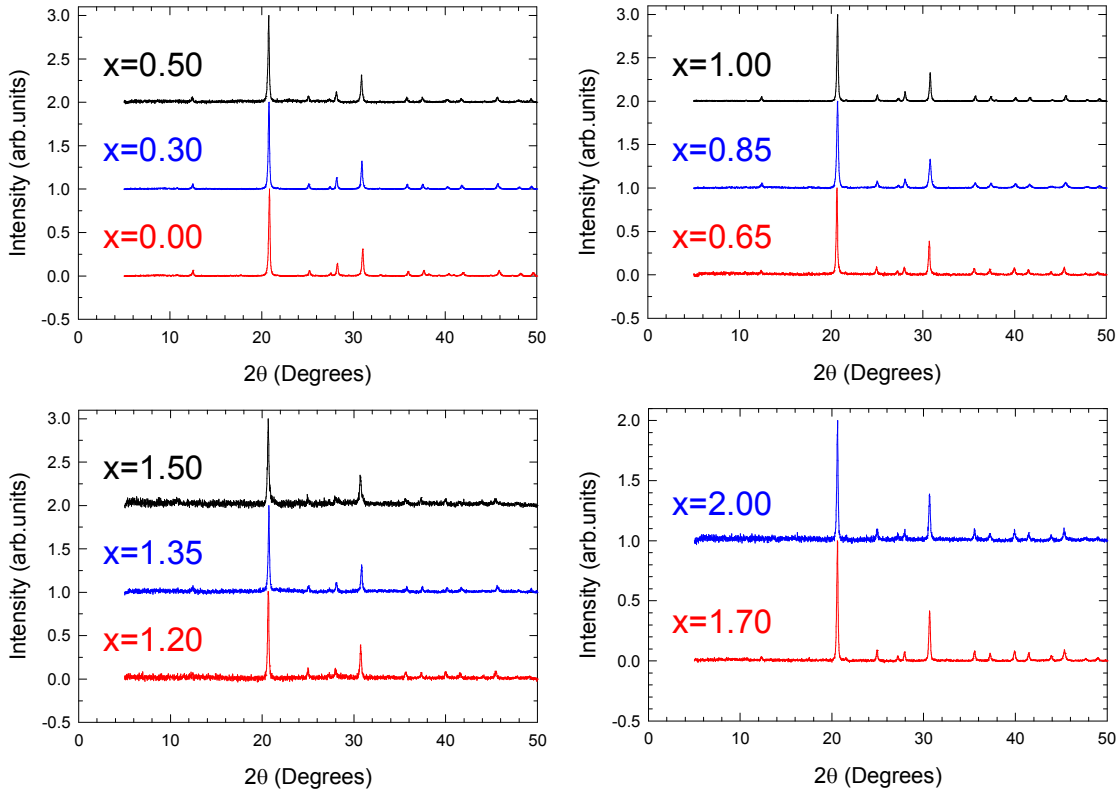

Fig 5.7: X-ray diffraction profiles of $Na_{2-x}K_xCsC_{60}$ collected with the Siemens D5000 powder diffractometer (Cu-K_α radiation) in capillary mode at room temperature. Samples are identified using three different colours.

Precursors Cs_6C_{60} and K_6C_{60} were not used in the synthesis of higher K-doped materials as the procedure itself was experimental and therefore its success was not guaranteed. Additionally, the practicality was questionable as vast quantities of each precursor would be required.

Table 5.1: Masses of the reagents used in the synthesis of $Na_{2-x}K_xC_{60}$ ($0.2 < x \leq 2.0$) materials. Samples MTM115_4 & MTM136_4 were annealed for one extra week. Final product mass is after all annealing protocols.

Sample ID	Nominal x	Moles of Na (mmol)	Moles of K (mmol)	Moles of Cs (mmol)	Moles of C_{60} (mmol)	Mass of Product (mg)
MTM129_3	0.00	0.348	--	0.173	0.173	150
MTM123_3	0.30	0.435	0.077	0.256	0.256	225
MTM115_4	0.50	0.304	0.102	0.203	0.203	180
MTM147_3	0.65	0.217	0.102	0.158	0.161	141
MTM136_4	0.85	0.174	0.128	0.150	0.151	127
MTM132_3	1.00	0.174	0.179	0.173	0.173	151
MTM145_3	1.20	0.174	0.256	0.218	0.218	188
MTM149_3	1.35	0.174	0.358	0.271	0.268	222
MTM142_3	1.50	0.087	0.256	0.173	0.173	147
MTM154_3	1.70	0.053	0.301	0.181	0.178	151
MTM143_3	2.00	--	0.332	0.166	0.167	141

5.2.4 Preparation of the $Na_{2-x}K_xCsC_{60}$ (x = 0.1, 0.2) solid solutions

Crystalline $Na_{2-x}K_xCsC_{60}$ materials were prepared by direct reaction of C_{60} (MER corporation, super gold grade, >99.9% purity) powder with a stoichiometric amount of Na (99.95% purity Aldrich), K_6C_{60} (section 5.2.1) and Cs_6C_{60} (section 5.2.2). First the desired amount of Na (Table 5.1) was placed into the bottom of a clean dry tantalum (Ta) cell (diameter 5 mm). Secondly the desired amount of K_6C_{60}, Cs_6C_{60} and C_{60} were weighed, mixed thoroughly, and then transferred into the Ta cell. The Ta cell was then loaded into a glass tube (diameter 12 mm), removed from the glove box, evacuated, and then sealed under a small pressure of He gas (300 Torr). Finally the reaction

mixture was placed in a furnace at room temperature followed annealing protocols identical to those of the previous samples: 200°C for 3 hours, 300°C for 18 hours and 350°C for 3 days. Following the initial annealing protocol the product was pelletised and annealed for a further period of 7 + 7 days at 430°C with one intermediate grinding.

Capillary data for quantitative analysis were collected on the Siemens D5000 X-ray powder diffractometer (λ = 1.5406 Å) in Debye-Scherrer geometry - 2 hr scans over a 2ϑ angular range of 5-40° with a step size of 0.015(6)°.

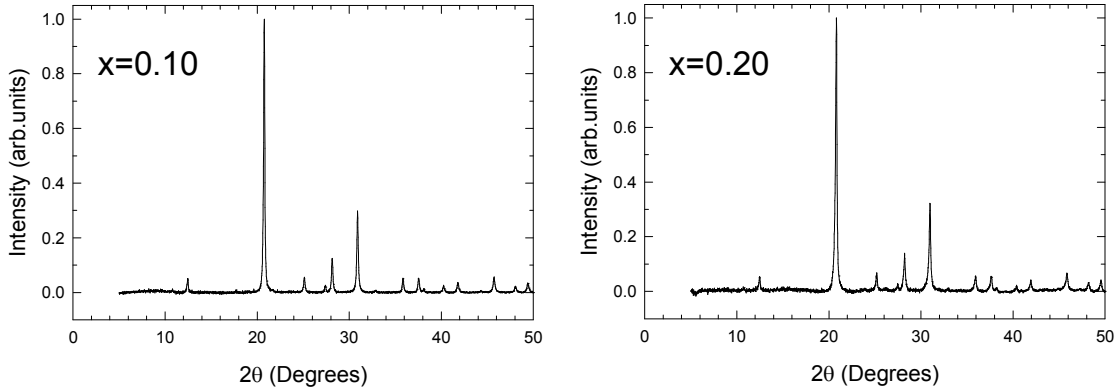

Fig 5.8: X-ray diffraction profiles of $Na_{2-x}K_xCsC_{60}$ (x =0.1, 0.2) collected with the Siemens D5000 powder diffractometer (Cu-K_α radiation) in capillary mode at room temperature.

The adopted experimental procedure utilised the alkali metal precursors (K_6C_{60} and Cs_6C_{60}) synthesised earlier. The two relevant balanced reactions are:

$$1.9Na + 0.1K + Cs + C_{60} \rightarrow Na_{1.9}K_{0.1}CsC_{60} \quad (1)$$

$$1.9Na + {}^{1}/_{60}K_6C_{60} + {}^{10}/_{60}Cs_6C_{60} + {}^{49}/_{60}C_{60} \rightarrow Na_{1.9}K_{0.1}CsC_{60} \quad (2)$$

The benefits of using reaction (2) are immediately apparent: there is smaller error introduced when weighing out K_6C_{60} (relative to K) and also this crystalline material is far easier to handle. Sample MTM148_3 was destroyed by exposure to air during an intermediate grinding; therefore synchrotron X-ray diffraction measurements were not performed.

Table 5.2: Masses of the reagents used in the synthesis of $Na_{2-x}K_xC_{60}$ ($0.0 < x \leq 0.2$) samples. Final product mass was that after all annealing protocols.

Sample ID	Nominal x	Mass of Na(mmol)	Mass of K_6C_{60}(mmol)	Mass of Cs_6C_{60}(mmol)	Mass of C_{60} (mmol)	Product (mg)
MTM131_3	0.10	0.478	$4.19x10^{-3}$	$4.28x10^{-2}$	0.208	199
MTM148_3	0.20	0.391	$7.33x10^{-3}$	$3.62x10^{-2}$	0.208	184

5.2.5 Quenching Protocol

The parent materials Na_2CsC_{60} and K_2CsC_{60} have very different structures and there is the possibility that, when solid solutions are synthesised, phase separation may occur. Therefore synthetic procedures where the products were isolated following rapid quenching from high temperatures were also investigated.

In the quenching experiments, approximately 50% of the products were used. The sample is sealed under 300 Torr of He into a 30 cm long quartz tube, diameter 12 mm. The top of the tube is distorted to prevent slippage when the tube is hung vertically. A quartz tube was used as the vessel needs to withstand extreme temperature shifts. The sealed vessel is suspended midway inside a vertical furnace (Fig 5.9), using two pieces of metal wire that are interlocked. Glass wool pushed into either end of the furnace ensures a good temperature gradient. The furnace is heated to 450^{o}C at a rate of 5^{o}C/min, and held at this temperature for 6 hours. After 6 hours a flask of liquid nitrogen is placed under the furnace and the glass wool is removed. Quickly the interlocked wire is cut and the vessel plummets into the liquid nitrogen thus creating an instant temperature change. The furnace is lifted over the vessel and allowed to stand for approximately 20 minutes. The vessel is removed and allowed to cool to room temperature before being taken into the glovebox. The vessel is then cut with standard glass cutting equipment and 0.5 mm capillaries are made. All samples

were quenched except the parent materials Na_2CsC_{60} and K_2CsC_{60}. SQUID data were collected for all these samples; however, synchrotron powder X-ray diffraction data were only collected for materials that were either merohedral $Fm\bar{3}m$ or mixed phase spherically disordered and merohedral $Fm\bar{3}m$ (i.e. $Na_{2-x}K_xCsC_{60}$; x > 0.5). On the D5000 diffractometer, the measured diffraction profiles are indistinguishable from those obtained for the slow-cooled samples at this resolution.

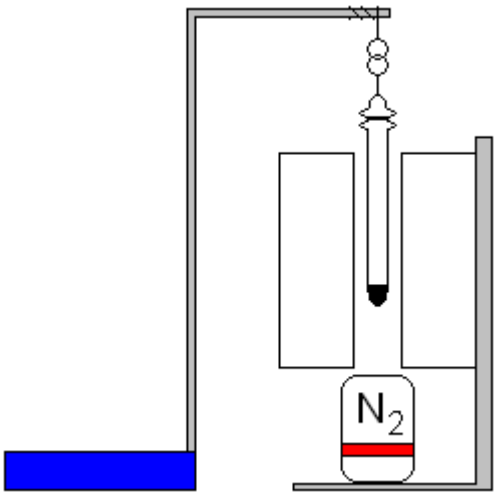

Fig 5.9: Setup for quenching experiments. The material is suspended in a vertical cylindrical furnace at 450°C. A liquid nitrogen-containing vessel is only added minutes before severing the tether.

5.3 Synchrotron X-ray Diffraction measurements

Small amounts (3-6 mg) of each sample were sealed in 0.5 mm glass capillaries, under ambient pressure Ar gas. Room temperature and low temperature data were collected on three different beamlines at the ESRF (ID31 and BM01) and the SRS (Station 9.1). Throughout the diffraction section estimated errors in the last digits are given in parentheses. On 9.1, the wavelength was λ = 0.60545(1) Å and the data were rebinned in the 2θ range 3-31° to a step size of 0.01°. On BM01 the wavelength was λ = 0.71170(1) Å and the data were rebinned in the 2θ range 0-40° to a step size of 0.017°. On ID31 the data were collected over two different experimental periods: (i)

with λ = 0.80007(6) Å and the data rebinned in the 2θ range 4-58^{o} to a step size of 0.005^{o} and (ii) with λ = 0.40289(6) Å and the data rebinned in the 2θ range 1-29^{o} to a step size of 0.002^{o}. On ID31 the room temperature data were collected outside the cryostat with the sample spinning (3000 rpm). For collecting low temperature data, the sample was remounted inside a liquid He flow cryostat, and cooled at a rate of 5 K/min to 20 K. The sample was also spinning during the low temperature data acquisition, but at a slower rate due to instrumental restrictions (1000 rpm).

There was some discrepancy that arose when comparing the results of the Rietveld analysis of the data obtained on the BM01 and 9.1 beamlines with those from ID31. Initial refinements showed that the cell parameters were somewhat different to those from identical samples ran on ID31. Therefore the cell parameters were fixed to the values obtained from the ID31 data and refine the wavelength of the 9.1 and BM01 experiments. The refined wavelength from the SRS experiment came to λ = 0.60592(2) Å and the wavelength of the BM01 experiment came to λ = 0.71124(2) Å. Analysis of the data was performed using the GSAS-equipped EXPGUI interface.

Within the inset of each refinement figure for materials containing the spherically disordered $Fm\bar{3}m$ phase it is noted that reflection (822)/(660) lacks intensity; however, no feasible explanation can be offered for this - occurring at $2\vartheta \approx 27.8^{o}$ when λ = 0.80007(6).

Due to the amount of space required the tables within subsequent diffraction subsections do not contain C_{60} co-ordinates for the spherically disordered $Fm\bar{3}m$ and $Pa\bar{3}$ structures. They can be found of the digital media appendices accompanying this thesis; however, relevant collective occupancies and temperature factors are given.

5.4 Na_2CsC_{60}, slow cooled protocol, room temperature

The synchrotron X-ray powder diffraction data at ambient temperature were refined using both the spherically disordered $Fm\bar{3}m$ (R_{wp} = 6.64%, R_{exp} = 5.82%) and $Pa\bar{3}$ (R_{wp} = 6.32%, R_{exp} = 5.82%) models. The obtained *R*-factors indicate that the

structure adopted is of $Pa\bar{3}$ symmetry, and this is confirmed via a visual comparison of the refinements in Fig 5.10. The values of the lattice constant and unit cell volume are: a = 14.1159(2) Å, V = 2812.7(1) Å^3. The fractional occupancy, N, of the Cs and Na atoms were allowed to vary converging to values of 0.911(8) and 0.865(14) respectively. In the $Pa\bar{3}$ model there are two C_{60} orientations related by a 60^o anticlockwise rotation of each C_{60} about their local [111] axes, and the total occupancy of the C_{60} sites was fixed at 1.0. 78(1)% of the C_{60} molecules reside in the preferred orientation where the electron rich 6:6 "double" bond of one molecule is facing the electron deficient pentagon face of an adjacent molecule, and 22(1)% reside in the less favourable orientation where the electron rich 6:6 bond is facing the centre of a 6-membered ring on an adjacent molecule.

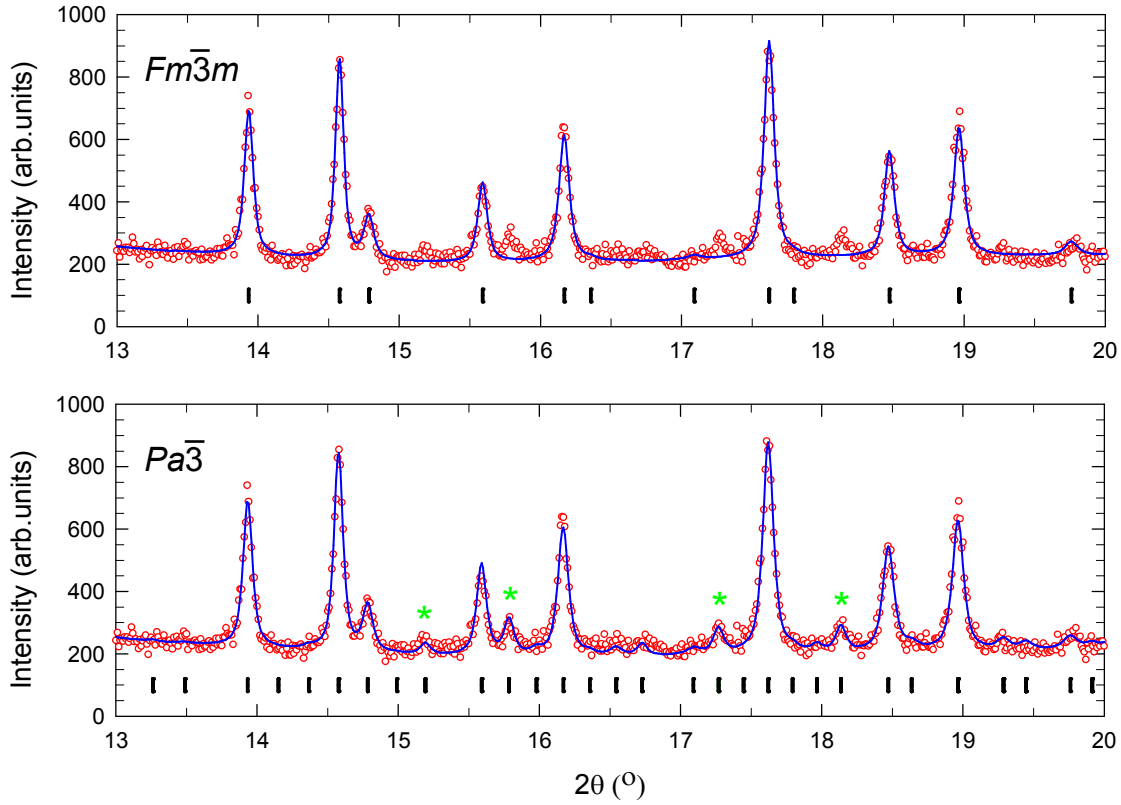

Fig 5.10: Comparison between the $Fm\bar{3}m$ and $Pa\bar{3}$ refinement models for sample Na_2CsC_{60}. From left to right; * = (523)/(611), * = (504)/(443)/(612), * = (623) and * = (552)/(633)/(712). All these reflections have mixed odd/even indices consistent with the primitive cubic symmetry of the structure.

Table 5.3: Results of the room temperature single-phase Rietveld refinement of the *Pa* $\bar{3}$ phase in the sample with overall nominal composition Na_2CsC_{60} (MTM129_3).

	x/a	*y/b*	*z/c*	*N*	B_{Iso}(Å^2)
Cs(1)	0.5	0.5	0.5	0.911(8)	3.9(1)
Na(1)	0.246(1)	0.246(1)	0.246(1)	0.865(14)	2.9(5)
C major	78(1)% - d(C-C) constrained to 1.45(1) Å			0.780(13)	1.5(2)
C minor	22(1)% - d(C-C) constrained to 1.45(1) Å			0.220(13)	1.5(2)

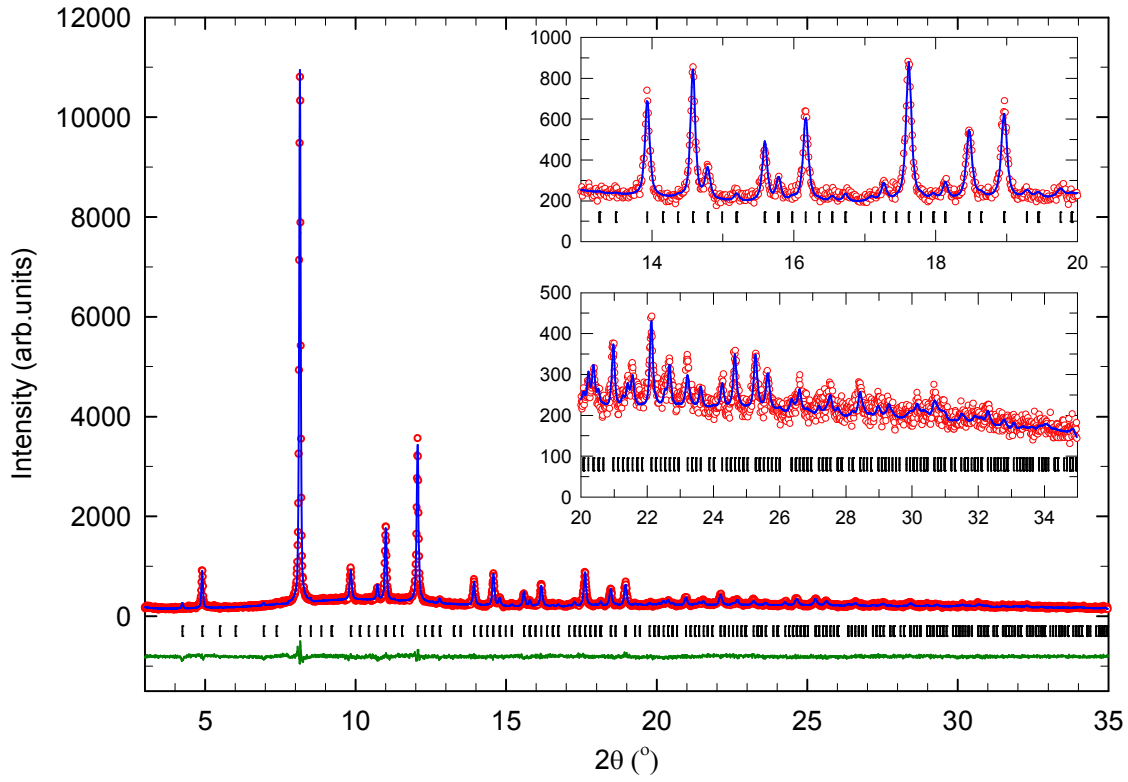

Fig 5.11: Observed (open red circles) and calculated (blue line) data of the room temperature synchrotron powder X-ray diffraction pattern for Na_2CsC_{60}. The bars represent the positions of the Bragg reflections for the cubic *Pa* $\bar{3}$ phase. The wavelength is λ = 0.60592(2) Å.

5.5 $Na_{2-x}K_xCsC_{60}$ with low K doping ($0 \leq x \leq 0.5$), slow cooled protocol, room temperature

The synchrotron X-ray powder diffraction data at room temperature were refined using the spherically disordered *Fm*$\bar{3}$*m*, merohedral *Fm*$\bar{3}$*m* and mixed phase *Fm*$\bar{3}$*m* models. The weighted profile and expected *R*-factors indicate that the structures adopted are spherically disordered *Fm*$\bar{3}$*m* (Table 5.4); this is confirmed via a visual comparison of the refinements, Fig 5.12. In the low K doping cases, the mixed phase model offers no significant improvement in refinement quality; the merohedral component of these refinements shows highly negative temperature factors and its inclusion seems only to account for a very slight asymmetry observed in the peak shape. The values of the lattice constants and unit cell volumes are listed in Table 5.4. If the samples were cubic *Pa*$\bar{3}$ structured, extra reflections would be observed; however, there is no visible evidence for this, and therefore it can be assumed the samples adopt the spherically disordered *Fm*$\bar{3}$*m* structure. This is also consistent with the large jump in cell parameter when compared to the parent material Na_2CsC_{60}, analysed in the previous sub-section.

The fractional occupancy, N, of Cs was fixed at 1.0 (allowing it to refine caused the Na:K ratio of the T_d cavity to be unreasonable) and the Na/K total occupancy was fixed at 1.0; however, the ratio was allowed to refine. In the spherically disordered *Fm*$\bar{3}$*m* model, the C_{60} molecules are translationally ordered; however, as the size of the Na^+ cation is smaller than the size of the T_d cavity they can rotate freely.

Table 5.4: Summary results of the Rietveld refinements of the diffraction data of the series $Na_{2-x}K_xCsC_{60}$ ($0.0 \leq x \leq 0.5$) at room temperature.

Parameter	*MTM129_3*	*MTM131_3*	*MTM123_3*	*MTM119_4*
Nominal x	0.00	0.10	0.30	0.50
λ (Å)	0.60592(2)	0.80007(6)	0.80007(6)	0.80007(6)
Two Phase - Mixed (Disordered / Merohedral)				
R_{wp} **(%)**	--	4.57	4.31	5.00
R_{exp} **(%)**	--	2.48	3.04	3.56
χ^2 **(%)**	--	3.396	2.010	1.973
Dis (%)	--	93.4(2)	88.0(1)	89.6(1)
Mero (%)	--	6.6(2)	12.0(6)	10.4(7)
Single Phase - Merohedral *Fm* $\bar{3}$ *m*				
R_{wp} **(%)**	--	9.19	7.62	7.79
R_{exp} **(%)**	--	2.48	3.04	3.56
χ^2 **(%)**	--	13.73	6.283	4.788
Single Phase - Disordered *Fm* $\bar{3}$ *m* / *Pa* $\bar{3}$				
R_{wp} **(%)**	6.32	4.76	4.55	5.20
R_{exp} **(%)**	5.82	2.48	3.04	3.56
χ^2 **(%)**	1.179	3.684	2.240	2.134
FCC *a* (Å)	14.1159(2)	14.1631(2)	14.1673(2)	14.17466(8)
FCC *V* (Å^3)	2812.7(1)	2841.1(1)	2843.6(1)	2847.99(5)
Refined stoichiometry	$Na_{1.79(3)}Cs_{0.91(1)}C_{60}$	$Na_{1.74(1)}K_{0.26(1)}CsC_{60}$	$Na_{1.71(1)}K_{0.29(1)}CsC_{60}$	$Na_{1.45(2)}K_{0.55(2)}CsC_{60}$

5.5.1 Sample $Na_{1.9}K_{0.1}CsC_{60}$ at room temperature

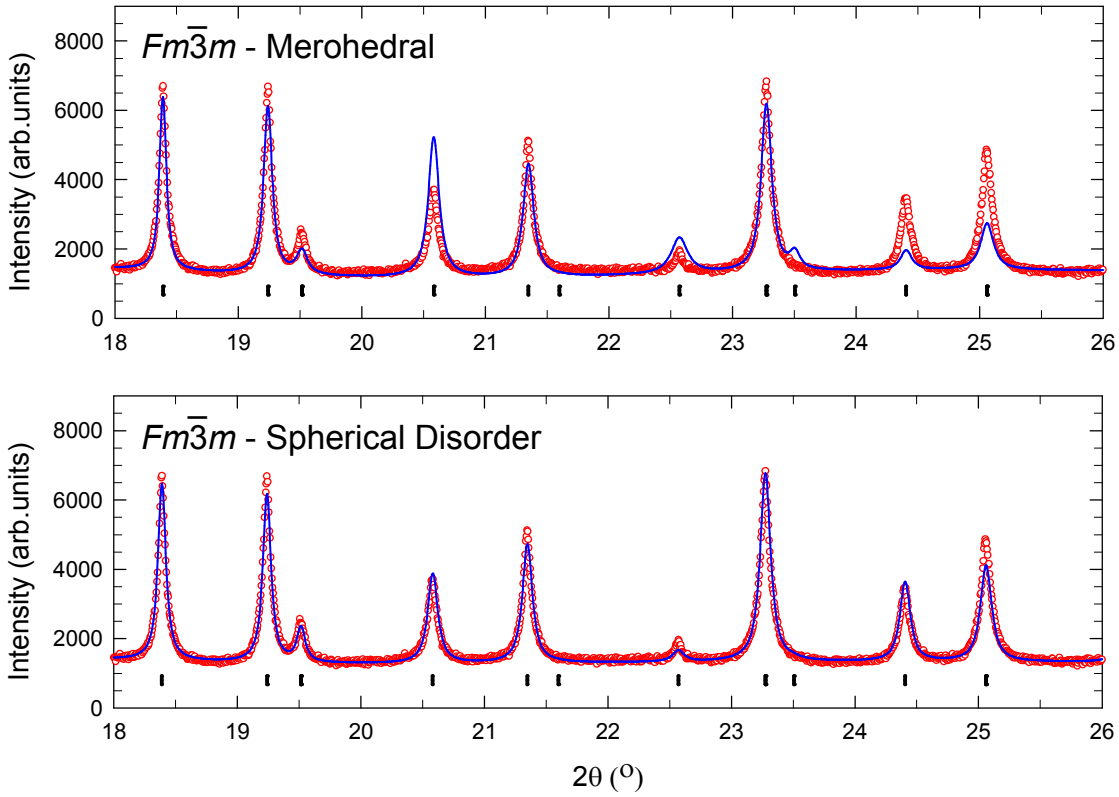

Fig 5.12: Comparison between the *Fm* $\bar{3}$ *m* spherically and *Fm* $\bar{3}$ *m* merohedrally disordered refinement models for the sample of nominal stoichiometry $Na_{1.9}K_{0.1}CsC_{60}$.

Table 5.5: Results of the room temperature single-phase Rietveld refinement of the spherically disordered *Fm* $\bar{3}$ *m* phase in the sample with overall nominal composition $Na_{1.9}K_{0.1}CsC_{60}$ (MTM131_3).

	x/a	*y/b*	*z/c*	*N*	B_{Iso}(Å^2)
Cs(1)	0.5	0.5	0.5	1.0	5.75(5)
Na(1)	0.25	0.25	0.25	0.871(7)	4.8(1)
K(1)	0.25	0.25	0.25	0.129(7)	4.8(1)
C(1-10)	55% - C's with same occupancy and B_{Iso}			0.069(1)	1.09(9)
C(11-20)	45% - C's with same occupancy and B_{Iso}			0.056(1)	1.09(9)

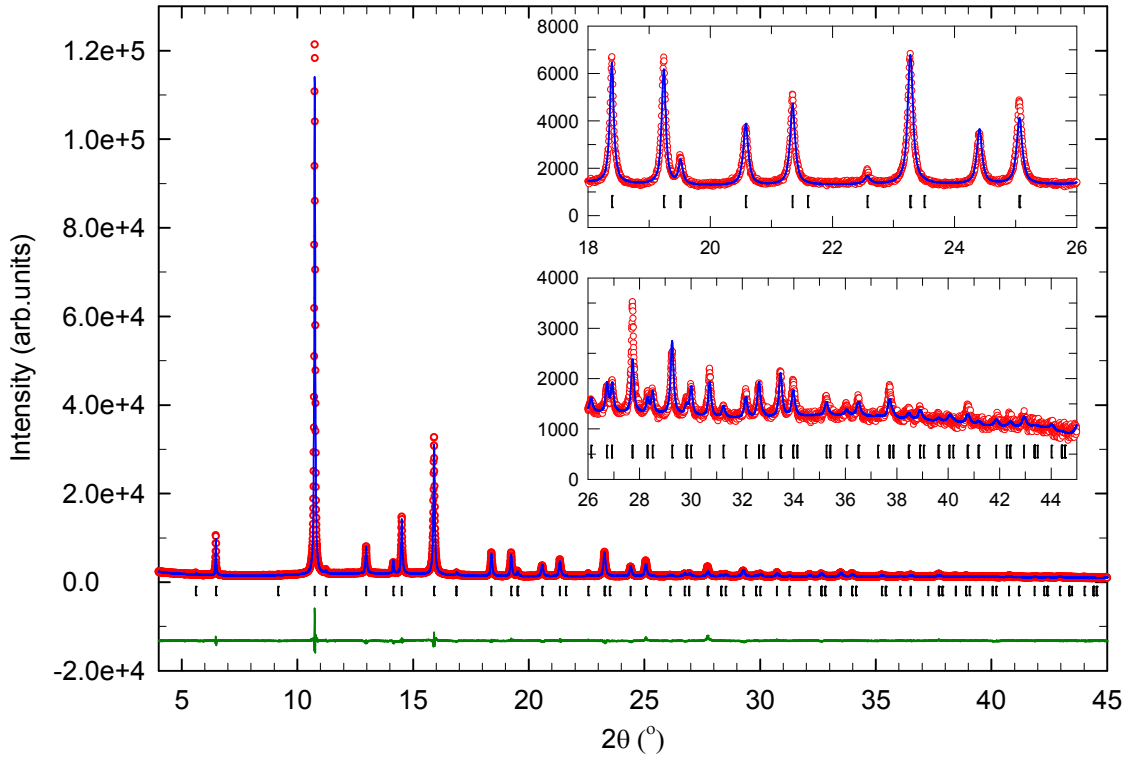

Fig 5.13: Observed (open red circles) and calculated (blue line) data of the room temperature synchrotron powder X-ray diffraction pattern for $Na_{1.9}K_{0.1}CsC_{60}$. The bars represent the positions of the Bragg reflections for the spherically disordered $Fm\bar{3}m$ phase. The wavelength is λ = 0.80007(6) Å.

5.5.2 Sample $Na_{1.7}K_{0.3}CsC_{60}$ at room temperature

Table 5.6: Results of the room temperature single-phase Rietveld refinement of the spherically disordered $Fm\bar{3}m$ phase in the sample with overall nominal composition $Na_{1.7}K_{0.3}CsC_{60}$ (MTM123_3).

	x/a	*y/b*	*z/c*	*N*	B_{Iso}(Å^2)
Cs(1)	0.5	0.5	0.5	1.0	5.96(5)
Na(1)	0.25	0.25	0.25	0.856(7)	5.2(1)
K(1)	0.25	0.25	0.25	0.144(7)	5.2(1)
C(1-10)	45% - C's with same occupancy and B_{Iso}			0.056(1)	1.20(9)
C(11-20)	55% - C's with same occupancy and B_{Iso}			0.069(1)	1.20(9)

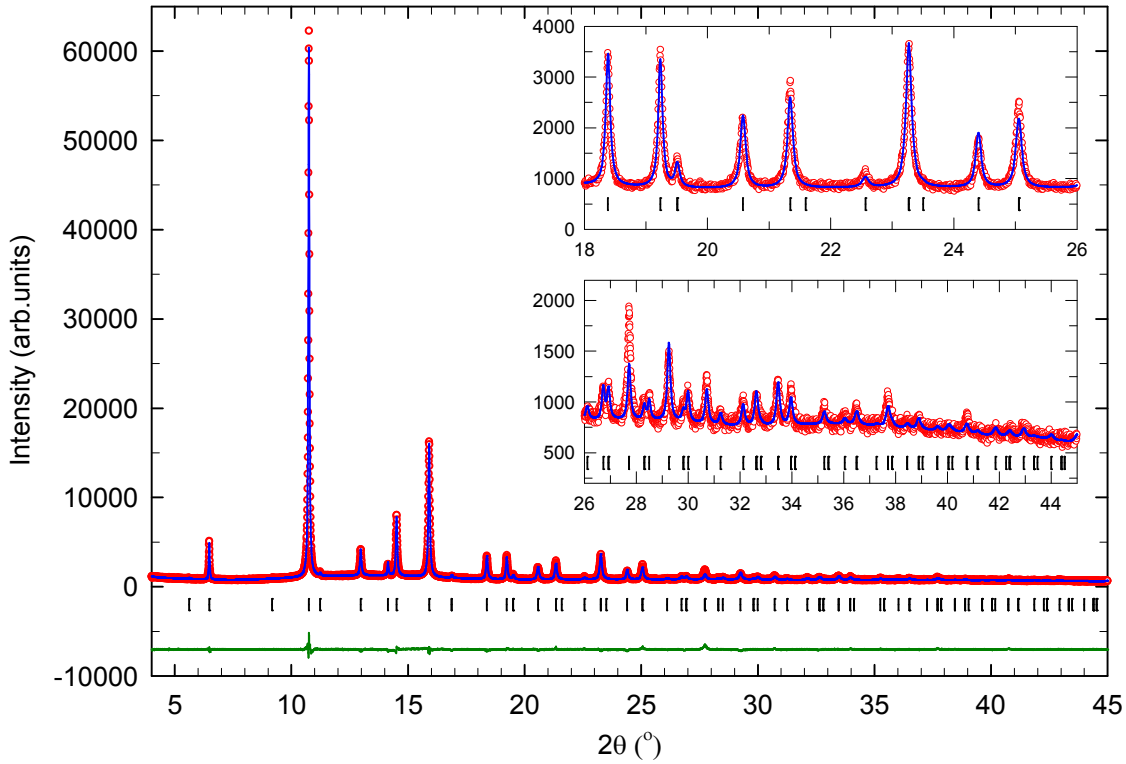

Fig 5.14: Observed (open red circles) and calculated (blue line) data of the room temperature synchrotron powder X-ray diffraction pattern for $Na_{1.7}K_{0.3}CsC_{60}$. The bars represent the positions of the Bragg reflections for the spherically disordered *Fm* $\bar{3}$ *m* phase. The wavelength is λ = 0.80007(6) Å.

5.5.3 Sample $Na_{1.5}K_{0.5}CsC_{60}$ at room temperature

Table 5.7: Results of the room temperature single-phase Rietveld refinement of the spherically disordered *Fm* $\bar{3}$ *m* phase in the sample with overall nominal composition $Na_{1.5}K_{0.5}CsC_{60}$ (MTM119_4).

	x/a	*y/b*	*z/c*	*N*	B_{Iso}(Å^2)
Cs(1)	0.5	0.5	0.5	1.0	6.82(5)
Na(1)	0.25	0.25	0.25	0.725(10)	4.9(2)
K(1)	0.25	0.25	0.25	0.275(10)	4.9(2)
C(1-10)	46% - C's with same occupancy and B_{Iso}			0.057(1)	0.7(1)
C(11-20)	54% - C's with same occupancy and B_{Iso}			0.068(1)	0.7(1)

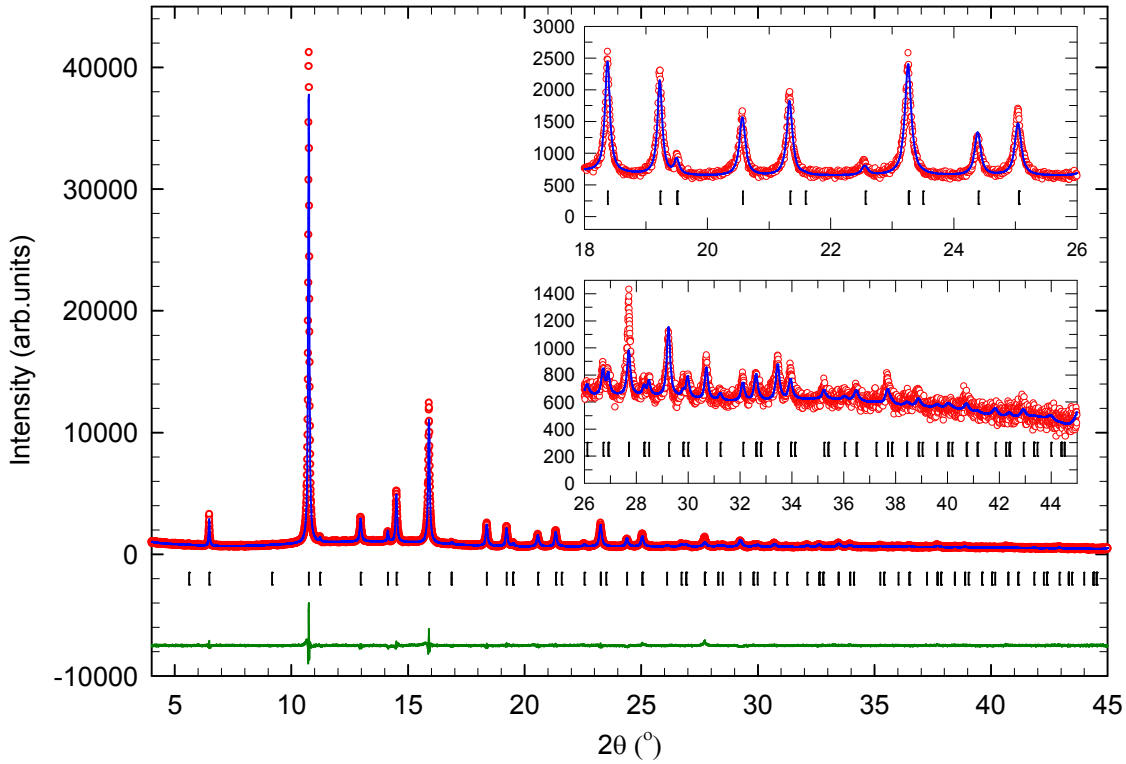

Fig 5.15: Observed (open red circles) and calculated (blue line) data of the room temperature synchrotron powder X-ray diffraction pattern for $Na_{1.5}K_{0.5}CsC_{60}$. The bars represent the positions of the Bragg reflections for the spherically disordered $Fm\bar{3}m$ phase. The wavelength is λ = 0.80007(6) Å.

5.6 $Na_{2-x}K_xCsC_{60}$ with medium K doping (0.5 < x < 1.5), slow cooled protocol, room temperature

The synchrotron X-ray powder diffraction data at room temperature were refined using the spherically disordered $Fm\bar{3}m$, merohedral $Fm\bar{3}m$ and mixed phase $Fm\bar{3}m$ models. The *R*-factors indicate that the structures adopted are a mixture of spherically disordered and merohedral $Fm\bar{3}m$, (Table 5.8), and this is confirmed via a visual comparison of the refinements, Fig 5.16 and Fig 5.20. The values of the lattice constants and unit cell volumes are listed in Table 5.8. In both phases the fractional occupancy, N, of Cs was fixed at 1.0 (allowing it to refine caused the Na:K ratio of the T_d cavity to be unreasonable) and the Na/K total occupancy was fixed at 1.0; however, the ratio was allowed to refine. The peak-shape parameters of the two $Fm\bar{3}m$ models

were constrained to be equal to each other. In the merohedral model the C_{60} molecules are ordered in two orientations that are related by a 90° rotation about the unit cell axes (in a ratio of 50:50), see section 5.1.2 for more information. In the mixed phase refinements the temperature factors of the T_d cations when the merohedral phase is minority are often negative, this is most likely due to its marginal contribution but exacerbated by the large peak overlap witnessed.

Table 5.8: Summary results of the Rietveld refinements of the diffraction data of the series $Na_{2-x}K_xCsC_{60}$ (1.5 > x > 0.5) at room temperature.

Parameter	*MTM149_3*	*MTM136_4*	*MTM132_3*	*MTM147_3*
Nominal x	0.65	0.85	1.00	1.35
λ (Å)	0.40289(6)	0.40289(6)	0.80007(6)	0.40289(6)
Single Phase - Merohedral *Fm*$\bar{3}$*m*				
R_{wp} **(%)**	9.39	7.40	7.23	7.93
R_{exp} **(%)**	4.74	4.26	2.76	5.05
χ^2 **(%)**	3.924	3.017	6.862	2.466
Single Phase - Disordered *Fm*$\bar{3}$*m*				
R_{wp} **(%)**	6.99	6.75	6.09	9.42
R_{exp} **(%)**	4.74	4.27	2.76	5.05
χ^2 **(%)**	2.175	2.499	4.869	3.480
Two Phase - Mixed (Disordered / Merohedral)				
R_{wp} **(%)**	6.39	5.71	4.79	7.14
R_{exp} **(%)**	4.74	4.27	2.76	5.05
χ^2 **(%)**	1.817	1.788	3.012	1.999
Dis (%)	75.7(2)	63.8(3)	65.0(3)	39.6(6)
Mero (%)	24.3(6)	36.2(6)	35.0(5)	60.4(4)
Dis - *a* (Å)	14.1895(2)	14.21450(3)	14.2089(3)	14.2609(4)
Dis - *V* (Å^3)	2857.0(1)	2872.4(2)	2868.7(2)	2900.3(3)
Refined Dis stoichiometry	$Na_{1.70(3)}K_{0.30(7)}CsC_{60}$	$Na_{1.35(4)}K_{0.65(4)}CsC_{60}$	$Na_{1.38(4)}K_{0.62(4)}CsC_{60}$	$Na_{0.7(1)}K_{1.3(1)}CsC_{60}$
Mero - *V* (Å^3)	14.1944(4)	14.2378(4)	14.2129(2)	14.2675(2)
Mero - *a* (Å)	2859.9(2)	2886.2(3)	2871.1(1)	2904.3(1)
Refined Mero stoichiometry	$Na_{0.8(1)}K_{1.2(1)}CsC_{60}$	$Na_{0.11(6)}K_{1.89(6)}CsC_{60}$	$Na_{0.84(7)}K_{1.16(7)}CsC_{60}$	$Na_{0.82(9)}K_{1.18(9)}CsC_{60}$

5.6.1 Sample $Na_{1.35}K_{0.65}CsC_{60}$ at room temperature

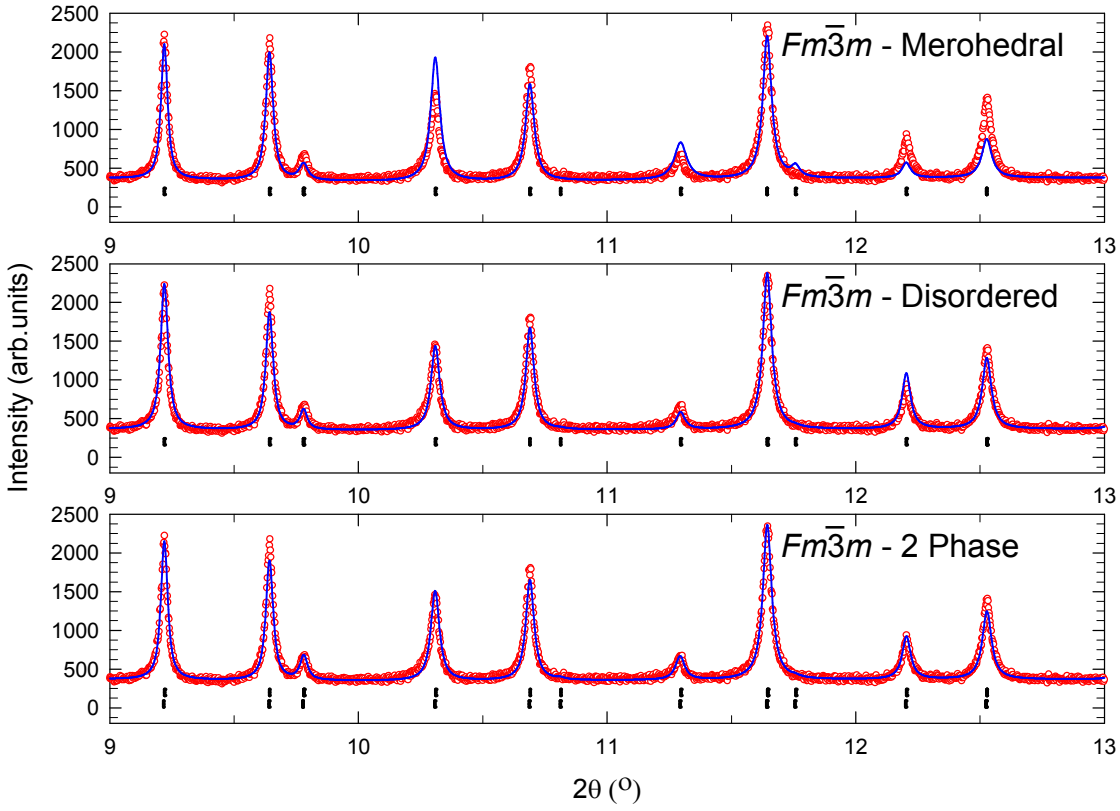

Fig 5.16: Comparison between the *Fm* $\bar{3}$ *m* spherically disordered, *Fm* $\bar{3}$ *m* merohedral and two-phase refinement models for the sample of nominal stoichiometry $Na_{1.35}K_{0.65}CsC_{60}$.

Table 5.9: Results of the room temperature two-phase Rietveld refinement of the spherically disordered *Fm* $\bar{3}$ *m* phase in the sample with overall nominal composition $Na_{1.35}K_{0.65}CsC_{60}$ (MTM149_3).

	x/a	*y/b*	*z/c*	*N*	B_{Iso}(Å^2)
Cs(1)	0.5	0.5	0.5	1.0	6.7(1)
Na(1)	0.25	0.25	0.25	0.850(16)	9.2(3)
K(1)	0.25	0.25	0.25	0.150(16)	9.2(3)
C(1-10)	62% - C's with same occupancy and B_{Iso}			0.077(1)	0.2(2)
C(11-20)	38% - C's with same occupancy and B_{Iso}			0.048(1)	0.2(2)

Table 5.10: Results of the room temperature two-phase Rietveld refinement of the merohedral *Fm* $\bar{3}$ *m* phase in the sample with overall nominal composition $Na_{1.35}K_{0.65}CsC_{60}$ (MTM149_3).

	x/a	*y/b*	*z/c*	*N*	B_{Iso}(Å^2)
Cs(1)	0.5	0.5	0.5	1.0	3.9(2)
Na(1)	0.25	0.25	0.25	0.410(47)	-0.4(2)
K(1)	0.25	0.25	0.25	0.590(47)	-0.4(2)
C(1)	0	0.0501	0.2430	0.5	1.2(2)
C(2)	0.2121	0.0810	0.1000	0.5	1.2(2)
C(3)	0.1810	0.1612	0.0501	0.5	1.2(2)

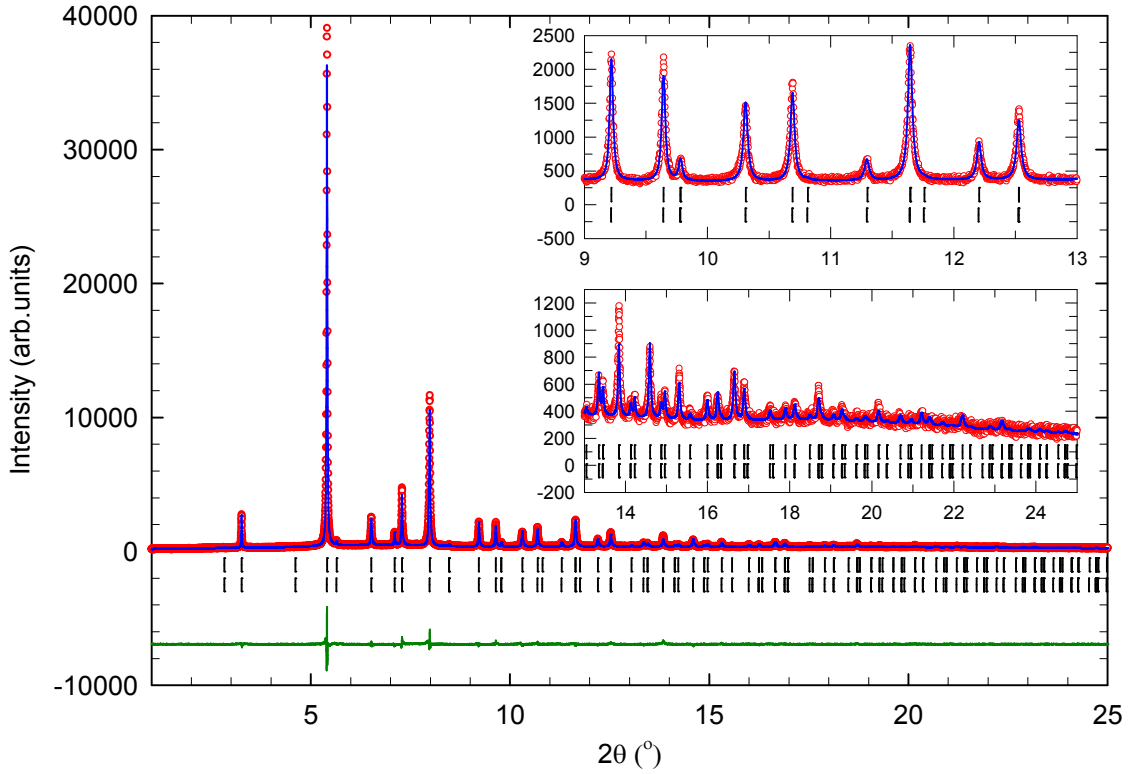

Fig 5.17: Observed (open red circles) and calculated (blue line) data of the room temperature synchrotron powder X-ray diffraction pattern for $Na_{1.35}K_{0.65}CsC_{60}$. The upper bars represent the positions of the Bragg reflections for the spherically disordered *Fm* $\bar{3}$ *m* phase, and the lower bars represent the merohedral *Fm* $\bar{3}$ *m* phase. The wavelength is λ = 0.40289(6) Å.

5.6.2 Sample $Na_{1.15}K_{0.85}CsC_{60}$ at room temperature

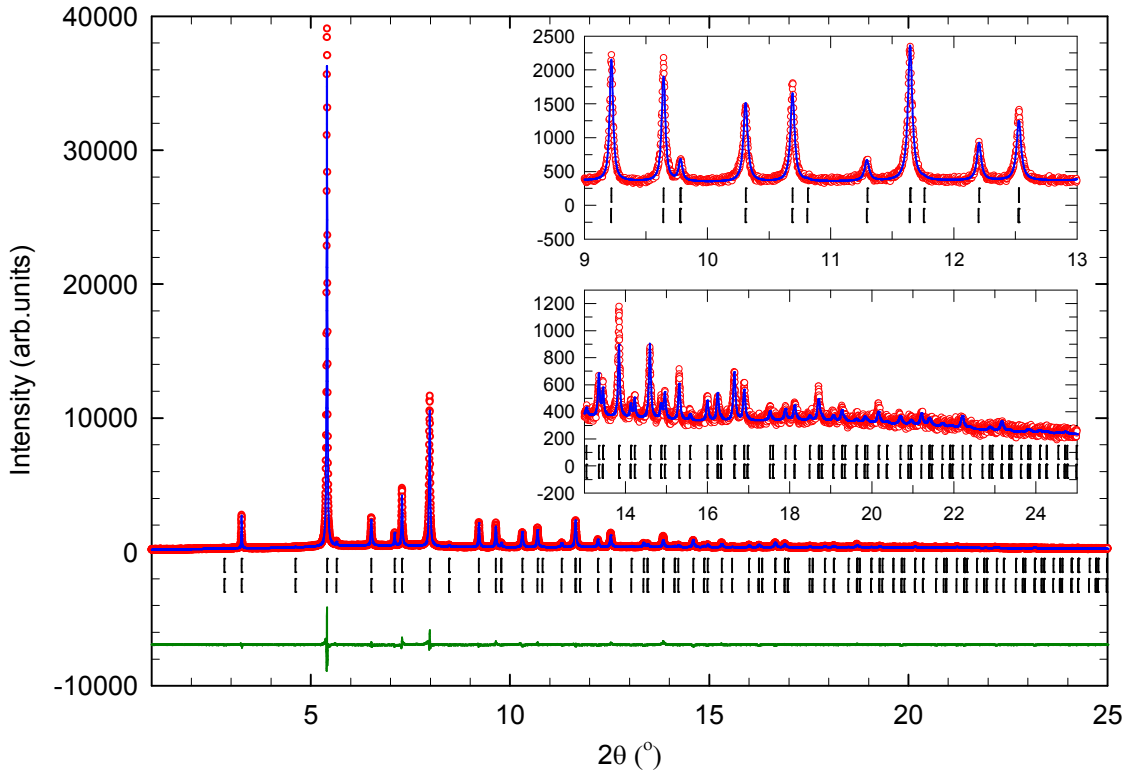

Fig 5.18: Observed (open red circles) and calculated (blue line) data of the room temperature synchrotron powder X-ray diffraction pattern for $Na_{1.15}K_{0.85}CsC_{60}$. The upper bars represent the positions of the Bragg reflections for the spherically disordered *Fm* $\bar{3}$ *m* phase, and the lower bars represent the merohedral *Fm* $\bar{3}$ *m* phase. The wavelength is λ = 0.40289(6) Å.

Table 5.11: Results of the room temperature two-phase Rietveld refinement of the spherically disordered *Fm* $\bar{3}$ *m* phase in the sample with overall nominal composition $Na_{1.15}K_{0.85}CsC_{60}$ (MTM136_4).

	x/a	*y/b*	*z/c*	*N*	B_{iso}(Å^2)
Cs(1)	0.5	0.5	0.5	1.0	5.9(1)
Na(1)	0.25	0.25	0.25	0.676(18)	9.3(4)
K(1)	0.25	0.25	0.25	0.324(18)	9.3(4)
C(1-10)	57% - C's with same occupancy and B_{iso}			0.071(2)	0.4(2)
C(11-20)	43% - C's with same occupancy and B_{iso}			0.054(2)	0.4(2)

Table 5.12: Results of the room temperature two-phase Rietveld refinement of the merohedral $Fm\bar{3}m$ phase in the sample with overall nominal composition $Na_{1.15}K_{0.85}CsC_{60}$ (MTM136_4).

	x/a	*y/b*	*z/c*	*N*	B_{iso}(Å^2)
Cs(1)	0.5	0.5	0.5	1.0	4.4(2)
Na(1)	0.25	0.25	0.25	0.055(30)	-0.7(1)
K(1)	0.25	0.25	0.25	0.945(30)	-0.7(1)
C(1)	0	0.0500	0.2422	0.5	0.1(2)
C(2)	0.2114	0.0807	0.0997	0.5	0.1(2)
C(3)	0.1804	0.1613	0.0500	0.5	0.1(2)

5.6.3 Sample $NaKCsC_{60}$ at room temperature

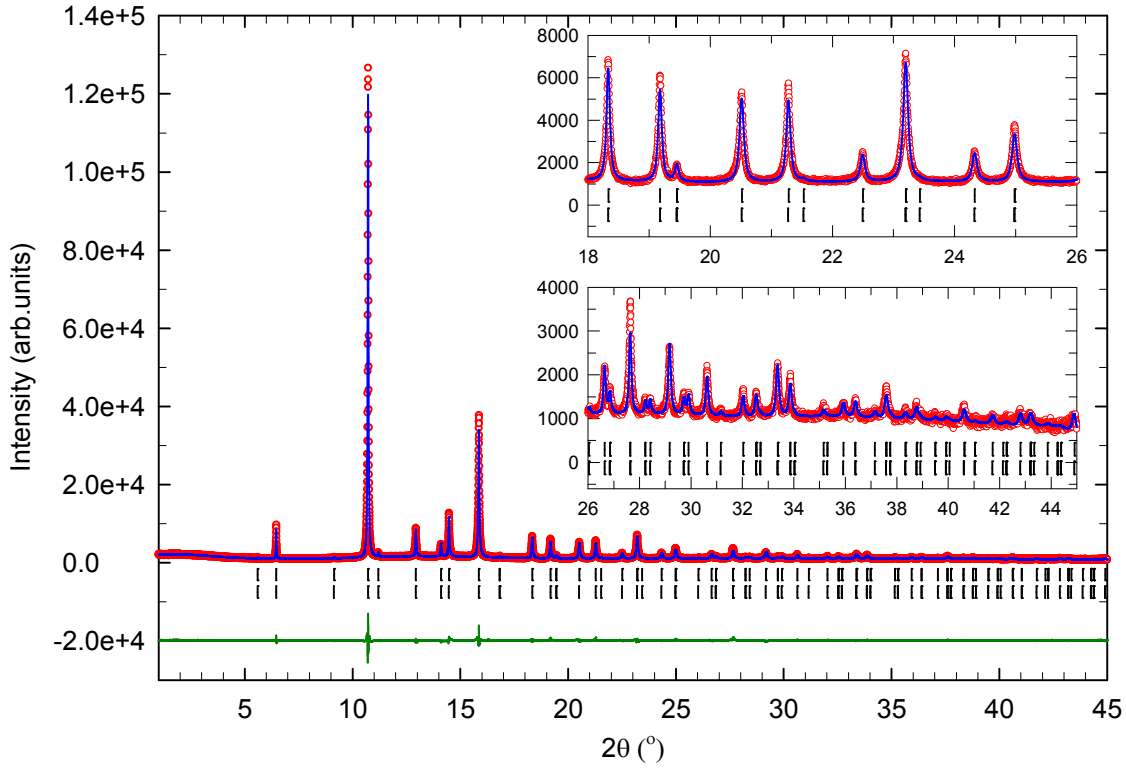

Fig 5.19: Observed (open red circles) and calculated (blue line) data of the room temperature synchrotron powder X-ray diffraction pattern for $NaKCsC_{60}$. The upper bars represent the positions of the Bragg reflections for the spherically disordered $Fm\bar{3}m$ phase, and the lower bars represent the merohedral $Fm\bar{3}m$ phase. The wavelength is λ = 0.80007(6) Å.

Table 5.13: Results of the room temperature two-phase Rietveld refinement of the spherically disordered *Fm* $\bar{3}$ *m* phase in the sample with overall nominal composition $NaKCsC_{60}$ (MTM132_3).

	x/a	*y/b*	*z/c*	*N*	B_{Iso}(Å^2)
Cs(1)	0.5	0.5	0.5	1.0	7.7(1)
Na(1)	0.25	0.25	0.25	0.693(21)	9.8(3)
K(1)	0.25	0.25	0.25	0.307(21)	9.8(3)
C(1-10)	66% - C's with same occupancy and B_{Iso}			0.082(2)	0.4(2)
C(11-20)	34% - C's with same occupancy and B_{Iso}			0.043(2)	0.4(2)

Table 5.14: Results of the room temperature two-phase Rietveld refinement of the merohedral *Fm* $\bar{3}$ *m* phase in the sample with overall nominal composition $NaKCsC_{60}$ (MTM132_3).

	x/a	*y/b*	*z/c*	*N*	B_{Iso}(Å^2)
Cs(1)	0.5	0.5	0.5	1.0	4.2(1)
Na(1)	0.25	0.25	0.25	0.420(33)	-0.4(2)
K(1)	0.25	0.25	0.25	0.580(33)	-0.4(2)
C(1)	0	0.0500	0.2427	0.5	-0.1(2)
C(2)	0.2118	0.0809	0.0999	0.5	-0.1(2)
C(3)	0.1807	0.1616	0.0500	0.5	-0.1(2)

5.6.4 Sample $Na_{0.65}K_{1.35}CsC_{60}$ at room temperature

Table 5.15: Results of the room temperature two-phase Rietveld refinement of the spherically disordered *Fm* $\bar{3}$ *m* phase in the sample with overall nominal composition $Na_{0.65}K_{1.35}CsC_{60}$ (MTM147_3).

	x/a	*y/b*	*z/c*	*N*	B_{Iso}(Å^2)
Cs(1)	0.5	0.5	0.5	1.0	6.6(3)
Na(1)	0.25	0.25	0.25	0.328(48)	9.7(5)
K(1)	0.25	0.25	0.25	0.672(48)	9.7(5)
C(1-10)	62% - C's with same occupancy and B_{Iso}			0.077(1)	0.0(3)
C(11-20)	38% - C's with same occupancy and B_{Iso}			0.048(1)	0.0(3)

Table 5.16: Results of the room temperature two-phase Rietveld refinement of the merohedral *Fm* $\bar{3}$ *m* phase in the sample with overall nominal composition $Na_{0.65}K_{1.35}CsC_{60}$ (MTM147_3).

	x/a	*y/b*	*z/c*	*N*	B_{Iso}(Å^2)
Cs(1)	0.5	0.5	0.5	1.0	4.0(2)
Na(1)	0.25	0.25	0.25	0.410(47)	0.5(1)
K(1)	0.25	0.25	0.25	0.590(47)	0.5(1)
C(1)	0	0.0501	0.2430	0.5	0.8(1)
C(2)	0.2121	0.0810	0.1000	0.5	0.8(1)
C(3)	0.1810	0.1612	0.0501	0.5	0.8(1)

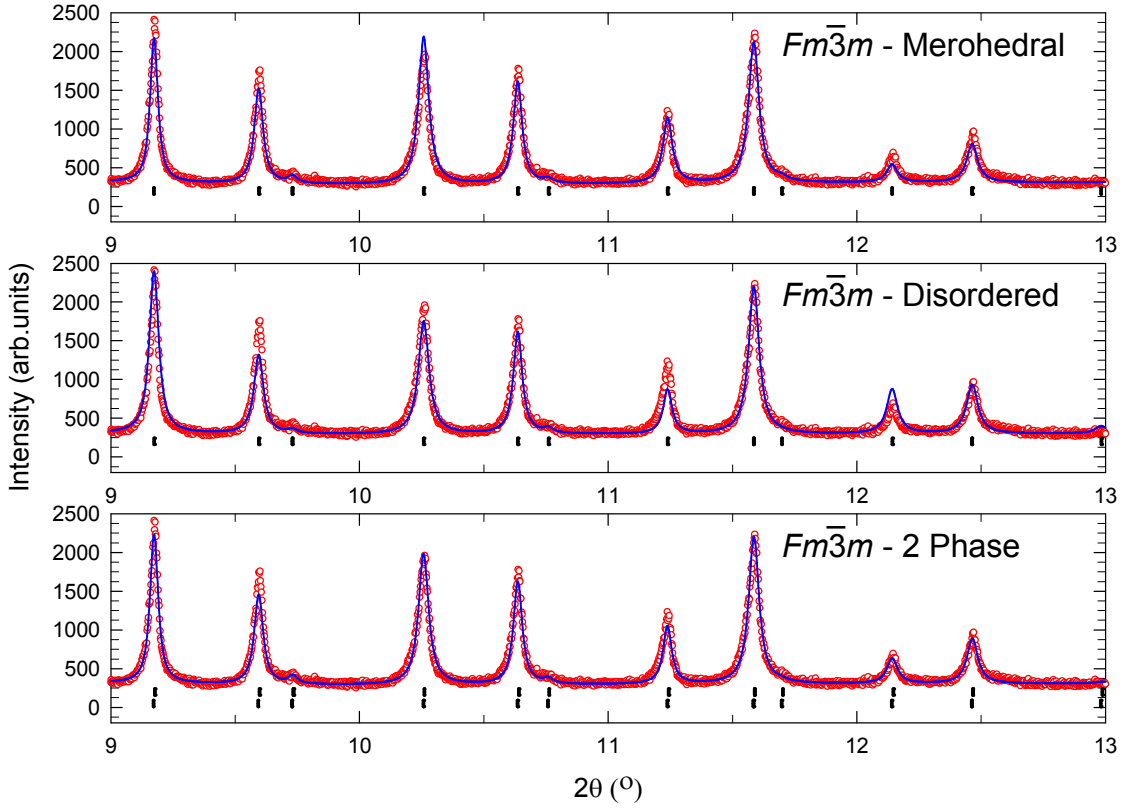

Fig 5.20: Comparison between the *Fm* $\bar{3}$ *m* spherically disordered, *Fm* $\bar{3}$ *m* merohedral and two-phase refinement models for the sample of nominal stoichiometry $Na_{0.65}K_{1.35}CsC_{60}$.

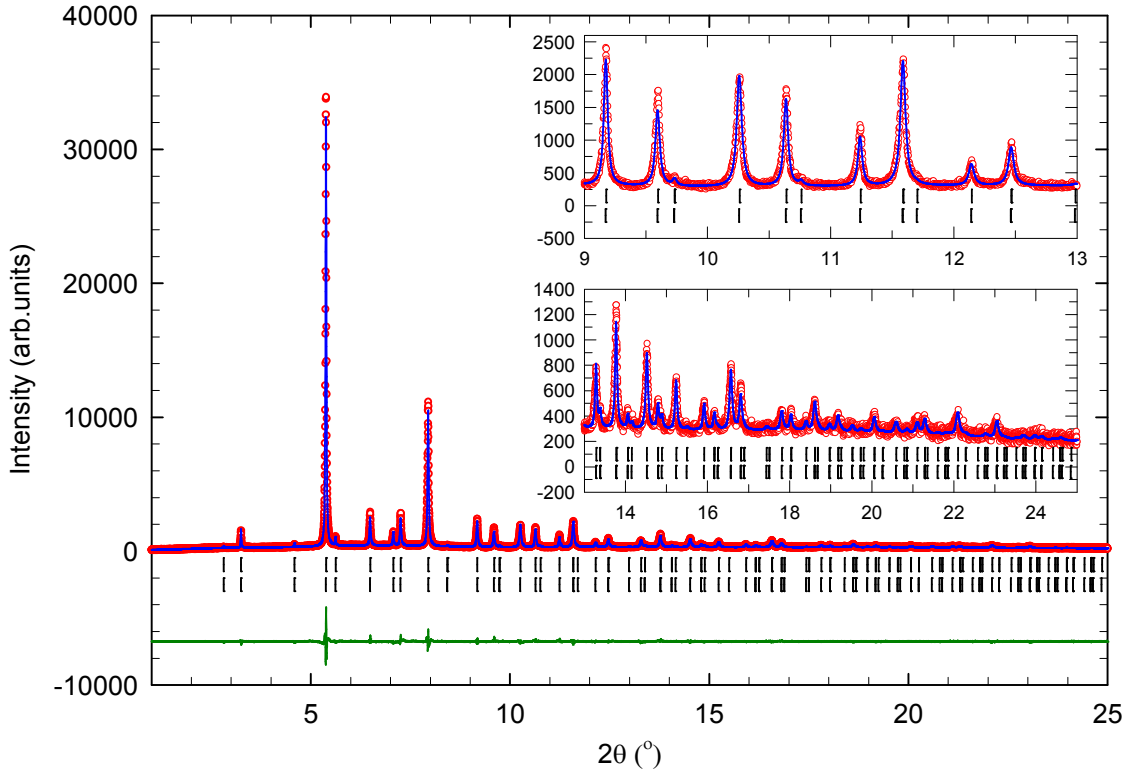

Fig 5.21: Observed (open red circles) and calculated (blue line) data of the room temperature synchrotron powder X-ray diffraction pattern for $Na_{0.65}K_{1.35}CsC_{60}$. The upper bars represent the positions of the Bragg reflections for the spherically disordered $Fm\bar{3}m$ phase, and the lower bars represent the merohedral $Fm\bar{3}m$ phase. The wavelength is λ = 0.40289(6) Å.

5.7 $Na_{2-x}K_xCsC_{60}$ with high K doping (2.0 ≥ x ≥ 1.5), slow cooled protocol, room temperature

The synchrotron X-ray powder diffraction data at room temperature were refined using the spherically disordered $Fm\bar{3}m$, merohedral $Fm\bar{3}m$ and mixed phase $Fm\bar{3}m$ models. The weighted profile and expected *R*-factors indicate that the structures adopted are merohedral $Fm\bar{3}m$ (Table 5.17), and this is confirmed via a visual comparison of the refinements, Fig 5.23. The values of the lattice constants and unit cell volumes are listed in Table 5.17. In the high K doping cases, the mixed phase model offers no significant improvement in refinement quality; the spherically disordered component of these refinements shows highly negative temperature

factors and its inclusion seems only to account for a very slight asymmetry observed in the peak shape. The fractional occupancy, N, of Cs was again fixed at 1.0 and the Na/K total occupancy was fixed at 1.0; however, the ratio was allowed to refine.

Table 5.17: Summary results of the Rietveld refinements of the diffraction data of the series $Na_{2-x}K_xCsC_{60}$ ($2.0 \geq x \geq 1.5$) at room temperature.

Parameter	*MTM142_4_3*	*MTM154_3*	*MTM143_3*
Nominal x	1.50	1.70	2.00
λ (Å)	0.40289(6)	0.40289(6)	0.71124(3)
Two Phase - Mixed (Disordered / Merohedral)			
R_{wp} **(%)**	8.66	5.90	3.48
R_{exp} **(%)**	4.67	4.42	4.21
χ^2 **(%)**	3.467	1.782	0.683
Dis (%)	68(1)	71.8(2)	84(1)
Mero (%)	32(1)	28.2(7)	16(1)
Single Phase - Disordered *Fm*$\bar{3}$*m*			
R_{wp} **(%)**	9.80	9.36	6.52
R_{exp} **(%)**	4.67	4.42	4.22
χ^2 **(%)**	4.404	4.484	2.387
Single Phase - Merohedral *Fm*$\bar{3}$*m*			
R_{wp} **(%)**	9.18	6.38	3.83
R_{exp} **(%)**	4.67	4.42	4.21
χ^2 **(%)**	3.864	2.084	0.828
FCC *a* (Å)	14.2687(8)	14.27790(4)	14.2937(5)
FCC *V* (Å^3)	2905.1(3)	2910.67(3)	2920.4(3)
Refined stoichiometry	$Na_{0.33(2)}K_{1.67(2)}CsC_{60}$.	$Na_{0.11(1)}K_{1.89(1)}CsC_{60}$	K_2CsC_{60}

5.7.1 Sample $Na_{0.5}K_{1.5}CsC_{60}$ at room temperature

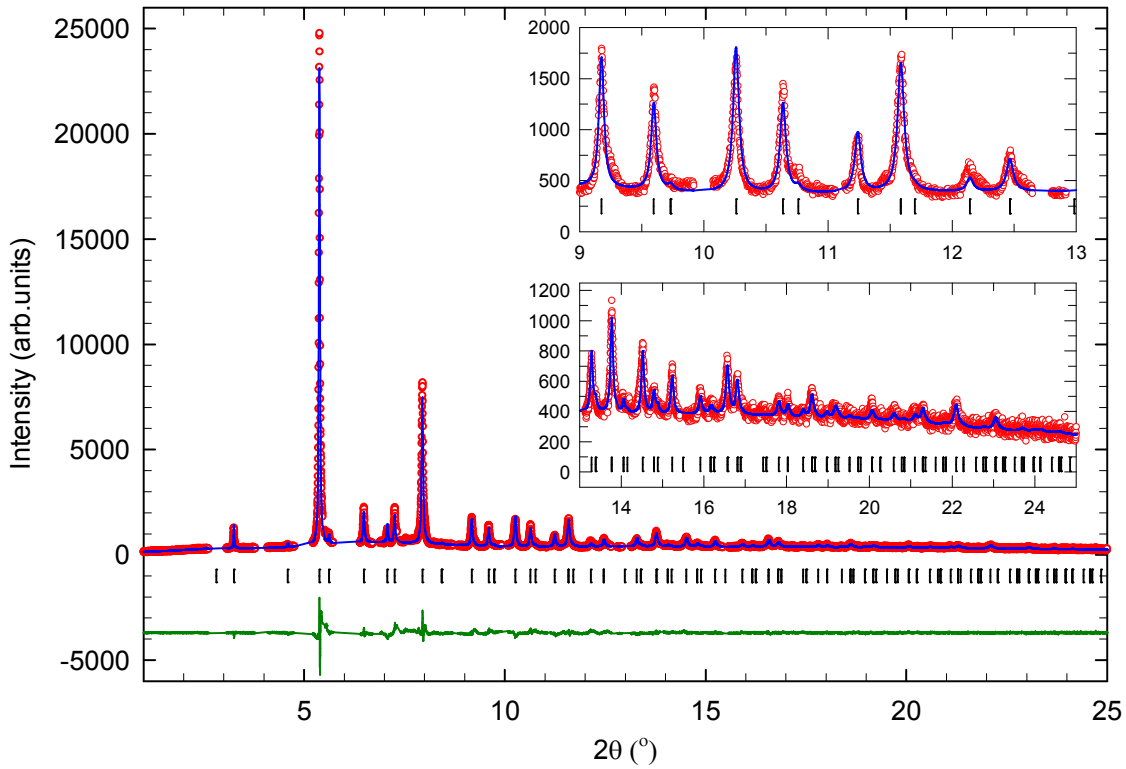

Fig 5.22: Observed (open red circles) and calculated (blue line) data of the room temperature synchrotron powder X-ray diffraction pattern for $Na_{0.5}K_{1.5}CsC_{60}$. The bars represent the positions of the Bragg reflections for the merohedral $Fm\bar{3}m$ phase. The wavelength is λ = 0.40289(6) Å. Excluded regions are attributed to unidentified impurities.

Table 5.18: Results of the room temperature single-phase Rietveld refinement of the merohedral $Fm\bar{3}m$ phase in the sample with overall nominal composition $Na_{1.5}K_{0.5}CsC_{60}$ (MTM142_4).

	x/a	*y/b*	*z/c*	*N*	B_{iso}(Å^2)
Cs(1)	0.5	0.5	0.5	1.0	5.58(9)
Na(1)	0.25	0.25	0.25	0.165(12)	2.8(2)
K(1)	0.25	0.25	0.25	0.835(12)	2.8(2)
C(1)	0	0.0498	0.2417	0.5	1.0(1)
C(2)	0.2110	0.0806	0.0995	0.5	1.0(1)
C(3)	0.1800	0.1610	0.0498	0.5	1.0(1)

5.7.2 Sample $Na_{0.3}K_{1.7}CsC_{60}$ at room temperature

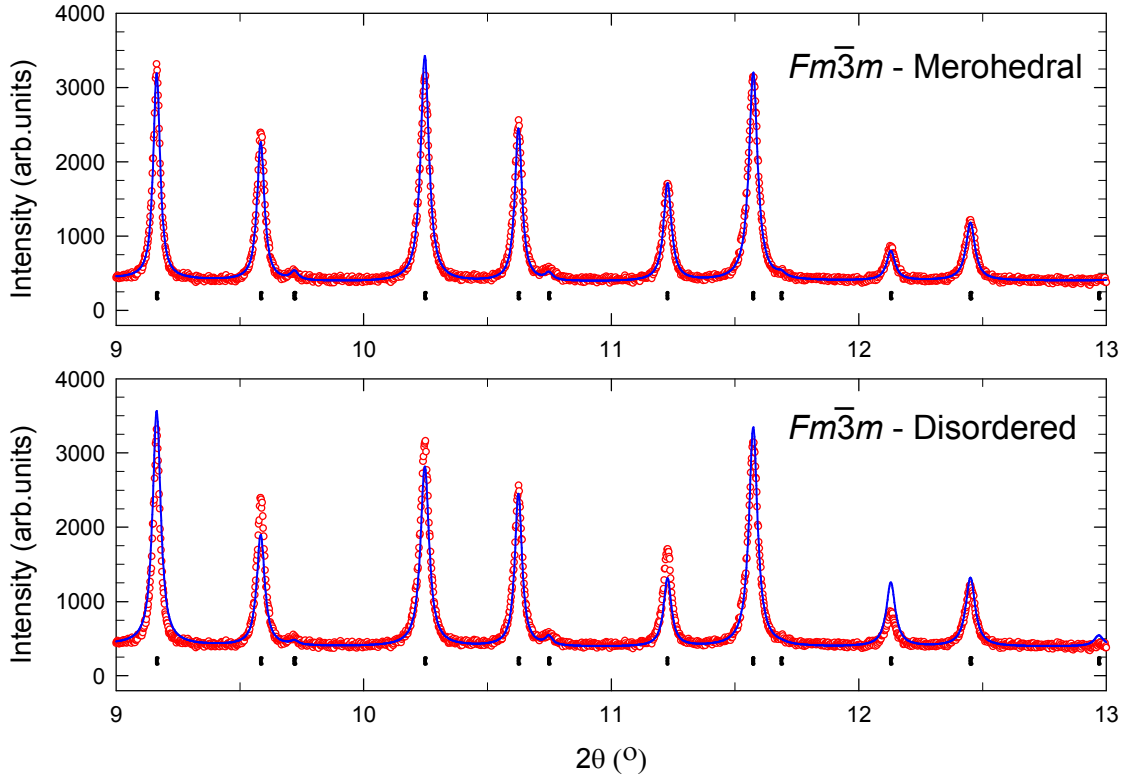

Fig 5.23: Comparison between the *Fm* $\bar{3}$ *m* spherically disordered and *Fm* $\bar{3}$ *m* merohedral refinement models for the sample of nominal stoichiometry $Na_{0.3}K_{1.7}CsC_{60}$.

Table 5.19: Results of the room temperature single-phase Rietveld refinement of the merohedral *Fm* $\bar{3}$ *m* phase in the sample with overall nominal composition $Na_{0.3}K_{1.7}CsC_{60}$ (MTM154_3).

	x/a	*y/b*	*z/c*	*N*	B_{iso}(Å^2)
Cs(1)	0.5	0.5	0.5	1.0	4.37(4)
Na(1)	0.25	0.25	0.25	0.056(6)	2.67(7)
K(1)	0.25	0.25	0.25	0.944(6)	2.67(7)
C(1)	0	0.0501	0.2430	0.5	1.25(5)
C(2)	0.2121	0.0810	0.1000	0.5	1.25(5)
C(3)	0.1810	0.1612	0.0501	0.5	1.25(5)

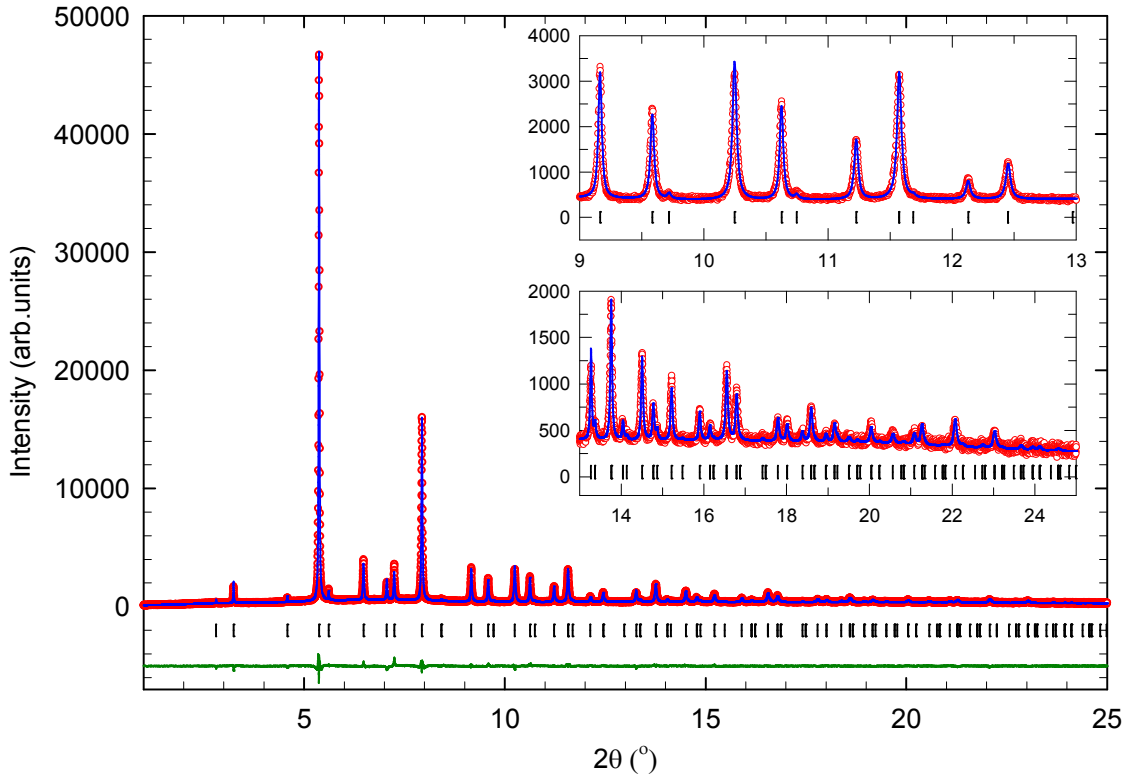

Fig 5.24: Observed (open red circles) and calculated (blue line) data of the room temperature synchrotron powder X-ray diffraction pattern for $Na_{0.3}K_{1.7}CsC_{60}$. The bars represent the positions of the Bragg reflections for the merohedral *Fm* $\bar{3}$ *m* phase. The wavelength is λ = 0.40289(6) Å.

5.7.3 Sample K_2CsC_{60} at room temperature

Table 5.20: Results of the room temperature single-phase Rietveld refinement of the merohedral *Fm* $\bar{3}$ *m* phase in the sample with overall nominal composition K_2CsC_{60} (MTM143_3).

	x/a	*y/b*	*z/c*	*N*	B_{Iso}(Å^2)
Cs(1)	0.5	0.5	0.5	1.0	4.32(9)
K(1)	0.25	0.25	0.25	1.0	0.5(1)
C(1)	0	0.0498	0.2413	0.5	-0.7(2)
C(2)	0.2106	0.0804	0.0993	0.5	-0.7(2)
C(3)	0.1797	0.1607	0.0498	0.5	-0.7(2)

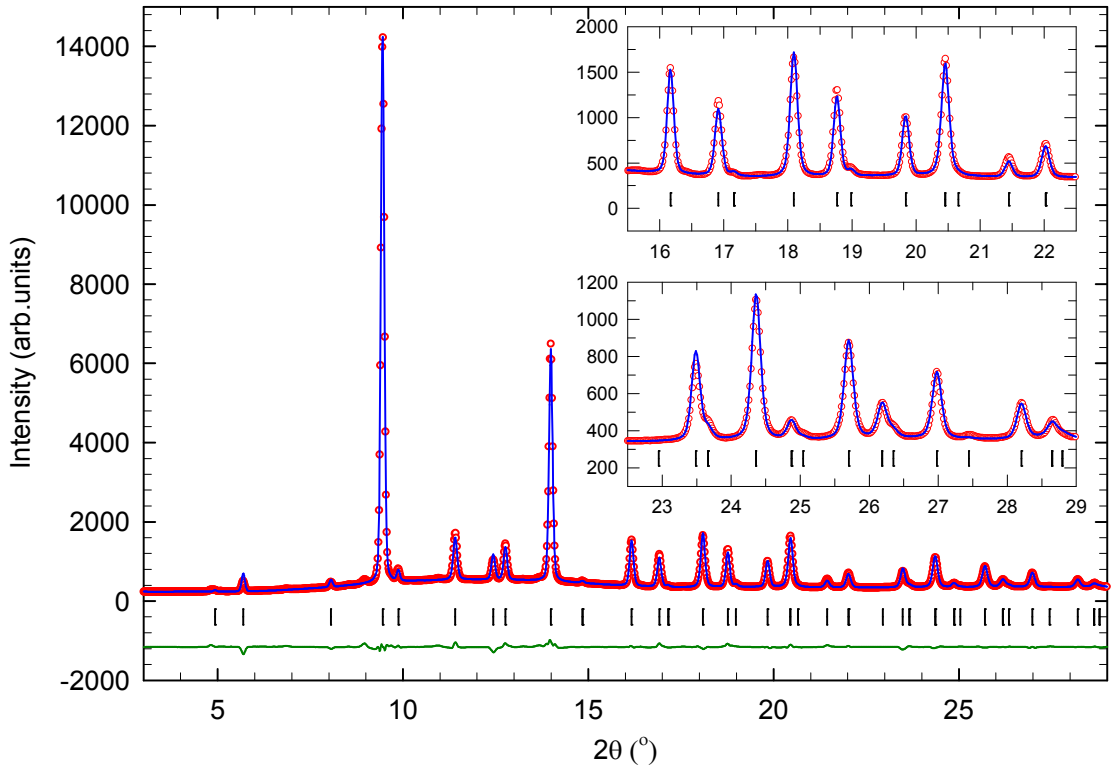

Fig 5.25: Observed (open red circles) and calculated (blue line) data of the room temperature synchrotron powder X-ray diffraction pattern for sample MTM143_3 K_2CsC_{60}. The bars represent the positions of the Bragg reflections for the merohedral *Fm* $\bar{3}$ *m* phase. The wavelength is λ = 0.71124(3) Å.

5.8 $Na_{2-x}K_xCsC_{60}$, slow cooled protocol, low temperature

5.8.1 Sample $Na_{1.9}K_{0.1}CsC_{60}$ at 20 K

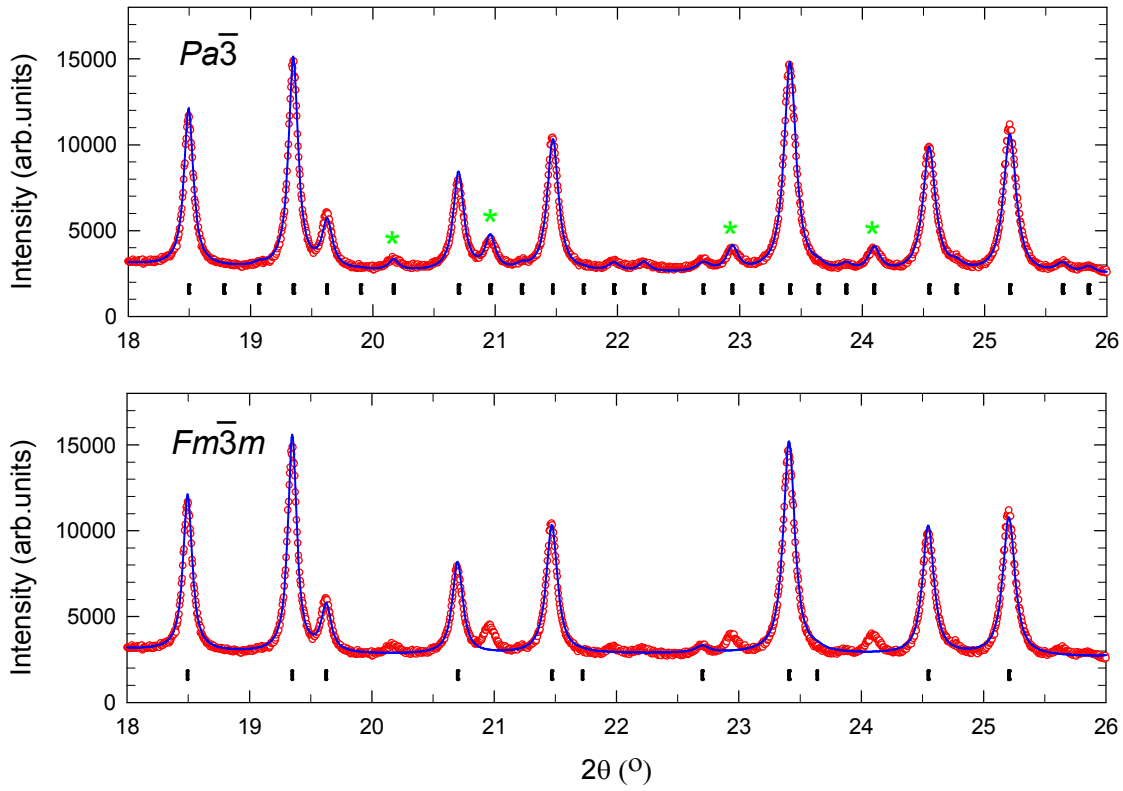

Fig 5.26: Comparison between spherically disordered *Fm* $\bar{3}$ *m* and *Pa* $\bar{3}$ refinement models. From left to right; * = (523)/(611), * = (504)/(443)/(612), * = (623) and * = (552)/(633)/(712).

Table 5.21: Results of the 20 K single-phase Rietveld refinement of the *Pa* $\bar{3}$ phase in the sample with overall nominal composition $Na_{1.9}K_{0.1}CsC_{60}$ (MTM131_3).

	x/a	*y/b*	*z/c*	*N*	B_{Iso}(Å^2)
Cs(1)	0.5	0.5	0.5	1.0	2.07(2)
Na(1)	0.25	0.25	0.25	0.947(5)	1.65(8)
K(1)	0.25	0.25	0.25	0.053(5)	1.65(8)
C major	77% - d(C-C) constrained to 1.45(1) Å			0.767(4)	0.26(4)
C minor	23% - d(C-C) constrained to 1.45(1) Å			0.233(4)	0.26(4)

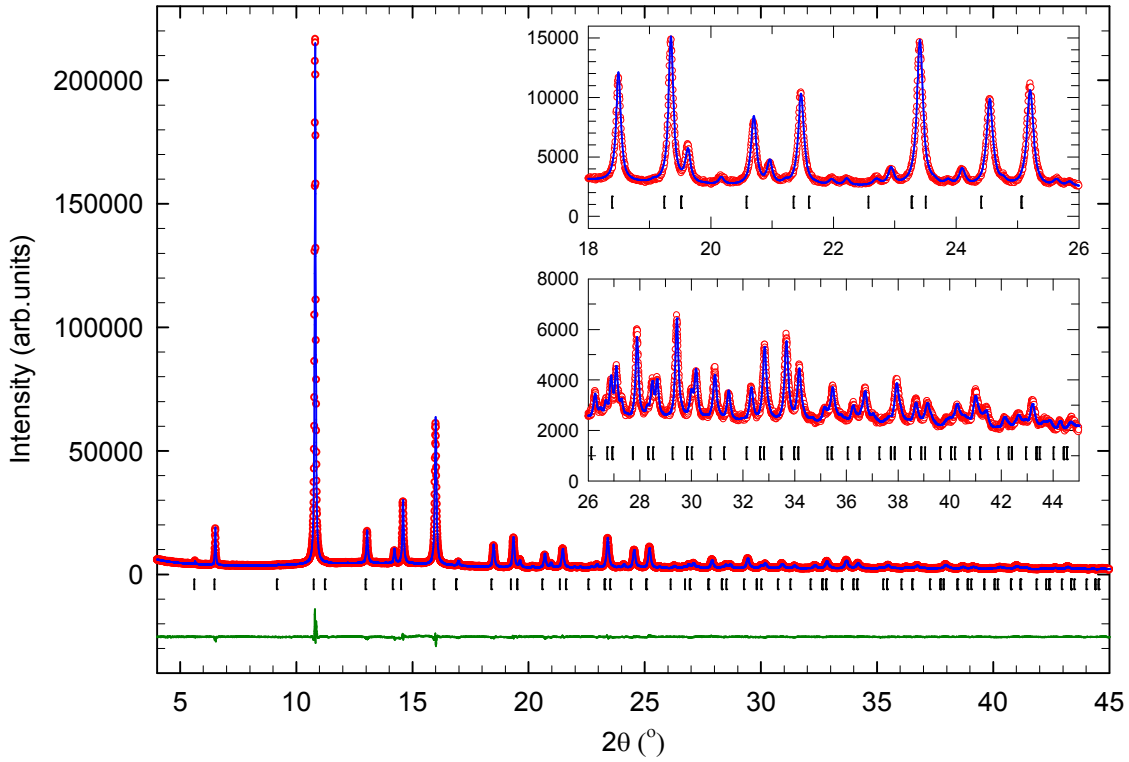

Fig 5.27: Observed (open red circles) and calculated (blue line) data of the 20 K synchrotron powder X-ray diffraction pattern for $Na_{1.9}K_{0.1}CsC_{60}$. The bars represent the positions of the Bragg reflections for the $Pa\bar{3}$ phase. The wavelength is λ = 0.80007(6) Å.

The synchrotron X-ray powder diffraction data collected at 20 K was refined using both the spherically disordered $Fm\bar{3}m$ (R_{wp} = 4.40%, R_{exp} = 1.59%) and $Pa\bar{3}$ (R_{wp} = 3.45%, R_{exp} = 1.59%) models. The *R*-factors indicate that the structure adopted is of $Pa\bar{3}$ symmetry, and this is confirmed via a visual comparison of the refinements in Fig 5.26. The values of the lattice constant and unit cell volume are: a = 14.0833(1) Å, V = 2793.25(8) $Å^3$. The fractional occupancy, N, of Cs was fixed at 1.0 and the Na/K total occupancy was fixed at 1.0; however, the ratio was allowed to refine converging to values of 0.947(5) and 0.053(5) respectively, thus resulting in a nominal stoichiometry of $Na_{1.89(1)}K_{0.11(1)}CsC_{60}$. 77% of the C_{60} molecules reside in the preferred orientation where the electron-rich 6:6 "double" bond of one molecule is facing the electron deficient pentagon face of an adjacent molecule, and 23% reside in the less favourable orientation where the electron rich 6:6 bond is facing the centre of a 6-membered ring on an adjacent molecule.

The room temperature data were consistent with a spherically disordered $Fm\bar{3}m$ structure; at low temperature, the $Pa\bar{3}$ structure is observed. There is a temperature-induced phase transition from $Fm\bar{3}m$ to $Pa\bar{3}$ similar to Na_2CsC_{60}.

5.8.2 Sample $Na_{1.5}K_{0.5}CsC_{60}$ at 20 K

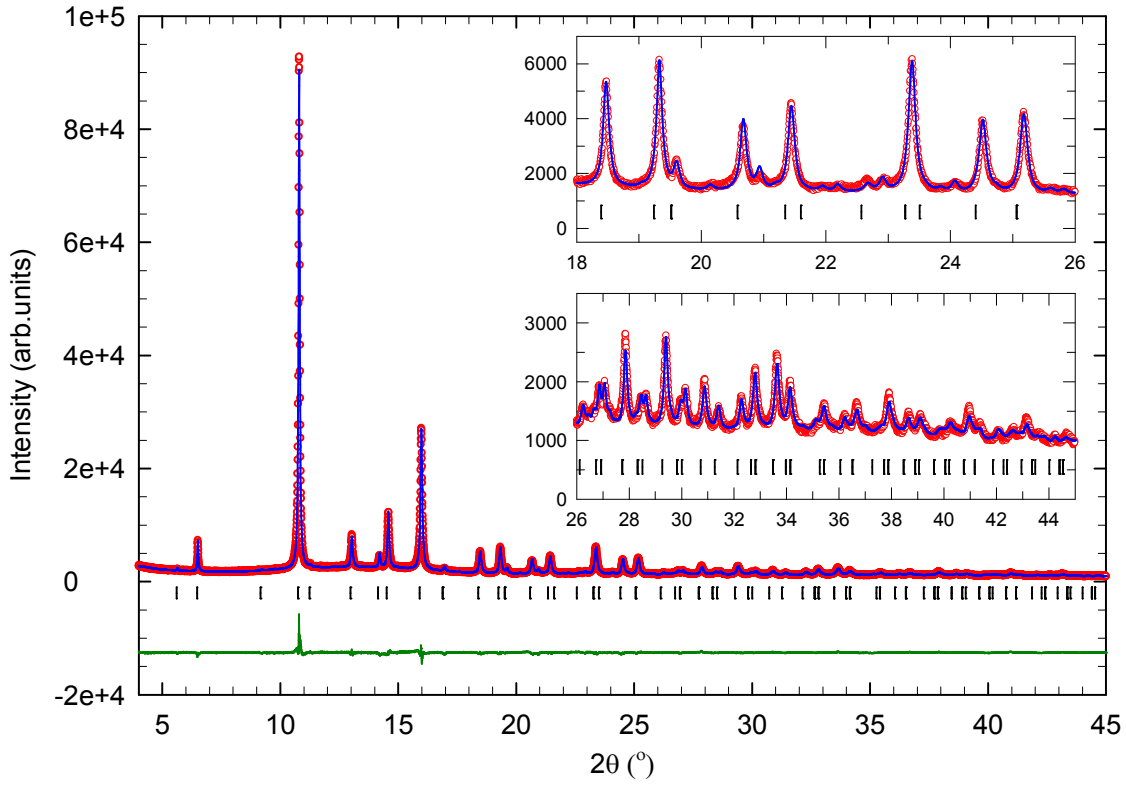

Fig 5.28: Observed (open red circles) and calculated (blue line) data of the 20 K synchrotron powder X-ray diffraction pattern for $Na_{1.5}K_{0.5}CsC_{60}$. The bars represent the positions of the Bragg reflections for the $Pa\bar{3}$ phase. The wavelength is λ = 0.80007(6) Å.

The synchrotron X-ray powder diffraction data at ambient temperature was refined using both the spherically disordered $Fm\bar{3}m$ (R_{wp} = 4.12%, R_{exp} = 1.79%) and $Pa\bar{3}$ (R_{wp} = 3.94%, R_{exp} = 1.78%) models. The *R*-factors indicate that the structure adopted is of $Pa\bar{3}$ symmetry. The values of the lattice constant and unit cell volume are: a = 14.0971(2) Å, V = 2801.5(1) $Å^3$. The fractional occupancy, N, of Cs was fixed at

1.0 and the Na/K total occupancy was fixed at 1.0; however, the ratio was allowed to refine converging to values of 0.815(7) and 0.185(7) respectively, thus resulting in a nominal stoichiometry of $Na_{1.63(1)}K_{0.37(1)}CsC_{60}$. 64% of the C_{60} molecules reside in the preferred and 36% in the less favourable C_{60}-C_{60} near-neighbour orientations.

Table 5.22: Results of the 20 K single-phase Rietveld refinement of the $Pa\bar{3}$ phase in the sample with overall nominal composition $Na_{1.5}K_{0.5}CsC_{60}$ (MTM119_4).

	x/a	*y/b*	*z/c*	*N*	B_{Iso}(Å^2)
Cs(1)	0.5	0.5	0.5	1.0	3.19(3)
Na(1)	0.25	0.25	0.25	0.815(7)	2.02(9)
K(1)	0.25	0.25	0.25	0.185(7)	2.02(9)
C major	64% - d(C-C) constrained to 1.45(1) Å			0.640(5)	1.28(6)
C minor	36% - d(C-C) constrained to 1.45(1) Å			0.360(5)	1.28(6)

5.8.3 Sample $Na_{1.35}K_{0.65}CsC_{60}$ at 20 K

Table 5.23: Results of the 20 K two-phase Rietveld refinement of the spherically disordered $Fm\bar{3}m$ phase in the sample with overall nominal composition $Na_{1.35}K_{0.65}CsC_{60}$ (MTM149_3).

	x/a	*y/b*	*z/c*	*N*	B_{Iso}(Å^2)
Cs(1)	0.5	0.5	0.5	1.0	3.23(8)
Na(1)	0.25	0.25	0.25	0.822(16)	6.5(2)
K(1)	0.25	0.25	0.25	0.178(16)	6.5(2)
C(1-10)	72% - C's with same occupancy and B_{Iso}			0.090(1)	-0.7(1)
C(11-20)	28% - C's with same occupancy and B_{Iso}			0.035(1)	-0.7(1)

Table 5.24: Results of the 20 K two-phase Rietveld refinement of the merohedral *Fm* $\bar{3}$ *m* phase in the sample with overall nominal composition $Na_{1.35}K_{0.65}CsC_{60}$ (MTM149_3).

	x/a	*y/b*	*z/c*	*N*	B_{Iso}(Å^2)
Cs(1)	0.5	0.5	0.5	1.0	2.2(3)
Na(1)	0.25	0.25	0.25	0.474(53)	0.2(3)
K(1)	0.25	0.25	0.25	0.526(53)	0.2(3)
C(1)	0	0.0503	0.2438	0.5	-2.1(3)
C(2)	0.2128	0.0813	0.1003	0.5	-2.1(3)
C(3)	0.1816	0.1624	0.0503	0.5	-2.1(3)

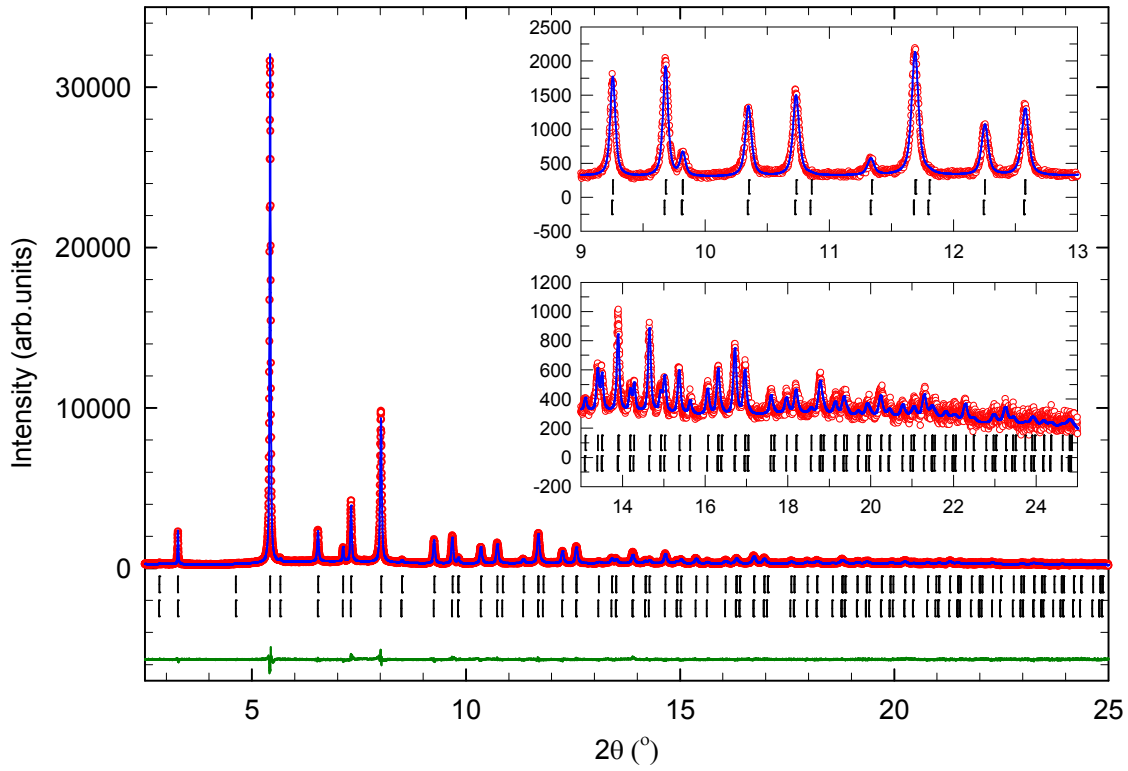

Fig 5.29: Observed (open red circles) and calculated (blue line) data of the 20 K synchrotron powder X-ray diffraction pattern for $Na_{1.35}K_{0.65}CsC_{60}$. The upper bars represent the positions of the Bragg reflections for the spherically disordered *Fm* $\bar{3}$ *m* phase, and the lower bars represent the merohedral *Fm* $\bar{3}$ *m* phase. The wavelength is λ = 0.80007(6) Å.

The synchrotron X-ray powder diffraction data at 20 K were refined using the spherically disordered $Fm\bar{3}m$ (R_{wp} = 7.14%, R_{exp} = 5.10%), merohedral $Fm\bar{3}m$ (R_{wp} = 11.24%, R_{exp} = 5.10%) and mixed phase $Fm\bar{3}m$ (R_{wp} = 6.29%, R_{exp} = 5.09%) models. The *R*-factors indicate that there is phase separation resulting in a mixture of spherically disordered and merohedral $Fm\bar{3}m$. The two-phase model offers a significant improvement in refinement quality with 79.3(2)% spherically disordered $Fm\bar{3}m$ and 20.7(6)% merohedral $Fm\bar{3}m$. The values of the lattice constants and unit cell volumes are: $Fm\bar{3}m$ disordered a = 14.1307(3) Å, V = 2821.6(2) Å^3 and $Fm\bar{3}m$ merohedral a = 14.1445(5) Å, V = 2829.9(3) Å^3. In both phases the fractional occupancy, N, of Cs and the Na/K total occupancy were fixed at 1.0; however, the Na/K ratio was allowed to refine converging to values for disordered $Fm\bar{3}m$: Na = 0.822(16), K = 0.178(16) and merohedral $Fm\bar{3}m$: Na = 0.474(53), K = 0.526(53). This results in stoichiometries for disordered $Fm\bar{3}m$ of $Na_{1.64(3)}K_{0.36(7)}CsC_{60}$ and merohedral $Fm\bar{3}m$ of $Na_{0.9(1)}K_{1.1(1)}CsC_{60}$. It is noted that the temperature factors of the C atoms in both phases are negative and is attributed to the excessive peak overlap that exists between both phases.

5.8.4 Sample $NaKCsC_{60}$ at 20 K

Table 5.25: Results of the 20 K two-phase Rietveld refinement of the spherically disordered $Fm\bar{3}m$ phase in the sample with overall nominal composition $NaKCsC_{60}$ (MTM132_3).

	x/a	*y/b*	*z/c*	*N*	B_{Iso}(Å^2)
Cs(1)	0.5	0.5	0.5	1.0	2.96(5)
Na(1)	0.25	0.25	0.25	0.756(17)	5.4(2)
K(1)	0.25	0.25	0.25	0.244(17)	5.4(2)
C(1-10)	69% - C's with same occupancy and B_{Iso}			0.086(1)	-0.8(1)
C(11-20)	31% - C's with same occupancy and B_{Iso}			0.039(1)	-0.8(1)

Table 5.26: Results of the 20 K two-phase Rietveld refinement of the merohedral $Fm\bar{3}m$ phase in the sample with overall nominal composition $NaKCsC_{60}$ (MTM132_3).

	x/a	*y/b*	*z/c*	*N*	B_{iso}(Å^2)
Cs(1)	0.5	0.5	0.5	1.0	3.97(7)
Na(1)	0.25	0.25	0.25	0.469(16)	0.4(1)
K(1)	0.25	0.25	0.25	0.531(16)	0.4(1)
C(1)	0	0.0503	0.2438	0.5	0.44(9)
C(2)	0.2128	0.0813	0.1003	0.5	0.44(9)
C(3)	0.1816	0.1624	0.0503	0.5	0.44(9)

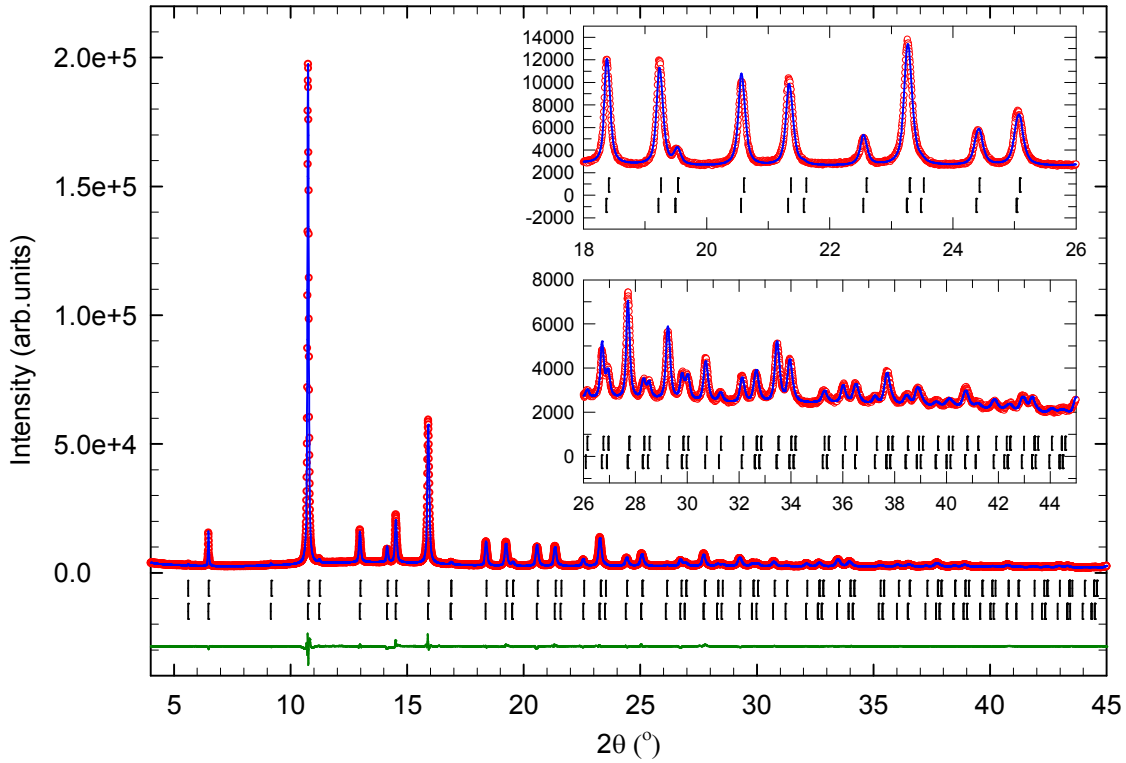

Fig 5.30: Observed (open red circles) and calculated (blue line) data of the 20 K synchrotron powder X-ray diffraction pattern for $NaKCsC_{60}$. The upper bars represent the positions of the Bragg reflections for the spherically disordered $Fm\bar{3}m$ phase, and the lower bars represent the merohedral $Fm\bar{3}m$ phase. The wavelength is λ = 0.80007(6) Å.

The synchrotron X-ray powder diffraction data at ambient temperature were refined using the spherically disordered $Fm\bar{3}m$ (R_{wp} = 5.43%, R_{exp} = 1.45%), merohedral $Fm\bar{3}m$ (R_{wp} = 6.42%, R_{exp} = 1.45%) and mixed phase $Fm\bar{3}m$ (R_{wp} = 3.37%, R_{exp} = 1.45%) models. The *R*-factors indicate that the structure adopted is a mixture of spherically disordered and merohedral $Fm\bar{3}m$. The two-phase model offers a significant improvement in refinement quality with 52.6(2)% spherically disordered $Fm\bar{3}m$ and 47.4(3)% merohedral $Fm\bar{3}m$. The values of the lattice constants and unit cell volumes are - $Fm\bar{3}m$ disordered: a = 14.1493(2) Å, V = 2832.7(1) Å^3 and $Fm\bar{3}m$ merohedral: a = 14.1791(2) Å, V = 2850.7(1) Å^3. In both phases the fractional occupancy, N, of Cs and the Na/K total occupancy were fixed at 1.0; however, the Na/K ratio was allowed to refine converging to values for disordered $Fm\bar{3}m$: Na = 0.756(17), K = 0.244(17) and merohedral $Fm\bar{3}m$: Na = 0.469(16), K = 0.531(16). This results in stoichiometries for disordered $Fm\bar{3}m$: $Na_{1.51(3)}K_{0.49(3)}CsC_{60}$ and merohedral $Fm\bar{3}m$: $Na_{0.94(3)}K_{1.06(3)}CsC_{60}$. It is noted that the temperature factors of the C atoms in the spherically disordered $Fm\bar{3}m$ phase are negative, and is again attributed to the difficulties associated with the excessive peak overlap between both phases.

5.9 Summary – structural properties of the slow cooled $Na_{2-x}K_xCsC_{60}$ series

The parent member of this series of materials, Na_2CsC_{60} is primitive cubic structured ($Pa\bar{3}$) at room temperature. This implies that the orientational order-disorder transition to the cubic $Fm\bar{3}m$ structure, observed by materials reported in the literature, occurs above room temperature[13]. In comparison to $Na_{1.9}K_{0.1}CsC_{60}$ at room temperature, a highly contracted cell parameter is noted which is consistent with the unit cell volume reduction that accompanies orientational ordering of the fullerene units.

Even as little as x ~ 0.1 K-doping of Na_2CsC_{60} is sufficient to drive the onset of the orientational ordering transition to temperatures higher than ambient as the

average size of the tetrahedral cation increases. The $Fm\bar{3}m$ to simple cubic $Pa\bar{3}$ phase transition occurs on cooling to 20 K for $Na_{2-x}K_xCsC_{60}$ samples with as high a nominal K-doping value as x ~ 0.5 ($Na_{1.5}K_{0.5}CsC_{60}$). It is interesting to note that the mean cation size in the tetrahedral hole reaches ~1.11 Å for this composition, just marginally smaller than the ideal 1.12 Å radius of the interstice itself. The low-temperature structure of the next sample in the $Na_{2-x}K_xCsC_{60}$ series is no longer single phase orientationally ordered. Instead when the nominal K-doping value reaches x ~ 0.65, the mean tetrahedral ion size is ~1.14 Å and the onset of phase separation (two-phase mixture of merohedrally and spherically disordered phases) is encountered. Moreover, no evidence is found from diffraction for a low-temperature transition to the $Pa\bar{3}$ phase. The phase composition of the various samples shown in Fig 5.31(c) is consistent with the sensitive influence of the K doping level on the structural response, – as x increases the structure evolves from spherically disordered $Fm\bar{3}m$ to merohedrally disordered $Fm\bar{3}m$ – in between the two extremes, there is a very broad miscibility gap where both phases co-exist.

In addition, the cubic cell parameter also increases as the size of the cation in the T_d cavity increases; notably the rate of change with the cation size for the merohedrally disordered phases is steeper than that for the spherically disordered phases, in which there is good fitting of the cations in the T_d cavity (Fig 5.31(a)).

In Fig 5.31(b), the unit cell volume against the refined K content of each phase is plotted as derived from the Rietveld analysis. While there is a clear trend in the volume dependence on x for the lightly and heavily K-doped phases, the situation is extremely complex in the two-phase co-existence region. It is clear that for each K-doping level in this region, there is phase separation into a K-poor spherically disordered phase and a K-rich merohedrally disordered phase. However, no systematic trend has been established. This problem presumably arises from the inability of the Rietveld refinements to accurately determine the cationic occupancies in the two co-existing phases, and stems from the fact that the cell constants of the two phases are very similar to each other resulting in a severe degree of overlap of the Bragg reflections of the two phases – no clearly resolved splittings are present even at the very high resolution of the synchrotron X-ray data. Therefore the refinement results

have been unable to establish clearly the K-doping level in the two components. For instance, the peak-shape parameters of the two $Fm\bar{3}m$ phases, while constrained to be equal to each other, were unable to refine simultaneously with the cationic occupancies.

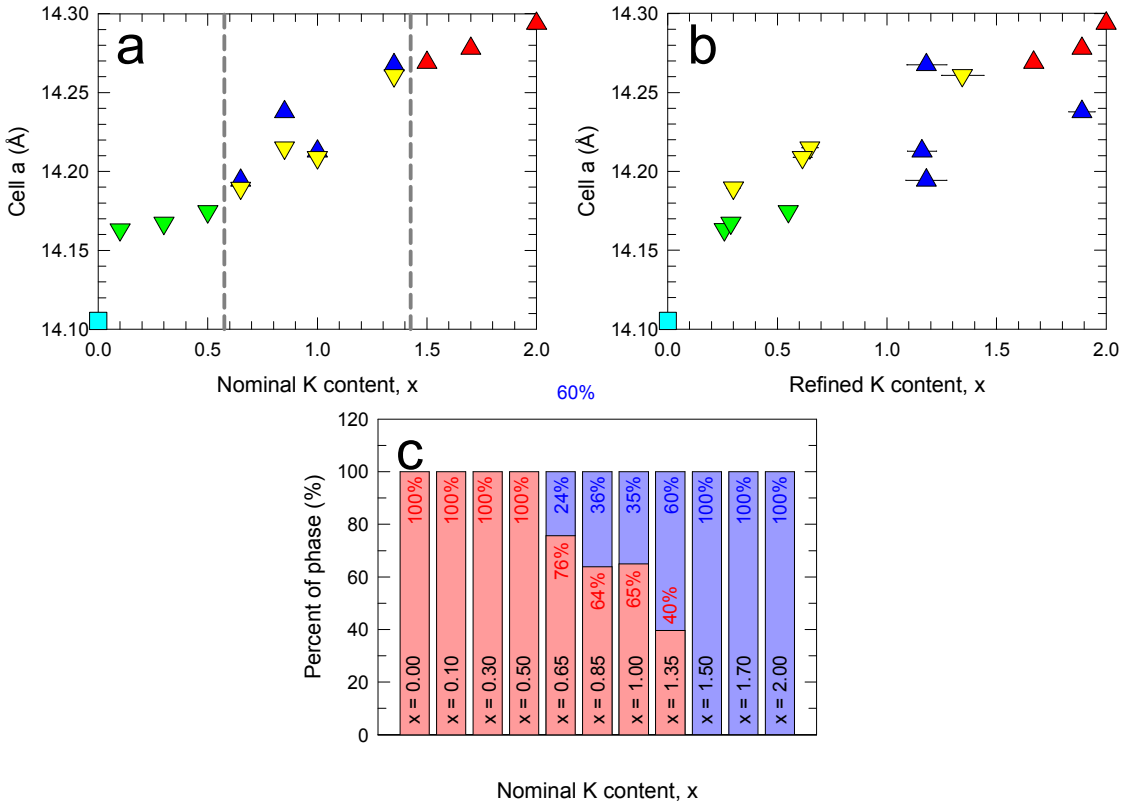

Fig 5.31: (a) Plot of the cell parameter as a function of the nominal stoichiometry in the series $Na_{2-x}K_xCsC_{60}$; the grey lines mark the boundaries of the three distinct regions of structural behaviour. **(b)** Plot of the cell parameter as a function of the refined K content. **(a+b)** Down (Up) triangles represent the disordered (merohedral) $Fm\bar{3}m$ model, squares $Pa\bar{3}$. Green (Red) accounts for the single phase disordered (merohedral) $Fm\bar{3}m$ model. Yellow (Blue) accounts for the disordered (merohedral) $Fm\bar{3}m$ phase in the two-phase region. **(c)** Phase percentage of each structural component with changing K content; red is the disordered $Fm\bar{3}m$ phase, blue the merohedral $Fm\bar{3}m$ one.

5.10 $Na_{2-x}K_xCsC_{60}$ with intermediate K doping level (0.5 < x < 1.5), quenched protocol, room temperature

The synchrotron X-ray powder diffraction data at room temperature were refined using the spherically disordered *Fm*$\bar{3}$*m*, merohedral *Fm*$\bar{3}$*m* and mixed phase *Fm*$\bar{3}$*m* models. The obtained *R*-factors indicate that the structures adopted are a mixture of spherically disordered and merohedral *Fm*$\bar{3}$*m*, (Table 5.27), and this is confirmed via a visual comparison of the refinements (Fig 5.32, Fig 5.36 and Fig 5.38). The values of the lattice constants and unit cell volumes are listed in Table 5.27. In both phases the fractional occupancy, N, of Cs and the Na/K total occupancy were fixed at 1.0; however, the Na/K ratio was allowed to refine. The peak-shape parameters of the *Fm*$\bar{3}$*m* models were constrained to be equal to each other.

Like samples produced utilising the slow-cooled protocol there are negative temperature factors associated with the minority phase of the sample, again the only rational explanation is to attribute this phenomena to the excessive peak overlap in existence between the two phases.

Table 5.27: Summary results of the Rietveld refinements of the diffraction data of the series $Na_{2-x}K_xCsC_{60}$ ($0.5 \leq x \leq 1.5$) at room temperature.

Parameter	*MTM149_3*	*MTM136_4*	*MTM132_3*	*MTM145_3*	*MTM147_3*
Nominal x	0.65	0.85	1.00	1.20	1.35
λ (Å)	0.40289(6)	0.40289(6)	0.40289(6)	0.40289(6)	0.40289(6)
Single Phase - Merohedral *Fm* $\bar{3}$ *m*					
R_{wp} **(%)**	9.38	7.83	8.78	8.32	8.28
R_{exp} **(%)**	6.60	5.20	6.20	7.02	7.08
χ^2 **(%)**	2.020	2.267	2.005	1.405	1.368
Single Phase - Disordered *Fm* $\bar{3}$ *m*					
R_{wp} **(%)**	7.76	7.01	7.84	9.03	10.03
R_{exp} **(%)**	6.60	5.20	6.20	7.01	7.07
χ^2 **(%)**	1.382	1.817	1.599	1.659	2.013
Two Phase - Mixed (Disordered / Merohedral)					
R_{wp} **(%)**	7.46	6.04	7.09	7.65	7.87
R_{exp} **(%)**	6.60	5.20	6.20	7.01	7.08
χ^2 **(%)**	1.278	1.349	1.308	1.191	1.236
Dis (%)	77.8(3)	61.5(4)	59.7(6)	42.6(8)	27.4(9)
Mero (%)	22.2(9)	38.5(6)	40.3(8)	57.4(6)	72.6(3)
Dis - *a* (Å)	14.1902(2)	14.2151(5)	14.2114(3)	14.2438(6)	14.2588(7)
Dis - *V* (Å^3)	2857.4(1)	2872.4(3)	2870.2(2)	2889.9(3)	2899.0(4)
Refined Dis stoichiometry	$Na_{1.64(5)}K_{0.36(5)}CsC_{60}$	$Na_{1.13(6)}K_{0.87(6)}CsC_{60}$	$Na_{1.41(8)}K_{0.59(8)}CsC_{60}$	$Na_{0.88(13)}K_{1.12(13)}CsC_{60}$	$Na_{0.44(22)}K_{1.56(22)}CsC_{60}$
Mero - *V* (Å^3)	14.1937(6)	14.2247(4)	14.2166(3)	14.2559(3)	14.2624(2)
Mero - *a* (Å)	2859.5(4)	2878.3(3)	2873.4(2)	2897.3(2)	2901.2(1)
Refined Mero stoichiometry	$Na_{1.02(15)}K_{0.98(15)}CsC_{60}$	$Na_{0.55(9)}K_{1.45(9)}CsC_{60}$	$Na_{0.78(12)}K_{1.22(12)}CsC_{60}$	$Na_{0.39(9)}K_{1.61(9)}CsC_{60}$	$Na_{0.15(7)}K_{1.85(7)}CsC_{60}$

5.10.1 Sample $Na_{1.35}K_{0.65}CsC_{60}$ at room temperature

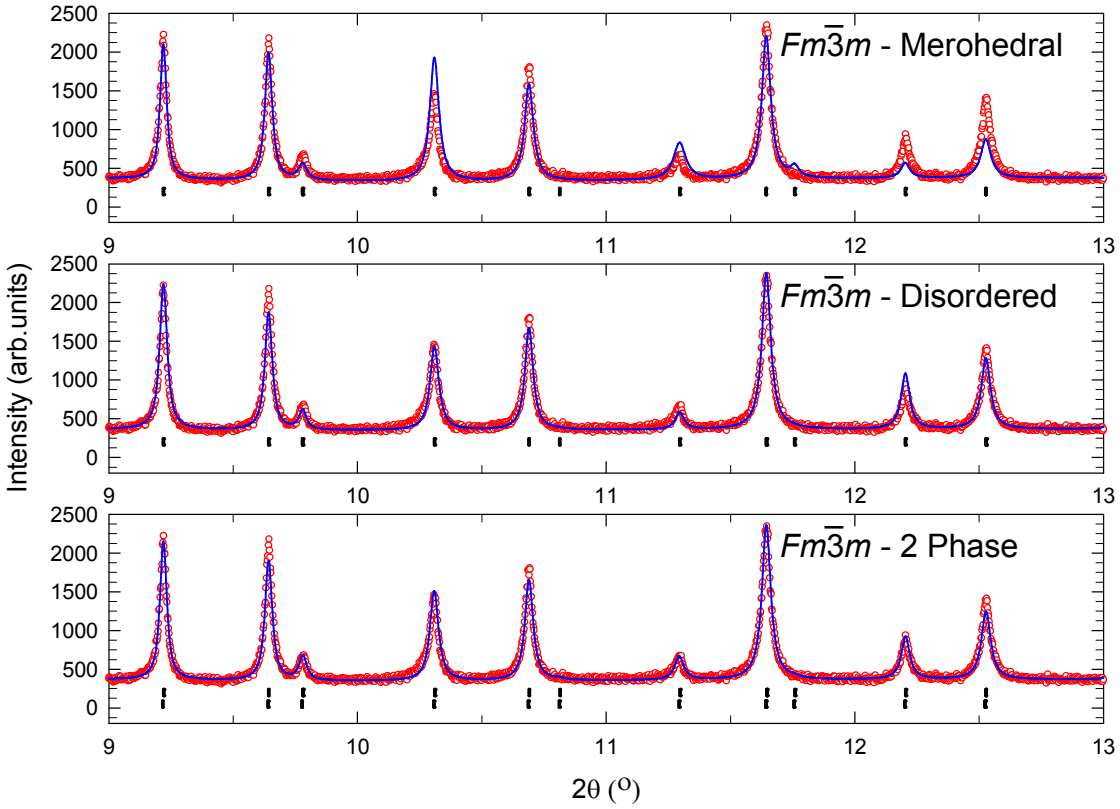

Fig 5.32: Comparison between the *Fm* $\bar{3}$ *m* spherically disordered, *Fm* $\bar{3}$ *m* merohedral and two-phase refinement models for the sample of nominal stoichiometry $Na_{1.35}K_{0.65}CsC_{60}$. In the lower refinement picture, the upper bars represent the positions of the Bragg reflections for the spherically disordered *Fm* $\bar{3}$ *m* phase, and the lower bars represent the merohedral *Fm* $\bar{3}$ *m* phase.

Table 5.28: Results of the room temperature two-phase Rietveld refinement of the spherically disordered *Fm* $\bar{3}$ *m* phase in the sample with overall nominal composition MTM149_3Q $Na_{1.35}K_{0.65}CsC_{60}$.

	x/a	*y/b*	*z/c*	*N*	B_{Iso}(Å^2)
Cs(1)	0.5	0.5	0.5	1.0	6.6(2)
Na(1)	0.25	0.25	0.25	0.822(24)	9.9(5)
K(1)	0.25	0.25	0.25	0.178(24)	9.9(5)
C(1-10)	58% - C's with same occupancy and B_{Iso}			0.073(2)	0.6(2)
C(11-20)	42% - C's with same occupancy and B_{Iso}			0.052(2)	0.6(2)

Table 5.29: Results of the room temperature two-phase Rietveld refinement of the merohedral *Fm* $\bar{3}$ *m* phase in the sample with overall nominal composition $Na_{1.35}K_{0.65}CsC_{60}$ (MTM149_3Q).

	x/a	*y/b*	*z/c*	*N*	B_{Iso}(Å^2)
Cs(1)	0.5	0.5	0.5	1.0	3.6(4)
Na(1)	0.25	0.25	0.25	0.508(77)	-1.2(4)
K(1)	0.25	0.25	0.25	0.492(77)	-1.2(4)
C(1)	0	0.0501	0.2430	0.5	1.1(4)
C(2)	0.2121	0.0810	0.1000	0.5	1.1(4)
C(3)	0.1810	0.1618	0.0501	0.5	1.1(4)

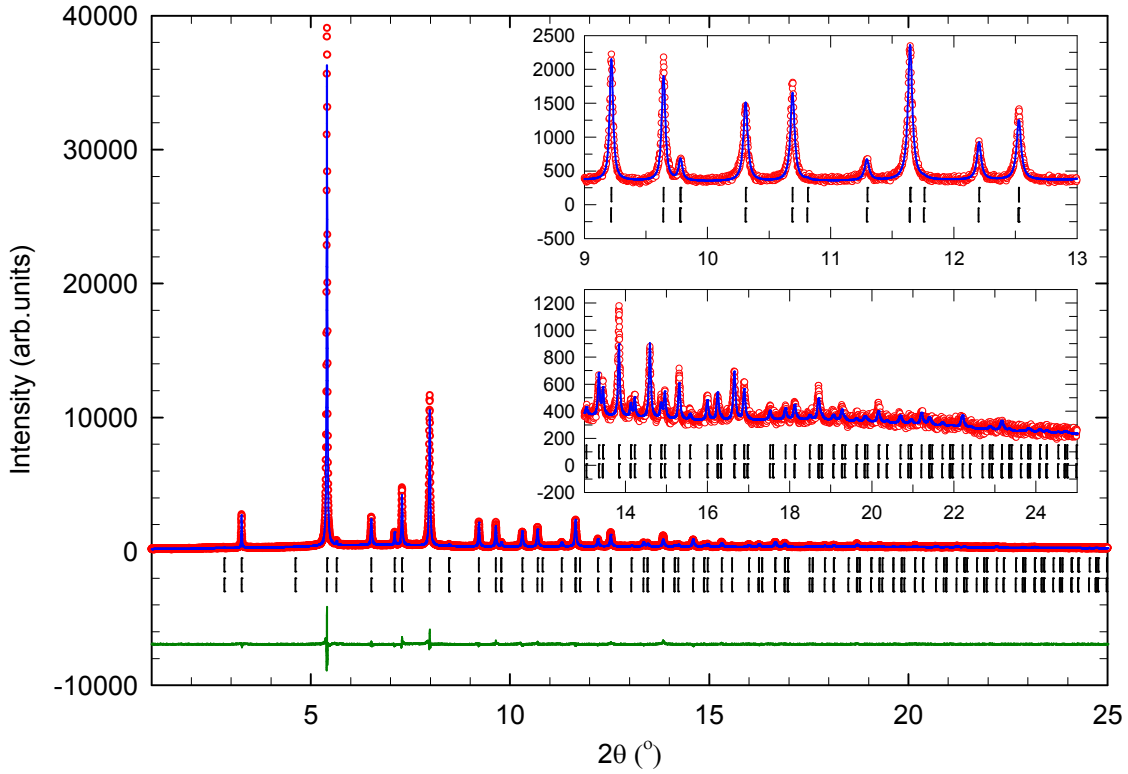

Fig 5.33: Observed (open red circles) and calculated (blue line) data of the room temperature synchrotron powder X-ray diffraction pattern for (quenched) $Na_{1.35}K_{0.65}CsC_{60}$. The upper bars represent the positions of the Bragg reflections for the spherically disordered *Fm* $\bar{3}$ *m* phase, and the lower bars represent the merohedral *Fm* $\bar{3}$ *m* phase. The wavelength is λ = 0.40289(6) Å.

5.10.2 Sample $Na_{1.15}K_{0.85}CsC_{60}$ at room temperature

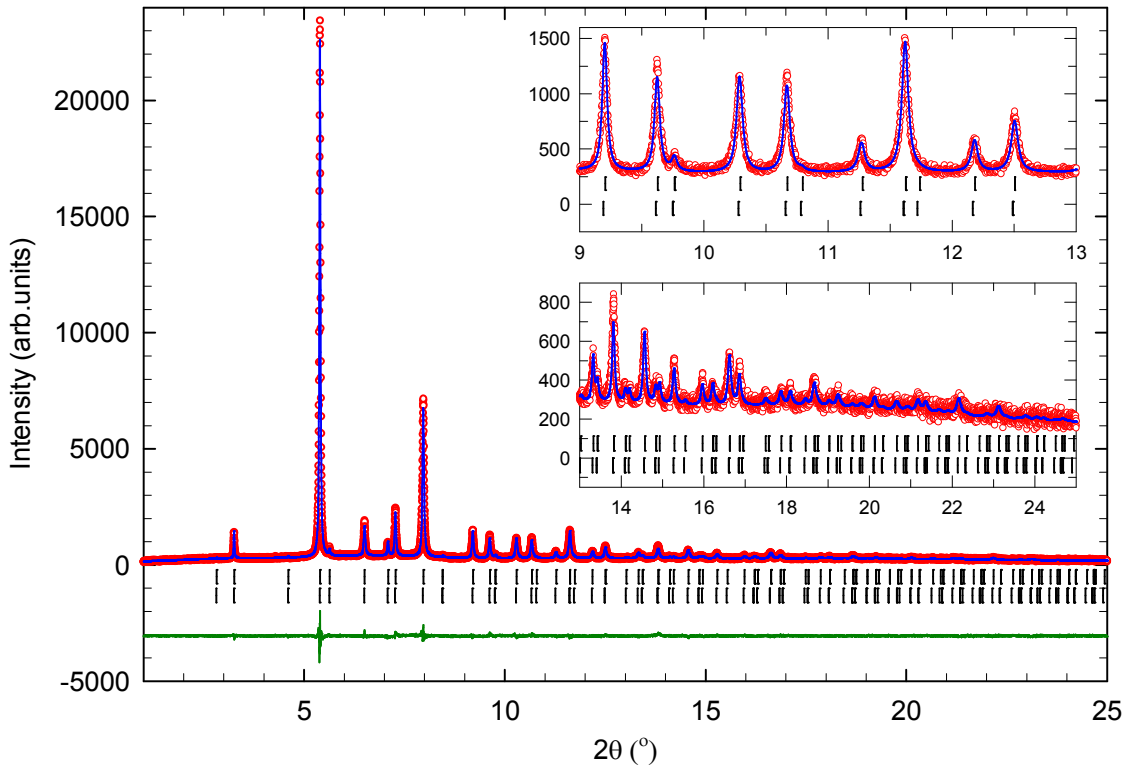

Fig 5.34: Observed (open red circles) and calculated (blue line) data of the room temperature synchrotron powder X-ray diffraction pattern for (quenched) $Na_{1.15}K_{0.85}CsC_{60}$. The upper bars represent the positions of the Bragg reflections for the spherically disordered *Fm* $\bar{3}$ *m* phase, and the lower bars represent the merohedral *Fm* $\bar{3}$ *m* phase. The wavelength is λ = 0.40289(6) Å.

Table 5.30: Results of the room temperature two-phase Rietveld refinement of the spherically disordered *Fm* $\bar{3}$ *m* phase in the sample with overall nominal composition $Na_{1.15}K_{0.85}CsC_{60}$ (MTM136_4Q).

	x/a	*y/b*	*z/c*	*N*	B_{Iso}(Å^2)
Cs(1)	0.5	0.5	0.5	1.0	6.3(2)
Na(1)	0.25	0.25	0.25	0.565(31)	9.6(4)
K(1)	0.25	0.25	0.25	0.435(31)	9.6(4)
C(1-10)	57% - C's with same occupancy and B_{Iso}			0.071(2)	-0.2(2)
C(11-20)	43% - C's with same occupancy and B_{Iso}			0.054(2)	-0.2(2)

Table 5.31: Results of the room temperature two-phase Rietveld refinement of the merohedral *Fm* $\bar{3}$ m phase in the sample with overall nominal composition $Na_{1.15}K_{0.85}CsC_{60}$ (MTM136_4Q).

	x/a	*y/b*	*z/c*	*N*	B_{Iso}(Å^2)
Cs(1)	0.5	0.5	0.5	1.0	4.3(2)
Na(1)	0.25	0.25	0.25	0.276(43)	-0.1(2)
K(1)	0.25	0.25	0.25	0.724(43)	-0.1(2)
C(1)	0	0.0500	0.2425	0.5	0.9(2)
C(2)	0.2116	0.0808	0.0998	0.5	0.9(2)
C(3)	0.1806	0.1615	0.0500	0.5	0.9(2)

5.10.3 Sample $NaKCsC_{60}$ at room temperature

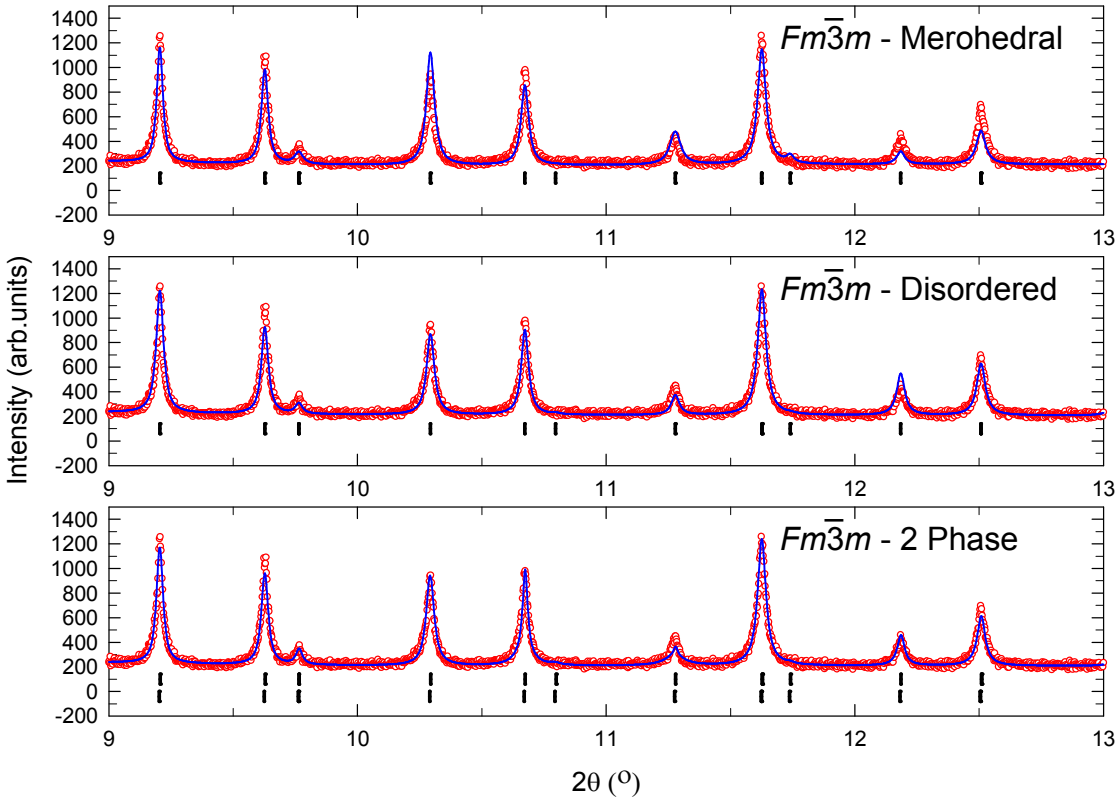

Fig 5.35: Comparison between the *Fm* $\bar{3}$ *m* spherically disordered, *Fm* $\bar{3}$ *m* merohedral and two-phase refinement models for the sample of nominal stoichiometry $NaKCsC_{60}$. In the lower refinement picture,

the upper bars represent the positions of the Bragg reflections for the spherically disordered $Fm\bar{3}m$ phase, and the lower bars represent the merohedral $Fm\bar{3}m$ phase.

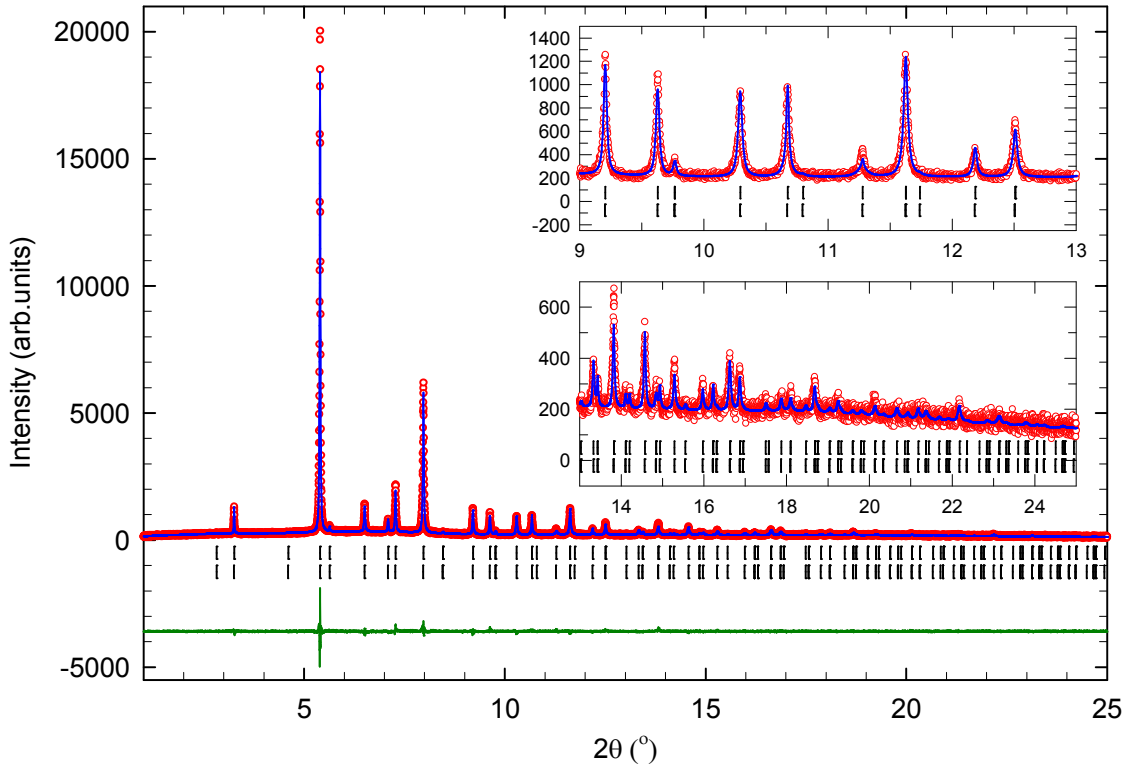

Fig 5.36: Observed (open red circles) and calculated (blue line) data of the room temperature synchrotron powder X-ray diffraction pattern for (quenched) $NaKCsC_{60}$. The upper bars represent the positions of the Bragg reflections for the spherically disordered $Fm\bar{3}m$ phase, and the lower bars represent the merohedral $Fm\bar{3}m$ phase. The wavelength is λ = 0.40289(6) Å.

Table 5.32: Results of the room temperature two-phase Rietveld refinement of the spherically disordered $Fm\bar{3}m$ phase in the sample with overall nominal composition $NaKCsC_{60}$ (MTM132_3Q).

	x/a	*y/b*	*z/c*	*N*	B_{Iso}(Å^2)
Cs(1)	0.5	0.5	0.5	1.0	6.0(2)
Na(1)	0.25	0.25	0.25	0.704(42)	8.6(5)
K(1)	0.25	0.25	0.25	0.296(42)	8.6(5)
C(1-10)	50% - C's with same occupancy and B_{Iso}			0.063(2)	0.4(2)
C(11-20)	50% - C's with same occupancy and B_{Iso}			0.062(2)	0.4(2)

Table 5.33: Results of the room temperature two-phase Rietveld refinement of the merohedral *Fm* $\bar{3}$ *m* phase in the sample with overall nominal composition $NaKCsC_{60}$ (MTM132_3Q).

	x/a	*y/b*	*z/c*	*N*	B_{Iso}(Å^2)
Cs(1)	0.5	0.5	0.5	1.0	4.9(3)
Na(1)	0.25	0.25	0.25	0.388(60)	0.5(3)
K(1)	0.25	0.25	0.25	0.612(60)	0.5(3)
C(1)	0	0.0500	0.2426	0.5	0.8(2)
C(2)	0.2118	0.0809	0.0998	0.5	0.8(2)
C(3)	0.1807	0.1616	0.0500	0.5	0.8(2)

5.10.4 Sample $Na_{0.8}K_{1.2}CsC_{60}$ at room temperature

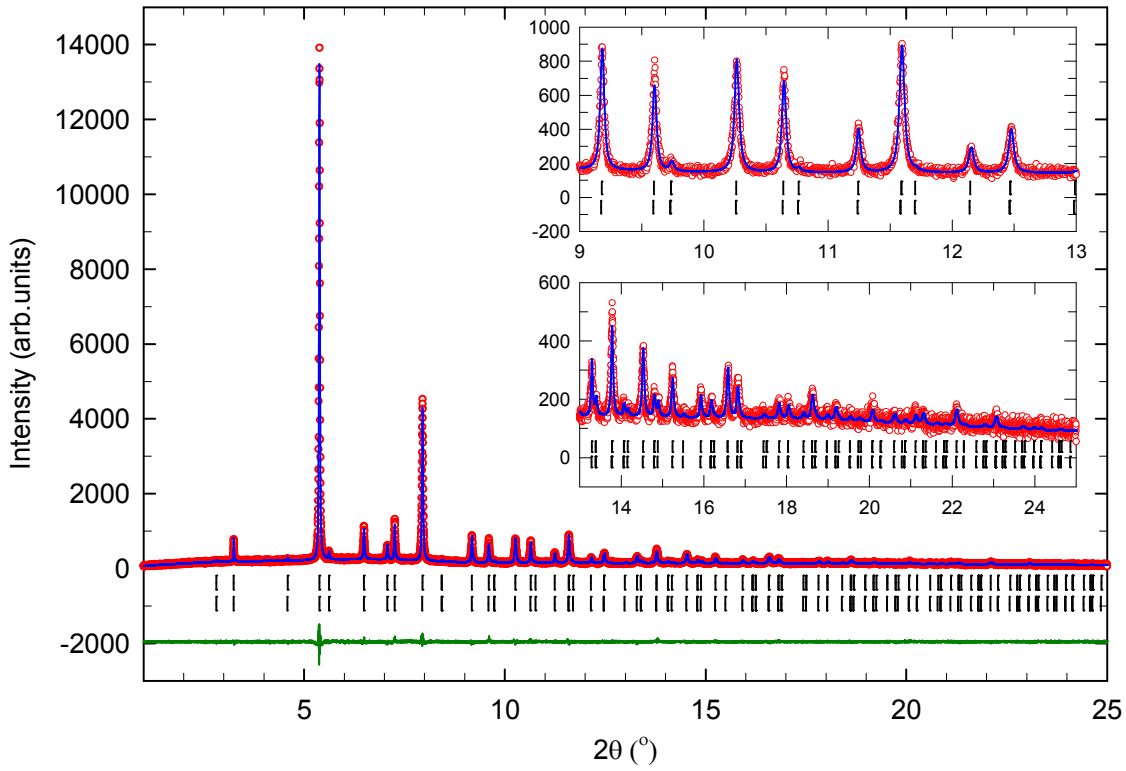

Fig 5.37: Observed (open red circles) and calculated (blue line) data of the room temperature synchrotron powder X-ray diffraction pattern for (quenched) $Na_{0.8}K_{1.2}CsC_{60}$. The upper bars represent the positions of the Bragg reflections for the spherically disordered *Fm* $\bar{3}$ *m* phase, and the lower bars represent the merohedral *Fm* $\bar{3}$ *m* phase. The wavelength is λ = 0.40289(6) Å.

Table 5.34: Results of the room temperature two-phase Rietveld refinement of the spherically disordered *Fm* $\bar{3}$ *m* phase in the sample with overall nominal composition $Na_{0.8}K_{1.2}CsC_{60}$ (MTM145_3Q).

	x/a	*y/b*	*z/c*	*N*	B_{Iso}(Å^2)
Cs(1)	0.5	0.5	0.5	1.0	5.7(3)
Na(1)	0.25	0.25	0.25	0.440(66)	9.0(7)
K(1)	0.25	0.25	0.25	0.560(66)	9.0(7)
C(1-10)	37% - C's with same occupancy and B_{Iso}			0.046(3)	-0.3(4)
C(11-20)	63% - C's with same occupancy and B_{Iso}			0.079(3)	-0.3(4)

Table 5.35: Results of the room temperature two-phase Rietveld refinement of the merohedral *Fm* $\bar{3}$ *m* phase in the sample with overall nominal composition $Na_{0.8}K_{1.2}CsC_{60}$ (MTM145_3Q).

	x/a	*y/b*	*z/c*	*N*	B_{Iso}(Å^2)
Cs(1)	0.5	0.5	0.5	1.0	4.5(2)
Na(1)	0.25	0.25	0.25	0.195(44)	1.1(2)
K(1)	0.25	0.25	0.25	0.805(44)	1.1(2)
C(1)	0	0.0499	0.2419	0.5	1.4(2)
C(2)	0.2112	0.0806	0.0996	0.5	1.4(2)
C(3)	0.1802	0.1611	0.0499	0.5	1.4(2)

5.10.5 Sample $Na_{0.65}K_{1.35}CsC_{60}$ at room temperature

Table 5.36: Results of the room temperature two-phase Rietveld refinement of the spherically disordered *Fm* $\bar{3}$ *m* phase in the sample with overall nominal composition $Na_{0.65}K_{1.35}CsC_{60}$ (MTM147_3Q)

	x/a	*y/b*	*z/c*	*N*	B_{Iso}(Å^2)
Cs(1)	0.5	0.5	0.5	1.0	5.7(4)
Na(1)	0.25	0.25	0.25	0.22(11)	9.1(8)
K(1)	0.25	0.25	0.25	0.78(11)	9.1(8)
C(1-10)	59% - C's with same occupancy and B_{Iso}			0.074(4)	-2.4(4)
C(11-20)	41% - C's with same occupancy and B_{Iso}			0.051(4)	-2.4(4)

Table 5.37: Results of the room temperature two-phase Rietveld refinement of the merohedral *Fm* $\bar{3}$ *m* phase in the sample with overall nominal composition $Na_{0.65}K_{1.35}CsC_{60}$ (MTM147_3Q).

	x/a	*y/b*	*z/c*	*N*	B_{Iso}(Å^2)
Cs(1)	0.5	0.5	0.5	1.0	4.8(2)
Na(1)	0.25	0.25	0.25	0.075(34)	1.7(2)
K(1)	0.25	0.25	0.25	0.925(34)	1.7(2)
C(1)	0	0.0501	0.2430	0.5	0.8(1)
C(2)	0.2121	0.0810	0.1000	0.5	0.8(1)
C(3)	0.1810	0.1618	0.0501	0.5	0.8(1)

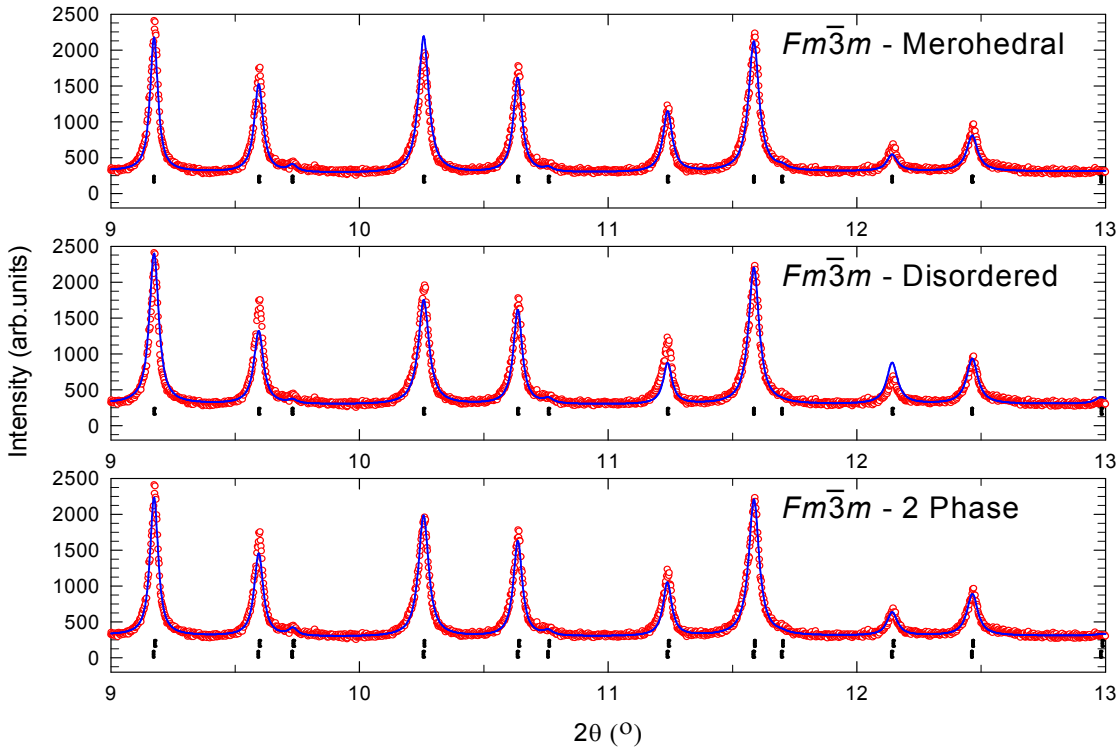

Fig 5.38: Comparison between the *Fm* $\bar{3}$ *m* spherically disordered, *Fm* $\bar{3}$ *m* merohedral and two-phase refinement models of nominal stoichiometry $Na_{0.65}K_{1.35}CsC_{60}$. In the lower refinement picture, the upper bars represent the positions of the Bragg reflections for the spherically disordered *Fm* $\bar{3}$ *m* phase, and the lower bars represent the merohedral *Fm* $\bar{3}$ *m* phase.

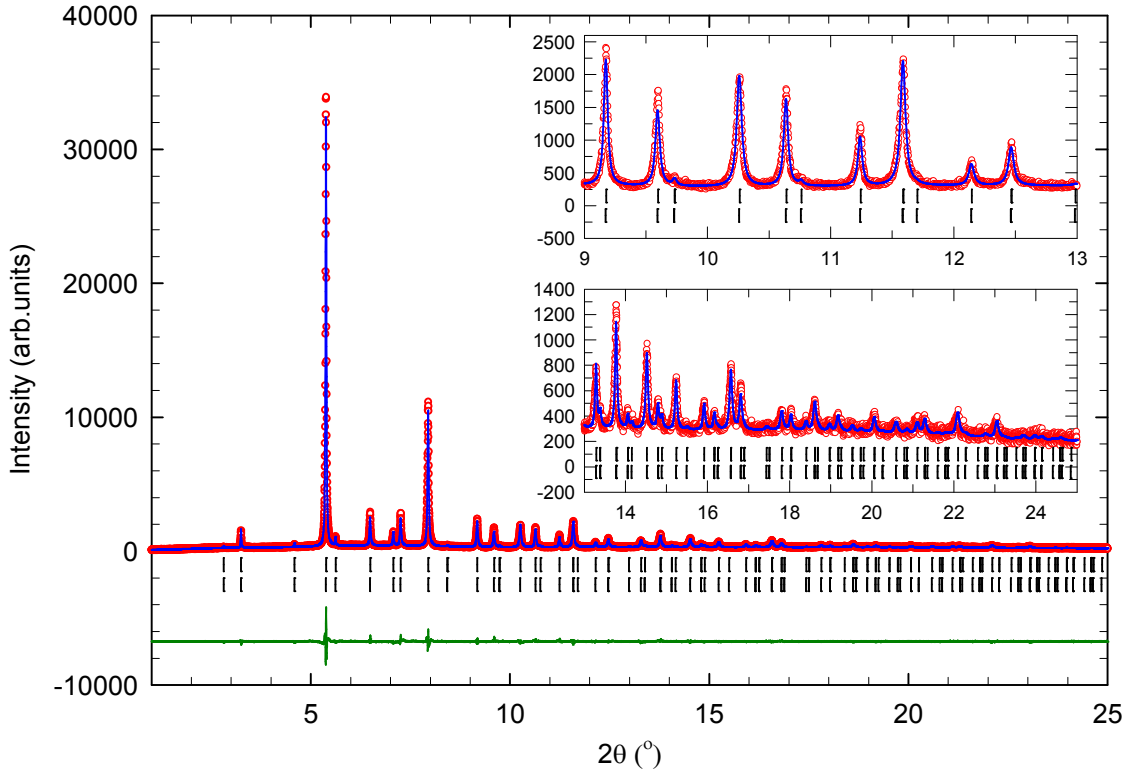

Fig 5.39: Observed (open red circles) and calculated (blue line) data of the room temperature synchrotron powder X-ray diffraction pattern for (quenched) $Na_{0.65}K_{1.35}CsC_{60}$. The bars represent the positions of the Bragg reflections for the merohedral $Fm\bar{3}m$ phase. The wavelength is λ = 0.40289(6) Å.

5.11 $Na_{2-x}K_xCsC_{60}$ with high K doping level (2.0 > x ≥ 1.5), quenched, room temperature

The synchrotron X-ray powder diffraction data at room temperature were refined using the spherically disordered $Fm\bar{3}m$, merohedral $Fm\bar{3}m$ and mixed phase $Fm\bar{3}m$ models. The obtained *R*-factors indicate that the structures adopted are merohedral $Fm\bar{3}m$ (Table 5.38), and this is confirmed via a visual comparison of the refinements, Fig 5.41. The values of the lattice constants and unit cell volumes are listed in Table 5.38. In the cases of high K doping, the mixed phase model offers no significant improvement in refinement quality, while the spherically disordered component of these refinements shows highly negative temperature factors for the

atoms. The fractional occupancy, N, of Cs and the Na/K total occupancy were fixed at 1.0; however, the ratio was allowed to refine.

Table 5.38: Summary results of the Rietveld refinements of the diffraction data of the series $Na_{2-x}K_xCsC_{60}$ ($2.0 > x \geq 1.5$) at room temperature.

Parameter	*MTM142_4*	*MTM154_3*
Nominal x	1.50	1.70
λ (Å)	0.40289(6)	0.40289(6)
Two Phase - Mixed (Disordered / Merohedral)		
R_{wp} **(%)**	7.34	6.69
R_{exp} **(%)**	6.10	6.34
χ^2 **(%)**	1.448	1.113
Dis (%)	26(1)	27.7(4)
Mero (%)	74(1)	72.3(1)
Single Phase - Disordered *Fm*$\bar{3}$*m*		
R_{wp} **(%)**	8.22	8.18
R_{exp} **(%)**	6.10	6.34
χ^2 **(%)**	1.816	1.665
Single Phase - Merohedral *Fm*$\bar{3}$*m*		
R_{wp} **(%)**	7.75	6.88
R_{exp} **(%)**	6.10	6.34
χ^2 **(%)**	1.614	1.178
FCC *a* (Å)	14.2589(4)	14.2787(2)
FCC *V* (Å^3)	2899.1(2)	2911.2(1)
Refined stoichiometry	$Na_{0.40(3)}K_{1.60(3)}CsC_{60}$	$Na_{0.00(2)}K_{2.00(2)}CsC_{60}$

5.11.1 Sample $Na_{0.5}K_{1.5}CsC_{60}$ at room temperature

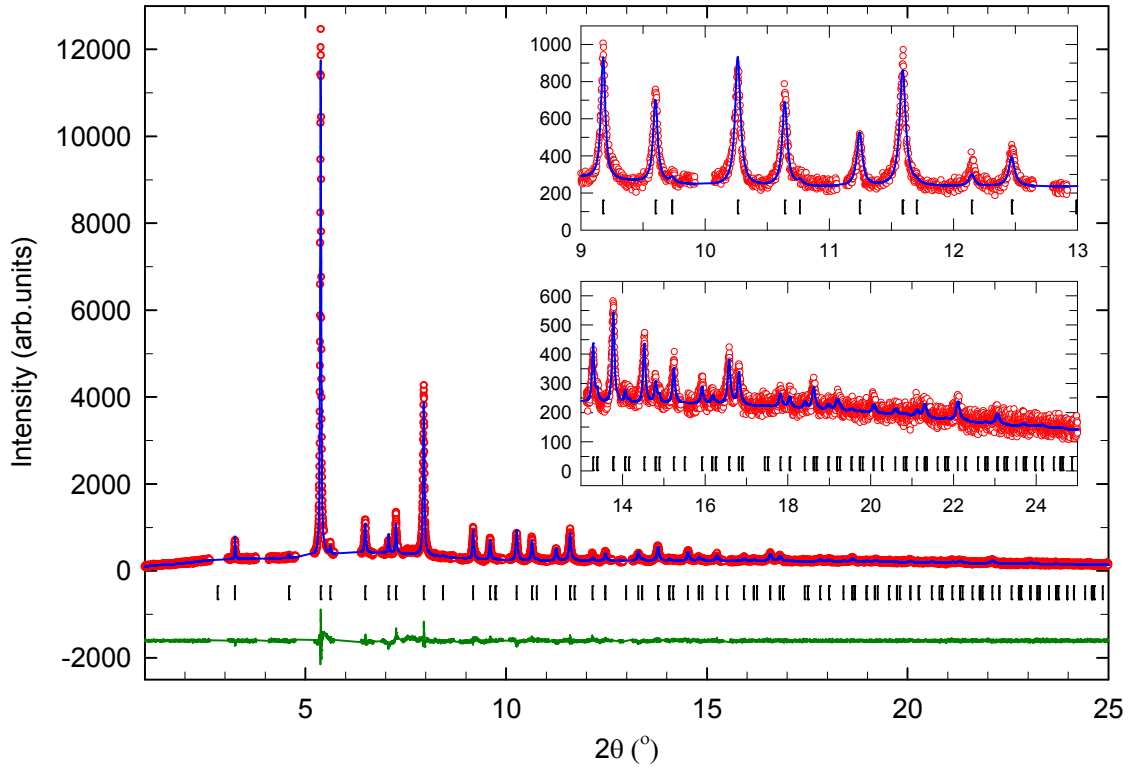

Fig 5.40: Observed (open red circles) and calculated (blue line) data of the room temperature synchrotron powder X-ray diffraction pattern for (quenched) $Na_{0.5}K_{1.5}CsC_{60}$. The bars represent the positions of the Bragg reflections for the merohedral *Fm* $\bar{3}$ *m* phase. The wavelength is λ = 0.40289(6) Å. Excluded regions are attributed to unidentifiable impurities.

Table 5.39: Results of the room temperature single-phase Rietveld refinement of the merohedral *Fm* $\bar{3}$ *m* phase in the sample with overall nominal composition $Na_{1.5}K_{0.5}CsC_{60}$ (MTM142_4Q).

	x/a	*y/b*	*z/c*	*N*	B_{Iso}(Å^2)
Cs(1)	0.5	0.5	0.5	1.0	5.8(1)
Na(1)	0.25	0.25	0.25	0.202(13)	3.1(2)
K(1)	0.25	0.25	0.25	0.798(13)	3.1(2)
C(1)	0	0.0499	0.2419	0.5	1.2(1)
C(2)	0.2111	0.0806	0.0995	0.5	1.2(1)
C(3)	0.1802	0.1611	0.0499	0.5	1.2(1)

5.11.2 Sample $Na_{0.3}K_{1.7}CsC_{60}$ at room temperature

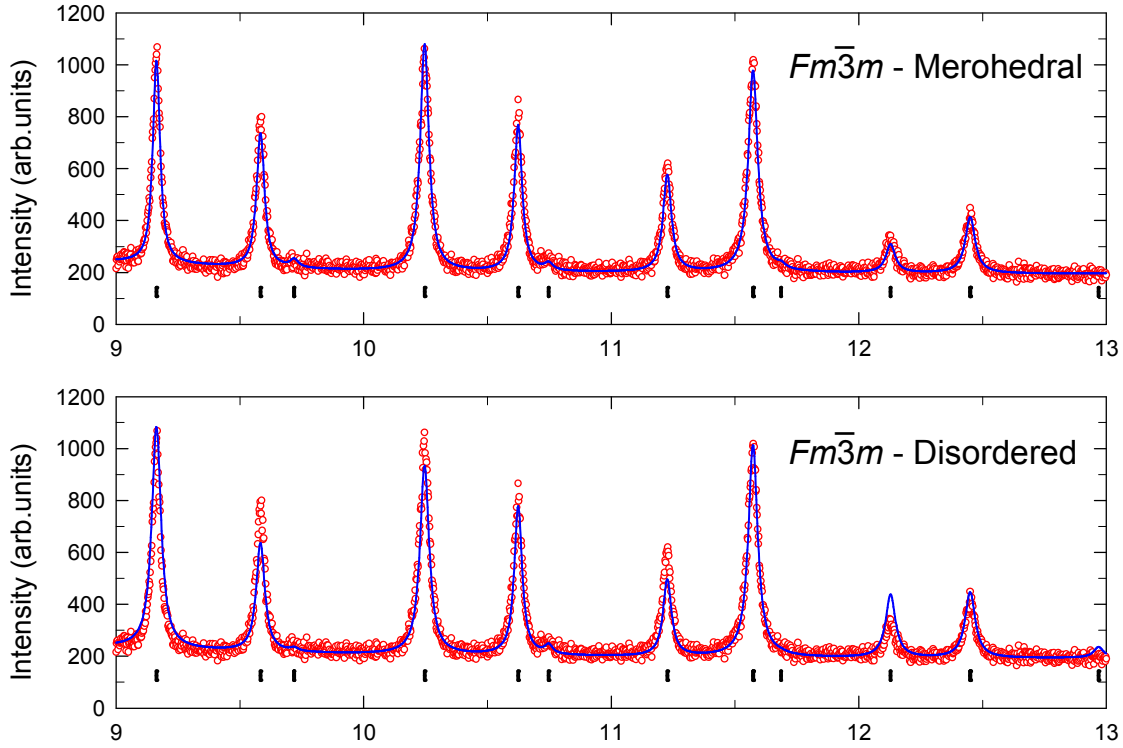

Fig 5.41: Comparison between the *Fm* $\bar{3}$ *m* spherically disordered and *Fm* $\bar{3}$ *m* merohedral models for the sample of nominal stoichiometry $Na_{0.3}K_{1.7}CsC_{60}$.

Table 5.40: Results of the room temperature single-phase Rietveld refinement of the merohedral *Fm* $\bar{3}$ *m* phase in the sample with overall nominal composition $Na_{0.3}K_{1.7}CsC_{60}$ (MTM154_3Q).

	x/a	*y/b*	*z/c*	*N*	B_{iso}(Å^2)
Cs(1)	0.5	0.5	0.5	1.0	4.24(6)
Na(1)	0.25	0.25	0.25	0.000(10)	2.8(1)
K(1)	0.25	0.25	0.25	1.000(10)	2.8(1)
C(1)	0	0.0501	0.2430	0.5	1.08(8)
C(2)	0.2121	0.0810	0.1000	0.5	1.08(8)
C(3)	0.1810	0.1612	0.0501	0.5	1.08(8)

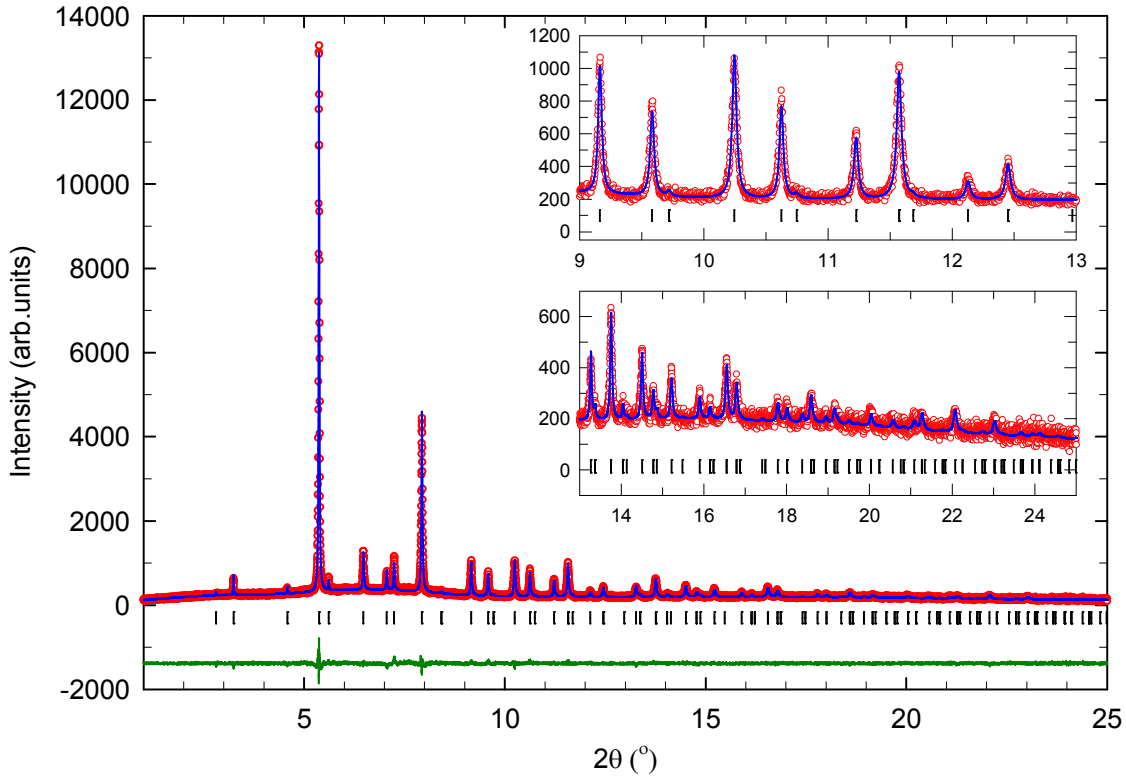

Fig 5.42: Observed (open red circles) and calculated (blue line) data of the room temperature synchrotron powder X-ray diffraction pattern for (quenched) $Na_{0.3}K_{1.7}CsC_{60}$. The upper bars represent the positions of the Bragg reflections for the spherically disordered $Fm\bar{3}m$ phase, and the lower bars represent the merohedral $Fm\bar{3}m$ phase. The wavelength is λ = 0.40289(6) Å.

5.12 $Na_{2-x}K_xCsC_{60}$, quenched, low temperature

5.12.1 Sample $Na_{1.65}K_{0.35}CsC_{60}$ at 20 K

The synchrotron X-ray powder diffraction data at 20 K were refined using the spherically disordered $Fm\bar{3}m$ (R_{wp} = 6.11%, R_{exp} = 4.31%), merohedral $Fm\bar{3}m$ (R_{wp} = 9.80%, R_{exp} = 4.31%) and mixed phase $Fm\bar{3}m$ (R_{wp} = 5.28%, R_{exp} = 4.31%) models. The *R*-factors indicate that the structure adopted is a mixture of spherically disordered and merohedral $Fm\bar{3}m$. The mixed phase model offers a significant improvement in refinement quality with 76.6(2)% spherically disordered $Fm\bar{3}m$ and 23.4(6)%

merohedral $Fm\bar{3}m$. The values of the lattice constants and unit cell volumes are: $Fm\bar{3}m$ disordered a = 14.1191(2) Å, V = 2814.6(1) Å^3 and $Fm\bar{3}m$ merohedral a = 14.1304(4) Å, V = 2821.2(2) Å^3. In both phases the fractional occupancy, N, of Cs and the Na/K total occupancy were fixed at 1.0; however, the ratios were allowed to refine converging to values for the spherically disordered $Fm\bar{3}m$: Na = 0.913(18), K = 0.087(18) and merohedral $Fm\bar{3}m$: Na = 0.482(56), K = 0.518(56). These result in refined stoichiometries for disordered $Fm\bar{3}m$ of $Na_{1.83(4)}K_{0.17(4)}CsC_{60}$ and for merohedral $Fm\bar{3}m$ of $Na_{1.0(1)}K_{1.0(1)}CsC_{60}$.

Table 5.41: Results of the 20 K two-phase Rietveld refinement of the spherically disordered $Fm\bar{3}m$ phase in the sample with overall nominal composition $Na_{1.35}K_{0.65}CsC_{60}$ (MTM149_3).

	x/a	*y/b*	*z/c*	*N*	B_{Iso}(Å^2)
Cs(1)	0.5	0.5	0.5	1.0	2.64(7)
Na(1)	0.25	0.25	0.25	0.913(18)	5.0(2)
K(1)	0.25	0.25	0.25	0.087(18)	5.0(2)
C(1-10)	72% - C's with same occupancy and B_{Iso}			0.090(1)	-0.3(1)
C(11-20)	28% - C's with same occupancy and B_{Iso}			0.035(1)	-0.3(1)

Table 5.42: Results of the 20 K two-phase Rietveld refinement of the merohedral $Fm\bar{3}m$ phase in the sample with overall nominal composition $Na_{1.35}K_{0.65}CsC_{60}$ (MTM149_3).

	x/a	*y/b*	*z/c*	*N*	B_{Iso}(Å^2)
Cs(1)	0.5	0.5	0.5	1.0	1.5(2)
Na(1)	0.25	0.25	0.25	0.482(56)	-1.5(2)
K(1)	0.25	0.25	0.25	0.518(56)	-1.5(2)
C(1)	0	0.0503	0.2438	0.5	0.6(2)
C(2)	0.2128	0.0813	0.1003	0.5	0.6(2)
C(3)	0.1816	0.1624	0.0503	0.5	0.6(2)

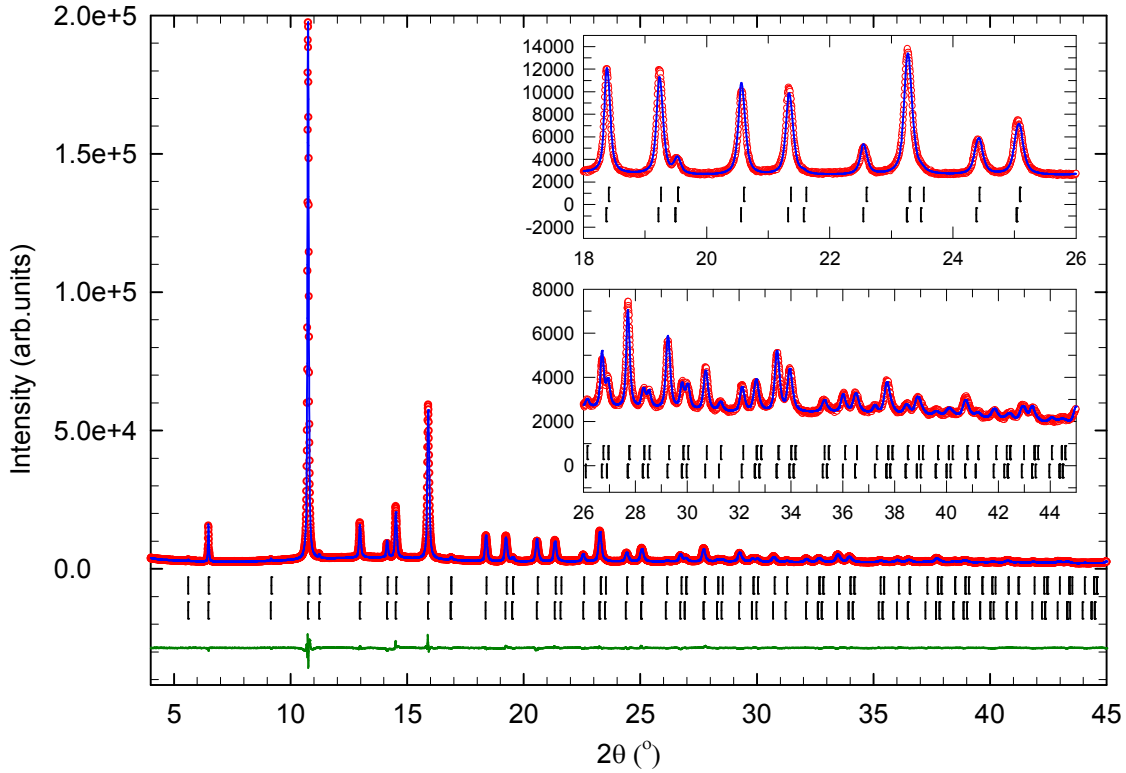

Fig 5.43: Observed (open red circles) and calculated (blue line) data of the 20 K synchrotron powder X-ray diffraction pattern for (quenched) $Na_{1.35}K_{0.65}CsC_{60}$. The upper bars represent the positions of the Bragg reflections for the spherically disordered $Fm\bar{3}m$ phase, and the lower bars represent the merohedral $Fm\bar{3}m$ phase. The wavelength is λ = 0.40289(6) Å.

5.13 Conclusions and Summary, results obtained upon quenching

In this subsection, the effect of changing the cooling protocol on the composition of the quaternary alkali fulleride samples was investigated. The emphasis was especially in the miscibility gap region where homogeneously-doped single phase samples were not available upon slow cooling to room temperature. Heating the samples to high temperature and rapidly quenching into liquid nitrogen could lead to the isolation of metastable single phase compositions. Of particular interest is the low K doping phase separation borderline in the phase field as potential isolation of

spherically disordered $Fm\bar{3}m$ phases to higher x could provide the route for higher superconducting transition temperatures (T_c) in this family of fullerides.

The relative fractions of the co-existing phases in the miscibility gap (Fig 5.44(c)) show that the difference between slow-cooling and quenching is very small. This implies that even higher annealing temperatures may be required to homogenise the samples before quenching. However, such temperatures promote competing decomposition or amorphisation of the products and are undesirable. One advantage of the quenching process was that the obtained diffraction profiles were of better quality as the broadness of the peaks was reduced and the asymmetry was suppressed. Additionally, a smoother trend is observed for the dependence of the cell parameter on the refined Na:K ratio of the T_d site (Fig 5.44 (b)).

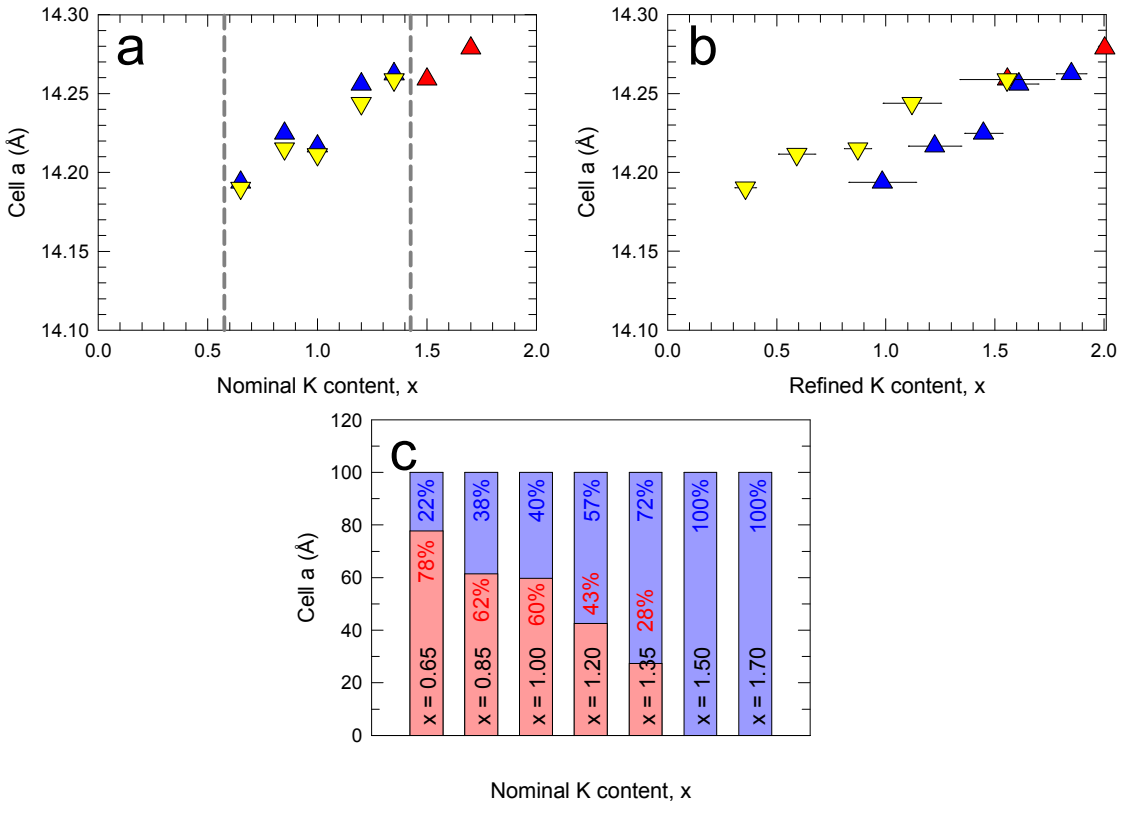

Fig 5.44: (a) Plot of the cell parameter as a function of the nominal stoichiometry in the series $Na_{2-x}K_xCsC_{60}$; the grey lines mark the boundaries of the three distinct regions of structural behaviour. **(b)** Plot of the cell parameter as a function of the refined K content. **(a+b)** Down (Up) triangles represent the disordered (merohedral) $Fm\bar{3}m$ model. Red accounts for the single phase merohedral $Fm\bar{3}m$ model.

Yellow (Blue) accounts for the disordered (merohedral) *Fm* $\bar{3}$ *m* phase in the two-phase region. **(c)** Phase percentage of each structural component with changing K content; red is the disordered *Fm* $\bar{3}$ *m* phase, blue the merohedral *Fm* $\bar{3}$ *m* one.

5.14 Magnetic Properties

Zero-field-cooled (ZFC) and field-cooled (FC) magnetic measurements at a field of 10 Oe were carried out on the series of fullerides, $Na_{2-x}K_xCsC_{60}$ ($2.00 \geq x \geq 0.00$). All measurements were carried out at ambient pressure. The aim of the measurements was the follow the evolution of T_c as the K doping level changes. The two structural families accessible in this phase field have distinct dependences of their T_c on unit cell volume but the crossover in the electronic behaviour from one family to the other had not been investigated before.

A small amount of material was loaded into a quartz tube inside the glove box. The sample and its containing vessel are then removed and sealed under 300 Torr of He gas. The quartz tube design was identical to that described before in Section 3.5.1. The samples were introduced into the MPMS5 cryostat at 100 K under zero field and cooled slowly to the base temperature of 1.8 K (ZFC). When stable at 1.8 K, a field of 10 Oe was applied and the magnetic response was measured as a function of temperature from 1.8 to 25 K for samples where $x \leq 1$ and from 1.8 to 30 K for samples where $x > 1$, at a rate of 0.25 K/min in a step size of 0.5 K. Using the same cooling protocol, the sample was cooled back to base temperature (with the field still switched on). FC measurements were then recorded on warming. The superconducting fraction and T_c definition were expressed using the guidelines presented in *section 2.5.5* of this thesis.

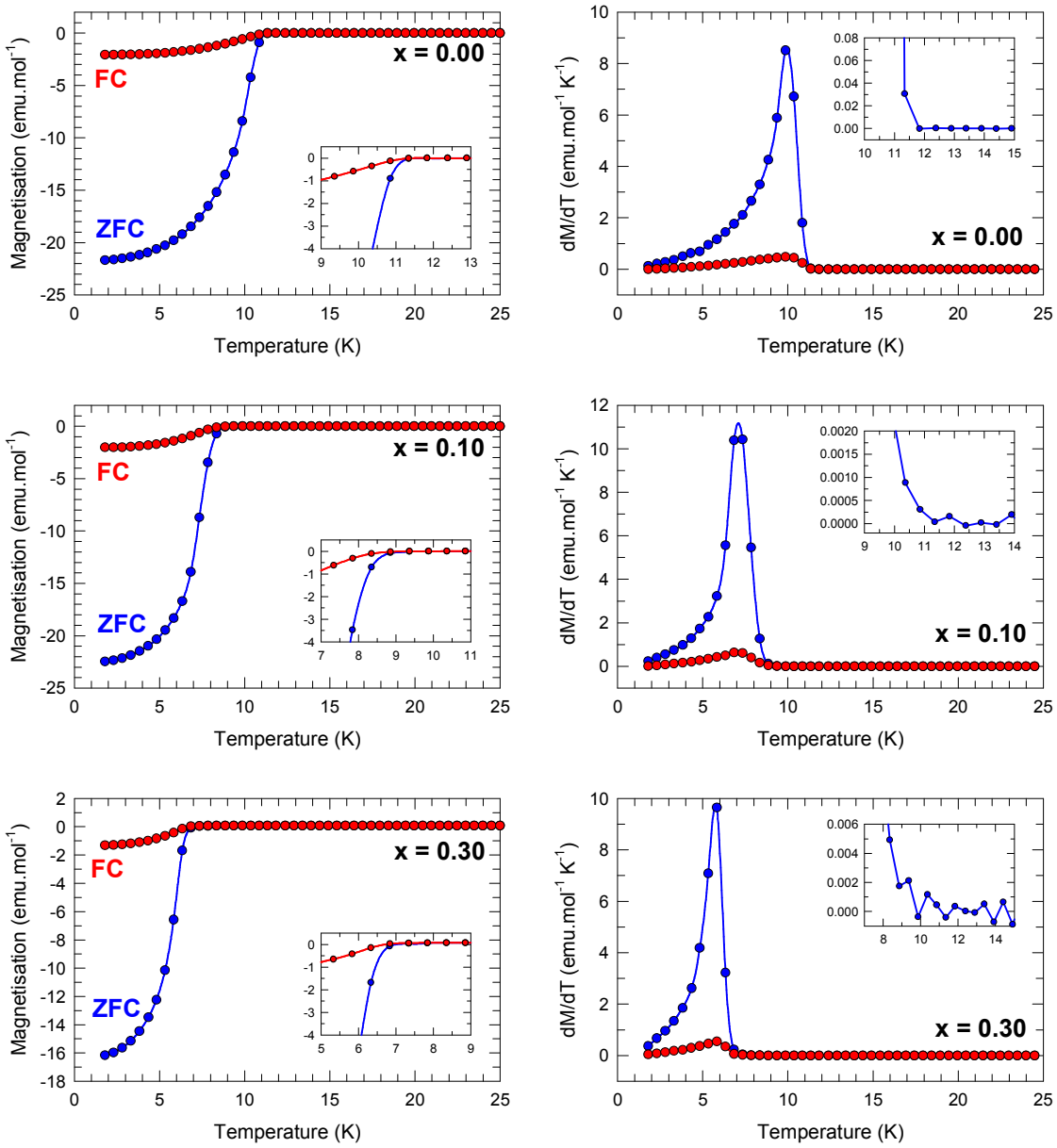

Fig 5.45: Temperature dependence of the 10 Oe ZFC (blue circles) and FC (red circles) DC magnetisation, *M* and its temperature derivative, d*M*/d*T* at ambient pressure for the compounds $Na_{2-x}K_xCsC_{60}$ (nominal x = 0, 0.1, 0.3) synthesised by "slow cooling".

Table 5.43: Superconducting fraction and T_c for slow-cooled samples $Na_{2-x}K_xCsC_{60}$ (nominal x = 0, 0.1, 0.3).

Sample	x	Mass (mg)	SC Fraction (%)	T_c (K)
MTM129_3	0	19	64.5	11.3
MTM131_3	0.1	24	66.0	9.9
MTM123_3	0.3	16	47.7	9.8

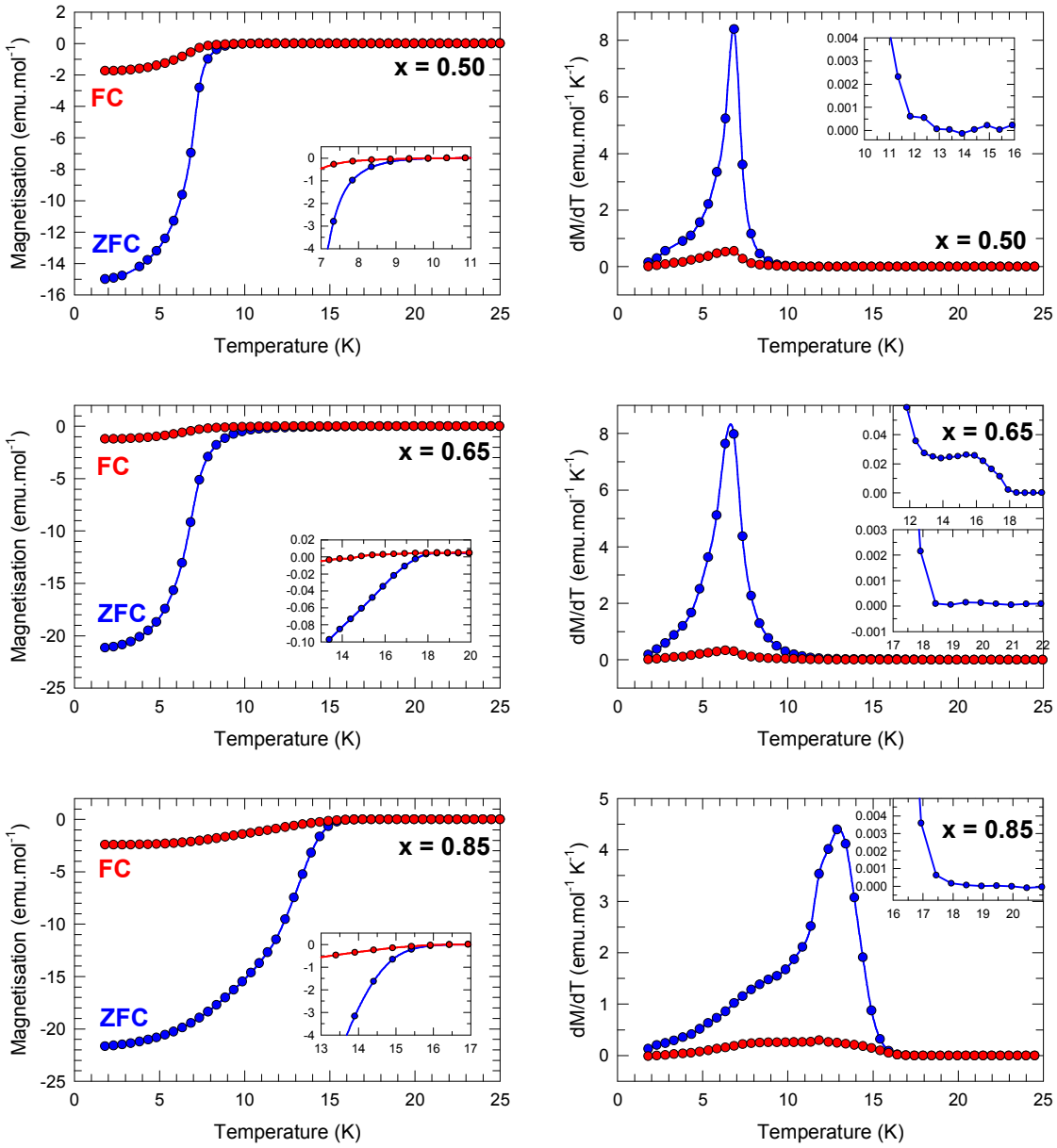

Fig 5.46: Temperature dependence of the 10 Oe ZFC (blue circles) and FC (red circles) DC magnetisation, *M* and its temperature derivative, d*M*/d*T* at ambient pressure for the compounds $Na_{2-x}K_xCsC_{60}$ (nominal x = 0.5, 0.65, 0.85) synthesised by "slow cooling".

Table 5.44: Superconducting fraction and T_c for slow-cooled samples $Na_{2-x}K_xCsC_{60}$ (nominal x = 0.5, 0.65, 0.85).

Sample	x	Mass (mg)	SC Fraction (%)	T_c (K)
MTM119_4	0.5	16	44.0	11.3
MTM149_3	0.65	20	61.8	13.4
MTM136_4	0.85	21	62.9	16.9

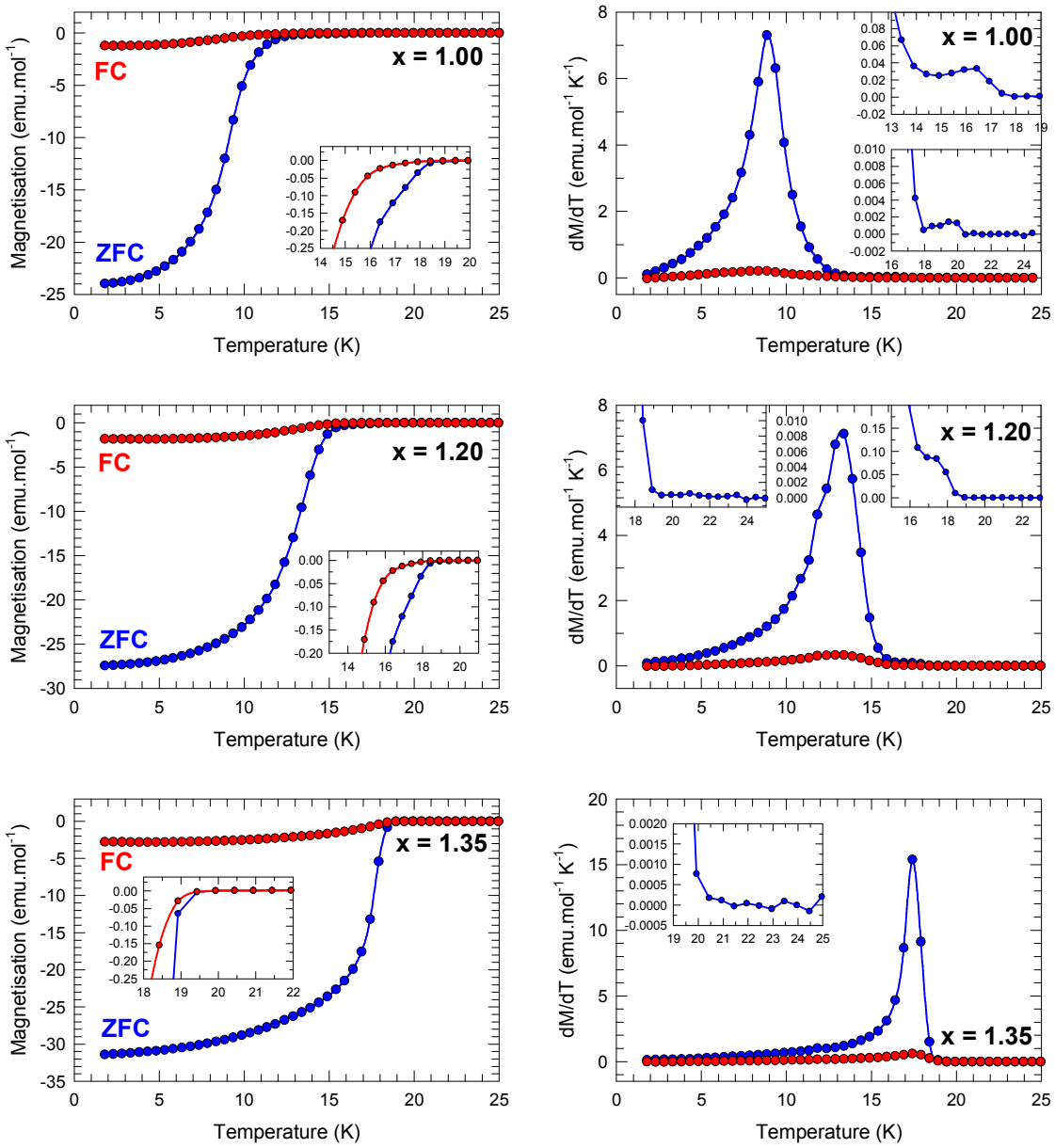

Fig 5.47: Temperature dependence of the 10 Oe ZFC (blue circles) and FC (red circles) DC magnetisation, *M* and its temperature derivative, d*M*/d*T* at ambient pressure for the compounds $Na_{2-x}K_xCsC_{60}$ (nominal x = 1, 1.2, 1.35) synthesised by "slow cooling".

Table 5.45: Superconducting fraction and T_c for slow-cooled samples $Na_{2-x}K_xCsC_{60}$ (nominal x = 1, 1.2, 1.35).

Sample	x	Mass (mg)	SC Fraction (%)	T_c (K)
MTM132_3	1	20	69.7	14.4
MTM145_3	1.2	24	79.8	17.9
MTM147_3	1.35	26	90.4	19.9

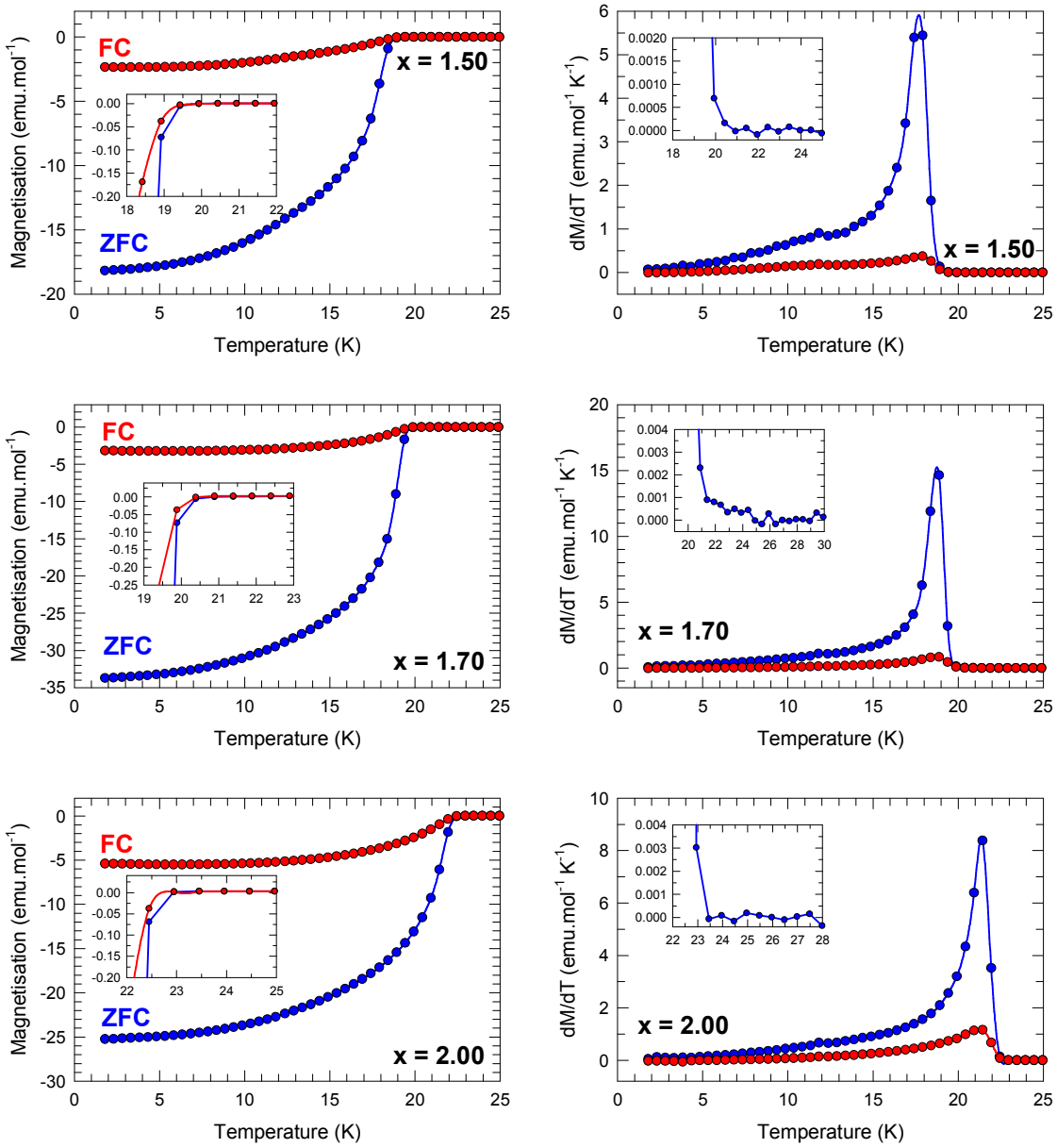

Fig 5.48: Temperature dependence of the 10 Oe ZFC (blue circles) and FC (red circles) DC magnetisation, *M* and its temperature derivative, d*M*/d*T* at ambient pressure for the compounds $Na_{2-x}K_xCsC_{60}$ (nominal x = 1.5, 1.7, 2) synthesised by "slow cooling".

Table 5.46: Superconducting fraction and T_c for slow cooled samples $Na_{2-x}K_xCsC_{60}$ (nominal x = 1.5, 1.7, 2).

Sample	x	Mass (mg)	SC Fraction (%)	T_c (K)
MTM142_4	1.5	25	52.2	19.9
MTM154_3	1.7	16	96.6	20.9
MTM143_3	2	16	72.1	22.9

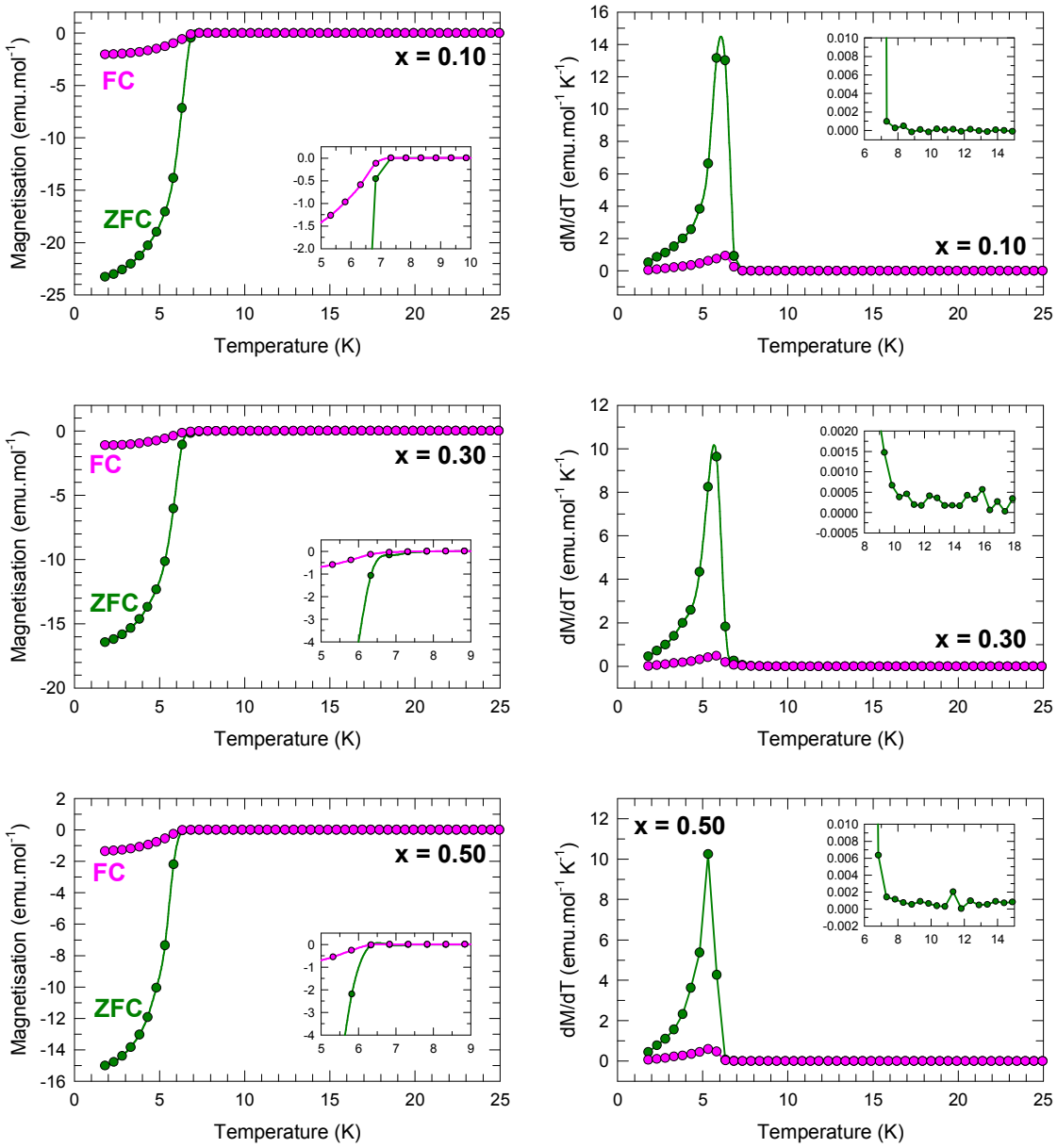

Fig 5.49: Temperature dependence of the 10 Oe ZFC (blue circles) and FC (red circles) DC magnetisation, *M* and its temperature derivative, d*M*/d*T* at ambient pressure for the compounds $Na_{2-x}K_xCsC_{60}$ (nominal x = 0.1, 0.3, 0.5) synthesised by "low temperature quenching".

Table 5.47: Superconducting fraction and T_c for quenched samples $Na_{2-x}K_xCsC_{60}$ (nominal x = 0.1, 0.3, 0.5).

Sample	x	Mass (mg)	SC Fraction (%)	T_c (K)
MTM131_3Q	0.1	24	68.4	7.3
MTM123_3Q	0.3	21	48.2	9.8
MTM119_4Q	0.5	17	44.0	7.3

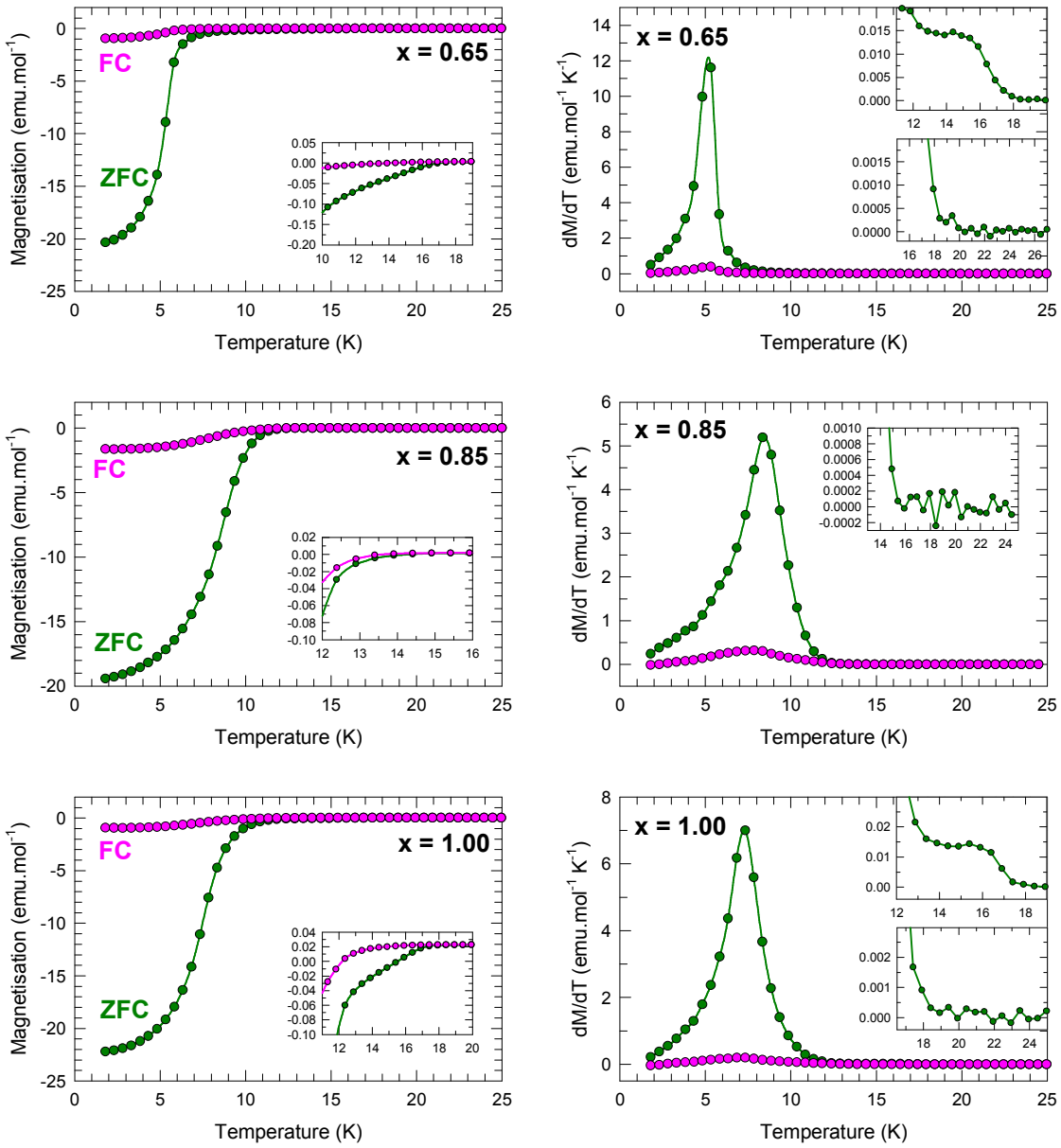

Fig 5.50: Temperature dependence of the 10 Oe ZFC (blue circles) and FC (red circles) DC magnetisation, *M* and its temperature derivative, d*M*/d*T* at ambient pressure for the compounds $Na_{2-x}K_xCsC_{60}$ (nominal x = 0.65, 0.85, 1) synthesised by "low temperature quenching".

Table 5.48: Superconducting fraction and T_c for quenched samples $Na_{2-x}K_xCsC_{60}$ (nominal x = 0.65, 0.85, 1).

Sample	x	Mass (mg)	SC Fraction (%)	T_c (K)
MTM149_3Q	0.65	30	59.4	13.4
MTM136_4Q	0.85	24	56.4	14.9
MTM132_3Q	1	22	64.6	13.4

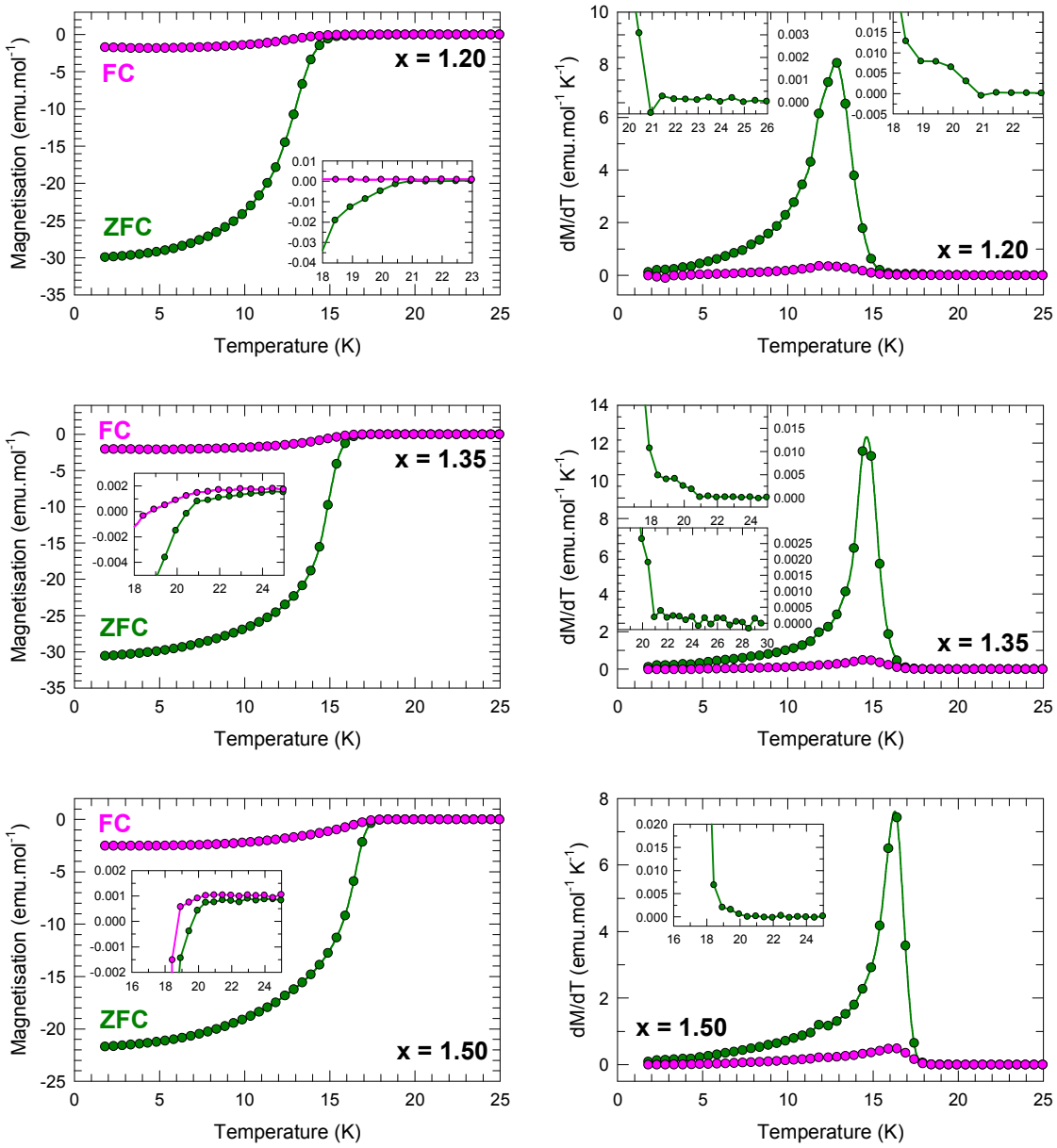

Fig 5.51: Temperature dependence of the 10 Oe ZFC (blue circles) and FC (red circles) DC magnetisation, *M* and its temperature derivative, d*M*/d*T* at ambient pressure for the compounds $Na_{2-x}K_xCsC_{60}$ (nominal x = 1.2, 1.35, 1.5) synthesised by "low temperature quenching".

Table 5.49: Superconducting fraction and T_c for quenched samples $Na_{2-x}K_xCsC_{60}$ (nominal x = 1.2, 1.35, 1.5).

Sample	x	Mass (mg)	SC Fraction (%)	T_c (K)
MTM145_3Q	1.2	25	86.4	18.4
MTM147_3Q	1.35	24	88.0	17.9
MTM142_4Q	1.5	21	62.5	18.4

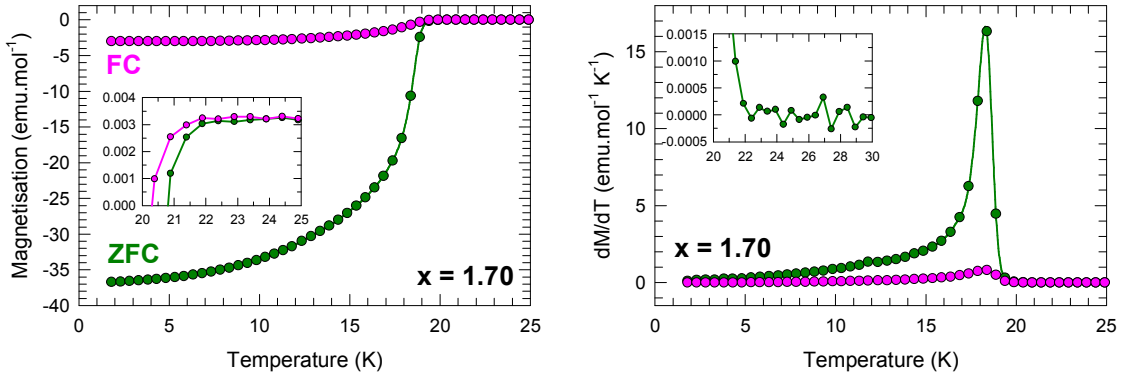

Fig 5.52: Temperature dependence of the 10 Oe ZFC (blue circles) and FC (red circles) DC magnetisation, *M* and its temperature derivative, d*M*/d*T* at ambient pressure for the compound $Na_{2-x}K_xCsC_{60}$ (nominal x = 1.7) synthesised by "low temperature quenching".

Table 5.50: Superconducting fraction and T_c for the quenched sample, $Na_{0.3}K_{1.7}CsC_{60}$.

Sample	x	Mass (mg)	SC Fraction (%)	T_c (K)
MTM154_3Q	1.70	23	96.1	21.4

As described in the opening section of the chapter, the rate of change of the T_c with unit cell volume is much steeper for materials that adopt the disordered $Fm\bar{3}m$ structure at ambient temperature (or the orientationally ordered $Pa\bar{3}$ structure at low temperatures). In order to push the isolation of these structures beyond the onset of the miscibility gap, differing synthetic protocols were employed (slow cooling vs quenching). The following diagrams provide a comparison of the ZFC magnetic measurements for compounds with the same composition (same preparation batch) but different thermal treatment.

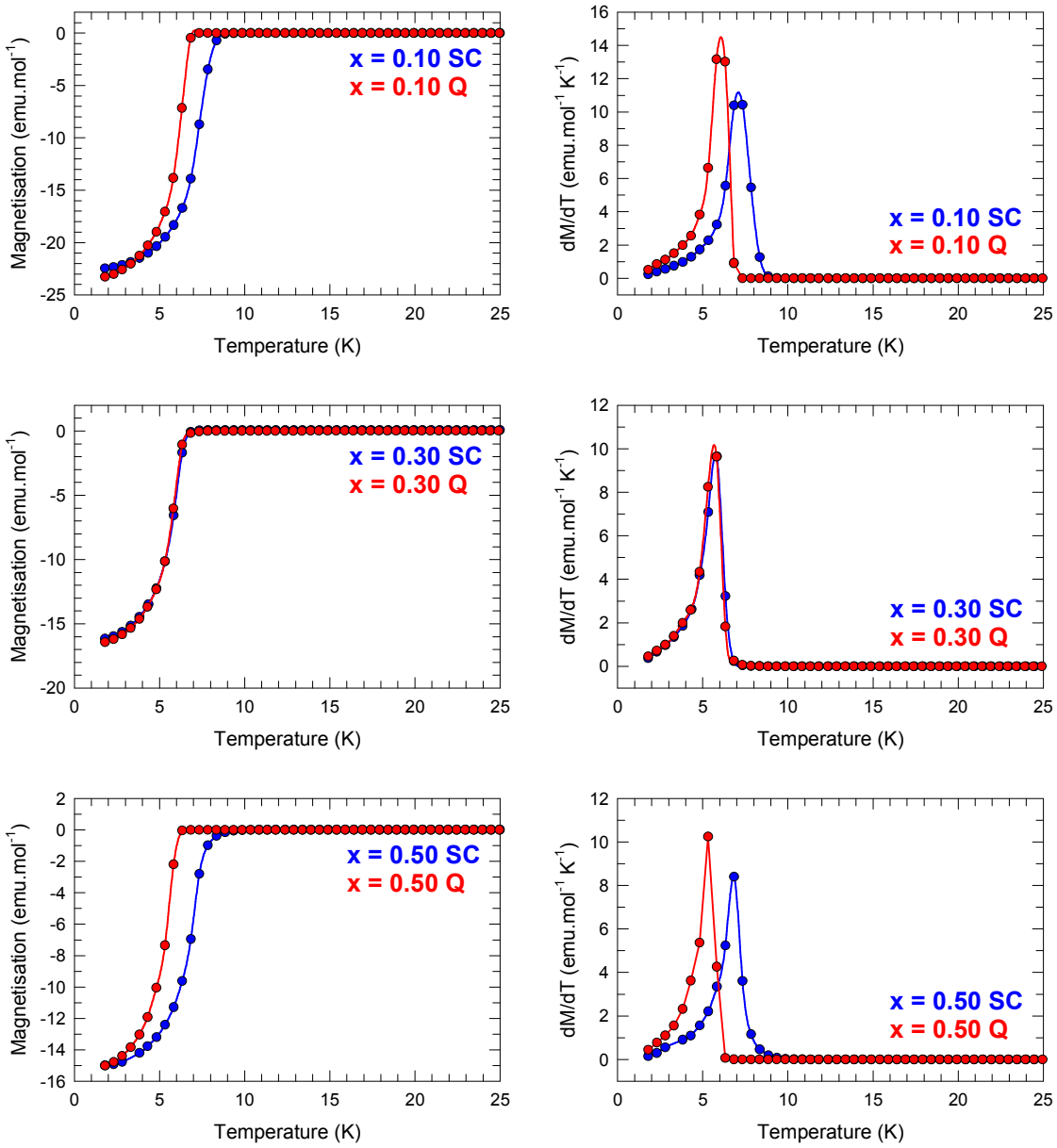

Fig 5.53: Comparison of the temperature dependence of the 10 Oe ZFC DC magnetisation, *M* and its temperature derivative, d*M*/d*T* at ambient pressure for the compounds $Na_{2-x}K_xCsC_{60}$ (nominal x = 0.1, 0.3, 0.5) synthesised by "slow cooling" (blue circles) and "low temperature quenching" (red circles).

Table 5.51: Superconducting Fraction and T_c for $Na_{2-x}K_xCsC_{60}$ samples (nominal x = 0.1, 0.3, 0.5).

Sample	x	SC Frac SC (%)	SC Frac Q (%)	T_c SC (K)	T_c Q (K)
MTM131_3	0.1	66.0	68.4	9.9	7.3
MTM123_3	0.3	47.7	48.2	10.4	9.8
MTM119_4	0.5	44.0	44.0	11.3	7.3

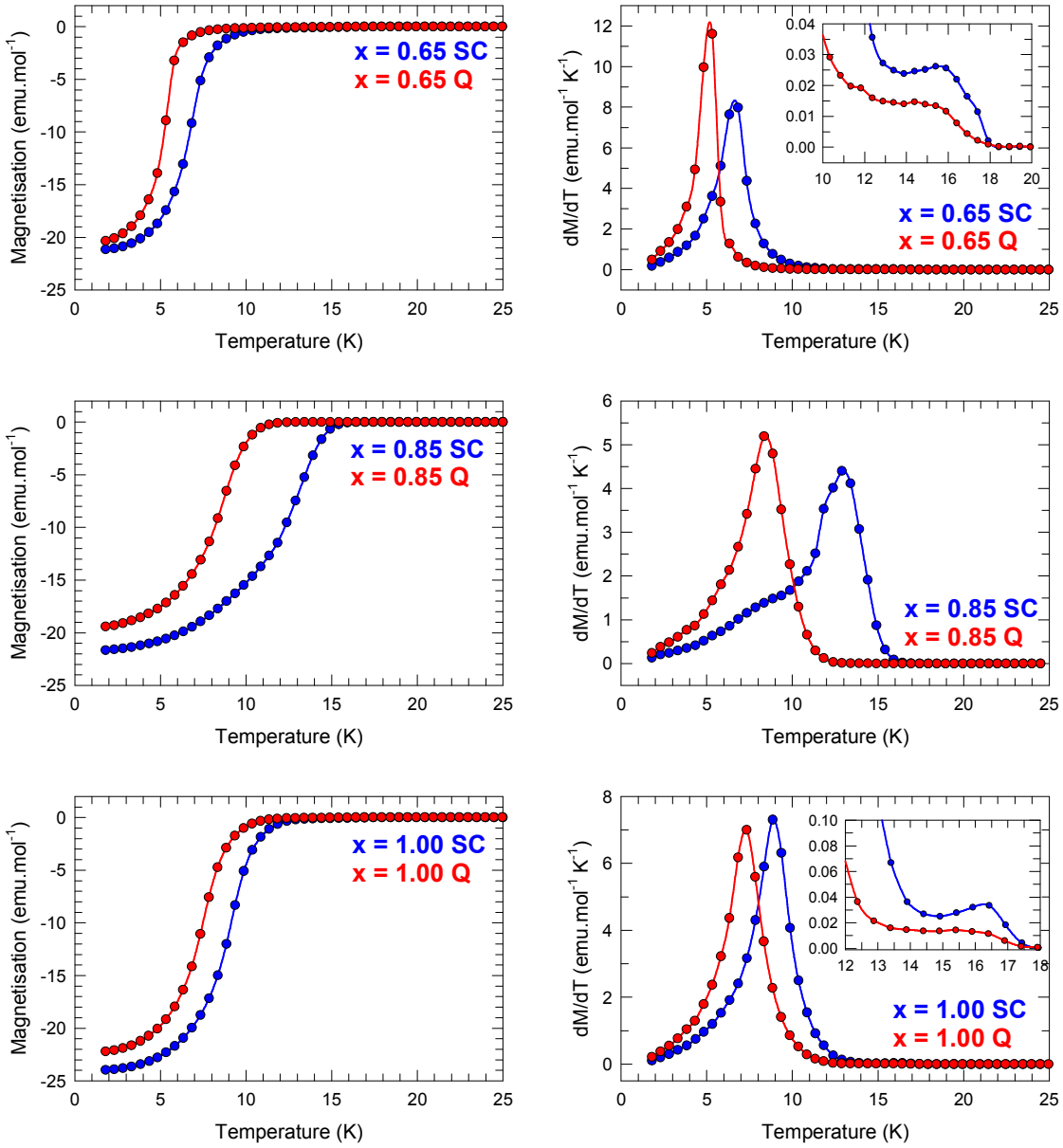

Fig 5.54: Comparison of the temperature dependence of the 10 Oe ZFC DC magnetisation, *M* and its temperature derivative, d*M*/d*T* at ambient pressure for the compounds $Na_{2-x}K_xCsC_{60}$ (nominal x = 0.65, 0.85, 1) synthesised by "slow cooling" (blue circles) and "low temperature quenching" (red circles).

Table 5.52: Superconducting Fraction and T_c for $Na_{2-x}K_xCsC_{60}$ samples (nominal x = 0.65, 0.85, 1).

Sample	x	SC Frac SC (%)	SC Frac Q (%)	T_c SC (K)	T_c Q (K)
MTM149_3	0.65	61.8	59.4	13.4	13.4
MTM136_4	0.85	62.9	56.4	16.9	14.9
MTM132_3	1	69.7	64.6	14.4	13.4

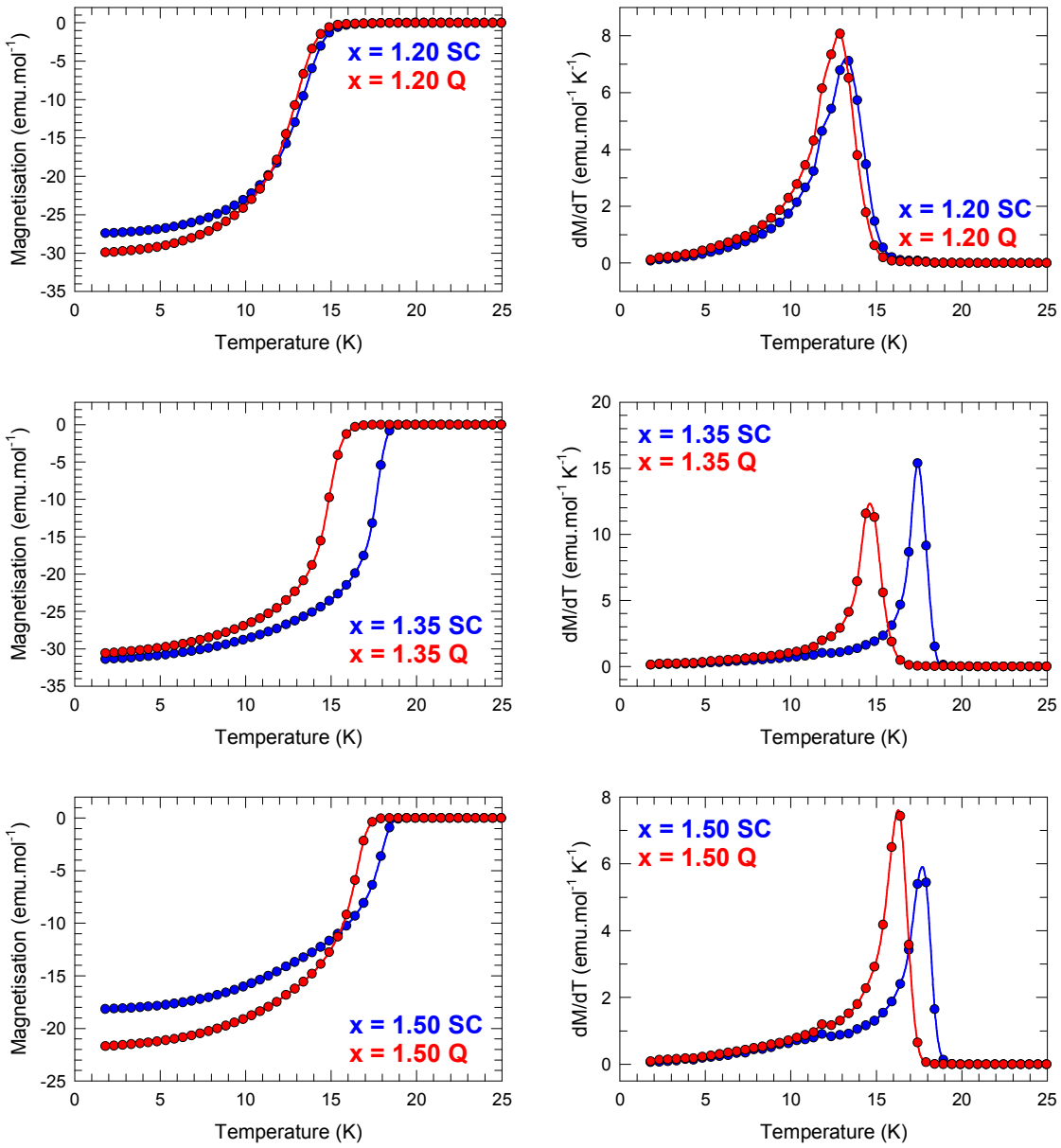

Fig 5.55: Comparison of the temperature dependence of the 10 Oe ZFC DC magnetisation, *M* and its temperature derivative, d*M*/d*T* at ambient pressure for the compounds $Na_{2-x}K_xCsC_{60}$ (nominal x = 1.25, 1.35, 1.5) synthesised by "slow cooling" (blue circles) and "low temperature quenching" (red circles).

Table 5.53: Superconducting Fraction and T_c for $Na_{2-x}K_xCsC_{60}$ samples (nominal x = 1.25, 1.35, 1.5).

Sample	x	SC Frac SC (%)	SC Frac Q (%)	T_c SC (K)	T_c Q (K)
MTM145_3	1.20	79.8	86.4	17.9	18.4
MTM147_3	1.35	90.4	88.0	19.9	17.9
MTM142_4	1.50	52.2	62.5	19.9	18.4

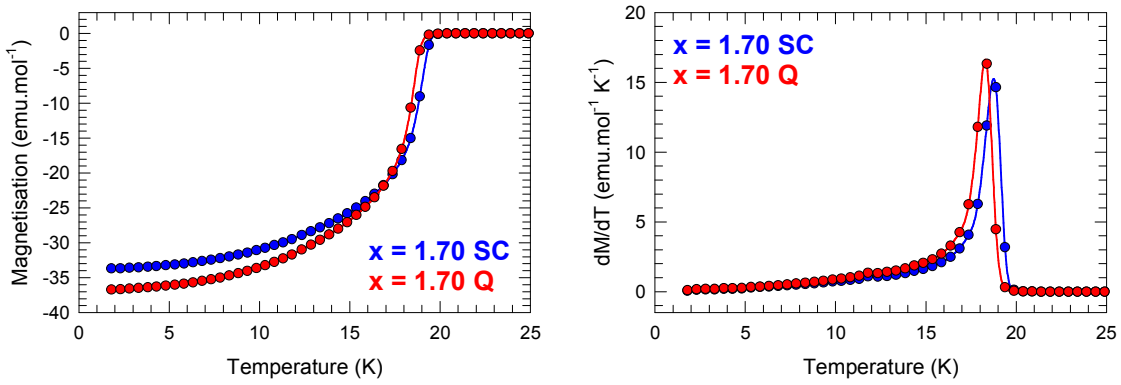

Fig 5.56: Comparison of the temperature dependence of the 10 Oe ZFC DC magnetisation, *M* and its temperature derivative, d*M*/d*T* at ambient pressure for the compounds $Na_{2-x}K_xCsC_{60}$ (nominal x = 1.25, 1.7) synthesised by "slow cooling" (blue circles) and "low temperature quenching" (red circles).

Table 5.54: Superconducting Fraction and T_c for $Na_{2-x}K_xCsC_{60}$ sample $Na_{0.3}K_{1.7}CsC_{60}$.

Sample	x	SC Frac SC (%)	SC Frac Q (%)	T_c SC (K)	T_c Q (K)
MTM154_3	1.70	96.6	96.1	20.9	21.4

5.15 Summary and Conclusions

The superconducting properties of the $Na_{2-x}K_xCsC_{60}$ series are affected by the reaction treatment of samples. In most studied compositions, quenching the sample leads to a slight suppression of the *onset* T_c. The functional form of the dM/dT function is quite instructive in this respect as it typically shows more than one change in slope. This could imply that more than one co-existing superconducting phase are present. Alternatively it could reflect grain boundary effects with higher onset T_c signalling intergrain superconductivity, followed at lower values by the onset of intragrain superconductivity. Quenching the samples, in nearly every case, affects the phase with the largest T_c (i.e. only data for lower T_c remains). This is best illustrated by the ZFC measurements of samples with x = 0.85. In the dM/dT vs T plot (Fig. 5.54), the slow-cooled sample shows two distinctive peaks that could arise from the presence of two superconducting phases. When the sample is quenched from high-temperature, only the low-T superconducting onset is evident. A similar situation is also encountered for

x = 0.65 where quenching leads to a sharper transition and the suppression of additional slope changes in the dM/dT vs T data.

For single phase samples in the low *x* part of the phase diagram (Fig 5.57(b)) such as $Na_{1.9}K_{0.1}CsC_{60}$, T_c appears to be somewhat suppressed upon quenching. Unfortunately structural data are not available for the quenched counter-parts of these samples precluding some discussion of the structural origin of this effect. If the samples at large *x* values are considered, such as $Na_{0.3}K_{1.7}CsC_{60}$, T_c was identical for both the slow-cooled and quenched cooling protocols. There is a slight narrowing in the dM/dT vs T plot; however, it can simply be attributed to enhanced homogeneity of the sample due to the increased annealing time at high temperature prior to quenching. If the superconducting fraction of each material is considered, shown in Fig 5.57(a), quenching has very little effect on the overall bulk superconductivity of the sample and there is no observable trend across the series. It is also worth noting that the relative fractions of the co-existing phases in the miscibility gap were essentially unaffected by the quenching protocol. Higher annealing temperatures may be required to homogenise the samples, but unfortunately such temperatures promote competing decomposition or amorphisation of the products; however, one effect of the quenching process was that the diffraction profiles were of somewhat better quality, consistent with improved crystallinity.

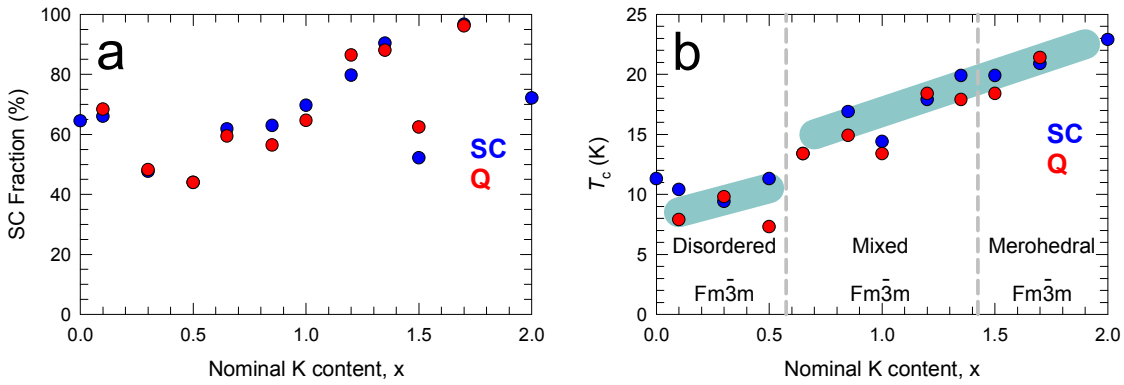

Fig 5.57: (**a**) Superconducting fraction versus sample composition for the two cooling protocols. (**b**) T_c versus sample composition for the two cooling protocols. In both graphs blue represents slow cooling, red quenching and the thick blue lines are guides to the eye. (error bars included, but smaller than points).

Fig 5.57(b) shows the evolution of T_c with nominal K doping level, x for the entire series of compositions. There is a quasi-linear dependence of the T_c on x with a pronounced discontinuity – a sharp increase in T_c by 3.3 K – appearing on entering the miscibility gap at x ~0.65. No comparable discontinuity appears on crossing into the single-phase merohedral systems above x ≈ 1.5. As the refined Na and K content of each phase has several errors associated with it, a better representation of the T_c dependence on composition can be obtained by considering how T_c varies as a function of the changes in the interfullerene separation, commonly plotted in these instances as the volume occupied per C_{60} molecule (Fig 5.58). The trends observed in these instances are quasi-linear and the rate of change of T_c is typical of that observed in merohedral $Fm\bar{3}m$ systems with systematic chemical substitution at the cationic sites. Fig 5.59 collects additional literature data for known A_3C_{60} phases. It is observed that the established trend does not follow that seen in $Na_2Rb_{1-x}Cs_xC_{60}$, where one observes a much steeper rate of change of T_c with cell volume. Instead, chemical substitution at the tetrahedral cavity in the system $Na_{2-x}K_xCsC_{60}$ mimics the effect of chemical and physical pressure observed in merohedral $Fm\bar{3}m$ materials.

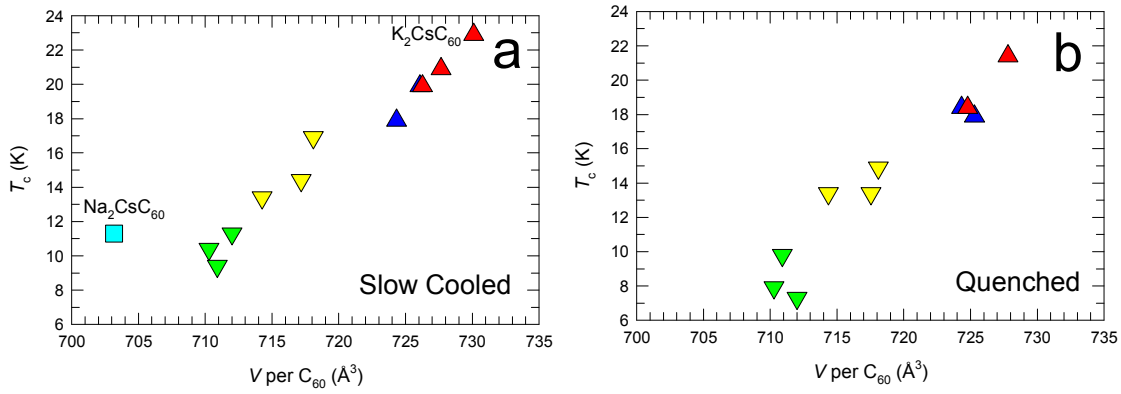

Fig 5.58: Change in T_c with volume per C_{60} at room temperature for both (**a**) slow cooled and (**b**) quenched samples. (**a+b**) Down (Up) triangles represent the disordered (merohedral) $Fm\bar{3}m$ model, squares $Pa\bar{3}$. Red accounts for the single phase merohedral $Fm\bar{3}m$ model. Yellow (Blue) accounts for the disordered (merohedral) $Fm\bar{3}m$ phase of the two-phase materials. The T_c's of the two-phase materials are attributed to whichever is the majority phase. (error bars included, but smaller than points).

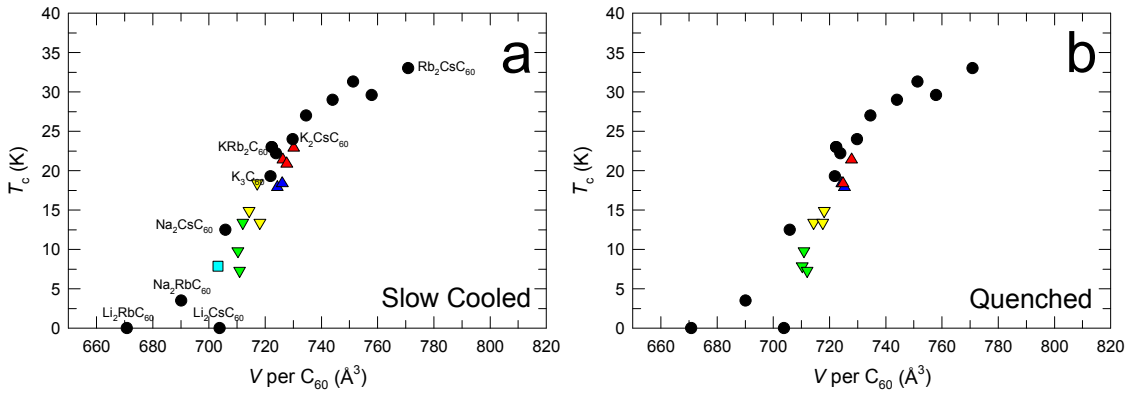

Fig 5.59: Change in T_c with K volume per C_{60} at room temperature for both (**a**) slow cooled and (**b**) quenched samples. (**a+b**) Down (Up) triangles represent the disordered (merohedral) *Fm* $\bar{3}$ *m* model, squares *Pa* $\bar{3}$. Red accounts for the single phase merohedral *Fm* $\bar{3}$ *m* model. Yellow (Blue) accounts for the disordered (merohedral) *Fm* $\bar{3}$ *m* phase of the two-phase materials. The black markers represent a silhouette of literature values for the T_c vs V per C_{60} of other *Fm* $\bar{3}$ *m* materials. The T_c's of the two-phase materials are attributed to whichever is the majority phase.

5.16 References

[1] Fleming R. M., Ramirez A. P., Rosseinsky M. J., Murphy D. W., Haddon R. C., Zahurak S. M., Makhija A. V. *Nature* **1991**, 352, 787-788

[2] Sparn G., Thompson J. D., Huang S. M., Kaner R. B., Diederich F., Whetten R. L., Gruner G., Holczer K. *Science* **1991**, 252, 1829-1831

[3] Zhou O., Vaughan G. B. M., Zhu Q., Fischer J. E., Heiney P. A., Coustel N., McCauley J. P., Smith A. B. *Science* **1992**, 255, 833-835

[4] Chen C. C., Kelty S. P., Lieber C. M. *Science* **1991**, 253, 886-888

[5] Movshovich R., Thompson J. D., Chen C. C., Lieber C. M. *Phys. Rev. B* **1994**, 49, 3619-3621

[6] Shannon R. D., *Acta Cryst. A* **1976**, 32, 751-767

[7] Heiney P. A., Fischer J. E., McGhie A. R., Romanow W. J., Denenstein A. M., McCauley J. P., Smith A.B., Cox D. E. *Phys. Rev. Lett.* **1991**, 66, 2911-2914

[8] Fischer J. E., Heiney P. A., *Phys. Chem. Solids* **1993**, 54, 1725-1757

[9] Prassides K., Christides C., Thomas I. M., Mizuki J., Tanigaki K., Hirosawa I., Ebbesen T. W. *Science* **1994**, 263, 950-954

[10] Tanigaki K., Hirosawa I., Ebbesen T. W., Mizuki J. I., Tsai J. S. *J. Phys. Chem. Solids* **1993**, 54, 1645-1653

[11] Stephens P. W., Mihaly L., Lee P. L., Whetten R. L., Huang S. M., Kaner R., Deiderich F., Holczer K. *Nature* **1991**, 351, 632-634

[12] Zhou O., Cox D. E. *J. Phys. Chem. Solids* **1992**, 53, 1373–1390

[13] Murphy D. W., Rosseinsky M. J., Fleming R. M., Tycko R., Ramirez A. P., Haddon R. C., Siegrist T., Dabbagh G., Tully J. C., Walstedt R. E. *J. Phys. Chem. Solids* **1992** 53, 1321-1332

[14] Diederichs J., Schilling J. S., Herwigs K. W., Yelons W. B. *J. Phys. Chem. Solids* **1997**, 58, 123-132

[15] Brown C. M., Takenobu T., Kordatos K., Prassides K., Iwasa Y., Tanigaki K. *Phys. Rev. B* **1999**, 59, 4439-4444

[16] Mizuki J., Takai M., Takahashi H., Mori N., Tanigaki K., Hirosawa I., Prassides K. *Phys. Rev. B* **1994**, 50, 3466-3469

[17] Yildirim T., Fischer J. E., Dinnebier R., Stephens P. W., Lin C. L. *Solid State Commun.* **1995**, 93, 269-274

Chapter 6

Summary, conclusions and future directions

6.1 Summary, conclusions and future directions

6.1.1 Overview of previous work

The discovery of C_{60} gave scientists the opportunity to explore the physical and chemical properties of a new carbon allotrope. Arguably superconductivity was one of the most important physical properties discovered during these investigations on compounds of C_{60}. This has led to a very extensive study of intercalated C_{60} salts of varying stoichiometries, (A_xC_{60}, A = alkali metal, $6 \geq x \geq 0$). Surprisingly metallic compositions are only encountered for the salts with stoichiometry A_3C_{60}, which become superconducting with a maximum T_c of 38 K for Cs_3C_{60} at elevated pressures. The high T_c values record for these bulk molecular superconductors are only surpassed by the atom-based high-T_c cuprates, MgB_2 and the iron pnictides.

The $A_2A'C_{60}$ salts (A, A' = alkali metal) can be divided into three structural families based on the orientations adopted by the C_{60} molecules and hence the resulting space group of the solids. The first family is encountered for A, A' = K, Rb, and Cs; these compounds adopt a merohedrally disordered FCC structure (space group $Fm\bar{3}m$). In these systems, the size of the T_d cavity (r = 1.12 Å) is not large enough to accommodate K^+ (r = 1.38 Å), Rb^+ (r = 1.49 Å) and Cs^+ (r = 1.70 Å) without structural deformation. As a result the rotational motion of the C_{60}^{3-} anions is restricted due to the steric repulsions between the intercalated ions and the fulleride units. The second family of superconductor (with A = Na^+ and A' = K^+, Rb^+, Cs^+) adopts an orientationally ordered primitive cubic structure ($Pa\bar{3}$) at low temperatures. In these systems the ionic radius of Na^+ (r = 1.02 Å) is smaller than the size of the T_d cavity and as a result the C_{60}^{3-} anions can rotate unhindered and therefore optimise the intermolecular fulleride-fulleride interactions. Tuning the lattice size by varying A' in these systems leads to a much steeper rate of change of T_c with interfulleride separation. The third family is encountered when A = Li^+ - these compounds adopt a spherically disordered FCC structure (space group $Fm\bar{3}m$), but they do not display any superconducting properties. It is worth noting that in all three families the O_h cavity (r = 2.06 Å) can easily accommodate K^+, Rb^+ and Cs^+ without affecting the structural properties.

Synthesis of highly expanded crystalline A_3C_{60} systems such as Cs_3C_{60} has remained elusive until recently where new solution-based low-temperature synthetic protocols involving solvents such as NH_3 and $MeNH_2$ were developed. The T_c of these systems reaches a maximum of 38 K for Cs_3C_{60} at elevated pressures; however, the phase identified as being responsible for this is not the FCC-structured material but rather the BCC-based one (space group $Pm\bar{3}n$). At ambient pressure, the low temperature electronic ground state is that of an antiferromagnetic insulator (AFI). Application of pressure suppresses the AFI state and induces a transition to the superconducting state; the transition appears to be of 1st-order and both antiferromagnetism and superconductivity co-exist over a limited pressure range.

6.1.2 Results of work contained in this thesis

One of the directions taken in this work was to try to explore in some detail structural and electronic properties of fulleride materials with composition $Rb_xCs_{3-x}C_{60}$. Two sets of crystalline materials were synthesised focusing on optimisation of the synthetic conditions to obtain BCC-structured A15 and FCC phases. One set of synthetic conditions utilised ammonia as the solvent (leading to phase mixtures rich in the FCC component), the other methylamine (leading to phase mixtures rich in the A15 phase). The ammonia-produced samples were annealed at 400^{o}C for 2-3 weeks, while the methylamine-synthesised samples were annealed at the much lower temperature of 180^{o}C for only 48 hours. In the case of the FCC-rich samples, the higher temperatures and longer annealing protocols enhanced the fraction and crystallinity of the FCC phase. In comparison shorter and lower temperature annealing protocols were utilised for the A15-rich materials as higher annealing temperatures disfavoured the formation of the A15 phase. For both sets of samples the non-superconducting BCO Cs_4C_{60} phase (space group *Immm*) is also present accounting for 7-35% of each material.

The unit cell volume of the FCC phases decreases monotonically with increasing Rb doping level. This trend is followed irrespective of whether the FCC component in

the multiphase mixtures is in majority or minority fraction. The effects of both physical and chemical pressure on the properties of the FCC phase have been successfully studied. As the Rb doping level increases, the maximum observed T_c decreases, e.g. the sample with nominal stoichiometry, $Rb_{0.50}Cs_{2.50}C_{60}$ shows a maximum T_c = 31.8 K (at 0.46 kbar), reduced from that of the parent material, Cs_3C_{60} at T_c = 35.7 K (at 0.73 kbar). Additionally, the unit cell volume where the maximum T_c occurs in each FCC-structured $Rb_xCs_{3-x}C_{60}$ phase increases as the amount of Rb decreases, and the composition of the parent material Cs_3C_{60} isolated. Each expanded FCC $Rb_xCs_{3-x}C_{60}$ phase displays a characteristic dome-like relationship between T_c and interfullerene separation, consistent with the importance of electronic correlations in determining the properties of these systems.

On the other hand, the samples in which the A15 $Rb_xCs_{3-x}C_{60}$ phases were targeted synthetically exhibited very little variation in properties as the nominal Rb doping level changed. For instance, the synchrotron X-ray diffraction measurements showed a variation in cell volume across the series of less than 0.1%. As explained in *chapter 4*, the A15 phase is not expected to exert the same lattice constant variation with Rb doping levels that is seen in the FCC; however, the low temperature refinements emphasise that the electron density in the distorted tetrahedral sites also exhibits very little variation. Additionally, the high pressure magnetisation measurements also provide evidence that the attempts to obtain solid solutions with the A15 structure were not successful and Rb is not introduced into these samples. The T_c has the same maximum value (38 K) and approximately occurs at the same cell pressure for all samples.

The second part of the work contained in this thesis is on the doping dependence of the $Pa\bar{3}$ to $Fm\bar{3}m$ structural transition by synthesizing the quaternary fulleride family, $Na_{2-x}K_xCsC_{60}$. It has been known for time that the T_c for the $Pa\bar{3}$ series displays a much steeper rate of change with changes in the interfulleride separation when compared to the family of merohedral $Fm\bar{3}m$ systems. Moreover, Na_2CsC_{60} is a key material in this family since it has the highest recorded T_c of a $Pa\bar{3}$ material. In order to try to extend the stability limit of the $Pa\bar{3}$ series, Na^+ was substituted by K^+ in a stepwise manner until the parent material K_2CsC_{60} composition (which has the

merohedral $Fm\bar{3}m$ structure) was reached. It is worth emphasising that in this particular case the isovalent chemical substitution in the T_d cavity was undertaken, something that has not been carried out before for the $Pa\bar{3}$ systems. The steep rate of change of T_c with cell volume has been observed before upon isovalent chemical substitution in the O_h cavity. As materials synthesised range across two different structural families, different cooling protocols were also utilised to probe the behaviour in the miscibility gap region. The magnetic properties of the materials were studied by SQUID magnetometry and the phase compositions by synchrotron X-ray powder diffraction.

It was found that chemical substitution in the T_d cavity for both slow cooled and quenched materials did not lead to the same steep rate of change of T_c with interfulleride separation, which has been reported before for materials with composition $Na_2Rb_xCs_{1-x}C_{60}$. Instead the results are more comparable to those obtained upon the application of external pressure on the parent Na_2CsC_{60}, where the rate of change of T_c with cell volume is comparable to that established for the merohedral $Fm\bar{3}m$ systems. In addition, including a quenching procedure in the sample preparation did not lead to any significant improvements. In the majority of the slow-cooled samples evidence was found for the presence of two superconducting phases; quenching the sample in every case enhanced the phase with the smallest T_c. In comparison to the literature results, the conclusion drawn is that the synthesis of $Pa\bar{3}$ materials with enhanced superconducting properties has not been successful. It appears therefore that cationic substitution only leads to drastic changes in T_c when the ions are co-intercalated in the octahedral cavity.

6.1.3 Future directions

Even though the present work offered a better understanding of the formation of the A15 Cs_3C_{60} phase, it has not been possible to obtain a series of solid solutions

with controlled Rb content. As the A15 structurally family has distinct electronic properties from those exhibited by the FCC analogues, it is of paramount importance to search for synthetic conditions (by altering the solvent employed and the subsequent heat treatment of the precursor) which will allow access – and therefore detailed structural and electronic studies – of this family of materials.

On the other hand, the FCC Cs_3C_{60} polymorph was found to be easily amenable to Rb substitution yielding a series of solid solutions. More extensive work is currently required for further characterisation of these FCC-rich materials. This should include a detailed study of the ambient pressure electronic and magnetic properties and a detailed comparison with the A15 phase. Given that the FCC structure is a frustrated topology for the development of antiferromagnetic order, it will be very interesting to search for signatures of this frustration (e.g. absence of long range AFM order in contrast to the AFM order observed in the A15 analogue below 46 K). In addition, high pressure X-ray diffraction studies are needed to confirm the absence of any structural transition accompanying the emergence of the superconducting state. Last but not least, further synthetic attempts - possibly deriving from the protocols established here – should be explored in making samples that are even richer in the FCC component with the ultimate aim being to obtain phase pure materials. Given the success achieved using ammonia- and methylamine-based precursors, additional solvent media need to be explored – these may include ethylamine ($EtNH_2$), dimethylamine, and trimethylamine, but also mixtures of solvents, such as ammonia and methylamine in various proportions.